Dissertation

submitted to the

Combined Faculty of Natural Sciences and Mathematics

of Heidelberg University, Germany

for the degree of

Doctor of Natural Sciences

Put forward by

Sven Spachmann

born in Mühlacker

Oral examination: July 13, 2021

Thermal Expansion and Magnetostriction of Layered Correlated Electron Systems

Referees: Prof. Dr. Rüdiger Klingeler

Prof. Dr. Maurits W. Haverkort

Thermal Expansion and Magnetostriction of Layered Correlated Electron Systems

This work presents high-resolution thermal expansion and magnetostriction studies revealing magnetoelastic coupling and thermodynamic properties of single-crystals of the correlated electron systems Gd_2PdSi_3, $Cu_3Bi(SeO_3)_2O_2Cl$, and $Cr_2Ge_2Te_6$. Magnetization and specific heat measurements complement the dilatometric investigations. Gd_2PdSi_3 is a metallic antiferromagnet with a complex phase diagram which shows three phase transitions already in zero-field. Among other magnetic orders it evolves a skyrmion lattice phase when a magnetic field is applied. This skyrmion lattice phase is strongly enhanced under the application of uniaxial pressure. New phase boundaries in the phase diagram are found and magnetoelastic coupling is quantified. The antiferromagnetic insulator $Cu_3Bi(SeO_3)_2O_2Cl$ is a multiferroic which shows geometric frustration. Its high-temperature structural phase transition is strongly affected by uniaxial pressure, whereas pressure only has small effects on the antiferromagnetic (AFM) transition at low temperatures. The low-temperature AFM phase exhibits a metamagnetic spin-flip transition for $B \parallel c$. Mixed-phase behavior and linear magnetoelastic coupling are observed in the transition region. Furthermore, the magnetic phase diagrams for the a- and b-axis of $Cu_3Bi(SeO_3)_2O_2Cl$ are constructed for the first time. $Cr_2Ge_2Te_6$ is a layered quasi-two-dimensional van der Waals material with a uniaxial magnetic anisotropy. The magnetoelastic coupling in $Cr_2Ge_2Te_6$ is directly measured and correlations up to high temperature are observed. Furthermore, the critical behavior around the ferromagnetic phase transition is analyzed and a Grüneisen analysis shows that applying uniaxial pressure leads to large changes in the critical temperature.

Thermische Ausdehnung und Magnetostriktion an geschichteten elektronisch korrelierten Systemen

In der vorliegenden Arbeit werden hochauflösende Messungen der thermischen Ausdehnung und Magnetostriktion an Einkristallen der elektronisch korrelierten Systeme Gd_2PdSi_3, $Cu_3Bi(SeO_3)_2O_2Cl$ und $Cr_2Ge_2Te_6$ vorgestellt. Hierbei werden sowohl die magnetoelastische Kopplung als auch thermodynamische Eigenschaften untersucht. Messungen der Magnetisierung sowie der spezifischen Wärme ergänzen die Dilatometrie. Gd_2PdSi_3 ist ein metallischer Antiferromagnet mit einem komplexen Phasendiagramm, das bereits im Nullfeld drei Phasenübergänge aufweist. Neben anderen magnetischen Ordnungen entwickelt Gd_2PdSi_3 in einem angelegten Magnetfeld eine Skyrmionengitter-Phase. Diese Phase wird durch uniaxialen Druck deutlich stabilisiert. Im Phasendiagramm werden neue Phasen entdeckt und die magnetoelastische Kopplung wird quantifiziert. Der antiferromagnetische Isolator $Cu_3Bi(SeO_3)_2O_2Cl$ ist ein multiferroisches Material mit geometrisch frustrierten Spins. Sein struktureller Phasenübergang bei hohen Temperaturen wird durch uniaxialen Druck stark verändert, wohingegen Druck nur schwache Auswirkungen auf den antiferromagnetischen (AFM) Phasenübergang bei tiefen Temperaturen hat. Die antiferromagnetische Phase bei tiefen Temperaturen zeigt einen metamagnetischen Spin-Flip-Übergang für $B \parallel c$. Im Bereich dieses Übergangs werden Mischphasen-Verhalten und eine lineare magnetoelastische Kopplung beobachtet. Des Weiteren werden die Phasendiagramme der a- und b-Achse zum ersten Mal erstelllt. $Cr_2Ge_2Te_6$ ist ein geschichtetes quasi-zweidimensionales van der Waals-Material mit uniaxialer magnetischer Anisotropie. Die magnetoelastische Kopplung in $Cr_2Ge_2Te_6$ wird direkt gemessen, wobei Korrelationen bis zu hohen Temperaturen beobachtet werden. Weiterhin wird das kritische Verhalten in der Nähe des ferromagnetischen Phasenübergangs analysiert und eine Grüneisenanalyse zeigt, dass uniaxialer Druck zu starken Änderungen der kritischen Temperatur führt.

Introduction

The research of correlated electron systems is an exciting and versatile field. On the one hand there is the quest for new materials which show exotic and novel properties, e.g., low-dimensional behavior and the realization of theoretically predicted phenomena such as the quantum spin liquid state [1]. On the other hand the efforts are plentiful to control and engineer these phenomena and to harness them for technological applications. Two special low-dimensional magnetic phenomena became particularly known to the public through the 2016 Nobel prize in physics which was awarded to the condensed matter physicists Haldane, Kosterlitz and Thouless *"for theoretical discoveries of topological phase transitions and topological phases of matter"*. Kosterlitz and Thouless had discovered that for antiferromagnetically coupled XY spins, i.e., spins constrained to a plane, an arrangement of magnetic vortices and antivortices forms in the plane upon cooling. These vortices contact each other at the Berezinskii-Kosterlitz-Thouless temperature and form a unique quasi-long-range ordered state [2–4]. Haldane, on the other hand, had investigated one-dimensional systems and found a fundamental difference between the excitations of integer and half-integer spin chains [5, 6]. These are only two of the many spectacular phenomena observed in correlated electron systems. Other intriguing phenomena include metal-to-insulator (Mott) transitions, heavy fermion behavior, superconductivity, and multiferroic effects [7].

In general, correlated electron materials are complex many-body systems in which models of non-interacting electrons, such as the free electron gas, are not applicable but electronic interactions have to be taken into account explicitly. Exactly computing the properties of such complex many-body systems on an atomic level is a matter of impossibility. Simplified models such as the Hubbard model or the Heisenberg model with effective Hamiltonians are therefore often applied to simplify the complexities and to reduce the degrees of freedom [8]. Statistical mechanics provides the principles and tools to then derive specific macroscopic thermodynamic properties from atomic or molecular behavior [9]. The behavior of the electrons themselves in electronically correlated systems can lie on wide a spectrum between two extremes: one extreme is the fully localized state, in which electrons are tightly bound to an atom. For such electronic states notions from atomic physics can be applied. The other extreme is

the delocalized state of itinerant electrons, where conventional band theory serves as a starting point to which correlation effects are added [7]. The delocalization of electrons is directly related to the exchange integral, i.e., the overlap of the electronic wave functions, and therefore also to the distance between atoms. This links the electronic state to the crystal lattice and elastic properties, and it introduces a route through which chemical or mechanical pressure can have large effects on the state of a system, especially on ordering phenomena.

Magnetic ordering phenomena, which are studied in this work on three particular materials, represent a large area in correlated electron systems research. Long-range magnetic orders can be manifold spanning from simple collinear and commensurate ferromagnetic or antiferromagnetic orders to complex and possibly incommensurate chiral or conical spin alignments. The research of some subgroups of these ordering phenomena has evolved more rapidly than others, e.g., the investigation of skyrmion systems is a field of research in its own right by now and skyrmionic spintronics applications may be available in the midterm future [10].

Competing interactions are a key ingredient for the more complex magnetic ordering phenomena. Geometric frustration is one example where the lattice geometry does not allow the magnetic exchange interactions to be completely satisfied as, e.g., for antiferromagnetically coupled spins on an equilateral triangular lattice. This leads to low ordering temperatures or in extreme cases even spin-liquid ground states. Besides the two-dimensional edge-sharing or corner-sharing triangular lattices, with the Kagomé lattice belonging to the latter, the FCC and pyrochlore lattices are three-dimensional lattices which have brought forth many compounds that exhibit strong geometric frustration [11, 12].

The first material studied in this work belongs to the class of rare-earth ternary intermetallics R_2TX_3 (R = rare-earth element, T = transition metal, X = Si, Ge, Ga, In) where both localized $4f$ electrons from the rare-earths and delocalized (transition metal) conduction electrons are present [13]. This introduces an indirect coupling mechanism between the $4f$ electrons via the conduction electrons, i.e., the Ruderman-Kittel-Kasuya-Yosida (RKKY) interaction. Depending on the interatomic distance and the size of the electronic orbitals these interactions can be ferromagnetic (FM) or antiferromagnetic (AFM). If the $4f$ ions are arranged appropriately, e.g., on a triangular lattice, geometric frustration may come into play. Gd_2PdSi_3 is an intriguing example where the RKKY interaction and geometric frustration lead to a skyrmion phase in a complex phase diagram of competing phases [14]. Many of the properties of Gd_2PdSi_3 have been established but the coupling between the spin and lattice degrees of freedom, the magnetoelastic coupling, has not been investigated. This is gap is filled in this work, along with a detailed thermodynamic analysis, especially of the skyrmion lattice phase.

Geometric frustration also plays an important role in the buckled-Kagomé antiferromagnet $Cu_3Bi(SeO_3)_2O_2Cl$, where competing FM and AFM interactions lead to an exotic canted antiferromagnetic order at low temperatures [15, 16]. Beyond this exotic magnetic order it also exhibits antiferroelectric [16] and even multiferroic [17] properties. This complex interplay of charge, spin and lattice degrees of freedom in $Cu_3Bi(SeO_3)_2O_2Cl$ is very inviting for an in-depth study of its magnetoelastic properties which are presented in this thesis.

Where magnetic interactions along one or two spatial dimensions are negligibly weak (quasi-)low-dimensional magnetism results. According to the theorem formulated by Mermin and Wagner a one- or two-dimensional system of isotropic (= Heisenberg) spins cannot order, neither ferro- nor antiferromagnetically, at a non-zero temperature [18]. However, if the spins have a preferred orientation and the system is not isotropic, long-range order, or at least quasi-long-range order as the one investigated by Berezinskii, Kosterlitz and Thouless for 2D XY spins [2–4], may result. The most extreme case of scalar, i.e., one-dimensional, spins is described by the well-known one-dimensional Ising model. In this model long-range order only develops at zero temperature. Ising spins on a two- or three-dimensional lattice, in contrast, order at a finite temperature, where the ordering temperature is comparable to the value of the exchange interaction parameter J [6, 19]. To transition from isotropic to anisotropic spin behavior a form of magnetic anisotropy needs to be introduced to a system. Magnetic anisotropy may arise from a single-ion anisotropy, i.e., the coupling of the crystal field to the spin direction via spin-orbit coupling, dipole-dipole interactions, shape anisotropy or from anisotropic exchange interactions.

The here reported ferromagnetic semiconductor $Cr_2Ge_2Te_6$ presents an interesting system with respect to anisotropy and low-dimensional order. $Cr_2Ge_2Te_6$ is a quasi-two-dimensional layered van der Waals material for which long-range order down to the bilayer has been proven [20]. Moreover, it exhibits a uniaxial magnetic anisotropy perpendicular to the van der Waals layers [21], which reorients to point along the in-plane directions under hydrostatic pressure above 1 GPa [22]. A study of the uniaxial pressure dependence of the critical temperature and critical magnetic field is presented in this work along with an investigation of its magnetoelastic properties.

Gd_2PdSi_3, $Cu_3Bi(SeO_3)_2O_2Cl$, and $Cr_2Ge_2Te_6$ belong to classes of correlated electron systems which hold great potential for future technological applications. Skyrmion materials are especially considered for 'abacus'-type applications such as the racetrack memory in information storage and logic technologies, as well as for nanoscale radio-frequency devices [10, 23]. Multiferroics hold the promise of low-power electric-field control of magnetism, but are also available for the opposite effect, i.e., magnetic-field control of electrical properties, which can be applied in bio-medical applications such as *in vivo* target drug delivery and enhanced scaffolds for tissue engineering.

The integration into photovoltaic devices is also investigated [24]. Lastly, quasi-two-dimensional magnetic materials are envisioned to be used in low-power spintronic and magnonic devices compatible with the complementary metal-oxide semiconductor (CMOS) technology [25].

Although the three materials studied in this work, a metal, a semiconductor and an insulator, are extremely different concerning their electronic properties, they are united by the presence of spin-lattice coupling, the competition between different degrees of freedom and critical phenomena at continuous phase transitions. Detecting phase transitions and understanding their nature is an essential part in the effort to fundamentally understand the interactions and mechanisms in correlated electron systems. This process is usually a jigsaw puzzle of results from many macroscopic and microscopic measurement techniques. For investigations of macroscopic properties thermodynamic response functions such as the thermal expansion and magnetostriction coefficients have proven highly valuable. They not only measure the pressure dependence of the entropy or magnetization of a thermodynamic system but also allow to directly observe the structural changes and effects of the coupling to the crystal lattice of the spin, charge or orbital degrees of freedom [9]. Capacitance dilatometry is capable of resolving relative length changes on the order of $\Delta L/L \approx 10^{-8}$ to 10^{-9}, i.e., tenths of an ångström or even below for the usually millimeter-sized samples, which is much smaller than the average atomic distance in solids [26]. This high-resolution and sensitivity allows for a detailed investigation of the phase diagram of solid-state systems as well as of their thermodynamic properties. High-resolution thermal expansion and magnetostriction measurements are applied throughout this work, complemented by magnetization and specific heat measurements where needed.

This work is structured as follows: In the **first chapter** a theoretical background on thermodynamics and phase transitions is established which provides the basis for understanding the measurements and results. **Chapter two** introduces the experimental method of high-resolution capacitance dilatometry and the setup used for the experiments. In the **third chapter** an investigation of the phase diagram, thermodynamic properties and magnetoelastic coupling in the skyrmion-hosting intermetallic Gd_2PdSi_3 is presented, with an emphasis on the effect of pressure on the skyrmion lattice phase. **Chapter four** contains a detailed analysis of the phase transitions in the multiferroic antiferromagnet $Cu_3Bi(SeO_3)_2O_2Cl$ with an additional focus on the magnetoelastic coupling and mixed-phase behavior for magnetic fields applied along the *c*-axis. In **chapter five** the quasi-two-dimensional van der Waals ferromagnet $Cr_2Ge_2Te_6$ is investigated. Correlations well above the critical temperature and the effect of uniaxial pressure on the magnetic anisotropy are two important aspects of the analysis. **Chapter six** concludes this work by summarizing the results of the investigations.

Table of Contents

Chapter 1

Theory

In this chapter basic thermodynamic definitions are given and the thermodynamic foundations of this work are laid out. The first section introduces thermodynamic potentials, which are the pillars of most of the subsequent discussions. Maxwell's relations are derived, which relate observables easily accessible in experiments to quantities that are hard to measure. Linear response functions are the observables that are measured in the experiments of this work. Importantly, the thermal expansion coefficient and specific heat are introduced as the pressure and temperature dependence of the entropy of a system, respectively, whereas the magnetostriction measures the pressure dependence of the magnetization. Finally, it is shown that a constant Grüneisen parameter relates to a single dominant energy scale. Discussions in this first section are mainly based on Ref. [27] (Ch. 16 and 28), Ref. [9] (Ch. 2) and Ref. [28] (Ch. 6).

The second section introduces different definitions of phase transitions, based on thermodynamic potentials as well as symmetry-breaking and order parameters. Furthermore, critical exponents and the corresponding (hyper)scaling relations are introduced, closely following Ref. [29]. Finally, the Clausius-Clapeyron and Ehrenfest relations are derived, which provide valuable tools to investigate the field and pressure dependence of phase transition temperatures and critical fields. These derivations can be found in similar form in Refs. [9, 27].

1.1 Thermodynamic Background

A function of state of a system can be any physical quantity with a well-defined value for each equilibrium state of the system. Such functions of state exhibit the very useful property of undergoing the same change from one equilibrium state to another, independent of the path traveled through parameter space. This also means that they have no time dependence and exact differentials (i.e., zero integrals along any closed loop in parameter space). The internal energy U represents such a state function, but it is not the only quantity to which this applies. Other state functions

often encountered in thermodynamics are the pressure p, volume V, temperature T, and the entropy S. Combining different of these state functions in a way that the resulting quantity has the dimensions of energy yields again a state function. These state functions with a unit of energy are called thermodynamic potentials. In principle an arbitrary number of thermodynamic potentials can be constructed, however, not all of them are useful. On top of the internal energy, three further potentials are extremely useful in thermodynamics and are therefore also widely used. These are

- the enthalpy H: $H = U + pV$,
- the Helmholtz function, or Helmholtz free energy, F: $F = U - TS$, and
- the Gibbs function, or Gibbs free energy, G: $G = H - TS$.

In the following section these thermodynamic potentials and their derivatives are briefly introduced.

1.1.1 Thermodynamic Potentials

The first law of thermodynamics states the conservation of energy for thermodynamic processes. A change in energy for any thermodynamic potential can therefore be expressed by its differential, e.g.,

$$dU = TdS - pdV \tag{1.1}$$

for the internal energy. Eq. (1.1) implies that the temperature T and pressure p can be expressed as differentials of the internal energy:

$$T = \left(\frac{\partial U}{\partial S}\right)_V \tag{1.2}$$

$$p = -\left(\frac{\partial U}{\partial V}\right)_S \tag{1.3}$$

Pressure and temperature can analogously be defined from the enthalpy H (Tab. 1.1). Both internal energy and enthalpy depend on the entropy S, which is very difficult to vary in experiments. The Helmholtz function $F(T, V)$ and the Gibbs function $G(T, p)$, with their easily accessible natural variables T, V and p do not suffer from this drawback and are therefore for experimental purposes the functions of choice. An overview of the four thermodynamic potentials, their differentials and first derivatives is given in Tab. 1.1. Note that the thermodynamic potentials can be transformed into each other by Legendre transforms.

As stated above, these basic definitions of the thermodynamic potentials can in

Table 1.1: Thermodynamic potentials along with their differentials, natural variables and first derivatives. Taken from [27].

Function of state		Differential	Natural variables	First derivatives	
Internal energy	U	$dU = TdS - pdV$	$U = U(S,V)$	$T = \left(\frac{\partial U}{\partial S}\right)_V$,	$p = -\left(\frac{\partial U}{\partial V}\right)_S$
Enthalpy	$H = U + pV$	$dH = TdS + Vdp$	$H = H(S,p)$	$T = \left(\frac{\partial H}{\partial S}\right)_p$,	$V = \left(\frac{\partial H}{\partial p}\right)_S$
Helmholtz function	$F = U - TS$	$dF = -SdT - pdV$	$F = F(T,V)$	$S = -\left(\frac{\partial F}{\partial T}\right)_V$,	$p = -\left(\frac{\partial F}{\partial V}\right)_T$
Gibbs function	$G = H - TS$	$dG = -SdT + Vdp$	$G = G(T,p)$	$S = -\left(\frac{\partial G}{\partial T}\right)_p$,	$V = \left(\frac{\partial G}{\partial p}\right)_T$

general be expanded by adding other thermodynamic potentials. This may be

- the chemical potential μ, which represents the energy absorbed or released by adding a particle to a thermodynamic system, multiplied by the change in particle number dN, μdN, or
- a magnetic moment $m = MV$ (where M is the volume magnetization of a system) in an applied magnetic field B, yielding a term $-mdB$.[1]

Since in this work magnetic solid-state systems are investigated where no change in particle number occurs, the chemical potential term is not relevant here. The magnetic moment term, in contrast, is very important in this context. Adding this term to the inner energy and applying two Legendre transforms then yields the modified total differentials for the Helmholtz and Gibbs functions

$$dF = -SdT - pdV - mdB \tag{1.4}$$

$$dG = -SdT + Vdp - mdB. \tag{1.5}$$

1.1.2 Maxwell Relations

The total differentials of thermodynamic potentials may be rewritten by partial differentials of their natural variables. Generally speaking, a state function f with variables x and y can be written as

$$df = \left(\frac{\partial f}{\partial x}\right)_y dx + \left(\frac{\partial f}{\partial y}\right)_x dy. \tag{1.6}$$

1 Note that throughout most of this work, as often done in standard English-speaking literature, the magnetic flux density $B = \mu_0(H + M)$ will be referred to as the magnetic field although, strictly speaking, H represents the magnetic field (strength). Referring to B as the magnetic field also avoids confusion with the Helmholtz function H in this chapter.

This in principle enables experimental access to measuring changes in the different thermodynamic quantities. However, not all quantities in the partial derivatives can be measured easily. Maxwell's relations are equations that build a bridge between quantities that are hard to measure and ones which are much easier to access experimentally. Since df in Eq. (1.6) is an exact differential one has

$$\left(\frac{\partial^2 f}{\partial x \partial y}\right) = \left(\frac{\partial^2 f}{\partial y \partial x}\right). \tag{1.7}$$

Defining

$$F_x = \left(\frac{\partial f}{\partial x}\right)_y \text{and} F_y = \left(\frac{\partial f}{\partial y}\right)_x \tag{1.8}$$

yields

$$\left(\frac{\partial F_y}{\partial x}\right) = \left(\frac{\partial F_x}{\partial y}\right). \tag{1.9}$$

This general idea can now be applied to each of the state functions U, H, F, and G to result in the four Maxwell's relations. For example looking at the Gibbs function one gets

$$dG = -SdT + Vdp \tag{1.10}$$

$$dG = \left(\frac{\partial G}{\partial T}\right)_p dT + \left(\frac{\partial G}{\partial p}\right)_T dp, \tag{1.11}$$

such that one can write $S = -(\partial G/\partial T)_p$ and $V = (\partial G/\partial p)_T$. Taking the second derivatives, since dG is an exact differential, one gets

$$\left(\frac{\partial^2 G}{\partial T \partial p}\right) = \left(\frac{\partial^2 G}{\partial p \partial T}\right), \tag{1.12}$$

$$-\left(\frac{\partial S}{\partial p}\right)_T = \left(\frac{\partial V}{\partial T}\right)_p \tag{1.13}$$

where the last line is Maxwell's relation derived from G. Analogously one obtains the remaining three Maxwell's relations from U, H, and F as

$$\left(\frac{\partial T}{\partial V}\right)_S = -\left(\frac{\partial p}{\partial S}\right)_V \tag{1.14}$$

$$\left(\frac{\partial T}{\partial p}\right)_S = \left(\frac{\partial V}{\partial S}\right)_p \tag{1.15}$$

$$\left(\frac{\partial S}{\partial V}\right)_T = \left(\frac{\partial p}{\partial T}\right)_V . \tag{1.16}$$

For the interested reader, the so-called thermodynamic square [30, 31] is one of many mnemonics to quickly recall the thermodynamic potentials and Maxwell's relations. Similar relations can be derived easily for systems including a magnetic moment or particles with chemical potential. Alternatively, they can be read off from extended versions of the mnemonic square [32–34].

1.1.3 Response Functions

The thermodynamic reaction of a system to a generalized force, such as T or p, is called a generalized susceptibility, or a response function. In this work linear response functions, such as the isobaric specific heat c_p or the isobaric volume thermal expansion coefficient β are measured:

$$C_p = \left(\frac{\partial H}{\partial T}\right)_p = T\left(\frac{\partial S}{\partial T}\right)_p = -T\left(\frac{\partial^2 G}{\partial T^2}\right)_p \tag{1.17}$$

$$\beta = \frac{1}{V}\left(\frac{\partial V}{\partial T}\right)_p = -\frac{1}{V}\left(\frac{\partial S}{\partial p}\right)_T = \frac{1}{V}\left(\frac{\partial^2 G}{\partial p \partial T}\right) \tag{1.18}$$

Maxwell's relations are applied here to emphasize the meaning of C_p and β, which respectively give a measure of the temperature dependence and the pressure dependence of the entropy of a system. In this work the molar specific heat, $c_\mathrm{p} = C_\mathrm{p}/N$, will usually be called the specific heat. Selected response functions are also shown in Tab. 1.2 along with their relation to the Gibbs function.

In the dilatometry setup in this work not the volume thermal expansion and magnetostriction are measured, but the linear thermal expansion coefficient α_i and linear

Table 1.2: Definition of selected response functions typically available in experiments.

Response function	Symbol	Definition	
Specific heat (constant pressure)	c_p	$T\left(\frac{\partial S}{\partial T}\right)_{p,B}$	$-T\left(\frac{\partial^2 G}{\partial T^2}\right)_{p,B}$
Thermal Expansion Coefficient	β	$\frac{1}{V}\left(\frac{\partial V}{\partial T}\right)_{p,B}$	$\frac{1}{V}\left(\frac{\partial^2 G}{\partial p \partial T}\right)_{p,B}$
Magnetostriction Coefficient	Λ	$\frac{1}{V}\left(\frac{\partial V}{\partial B}\right)_{p,T}$	$\frac{1}{V}\left(\frac{\partial^2 G}{\partial p \partial B}\right)_{p,T}$
Isothermal Compressibility	κ	$-\frac{1}{V}\left(\frac{\partial V}{\partial p}\right)_{T,B}$	$-\frac{1}{V}\left(\frac{\partial^2 G}{\partial p^2}\right)_{T,B}$
Magnetic Susceptibility	$\chi(B)$	$\left(\frac{\partial M}{\partial B}\right)_{p,T}$	$-\frac{1}{V}\left(\frac{\partial^2 G}{\partial B^2}\right)_{p,T}$
Magnetic Susceptibility	$\chi(T)$	$\left(\frac{\partial M}{\partial T}\right)_{p,B}$	$-\frac{1}{V}\left(\frac{\partial^2 G}{\partial T \partial B}\right)_{p,B}$

magnetostriction λ_{ij}:

$$\alpha_i = \frac{1}{L_i}\left(\frac{\partial L_i}{\partial T}\right)_p = \left(\frac{\partial \ln L_i}{\partial T}\right)_p \tag{1.19}$$

$$\lambda_{ij} = \frac{1}{L_i}\left(\frac{\partial L_i}{\partial B_j}\right)_{T,p} \tag{1.20}$$

L_i is the length of the system (i.e., the investigated sample) along the i-axis. If α_i is measured for three different crystallographic axes a, b, c spanning the volume of a sample the volume expansion coefficient can be calculated as $\beta = \alpha_\mathrm{a} + \alpha_\mathrm{b} + \alpha_\mathrm{c}$. The definition of the linear magnetostriction tensor λ_{ij} implies that in general the applied magnetic field and measured length changes do not have to be along the same direction. In the setup in this work, however, the magnetic field is aligned along the measurement direction, $B \parallel dL(B)$, such that $i = j$ and $\lambda_{ij} = \lambda_i$.

Finally, it is important to note that the magnetostriction coefficient Λ measures the change in magnetization $M = m/V$ under hydrostatic pressure p

$$\Lambda = \frac{1}{V}\left(\frac{\partial V}{\partial B}\right)_{p,T} = \frac{1}{V}\left(\frac{\partial^2 G}{\partial p \partial B}\right)_{p,T} = -\left(\frac{\partial M}{\partial p}\right)_{p,T}. \tag{1.21}$$

The same holds for λ_{ij} and uniaxial pressure p_i

$$\lambda_{ij} = \frac{1}{L_i}\left(\frac{\partial L_i}{\partial B_j}\right)_{p,T} = \frac{1}{L_i}\left(\frac{\partial^2 G}{\partial p_i \partial B_j}\right)_{p,T} = -\left(\frac{\partial M_j}{\partial p_i}\right)_{p,T}. \tag{1.22}$$

1.1.4 Grüneisen Parameters

In the original work by Grüneisen a lattice of atoms in an anharmonic potential and their lattice vibrations were investigated for different thermodynamic processes [35]. The Grüneisen parameter γ was therein defined as the change in lattice vibration frequency ω_{vib} caused by a volume change dV,

$$\gamma = -\frac{V}{\omega_{\mathrm{vib}}}\frac{\partial \omega_{\mathrm{vib}}}{\partial V} = -\frac{\partial \ln \omega_{\mathrm{vib}}}{\partial \ln V}. \tag{1.23}$$

As shown in Ref. [36] (Ch. 6.3), this change in lattice vibration frequency can be related to both the thermal expansion and specific heat of a system, resulting in

$$\gamma_i = \frac{3\kappa_{\mathrm{T}}\alpha_i V}{c_{\mathrm{v}}} \tag{1.24}$$

$$\gamma_{\mathrm{vol}} = \frac{\kappa_{\mathrm{T}}\beta V}{c_{\mathrm{v}}}, \tag{1.25}$$

where κ_{T} is the isothermal compressibility and c_{v} the specific heat at constant volume.

Alternatively the total differential of the entropy of a system with respect to T and V can be considered to arrive at a definition of Γ:

$$dS = \left(\frac{\partial S}{\partial T}\right)_V dT + \left(\frac{\partial S}{\partial V}\right)_T dV \tag{1.26}$$

$$= C_V d(\ln T) + \frac{\beta V}{\kappa_T} d(\ln V), \tag{1.27}$$

such that at constant entropy ($dS = 0$) one obtains

$$\frac{\beta V}{\kappa_T C_V} = -\left(\frac{\partial \ln T}{\partial \ln V}\right)_S \equiv \Gamma(T, V). \tag{1.28}$$

Analogously, a Grüneisen parameter can be defined using C_{p} and the adiabatic compressibility, i.e., as

$$\Gamma(T, V) \equiv \frac{V}{\kappa_S T}\frac{\partial S/\partial p}{\partial S/\partial T} = \frac{\beta V}{\kappa_S C_p} \tag{1.29}$$

If the total entropy of a system has contributions from different degrees of freedom, $S = \sum_n S_n$, Eq. (1.26) shows that for each contribution a separate Grüneisen parameter $\Gamma_n = (\partial S/\partial \ln V_T)/C_n$ can be defined. The Grüneisen parameter for the

whole system is then an average weighted by the contribution to the heat capacity of each component:

$$\Gamma = \sum_n \Gamma_n C_n / \sum_n C_n \tag{1.30}$$

It can be shown that whenever all energy states of a system scale to the same single characteristic energy $J(V)$, such that $S = S(T/J)$, one obtains

$$\beta = -\frac{1}{V}\left(\frac{\partial S}{\partial p}\right)_T = \frac{1}{V}\frac{T}{J^2}\left(\frac{\partial J}{\partial p}\right)_T S' = \frac{1}{V}\frac{T}{J}\left(\frac{\partial \ln J}{\partial p}\right)_T S' \tag{1.31}$$

$$C_V = T\left(\frac{\partial S}{\partial T}\right)_V = \frac{T}{J}S'. \tag{1.32}$$

The ratio between thermal expansion coefficient and specific heat

$$\frac{\beta}{C_V} = \frac{1}{V}\frac{\partial \ln J}{\partial p} \tag{1.33}$$

is then a constant, i.e., independent of temperature. In this case a single dominant and temperature independent Grüneisen parameter exists with

$$\Gamma = \frac{1}{\kappa_T}\frac{\partial \ln J}{\partial p} = -\frac{\partial \ln J}{\partial \ln V}, \tag{1.34}$$

where the definition of the isothermal compressibility and Eq. (1.28) were applied. These results are applied throughout this work to determine the pressure dependence of the respective dominating energy scale.

Note that although the definitions of the Grüneisen parameter presented above are the most widely used ones, other Grüneisen parameters may be met in the literature [9], and may also be referred to as Grüneisen functions. In this work the Grüneisen parameter Γ is defined explicitly where it is put to use. All of the definitions in this work exclude the isothermal compressibility κ such that Γ is not dimensionless.

1.2 Phase Transitions

A system in contact with its surroundings tends to minimize one of the thermodynamic potentials defined above (U, H, F, and G) to reach equilibrium. Which of the potentials is minimized depends on the constraints applied to the system, e.g., G is minimized when T and p are fixed. The lowest possible energy state of a system is

the so-called ground state, minimizing the sum of all interactions in a system.

Considering the Gibbs free energy for a magnetic system, $G = U + pV - TS - mB$, and its total differential $dG = -SdT + Vdp - mdB$, one may imagine that if the external parameters of the system, such as temperature, pressure or magnetic field, are varied, an instability can occur due to the possibility of attaining a lower energy state by a change in entropy, volume or magnetization. This then leads to a transition between two distinct phases. A well-known example of phase transitions is the boiling of water, where the gain in entropy ($dG < 0$) by a transition from a liquid to a gaseous phase outweighs the volume increase ($dG > 0$). Another almost equally well-known transition is from a paramagnetic phase to a ferromagnetic phase below a critical temperature, where the long-range ordering of magnetic spins leads to a decrease in entropy ($dG > 0$), but also to a net magnetization ($dG < 0$), with an overall decrease in G.

1.2.1 Classifications of Phase Transitions

Different ways to classify phase transitions have been proposed in the past. The historic Ehrenfest classification of phase transitions defined the order of a phase transition as the order of the lowest differential of G that shows a discontinuity at the critical temperature T_c. By this definition a first-order transition is marked by a discontinuity in the entropy $S = -(\partial G/\partial T)_p$ or the volume $V = -(\partial G/\partial p)_T$. A second-order transition, on the other hand, exhibits a discontinuous jump in one of the response functions shown in Tab. 1.2, e.g., in the specific heat or the thermal expansion coefficient. This classification has, however, proven inadequate for a general description of phase transitions beyond the first order [9]. A more modern classification of phase transitions only discriminates between phase transitions that show a latent heat, called "first-order" or "discontinuous", and phase transitions that do not. The latter are called continuous phase transitions and also include the higher-order phase transitions according to the historic Ehrenfest classification.

Many, though not all, phase transitions involve the breaking of at least one symmetry of a system. For the paramagnetic-to-ferromagnetic transition mentioned above the spins possess a rotational symmetry in the high-temperature paramagnetic phase, but not in the ferromagnetic phase below T_c. At the same time the symmetry of the crystal lattice does not necessarily change at T_c. Symmetry-breaking therefore allows for another classification of phase transitions. This classification uses the concept of an order parameter. An order parameter is an observable that measures the degree of order in one property of a system, e.g., in the magnetization, as it transitions from one phase to another. Usually it is defined as zero above the phase transition and finite below, and often normalized such that it reaches a value of one when full order with respect to the order parameter is achieved. For first-order transitions

the order parameter changes discontinuously, whereas it varies continuously for continuous transitions. Examples of order parameters for the systems investigated in this work include the magnetization M (which may be normalized by the saturation magnetization, M/M_S) for ferromagnets, the sublattice magnetization $\vec{M} = \vec{M}_1 - \vec{M}_2$ for antiferromagnets, or the polarization $\vec{P}$ for ferroelectrics. An order parameter can be a scalar, a vector or a higher-rank tensor depending on the symmetry-breaking it describes.

1.2.2 Critical Exponents

For continuous phase transitions the mean value of an order parameter is zero above a critical temperature (or more general a critical point), whereas deviations from the mean in space and time, i.e., fluctuations, can be non-zero. As a critical point is approached the typical length scale of fluctuating clusters, the correlation length ξ, increases. At the critical point it then diverges as

$$\xi \propto |t|^{-\nu} \tag{1.35}$$

where ν is the critical exponent of the correlation length and t is a dimensionless measure for the distance to the critical point. If the critical point occurs at a temperature $T_\mathrm{c} \neq 0$ the reduced temperature $t = |T - T_\mathrm{c}|/T_\mathrm{c}$ can be defined. Fluctuations around a critical point do not only show spatial but also temporal correlations. A measure for temporal correlations is the typical time scale on which fluctuations decay, the correlation time τ_c. Approaching a critical point τ_c also diverges according to

$$\tau_\mathrm{c} \propto \xi^z \propto |t|^{-\nu z}, \tag{1.36}$$

where z is the dynamical critical exponent. In particular, the characteristic times for relaxation and transport processes usually diverge upon approaching T_c. This phenomenon is known as critical slowing down. In terms of fluctuating spins in a ferromagnet this can be understood as follows: as the temperature approaches T_c from above, the correlation length increases, i.e., correlated blocks of spins of increasing size form. To cause a fluctuation, a large block of spins needs to be flipped, which is a slow process, and as the blocks increase in size τ_c diverges. These divergences in correlation lengths and times resulting in singularities of physical observables are called the critical behavior. Close to the critical point there is no other characteristic length or time scale than ξ or τ_c [29]. As noted by Kadanoff [37] this is the reason behind the scaling hypothesis by Widom [38].

In addition to the critical exponents ν and z there are a number of other exponents which are widely used. They describe the dependence of the order parameter, its

correlations, and different response functions on the distance from the critical point and on the field conjugate to the order parameter. Tab. 1.3 summarizes the most common definitions. Note that not all of the exponents defined in Tab. 1.3 are

Table 1.3: Definitions of the commonly used critical exponents in reference to the magnetization m as the order parameter with B being the magnetic field. Taken from Ref. [29].

	Exponent	Definition	Conditions
Specific heat	α	$c_\mathrm{p} \propto \lvert t\rvert^{-\alpha}$	$t \to 0, B = 0$
Order parameter	β	$m \propto (-t)^{\beta}$	$t \to 0$ from below, $B = 0$
Susceptibility	γ	$\chi \propto \lvert t\rvert^{-\gamma}$	$t \to 0, B = 0$
Critical isotherm	δ	$B \propto \lvert m\rvert^{\delta}\mathrm{sign}(m)$	$B \to 0, t = 0$
Correlation length	ν	$\xi \propto \lvert t\rvert^{-\nu}$	$t \to 0, B = 0$
Correlation function	η	$G(r) \propto \lvert r\rvert^{-d+2-\eta}$	$t = 0, B = 0$
Dynamical exponent	z	$\tau_\mathrm{c} \propto \xi^{z}$	$t \to 0, B = 0$

independent from one another. Based on the homogeneity relation for the free energy, scaling laws for the four thermodynamic exponents α, β, γ, δ can be obtained,

$$\alpha + 2\beta + \gamma = 2 \tag{1.37}$$

$$\alpha + \beta(\delta + 1) = 2 \tag{1.38}$$

as well as two so-called hyperscaling relations for the correlation length and the correlation function,

$$2 - \alpha = d\nu \tag{1.39}$$

$$2 - \eta = \frac{\gamma}{\nu}. \tag{1.40}$$

A set of critical exponents completely characterizes the critical behavior at a particular phase transition. Remarkably, results from renormalization group theory and numerical calculations have shown that the behavior near the critical point depends only on a few parameters: (a) The dimensionality of the order parameter, D (and therefore the symmetries of the Hamiltonian); (b) the lattice dimensionality, d; (c) the range of interactions, i.e., whether interactions in the system are long-ranged or short-ranged [39]. This means that universal scaling laws exist, which are independent of a specific thermodynamic system under study and there exist classes, so-called universality classes, that are the same for many different phase transitions. A list of universality classes, such as the 2D Ising, 3D Ising, 3D XY and 3D Heisenberg ones, and their critical exponents calculated using renormalization group theory is given

in Tab. 1.4.

Table 1.4: Critical exponents for different physical models according to calculations applying renormalization group theory.
D: Dimensionality of the order parameter, d: Lattice dimensionality.

Critical Exponents for Different Physical Models									
Model	D	d	α	β	γ	δ	n	l	Ref.
Mean field theory (MFT)	any	any	0	0.5	1	3	0.667	1.333	[40]
Tricritical MFT	any	any	0.5	0.25	1	5	0.4	1.2	[41]
3D Heisenberg	3	3	–0.12	0.365	1.386	4.8	0.637	1.208	[41]
3D XY	2	3	–0.01	0.345	1.316	4.81	0.606	1.208	[41]
3D Ising	1	3	0.11	0.325	1.24	4.82	0.569	1.207	[41]
2D Ising	1	2	0	0.125	1.75	15			[42]

Significantly, both the mean-field model and the 2D Ising model exhibit a critical exponent $\alpha = 0$. From

$$|t|^{-\alpha} = e^{-\alpha \cdot \ln(|t|)} = 1 - \alpha \cdot \ln(|t|) + \mathcal{O}(\alpha^2) \tag{1.41}$$

it becomes visible that a purely logarithmic divergence is expected for $|t| \to 0$ and $\alpha \to 0$. The difference between the mean-field and the 2D Ising model is that for the mean-field model α is discontinuous at the phase transition whereas it is not for the 2D Ising model. Defining α_- for $T < T_\mathrm{C}$ and α_+ for $T > T_\mathrm{C}$ we hence have $\alpha_- = \alpha_+$ for the 2D Ising model, and $\alpha_- \neq \alpha_+$ for the mean-field model. The critical exponents α and β will be used in this work to analyze the critical behavior in the thermal expansion coefficient and relative length changes. To avoid confusion with the thermal expansion coefficients the critical exponents will be called $\alpha_\pm$ and β_c. For the thermal expansion coefficient a scaling with the critical exponent $\alpha_\pm$ is valid if the assumption $\alpha \propto c_\mathrm{p}$ holds.

1.2.3 Clausius-Clapeyron and Ehrenfest Relations

From the classification of phase transitions and the definition of the thermodynamic potentials important relations arise for discontinuous and continuous phase transitions. At the phase boundary of first-order transitions, between two phases 1 and 2, the Gibbs free energy $G(T,p,B)$ is continuous, i.e.,

$$G_1(T,p,B) = G_2(T,p,B) \tag{1.42}$$

Where G_1 and G_2 are defined for the respective phases 1 and 2. Along the phase boundary, the equation

$$G_1(T+dT, p+dp, B+dB) = G_2(T+dT, p+dp, B+dB) \tag{1.43}$$

holds, such that

$$dG_1(T, p, B) = dG_2(T, p, B). \tag{1.44}$$

Applying Eq. (5) to Eq. (1.44) yields

$$-S_1 dT + V_1 dp - m_1 dB = -S_2 dT + V_2 dp - m2dB, \tag{1.45}$$

with the entropy S_i, volume V_i and magnetic moment m_i in phases 1 and 2 for $i = 1{,}2$. Following the phase boundary such that $dB = 0$ and rearranging Eq. (1.45) leads to

$$\left(\frac{dp}{dT}\right)_B = \frac{S_2 - S_1}{V_2 - V_1} = \frac{\Delta S}{\Delta V}, \tag{1.46}$$

which is known as the Clausius-Clapeyron equation, where sometimes ΔS is replaced by the latent heat $L = T\Delta S$. This equation shows that the gradient of the phase boundary in the $T - p$ plane is purely determined by the change in entropy (or equivalently the latent heat), the temperature at the phase boundary (i.e., T_c), and the difference in volume between the two phases. Analogously, in the $T - B$ and $p - B$ planes Clausius-Clapeyron-like relations can be obtained [9]:

$$\left(\frac{\partial T}{\partial B}\right)_p = -\frac{\Delta m}{\Delta S} \tag{1.47}$$

$$\left(\frac{\partial B}{\partial p}\right)_T = \frac{\Delta m}{\Delta V} \tag{1.48}$$

When uniaxial pressure p_i is applied along the i-axis of the system instead of hydrostatic pressure p, the jump in volume changes to a jump in length, and ΔV needs to be replaced with $V_m \Delta L_i / L_i$, where V_m is the molar volume. The dependence of a critical temperature on an applied magnetic field in Eq. (1.47) can be derived from the B vs. T phase diagram. With this information the entropy change at a first-order phase transition can be calculated if no measurement for it exists. This then enables calculating the initial pressure dependence, i.e., for $p \to 0$, of the critical temperature from measurements of the thermal expansion according to Eq. (1.46).

For a second-order phase transition the first derivatives of G, i.e., S, V and m, are continuous across a phase transition and $S_1 = S_2$, $V_1 = V_2$. $m_1 = m_2$ along the phase

boundary. Following the phase boundary such that $dB = 0$ one obtains

$$\left(\frac{\partial S_1}{\partial T}\right)_p dT + \left(\frac{\partial S_1}{\partial p}\right)_T dp = \left(\frac{\partial S_2}{\partial T}\right)_p dT + \left(\frac{\partial S_2}{\partial p}\right)_T dp \tag{1.49}$$

$$\frac{c_{\mathrm{p},1}}{T} dT - V\beta_1 dp = \frac{c_{\mathrm{p},2}}{T} dT - V\beta_2 dp \tag{1.50}$$

$$\left(\frac{dT}{dp}\right)_B = TV\frac{\Delta\beta}{\Delta c_{\mathrm{p}}}. \tag{1.51}$$

A Maxwell relation and the definitons of c_{p} and β were applied to finally arrive at Eq. (1.51), which is the Ehrenfest relation. For uniaxial pressure along the i-axis p can be changed to p_i and β changes accordingly to the linear thermal expansion coefficient α_i. Further Ehrenfest-like relations can be obtained along the phase boundary for $dT = 0$ and $dp = 0$. These will be mentioned in the text where they are applied.

Chapter 2

Experimental Methods and Setup

The results presented in this work were mainly obtained by thermal expansion and magnetostriction measurements using high-resolution capacitance dilatometry. These data are complemented by magnetization and specific heat measurements. High-resolution capacitance dilatometry, the measurement setup, and related steps for calibration and preparation of measurements are briefly introduced in the following sections. Details for the magnetization and specific heat measurement devices are given as well.

2.1 High-Resolution Capacitance Dilatometry

Measurement techniques which detect microscopic length changes of atomic positions and distances in a material – such as X-ray and neutron diffraction measurements – routinely achieve a resolution of $\Delta a/a \sim 10^{-5}$ [9] for changes in lattice parameter a. High-resolution capacitance dilatometry on the other hand offers a technique for measuring macroscopic properties – uniaxial bulk length changes – with an otherwise unattainable extreme sensitivity for length changes on the order of $\Delta \mathrm{L}/\mathrm{L} = 10^{-8}$ to 10^{-9} [26]. The resolution of capacitance dilatometry is thus at least one order of magnitude better than what interferometric techniques can achieve [43] and at least three orders of magnitude better than strain-gauge techniques [44].

2.1.1 Measurement Principle

The measurement principle of capacitance dilatometry is based on the dependence of the capacitance C of two parallel capacitance plates on their distance d. A sample of length L is clamped between a movable plate and a fixed frame, to which the second plate is attached. For an ideal plate capacitor with surface area A, the capacitance is given by

$$C = \varepsilon_\mathrm{r}\varepsilon_0\frac{A}{d} \tag{2.1}$$

where $\varepsilon_0 = 8.8542 \cdot 10^{-12}$ F/m is the vacuum permittivity and ε_r the dielectric constant of the medium in between the capacitor plates. All measurements were performed in a dilute helium gas environment (10 mbar to 30 mbar). At ambient pressure and room temperature $\varepsilon_{r,He} \approx 1.00007(1)$ [45], which, at low pressures, enables us to safely assume $\varepsilon_r = 1$.

If a sample changes length by ΔL, this is directly translated to a change in plate distance Δd for the capacitor. For circular plates of radius r, an initial capacitance C_0, and a final capacitance C we obtain from Eq. (2.1)

$$\Delta L = \Delta d = \varepsilon_0 \pi r^2 \frac{C - C_0}{C \cdot C_0}. \tag{2.2}$$

Including a correction for the non-parallel alignment of the plates according to Pott and Schefzyk [46], the length change can be determined as

$$\Delta L = \Delta d = \varepsilon_0 \pi r^2 \frac{C - C_0}{C \cdot C_0} \left(1 - \frac{C \cdot C_0}{C_{\max}^2}\right). \tag{2.3}$$

From this value, the relative length change $dL(T)/L$ w.r.t. the room temperature length L and its derivative with respect to temperature, the uniaxial thermal expansion coefficient $\alpha_i = 1/L_i \; dL_i/dT$, are calculated. In our evaluation routine, C_0 is the capacitance at the beginning of a temperature or field sweep, i.e., usually the capacitance at lowest temperatures for a temperature sweep.

2.1.2 Dilatometers: Cell Design

In this work, a three-terminal capacitance standard-dilatometer from *Kuechler Innovative Measurement Technology* was used for most of the measurements, with $r = 7$ mm and $C_{\max} = 146$ pF [26]. A few measurements, mostly in zero field, were also performed in a mini-dilatometer ($r = 5$ mm, $C_{\max} = 95$ pF) [47]. Unless mentioned otherwise, the measurements shown in this work were performed in the standard-dilatometer.

The setup of both dilatometers is very similar and will be briefly explained here on the basis of the standard-dilatometer. A more thorough description of the two devices and their design can be found in [26, 47]. Schematic drawings and a photograph of the standard-dilatometer are shown in Fig. 2.1. Except for some insulating spacers, all parts are machined out of high-purity beryllium-copper ($Cu_{0.9816}Be_{0.0184}$). The lower capacitor plate (6 in Fig. 2.1) is mounted to the fixed outer cell frame (3), while the upper capacitor plate (5) is fixed to the movable part (1). This movable part is held in the frame by two 30 μm thick BeCu leaf springs (2), which allow the upper

plate only to move vertically in this parallelogram suspension. The sample is fixed by means of an adjustment screw (9) between the outer frame (3) and the movable part (1). To prevent warping of the sample during positioning, the adjustment screw (9) contains a piston (10) hung up on the head of the screw. Furthermore, the piston has a hole in it through which a needle is placed during sample preparation to prevent the rotation of the piston and thus of the sample.

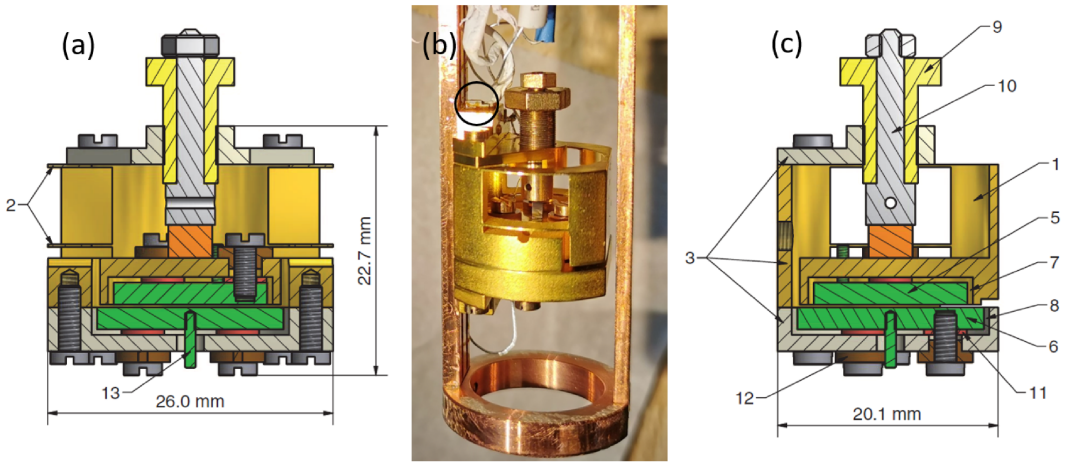

Figure 2.1: (a) Cross section, (b) photograph and (c) longitudinal section of the standard-dilatometer. Labels refer to (1) movable part, (2) BeCu flat springs, (3) fixed outer cell frame, (4) sample, (5) upper capacitor plate, (6) lower capacitor plate, (7) upper guard ring, (8) lower guard ring, (9) adjustment screw, (10) piston, (11) sapphire washer, (12) insulating piece of vespel, and (13) electrical connection. The black circle in (b) marks the position of the thermometer. (a) and (c) are taken from [26].

2.1.3 Experimental Setup

The dilatometer is mounted on a frame made from high-purity copper as seen in Fig. 2.1(b). This copper frame is in turn attached to a plastic spacer which is attached to a rod with several heat shields. For measurements this rod is placed inside a long cylindrical mantle made from non-magnetic stainless steel and a piece of copper at its end, i.e., around the copper frame with the dilatometer. This copper part ensures good thermal contact to the surroundings. After sample mounting the volume inside the sample rod is pumped to a pressure below $2 \cdot 10^{-4}$ mbar using a turbomolecular pump and flushed with helium gas three times. After the third pumping 30 mbar of helium gas are released into the sample rod, acting as an exchange gas. The sample rod is then mounted into a commercial Oxford Instruments Integra AC ^{4}He flow cryostat with a Variable Temperature Insert (VTI) and a 15 T superconducting Nb_3Sn magnet. The VTI serves to control the temperature in a wide range between 1.5 K and 300 K, using a heater (ITC heater) and a needle valve. The needle valve

is set between 38% and 42% and regulates the helium flow from the helium reservoir into the VTI sample space. An intelligent temperature control iTC 5035 is used to control the VTI. The temperature of the sample is measured using a *Cernox 1050-SD* thermometer attached to the top of the standard-dilatometer (front of the mini-dilatometer) and a LakeShore 340 (LS) temperature controller. The 15 T magnet is controlled by an intelligent Power Supply iPS 120-10. For measuring the capacitance the dilatometer is connected to an Andeen-Hagerling AH2550A capacitance bridge by shielded coaxial cables [48]. This capacitance bridge has a resolution of 0.8 aF $= 8 \cdot 10^{-7}$ pF, which is below the resolution of the dilatometer. All data are recorded on a measurement computer. A schematic drawing of the setup is shown in Fig. 2.2.

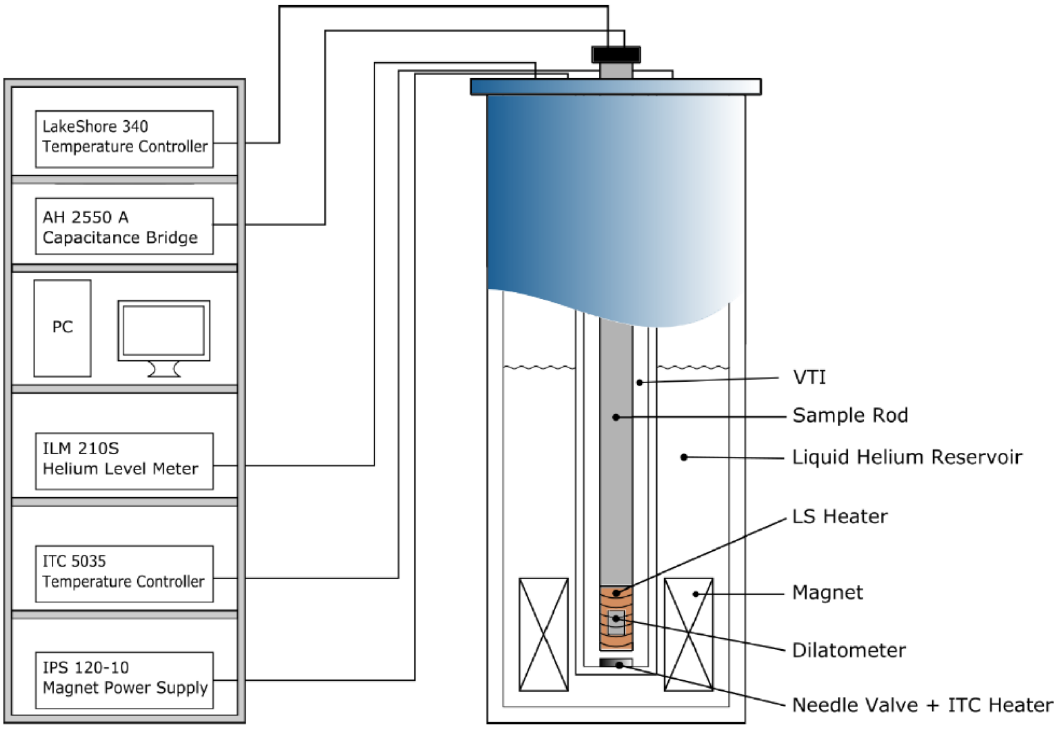

Figure 2.2: Schematic drawing of the experimental setup. ILM refers to an intelligent level meter. Other abbreviations are explained in the text. Taken from [49].

2.1.4 Cell-Effect: Calibration of a Dilatometer

Due to the way the dilatometer cell used in this work is constructed, it does not measure the absolute length change of the sample ΔL^{sample}, but the length change relative to the expansion or contraction of the cell, $\Delta L^{\text{sample}}_{\text{meas}}$. The so-called cell effect ΔL^{cell} is measured along with $\Delta L^{\text{sample}}_{\text{meas}}$. Following the definition of ΔL^{cell} by

Kuechler et al. [26] we have:

$$\Delta L_{\mathrm{meas}}^{\mathrm{sample}} = \Delta L^{\mathrm{sample}} - \Delta L^{\mathrm{cell}} \tag{2.4}$$

To calibrate ΔL^{cell} high-purity copper (99.999%) is measured as a reference material, since it is expected to exhibit a thermal expansion coefficient close to the cell body material $Cu_{0.9816}Be_{0.0184}$. The thermal expansion of copper in the relevant temperature range is well known from literature [50] and applied to measure the empty cell effect as

$$\Delta L_{\mathrm{meas}}^{\mathrm{Cu}} = \Delta L^{\text{empty cell}} = \Delta L_{\mathrm{lit}}^{\mathrm{Cu}} - \Delta L^{\mathrm{cell}}. \tag{2.5}$$

The cell effect ΔL^{cell} is thus the difference between the length change of the copper sample and the empty cell effect. It results mainly from the fact that by measuring a sample with a length L_0 a corresponding part of the CuBe-cell of the same length is missing:

$$\Delta L^{\mathrm{cell}} = \Delta L_{\mathrm{lit}}^{\mathrm{Cu}} - \Delta L^{\text{empty cell}}. \tag{2.6}$$

For each measurement of a sample, a high-purity copper sample of roughly the same size was measured to keep additional errors small. The true length of the sample was then obtained by adding the calibrated cell effect to the measured length change $\Delta L_{\mathrm{meas}}^{\mathrm{sample}}$

$$\Delta L^{\mathrm{sample}} = \Delta L_{\mathrm{meas}}^{\mathrm{sample}} + \Delta L^{\mathrm{cell}} \tag{2.7}$$

$$= \Delta L_{\mathrm{meas}}^{\mathrm{sample}} - \Delta L^{\text{empty cell}} + \Delta L_{\mathrm{lit}}^{\mathrm{Cu}} \tag{2.8}$$

Finally, the relative length change of the sample normalized to its room temperature length L_0 is given by

$$\left(\frac{\Delta L}{L_0}\right)^{\mathrm{sample}} = \frac{\Delta L_{\mathrm{meas}}^{\mathrm{sample}} - \Delta L^{\text{empty cell}}}{L_0} + \left(\frac{\Delta L}{L}\right)_{\mathrm{lit}}^{\mathrm{Cu}}. \tag{2.9}$$

The room temperature length is measured using a micrometer screw.

The cell effect for magnetostriction measurements was also considered in this work. For a sample of 2.040 mm a relative length change of $\Delta L/L \approx 2-3\cdot 10^{-7}$ from 0 T to 15 T was observed at 2 K. On the basis of this observation no background correction was applied to magnetostriction measurements which – at low temperatures – showed length changes on the order of 10^{-4} to 10^{-5}.

2.1.5 Sample Mounting and Applied Pressure

In rest position, the capacitance of the dilatometer is about 5.4 pF, which corresponds roughly to a distance of 0.25 mm between the capacitor plates. Depending on the sample properties – especially their stiffness and brittleness – the samples were mounted at capacitances between 6 pF (to prevent bending or breaking) and 22 pF. Mounting the sample necessarily applies a uniaxial stress, a force of a few N, onto the sample surface [26]. To estimate the applied pressure on the sample surfaces the spring constants of our standard- and mini-dilatometer had previously been measured by S. Krippendorf [51] and M. Hoffmann [52]. Resulting pressures are typically on the order of kPa to MPa. More precise estimations will be mentioned where necessary.

2.1.6 Measurement Routine

Thermal expansion measurements were performed in a zero-field cooled manner unless stated otherwise. Cooling rates varied between 1 K/min and 4 K/min. Upon cooling from high temperatures (roughly 200 K and above) a relaxation sweep was performed, i.e., a sweep from 2 K to 50 K or 60 K and back to 2 K at rates of 1 K/min to 1.5 K/min in order to release strains in the sample from previous rapid cooling.

Magnetostriction measurements were performed after a waiting time of 60 min to 120 min to ensure thermalization of the sample and a stable temperature during the field sweeps. Sweeping rates were typically set at 0.2 T/min or 0.3 T/min.

2.2 Magnetization and Specific Heat Measurements

Measurements of the isothermal magnetization and static magnetic susceptibility $\chi(T) = M(T)/B$, in a temperature range between 1.8 K and 300 K and fields up to 7 T, were performed in a Magnetic Properties Measurements System (MPMS3) from Quantum Design. The MPMS3 combines a SQUID (Superconducting Quantum Interference Device) magnetometer with Vibrating Sample Magnetometry (VSM) to combine speed and high sensitivity.

Isothermal magnetization measurements at temperatures between 1.8 K and 300 K and in fields up to 14 T were performed in a Physical Properties Measurement System (PPMS) from Quantum Design using the VSM option. For magnetization measurements in field and temperature, samples were clamped between two quartz cylinders in brass sample holders and additionally fixed with a small amount of high temperature vacuum grease.

Specific heat measurements in temperatures down to 170 mK and fields up to 14 T

were also performed on the PPMS, using a dilution refrigerator insert for lowest temperatures down to 50 mK. Unless stated otherwise, specific heat data in this work were measured by Ahmed Elghandour.

Chapter 3

Magnetoelastic Coupling in the Skyrmion Lattice Magnet Gd_2PdSi_3

The data presented has been nearly completely measured and analyzed by the first author, and the manuscript draft has been written by him. Specifically:

- Except for the specific heat data (Fig. 1c, Fig. 3b, Fig. S3) all data have been measured by S. Spachmann, including orienting and preparing the samples. All plots were created by S. Spachmann.
- The data analysis (except for the fitting of low-temperature specific heat in Fig. 1c, inset) including construction of the phase diagram has been completely done by S. Spachmann.
- The manuscript draft has been written by S. Spachmann and he communicated with the reviewers.
- A. Elghandour measured the specific heat and took part in discussions on these data.
- M. Frontzek and W. Löser provided the samples and took part in some discussions.
- R. Klingeler supervised the measurements and supported data analysis.
- All authors proofread the manuscript.

Abstract

We report detailed thermodynamic studies on high-quality single crystals of the centrosymmetric skyrmion-hosting intermetallic Gd_2PdSi_3 by means of high-resolution capacitance dilatometry in fields up to 15 T which are complemented by specific heat and magnetization studies. Our dilatometric measurements show magnetoelastic effects associated with antiferromagnetic order at $T_{N1} = 22.3$ K and $T_{N2} = 19.7$ K, as well as strong field effects in an applied magnetic field of 15 T up to 200 K (150 K) for $B \parallel c$ ($B \parallel a^*$, i.e. $B \perp c$). The data allow us to complete the magnetic phase diagram, including a new feature at $T^* \approx 12$ K below which a new degree of freedom becomes relevant. For the first time, the magnetic B vs. T phase diagram for the a^*-axis is also reported. Grüneisen analysis shows the onset of magnetic contributions around 60 K, i.e., well above T_{N1}. Uniaxial pressure dependencies of opposite sign, -1.3 K/GPa and 0.3 K/GPa, are extracted for the out-of-plane and in-plane directions at T_{N1}. For T^* we obtain $\partial T^*/\partial p_c = 1.4$ K/GPa. In particular we elucidate thermodynamic properties of the recently discovered skyrmion lattice phase and show that it is strongly enhanced by uniaxial pressure.

3.1 Introduction

Ternary intermetallic compounds of the type R_2TX_3 (R = rare earth, T = transition metal, X = element of main groups III to V) [13, 54] have been investigated extensively over the past decades, due to their variety of intriguing electronic properties ranging from superconductivity [55], giant magnetoresistance (GMR) [56–58], ferromagnetism [59] and incommensurate spin structures [14, 60], phenomena related to Kondo physics and heavy fermions [61–63], to non-Fermi-liquid [61] and spin-glass behavior [64–67]. This is particularly evident in the title material Gd_2PdSi_3 where a skyrmion lattice phase featuring giant topological Hall and Nernst effect was discovered recently [14, 68, 69].

Most members of the R_2PdSi_3 family of ternary silicides crystallize in a highly symmetric AlB_2-derived hexagonal structure (space group P6/mmm) with triangular lattice layers of R^{3+} magnetic sites sandwiching honeycomb nets of Pd/Si sites. While the Pd and Si ions were originally believed to be distributed statistically [70], an X-ray and neutron diffraction study by Tang et al. showed for Ho_2PdSi_3 that these ions actually order into a superstructure along both in- and out-of-plane directions, while the overall centrosymmetry of the structure is retained [71]. This leads to two nonequivalent sites for the R^{3+} ions, which has been shown to affect the magnetism in an applied magnetic field for Er_2PdSi_3 [72]. While no structural phase transition has been detected for R = Gd, Tb, Dy, Ho, Er and Tm, most R_2PdSi_3 compounds show long-range magnetic order at low temperatures [73–75].

These various ordering phenomena are driven by a delicate interplay of indirect exchange coupling mediated by the conduction electrons, i.e., the Rudermann-Kittel-Kasuya-Yosida (RKKY) interaction, spin-orbit coupling and the influence of crystal field (CF) effects. The Gd^{3+} ions in Gd_2PdSi_3, however, with a half-filled $4f$ shell, have vanishing orbital momentum ($\mathbf{J} \approx \mathbf{S} = 7/2$) and are not influenced by crystal field effects. Magnetic order, therefore, arises from the RKKY interaction and dipole-dipole interactions. Gd_2PdSi_3 exhibits two successive phase transitions around $T_N = 21$ K [60] and was found to exhibit a skyrmion lattice (SkL) phase of Bloch-type skyrmions in low magnetic fields applied along the c-axis [14]. A number of incommensurate spin structures both in zero-field as well as in higher applied magnetic fields have been identified [60] and the phase diagram in fields up to 9 T has been established through resistance and magnetization measurements as well as resonant X-ray scattering [14, 60, 73, 76]. Single crystal X-ray and neutron diffraction measurements yielded lattice parameters at 300 K (2 K) of $a = 4.079$ Å (4.066 Å) and $c = 4.098$ Å (4.091 Å), i.e. $\Delta a/a = 3.2 \cdot 10^{-3}$ and $\Delta c/c = 1.7 \cdot 10^{-3}$ [71].[1]

Except for these measurements of the lattice parameters, however, there is at present no study on magnetoelastic effects in Gd_2PdSi_3. Therefore, with a particular focus on the skyrmion lattice phase, we report detailed dilatometric studies of Gd_2PdSi_3 in a wide range of temperatures and magnetic fields. Our thermal expansion and magnetostriction data show pronounced magnetoelastic coupling and field effects extending up to temperatures of 150 K and above. Moreover, we uncover yet unreported phases and an anomaly in zero-field which appears well below the Néel transitions at $T_{N1} = 22.3(5)$ K and $T_{N2} = 19.7(5)$ K, thereby evidencing competing interactions already in zero-field. We update the magnetic phase diagram for $B \parallel c$-axis, present for the first time the phase diagram for $B \parallel a^*$-axis, and discuss in detail the thermodynamic properties for $B \parallel c$. Our results in particular elucidate the skyrmion lattice phase and we show that it is enhanced by uniaxial pressure.

3.2 Experimental Methods

Single crystals of Gd_2PdSi_3 have been grown by the optical floating-zone method as reported in Ref. [77, 78] and were previously studied by AC susceptibility, neutron diffraction [73], and angle-resolved photoemission spectroscopy [79]. The magnetization was studied in the temperature regime from 1.8 K to 300 K in magnetic fields up to 7 T in a Magnetic Properties Measurement System (MPMS3, Quantum Design) and up to 14 T in a Physical Properties Measurement System (PPMS, Quantum Design) using the Vibrating Sample Magnetometry (VSM) option. Specific heat measurements were performed on a PPMS-14 using a relaxation method on

1 Here, $\Delta a = a(300\text{ K}) - a(2\text{ K})$ and Δc analogously.

single crystals of $m = 20.79$ mg (2 K-300 K) and 13.49 mg (0.15 K-3 K). High-resolution dilatometry measurements were performed by means of a three-terminal high-resolution capacitance dilatometer in a home-built setup placed inside a Variable Temperature Insert (VTI) of an Oxford magnet system [26, 80]. With this dilatometer, the relative length changes dL_i/L_i along the crystallographic c and a^* directions, respectively, were studied on an oriented cuboid-shaped single crystal of dimensions $2.480 \times 1.300 \times 1.459$ mm^3. Measurements were performed at temperatures between 2 K and 300 K in magnetic fields up to 15 T, applied along the direction of the measured length changes, and the linear thermal expansion coefficients $\alpha_i = 1/L_i \cdot dL_i(T)/dT$ were derived. In addition, the field-induced length changes $dL_i(B_i)$ were measured at various fixed temperatures between 1.7 K and 200 K in magnetic fields up to 15 T. The longitudinal magnetostriction coefficient $\lambda_i = 1/L_i \cdot dL_i(B_i)/dB_i$ was derived from $dL_i(B_i)$.

3.3 Experimental Results

3.3.1 Evolution of Magnetic Order at $B = 0$

Uniaxial thermal expansion and specific heat show pronounced anomalies around 20 K which are associated with the onset of long-range magnetic order (Fig. 3.1). Close inspection of the anomalies indicates the proximity of not only one, but two phase transitions around T_N. While the anomaly at $T_{N1} = 22.3(5)$ K is seen as a jump in α_i, the anomaly at $T_{N2} = 19.7(5)$ K (20.3(5) K for the a^*-axis) is expressed as a peak. This observation confirms the results by Hirschberger et al. of two consecutive phase transitions in zero field [60]. Beyond these two known transitions, however, our data display a third anomaly indicative of a phase transition which has not been reported for single crystals of Gd_2PdSi_3. This anomaly, marked by $T^* \approx 13$ K in the inset of Fig. 3.1(b), is visible as a broad jump for both directions in α_i which extends between 10 K and 15 K and will be discussed in more detail below.

The specific heat data show the three observed features at T_{N1}, T_{N2} and T^*, too (Fig. 3.1(c)). The shape of the anomalies in c_p is analogous to their shape in $\alpha_\perp$. At very low temperatures below about 400 mK a quasi-linear behavior of c_p/T vs. T^2 is found (see the inset of Fig. 3.1(c)) reminding of similar observations in Lu_2PdSi_3 and Ce_2PdSi_3 [62, 81]. In this temperature regime, the data are described well by a linear and a cubic term, i.e., $c_p/T = \gamma + \beta T^2$. The quasi-linear term is described by an effective Sommerfeld coefficient $\gamma = 52(5)$ mJ/(mol K^2). This parameter is in between the values obtained for Lu_2PdSi_3 (6.9 mJ/(mol K^2)) and Ce_2PdSi_3 (108 mJ/(mol K^2)), the latter being discussed as evidence of heavy-fermion behaviour [62]. Whereas phonons can be neglected in this temperature regime, the coefficient $\beta = 1.25(3)$ J/(mol K^4) is rather large and reflects the contribution of low-energy antiferromagnetic excitations.

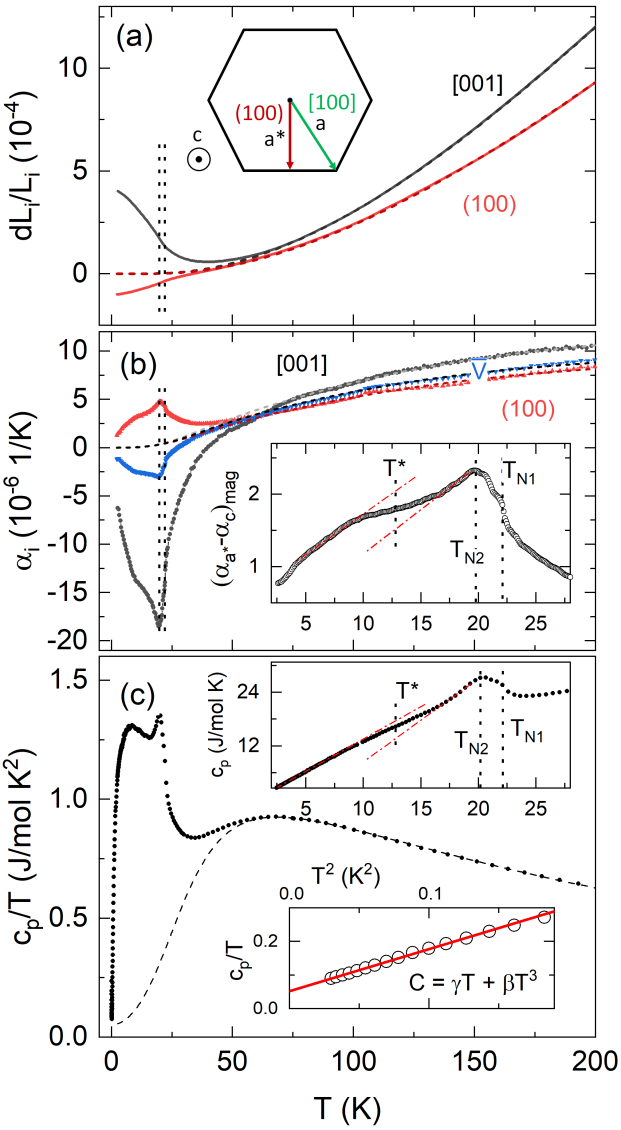

Figure 3.1: (a) Relative length changes dL_i/L_i along the c and a*-crystallographic directions. Directions w.r.t. the Gd lattice are indicated in the inset. (b) Associated linear thermal expansion coefficients α_i as well as the calculated 1/3 volume expansion α_V. The inset displays the difference $\alpha_{a^*,mag} - \alpha_{c,mag}$ of the background corrected thermal expansion coefficients $\alpha_{i,mag} = \alpha_i - \alpha_{ph}$. Vertical dashed lines indicate two phase transitions and the dashed-dotted line (inset) is a guide to the eye highlighting a feature around T^*. (c) Specific heat c_p/T (black markers). Inset: Low-temperature regime plotted as c_p/T vs. T^2. The solid red line shows a fit with $c_p = \gamma T + \beta T^3$. Dashed curves in all graphs mark the non-magnetic background as explained in the text.

The dashed lines in Fig. 1 show the phononic and electronic contributions to the relative length changes, thermal expansion coefficients, and specific heat. In order to obtain these contributions, the specific heat of the non-magnetic analog Lu_2PdSi_3 as reported by Cao et al. [81] was fitted by phononic Debye and Einstein terms, as well as an electronic term, according to

$$c_p^{el,ph} = \gamma T + n_{\mathrm{D}} D\left(\frac{T}{\Theta_D}\right) + n_{\mathrm{E}} E\left(\frac{T}{\Theta_E}\right) \tag{3.1}$$

where γ is the Sommerfeld coefficient, n_{D} and n_{E} are constants, $D(T/\Theta_{\mathrm{D}})$ and $E(T/\Theta_{\mathrm{E}})$ are the Debye and Einstein functions with the Debye and Einstein temperatures Θ_{D} and Θ_{E}. The fit to the Lu_2PdSi_3 specific heat data yields $\Theta_{\mathrm{D}} = 213$ K, $\Theta_{\mathrm{E}} = 454$ K, with $n_{\mathrm{D}} = 3.69$ and $n_{\mathrm{E}} = 1.98$. γ was fixed to the value reported by Cao et al. of 6.93 mJ/(mol K^2). Compared to $\Theta_{\mathrm{D}} = 191$ K by Cao et al., extracted from the low temperature regime, our value is slightly larger.

Scaling the Debye and Einstein temperatures by the different masses of Lu and Gd we obtain a scaling factor [82] of $\Theta_{\mathrm{D,LPS}}/\Theta_{\mathrm{D,GPS}} = 0.962$. The specific heat and thermal expansion of Gd_2PdSi_3 were thus fitted with fixed $\Theta_{\mathrm{D}} = 222$ K $= \Theta_{\mathrm{D,LPS}}/0.962$ and correspondingly $\Theta_{\mathrm{E}} = 471$ K. For the fit to the specific heat, $\gamma = 52$ mJ/(mol K^2) was also fixed. For the thermal expansion the electronic contribution was negligibly small and therefore omitted, i.e. it was fitted by

$$\alpha^{ph} = n_{\mathrm{D}} D\left(\frac{T}{\Theta_D}\right) + n_{\mathrm{E}} E\left(\frac{T}{\Theta_E}\right) \tag{3.2}$$

with parameters n_{D} and n_{E}. The phononic contributions to dL_i/L_i in Fig. 1(a) were obtained by integrating the background obtained for the respective α_i.

Subtracting the electronic and phononic backgrounds from the specific heat and thermal expansion coefficients yields their respective magnetic contributions which extend up to about 60 K. This agrees with the temperature regime where the magnetization exhibits a non-linear field dependence up to 7 T (see Fig. S1). From $c_{\mathrm{p,mag}}/T$ the changes in magnetic entropy, S_{mag}, above 150 mK are calculated. We obtain a constant $\Delta S_{\mathrm{mag}}(T > 150\ \mathrm{mK}) = 31.3$ J/(mole K) above 60 K, which is 90% of the full expected magnetic entropy of $2R\ln 8 = 34.6$ J/(mole K), where R is the universal gas constant.

Returning to the thermal expansion data, we see that the anomalies in the thermal expansion coefficients, at T_{N1} and T_{N2}, are of opposite sign for the c- and a^*-axis, indicating opposite pressure dependencies $\partial T_{\mathrm{N}i}/\partial p_{\mathrm{c}} < 0$ and $\partial T_{\mathrm{N}i}/\partial p_{\mathrm{a}^*} > 0$. The volume thermal expansion also indicates a negative hydrostatic pressure dependence

$\partial T_{\mathrm{N}i}/\partial p < 0$ for both antiferromagnetic transitions.

The Grüneisen ratio of the thermal expansion coefficient and the specific heat is a valuable quantity to determine the relevant energy scales driving the system and to quantify its pressure dependencies. In the presence of one dominant energy scale ε, this ratio is independent of temperature and enables the determination of the pressure dependence of ε, i.e. [83, 84],

$$\Gamma_i = \frac{\alpha_i}{c_{\mathrm{p}}} = \frac{1}{TV_{\mathrm{m}}} \frac{\partial S/\partial p_i}{\partial S/\partial T} = \frac{1}{V_{\mathrm{m}}} \frac{\partial \ln \varepsilon}{\partial p_i}. \tag{3.3}$$

Here, V_{m} is the molar volume and the index i indicates a linear direction or the volume. At T_{N}, Eq. 3.3 converts to $\Gamma = (T_{\mathrm{N}} V_m)^{-1} \cdot \partial T_{\mathrm{N}}/\partial p$. Comparing the magnetic contributions $\alpha_{i,\mathrm{mag}}$ and $\mathrm{c_{p,mag}}$ hence allows to identify temperature regimes where the Grüneisen relation implies only one dominant energy scale while appropriate scaling enables to read off the respective parameter $\Gamma_{\mathrm{i,mag}}$. As shown in Fig. 3.2, the overall behavior of $\alpha_{i,\mathrm{mag}}$ and $\mathrm{c_{p,mag}}$ is similar except for a distinct jump in $\alpha_{i,\mathrm{mag}}$ at ~ 12 K which is much less pronounced in the magnetic specific heat. In both cases, magnetic contributions start to evolve around 60 K.

Despite the overall similar behavior, there are differences at higher temperatures, too. While the a*-axis shows a nearly perfect overlap between $\alpha_{i,\mathrm{mag}}$ and $\mathrm{c_{p,mag}}$ down to 14 K as shown in Fig. 3.2(a), we only observe a very good agreement around $\mathrm{T_{N1}}$ and $\mathrm{T_{N2}}$ for the c-axis, in a range from 17 K to about 23 K. We also note that below ∼14 K our results indicate the failure of Grüneisen scaling rather than the presence of just a different scaling parameter.

Our data, however, clearly imply the presence of a single dominant energy scale at and around the magnetic ordering temperatures $\mathrm{T_{N1}}$ and $\mathrm{T_{N2}}$. The obtained Grüneisen parameters amount to $\Gamma_{\mathrm{c,mag}} = -91(13) \cdot 10^{-8}$ mol/J and $\Gamma_{\mathrm{a^*,mag}} = 22(3) \cdot 10^{-8}$ mol/J. From these values, moderate pressure dependencies are derived, i.e., we obtain negative pressure dependencies $\partial T_{\mathrm{N1}}/\partial p_{\mathrm{c}} = -1.3(2)$ K/GPa and $\partial T_{\mathrm{N2}}/\partial p_{\mathrm{c}} = -1.4(2)$ K/GPa for uniaxial pressure applied along the c-axis. The uniaxial pressure dependencies for $p \parallel a$*-axis are positive and more than a factor of four smaller, i.e., 0.31(5) K/GPa for $\mathrm{T_{N1}}$ and 0.34(5) K/GPa for $\mathrm{T_{N2}}$.

While our data hence evidence that the ordering phenomena at $\mathrm{T_{N1}}$ and $\mathrm{T_{N2}}$ are governed by the same energy scale, an additional energy scale becomes relevant upon further cooling, around T^*, as proven by the failure of Grüneisen scaling (cf. Fig. 3.2). Closer inspection of the associated anomalies implies not only a broad jump-like increase in the thermal expansion coefficients but also a less pronounced anomaly in $\mathrm{c_p}$ which is visible much more clearly in the $\mathrm{c_p}/T$ data in Fig. 3.1c.

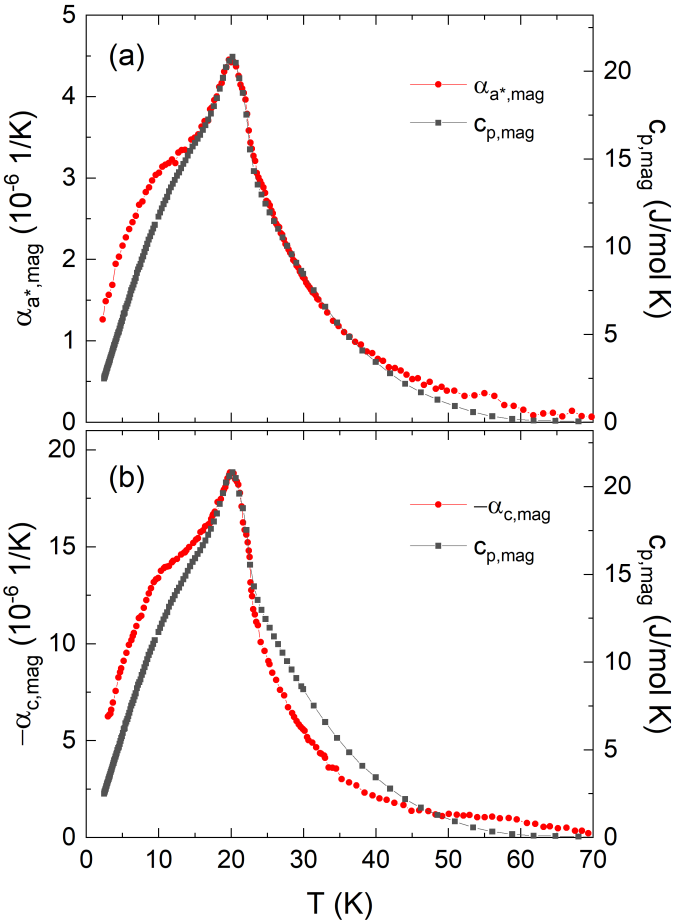

Figure 3.2: Magnetic contributions to the thermal expansion coefficient (left ordinate) and specific heat (right ordinate) for (a) the a^*-axis and (b) the c-axis after subtracting phononic and electronic contributions as described in the text.[a]

[a] The T-scale for $\alpha_{c,mag}$ was shifted by +0.4 K to match the specific heat anomaly.

In an attempt to deduce the anomaly size associated with the respective features we obtain $\Delta c_p^* \approx 2.7(5)$ J/(mole K), $\Delta\alpha_V^* \approx 1.8 \cdot 10^{-6}$/K, $\Delta\alpha_c^* \approx 4.1(6) \cdot 10^{-6}$/K, $\Delta\alpha_{a^*}^* \approx -1.0(3) \cdot 10^{-6}$/K. The changes in magnetization around T* are very small for both axes and could not be seen in the isothermal magnetization $M(B)$. However, temperature sweeps of the magnetization in static field evidence a jump in $\partial\chi/\partial T$, which is visible for $B \geq 0.2$ T (0.25 T) for $B \parallel c$ ($B \parallel a^*$) (see SI, Fig. S10(a)). At 0.2 T the jump height amounts to $5.6(1.4) \cdot 10^{-3} \mu_B$/(f.u. K). Further values are listed in Tab. S7.

3.3.2 Thermal Expansion at B $\neq$ 0 and Magnetostriction

The effect of high magnetic fields on the thermal expansion and specific heat is shown in Fig. 3.3. A number of observations can be made: (1) The sharp features indicating phase transitions are absent at $B = 15$ T. (2) Significant entropy is shifted to higher temperatures and, at $B = 15$ T, significant field effects are visible at least up to 150 K in all shown quantities, in particular for α_c even up to about 200 K. (3) Magnetostriction from 0 T to 15 T is positive (negative) for the c-axis (a^*-axis), and (4) the temperature region of negative thermal expansion of the c-axis extends up to about 65 K at 15 T, compared to 38 K in zero-field. Note, that the magnetostriction data fully agree to the thermal expansion data at $B \neq 0$ T as shown by the (green) vertical lines in the inset of Fig. 3.3.

Magnetostriction data at $T \approx 2$ K shown in Fig. 3.4(a) and (d) further confirm strong magnetoelastic coupling and in addition clearly show the field-induced phase transitions. For comparison the isothermal magnetic susceptibility $\chi(B) = \partial M(B)/\partial B$ is also presented on the same field scale for both directions (Fig. 3.4(b-c)). Considering the data for $B \parallel c$, four anomalies can be identified (Fig. 3.4(a)): Up to 3.5 T, there are two sharp peaks in λ_c signalling jumps in $dL_c(B)$ with only small field-hysteresis, followed by a broad peak with a large hysteresis of $\sim$0.8 T. The size of the anomalies for up- and down-sweep differs strongly. All three anomalies indicate discontinuous phase transitions. Corresponding anomalies and hystereses are also visible in the magnetic susceptibility. In addition, there is a broad downward jump in λ_c at around 9 T, above which magnetostriction becomes virtually zero which is also reflected by small χ, i.e., rather full alignment of magnetic moments in field (please note the logarithmic scale in Fig. 3.4(b) and (c)). The overall region where hysteresis is visible extends from about 6 T down to the lowest fields (see the inset in Fig. 3.4(a)) but no remanent magnetostriction is visible which would indicate irreversible changes in the sample, e.g., through domain effects. Four features are also visible in λ_{a^*} for $B \parallel a^*$ (Fig. 3.4(d)). These anomalies are smaller in magnitude, much broader and less well-defined than for the c-axis. Similar to the findings for $\lambda_c(B \parallel c)$, there is a jump at higher fields, at about 7.3 T, but here of opposite sign. Again, it signals a continuous transition to the saturated phase of vanishing magnetostriction. In contrast to $B \parallel c$, the magnetostriction measurements $dL_{a^*}(B \parallel a^*)$ feature pronounced remanent magnetostriction below 5 K, i.e., non-zero overall length changes after sweeping the field from 0 T to 15 T and back to 0 T. At 1.8 K, this amounts to $(\Delta L/L)_{\mathrm{rem}} = 1.4 \cdot 10^{-5}$. We attribute this observation to the irreversible effects of structural or magnetic domains as seen, e.g., in $CoCl_2$ [85], $NiCl_2$ [86] and $NiTiO_3$ [87]. Such irreversible domain effects seem to be absent in the measurements along the c-axis. The transition between a multidomain and single domain state may thus be fully reversible for $B \parallel c$. We conclude that hysteresis found for $B \parallel a^*$ below 3.5 T is both due to the discontinuous nature of the phase transitions and domain

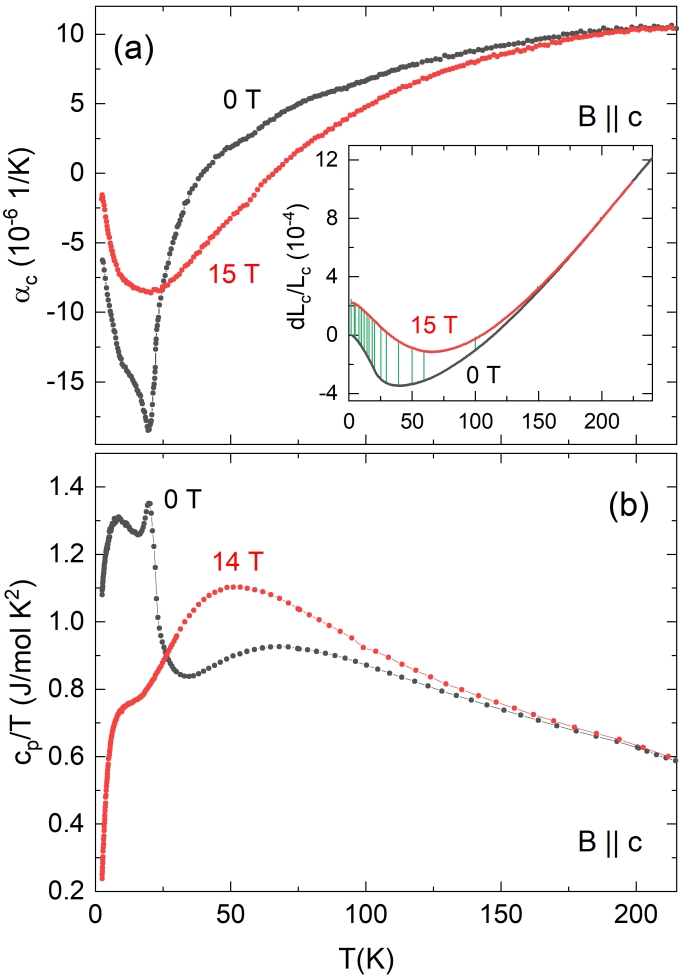

Figure 3.3: The effect of high fields on (a) the thermal expansion coefficient (B = 15 T) and (b) the specific heat c_p/T (B = 14 T) as compared to zero-field measurements. The inset in (a) shows the relative length changes. Vertical green bars indicate magnetostriction data from 0 T to 15 T at several temperatures.

effects.

Both data sets, hence, imply a series of four phase transitions in magnetic field, at $T \approx 2$ K, which is also corroborated by magnetization studies (also see Fig. S7) and agrees to the recently published phase diagram for $B \parallel c$ [60]. Following the notations in Refs. [14, 60] for the phases appearing for $B \parallel c$, we label the respective phases as IC-1, A, IC-2, DP, and field induced ferromagnetic (fiFM) phase, with IC-1/IC-2 being characterized by incommensurate spin configurations, A by the formation of a skyrmion lattice (SkL), and DP by the depinning of the direction of magnetic moments (see also the phase diagram in Fig. 3.6). We note, however, that

while the magnetostriction data evidence field-driven structural changes, domain effects may obscure the actual phase transitions up to the field and temperature regions at which a single domain state is achieved. In particular, broad peaks in the magnetostriction coefficients as seen in λ_{a^*} (Fig. 3.4(b), S4(e) and (f)) do not necessarily indicate the actual phase boundaries, but the peak positions may differ from those found in the magnetization studies, as shown by a phenomenological model by Kalita et al. [85]. Therefore, for the further thermodynamic analysis of the phase boundaries as well as the construction of the phase diagram, for $B \parallel a^*$ we will only consider anomalies in the magnetostriction which can directly be linked to anomalies in isothermal magnetization.

In order to obtain the phase boundaries, we have performed thorough magnetostriction and isothermal magnetization studies at various fixed temperatures as well as corresponding temperature sweeps at fixed magnetic field (see Figs. S4, S5, S7) [1]. This is demonstrated in Fig. 3.5, where the thermal expansion coefficients in low fields up to 3 T and the corresponding magnetization data are presented. For $B \parallel c$ (Fig. 3.5(a) and (b)), the evolution of two different phase boundaries can be traced straightforwardly. Specifically, applying small fields yields a suppression of T_{N2} while the jump at T_{N1} becomes more distinguished. In increasing field T_{N1} is also suppressed to lower temperature, but to a smaller extent (Fig. 3.5a). Above 0.3 T the peak assigned to T_{N2} at zero-field changes its shape, signaling the transition from the previously reported skyrmion lattice A phase to the IC-2 phase. It is associated with a jump $\Delta\chi_c^A$ in the static susceptibility from one T-independent value to another (Fig. 3.5(b)). At 0.4 T, a second feature corresponding to the transition from the A phase to the IC-1 phase is visible in both α_c and χ_c, while above 0.9 T (1 T for χ_c) all features below T_{N1} are gone. Quantitatively, $\Delta\chi_c^A$ gradually decreases from 0.91 μ_B/Gd^{3+} at 0.9 T and 8.6 K to 0.36 μ_B/Gd^{3+} at 0.4 T and 16.4 K. The pronounced jump in α_c at T_{N1} corresponds to a kink in the static susceptibility, i.e., a jump in its derivative (see SI, Fig. S7).

As mentioned before, anomalies seen for measurements along the a^*-axis are in general much weaker and less well-defined than for the c-axis. Furthermore, the evolution of anomalies in the thermal expansion and the static susceptibility along the a^*-axis is even more complex than for $B \parallel c$ (Fig. 3.5(c) and (d)). In zero-field, the anomaly at T^* is also visible (see Fig. 3.1, as well as SI, Fig. S10(d)) and can be traced up to 0.4 T in $\partial\chi/\partial T$. Also, a jump in $\alpha_\perp$ evolving from T_{N1} can be followed to lower temperatures for increasing fields, corresponding to a jump in $\partial\chi/\partial T$. Above 0.6 T this jump in $\partial\chi/\partial T$ splits into two jumps, uncovering an additional phase

1 Magnetization measurements have been performed following the zero-field cooling (ZFC) protocol unless stated otherwise, i.e., the sample was cooled to lowest temperatures before the field was applied and the data were recorded during warming.

between the IC-2 and fiFM phases, while we only see one broad jump in $\alpha_\perp$.

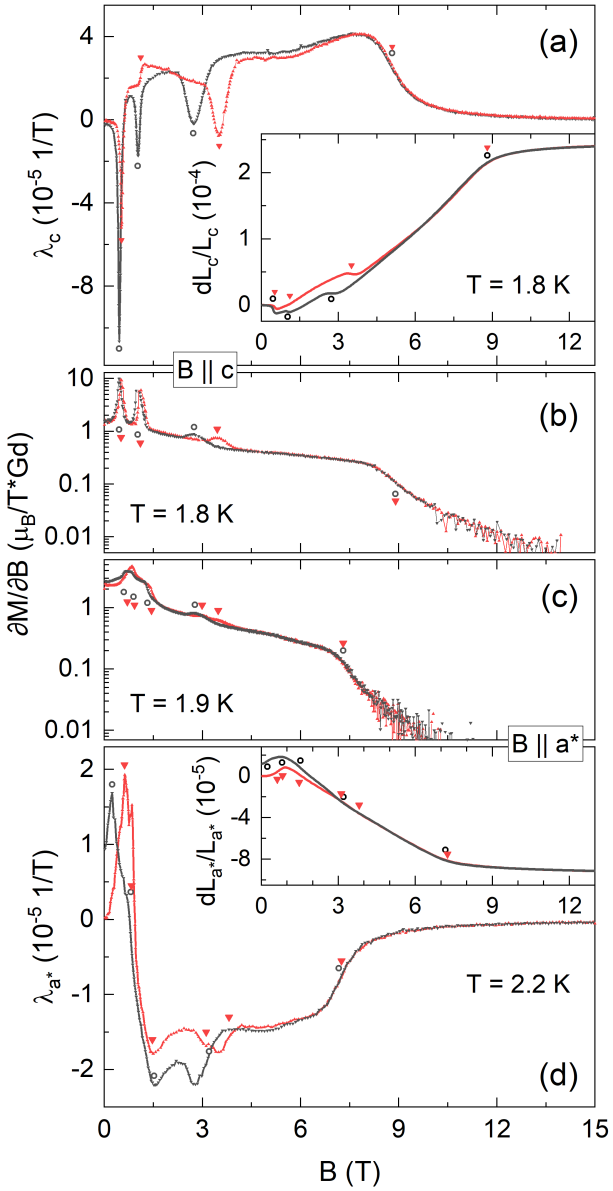

Figure 3.4: Magnetostriction coefficients λ_i ($i = c$, a^*) and isothermal magnetic susceptibility, $\partial M/\partial B$, at temperatures around 2 K, for $B \parallel c$ (a-b) and $B \parallel a^*$ (c-d). Note the logarithmic scale in (b) and (c). Insets in (a) and (d) show the relative length changes $dL_\mathrm{i}(B)/L_\mathrm{i}$. Triangles and empty circles mark anomalies in (a-d). Red markers and lines represent up-sweeps, black ones down-sweeps.

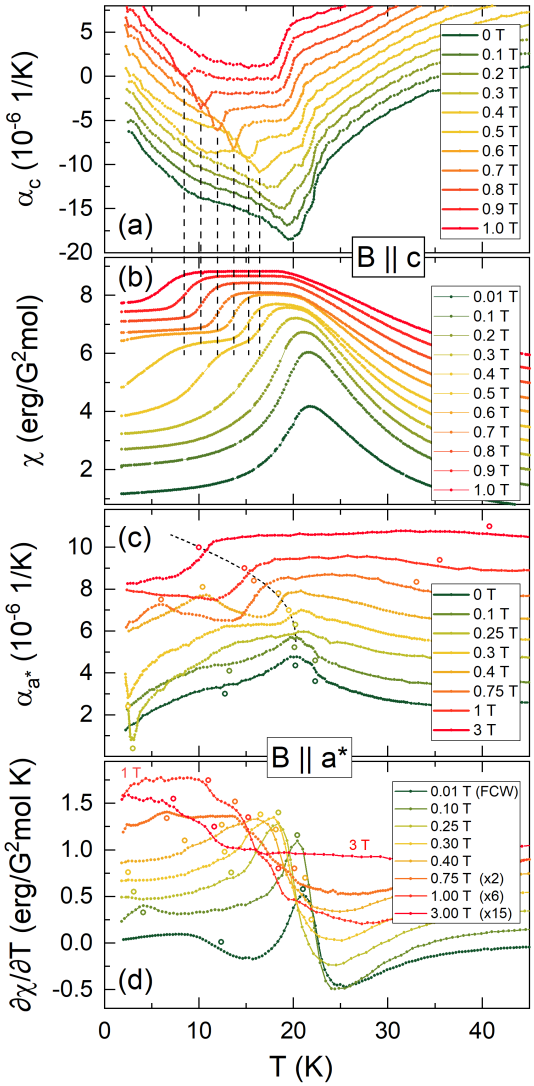

Figure 3.5: Thermal expansion coefficients (a,c) and static magnetic susceptibility $\chi = M/B$ (b), respectively its derivative $\partial\chi/\partial T$ (d), for (a-b) $B \parallel c$ and (c-d) $B \parallel a^*$. Curves are offset vertically by (a) $1.6{\cdot}10^{-6}$/K, (b) 0.5 erg/(G^2 mol), (c) $1{\cdot}10^{-6}$/K, and (d) 0.2 erg/(G^2 mol K), respectively, for better visibility. 0.75 T to 3 T data in (d) are multiplied by a constant as indicated in the legend and 3 T data is offset by 1.5 erg/(G^2 mol K) instead of 1.4 erg/(G^2 mol K). "FCW" indicates a field-cooled-warming measurement.[a] Empty circles mark temperature positions of the anomalies as extracted for the phase diagram.

[a] For the field-cooled warming protocol, the sample is cooled in the applied field to the lowest temperatures and measured during the subsequent warming process.

3.4 Discussion

From our detailed dilatometric and thermodynamic data we construct the phase diagrams for the c- and a^*-axes in Fig. 3.6. While the general features for $B \parallel c$ confirm previous results [14, 60, 76], our data evidence two phases in zero-field which were previously unknown: (1) Our isothermal magnetization data between 19 K and 22 K (SI, Fig. S7) clearly indicate that the IC-2 phase does not extend to zero field, but there is a separate pocket closed off by a phase boundary extending from the edge of the A(SkL) phase to $T_{N1} = 22.3$ K. We label this new phase IC-3, since incommensurate spin structures were previously reported for this temperature regime [14]. (2) Furthermore, the phase boundary at T^* splits the IC-1 phase into IC-1 and IC-1' (Fig. 3.1(b) inset). The yet unreported phase diagram for $B \parallel a^*$ in general shows a similar behavior, with the critical fields of the IC-1' and IC-4 phases at lowest temperatures assuming higher values than IC-1' and the A phase for the c-axis. The IC-4 phase appearing for $B \parallel a^*$ (see Fig. 3.6b) reminds of the A(SkL) phase for $B \parallel c$, however, it was shown previously by angle-dependent resistivity measurements in the a^*-c-plane at 2 K that it does not connect to the A(SkL) phase [88]. The magnetic structure of this phase needs to be clarified by diffraction studies. One major difference between the phase diagrams is seen for $B \parallel a^*$, where the IC-2 phase is not directly adjacent to the field-induced FM phase, but there is an additional phase (labelled B) in between (see Fig. 3.5(c) and (d)). The B phase is bordered by two jumps both in c_p as well as in $\partial\chi/\partial T$.

From the anomalies in the thermal expansion, specific heat and magnetization at the phase boundaries we calculated the uniaxial pressure and field dependence of the critical temperatures and critical fields, as well as the entropy changes at the phase boundaries for $B \parallel c$-axis. Considering $T^*(B)$ marking a continuous phase transition, the associated jumps in specific heat (Δc_p), magnetic susceptibility ($\Delta(\partial M/\partial B)$), and thermal expansion coefficient ($\Delta\alpha$) are connected with the magnetic field and pressure dependencies of T^* by the Ehrenfest-type relations (see e.g. Ref. [9, 89])

$$\left(\frac{\partial T^*}{\partial B_i}\right)_p = -T^* \frac{\Delta(\frac{\partial M_i}{\partial T})_B}{\Delta c_{p,B}} \tag{3.4}$$

and

$$\left(\frac{\partial T^*}{\partial p_i}\right)_B = T^* V_m \frac{\Delta\alpha_i}{\Delta c_p}. \tag{3.5}$$

Using the molar volume $V_m = 7.06 \cdot 10^{-5}$ m^3/mol (see Ref. [73]) as well as the anomaly values presented above and in Tab. S7 – for their extraction from the

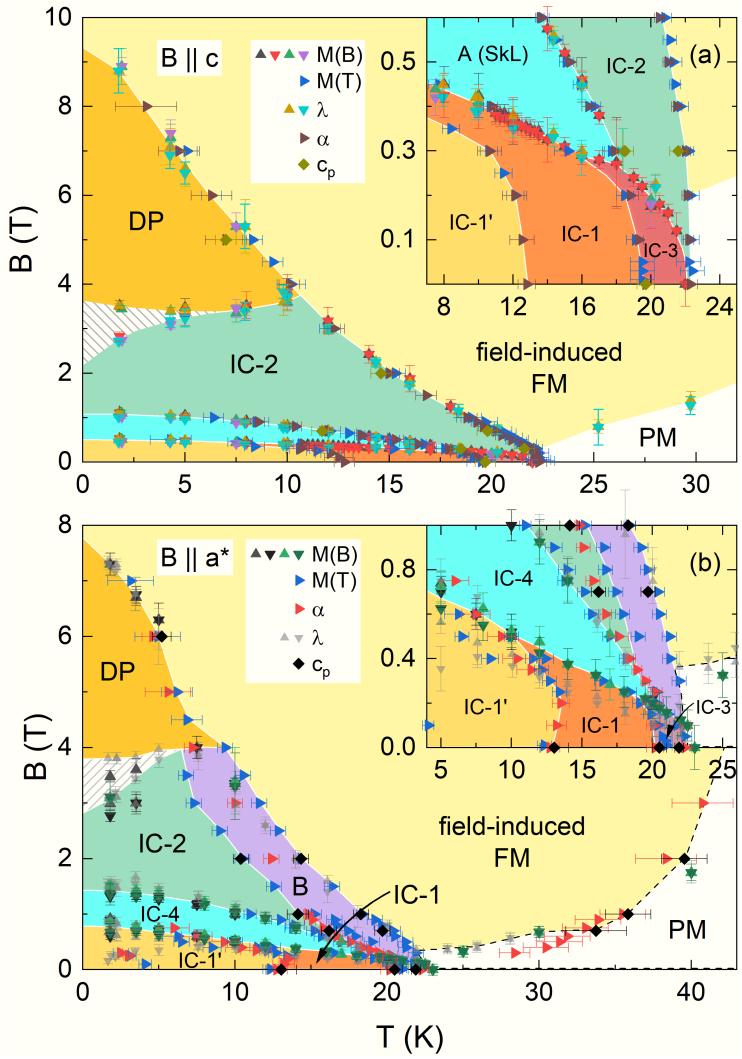

Figure 3.6: Phase diagrams for (a) $B \parallel c$ and (b) $B \parallel a^*$ constructed from different experimental techniques as indicated in the legends. The shaded areas show two strong hysteresis regimes. The abbreviations for the phases are: paramagnetic (PM), incommensurate magnetic orders (IC-x), antiferromagnetic (A,B), antiferromagnetic skyrmion lattice (SkL), and depinned phase (DP).

experimental data see the supplement, Fig. S10 – we obtain a moderate uniaxial pressure dependence of $\partial T^*/\partial p_c = -1.4(3)$ K/GPa. In a field of 0.2 T, the field dependence is very small and amounts to only $\partial T^*/\partial B_c = -37(13)$ mK/T. At 0.3 T, $\partial T^*/\partial B_c$ rises to $-0.28(18)$ K/T. These results demonstrate that the IC-1 phase is stabilized both under pressure and applied field at the expense of the IC-1' phase. Also, from these values we can calculate the expected jump in $\partial M/\partial B$ ($\Delta\chi$), at

$T^*(B)$ via

$$\left(\frac{\partial T^*}{\partial B}\right)_p = -\frac{\Delta\left(\frac{\partial M}{\partial B}\right)_{p,T}}{\Delta\left(\frac{\partial M}{\partial T}\right)_{p,B}}. \tag{3.6}$$

At 0.2 T this yields $\Delta\chi = -2 \cdot 10^{-4}\mu_\mathrm{B}/(\mathrm{f.u.\ T})$, which is well below the resolution limit of our experiment, explaining why our isothermal magnetization studies do not show anomalies at T^* (see SI, Fig. S10). Note, that in an early report on Gd_2PdSi_3 by Mallik et al. the authors detected a jump in the effective local field $|B_{eff}|$ at 15 K by Mössbauer spectroscopy and attributed it to a lower ordering temperature of one of the two Gd sites in Gd_2PdSi_3. This transition was not detected in any of the later reports on single crystalline samples, but our results presented in this work clearly confirm its presence.

The phase boundaries between the A(SkL), IC-2, and DP phases are of discontinuous nature, exhibiting jumps $\Delta L_i/L_i$ in the length changes and ΔM in the magnetization (i.e., Δm in magnetic moment). Therefore, the Clapeyron equations [9]

$$\left(\frac{\partial T_c}{\partial p_i}\right)_B = V_\mathrm{m}\frac{\frac{\Delta L_i}{L_i}}{\Delta S} \tag{3.7}$$

$$\left(\frac{\partial T_c}{\partial B_i}\right)_p = -\frac{\Delta m_i}{\Delta S} = -\frac{\Delta(M_i \cdot V)}{\Delta S} \tag{3.8}$$

$$\left(\frac{\partial B_c}{\partial p_i}\right)_T = V_\mathrm{m}\frac{\frac{\Delta L_i}{L_i}}{\Delta m_i} \tag{3.9}$$

apply for the pressure and field dependence of the respective critical temperatures T_c and critical fields B_c. Hence, the observed slopes $\partial T_c/\partial B$ (see Tab. S1–S4) and the jumps ΔM allow us to obtain the associated entropy changes ΔS.

For the transition from the incommensurate IC-1' phase to the skyrmion lattice A phase, a jump $\Delta M = 0.99(10)\mu_\mathrm{B}$/Gd accompanies the c-axis contraction of $\Delta dL_\mathrm{c}/L_\mathrm{c} = -10.8(1.1) \cdot 10^{-6}$ at 4.3 K. Applying the above-mentioned thermodynamic relations yields small entropy changes on the order of $\Delta S_\mathrm{calc} = 125(13)$ mJ/mol K and a negative uniaxial pressure dependence of $\partial T_\mathrm{c}/\partial p_i = -6.1(9)$ K/GPa. At higher temperatures these values decrease down to 110(11) mJ/mol K and $-1.5(2)$ K/GPa at 16 K (see Tab. S1). The c-axis also contracts at the transition from the skyrmion lattice A phase to the IC-2 phase, but these contractions are much

smaller ($\Delta dL_c/L_c = -2.4(3) \cdot 10^{-6}$ at 4.3 K) while the jumps in magnetization again roughly correspond to one Bohr magneton per Gd ion ($\Delta M = 1.01(11)\mu_B$/Gd at 4.3 K). Accordingly, this phase boundary shows much smaller pressure dependence, i.e., $\partial T_c/\partial p_i = -0.47(7)$ K/GPa at 4.3 K (see Tab. S2). At the same time, the steeper slope of the phase boundary $B_c(T)$ implies larger changes in entropy of 360(40) mJ/mol K at 4.3 K which increases to almost 600(60) mJ/mol K at 16 K. We note that the analysis of anomalies from temperature instead of field sweeps confirms these values (Tab. S3). Looking at higher fields, the slope of the phase boundary from IC-2 to the depinned phase (DP) is very small, changing from a small negative slope below 6 K to a small positive slope above. Considering the measured anomalies $\Delta M = 0.08(4)\mu_B$/Gd at 4.3 K, this yields negligible associated entropy changes (Tab. S4). In contrast, there are pronounced lattice effects ($\Delta dL_c/L_c = -17(2) \cdot 10^{-6}$ at 1.77 K) yielding a very large pressure dependence for the phase boundary IC-2 $\rightarrow$ DP.

The results of the thermodynamic analyses are shown in table I as well in tables S1 to S4 in the supplement. In particular, our analysis evidences pronounced negative uniaxial pressure dependencies for all three phase transitions between IC-1/IC-1', A(SkL), IC-2 and DP at low temperatures. This implies that the IC-1'/IC-1, A(SkL) and IC-2 phases are all destabilized by pressure along the *c*-axis with respect to the higher temperature phases, i.e., the field-induced FM phase – and the paramagnetic phase at low fields – is stabilized.

In particular, our data for $B \parallel c$ provide further information on the skyrmion phase. Both the onset of the SkL phase from incommensurate magnetic order IC-1/IC-1' and its transition into the incommensurate IC-2 phase are discontinuous in nature. In both cases, transitions are associated with the increase of magnetization by about 1 μ_B/Gd. Rather flat phase boundaries in the magnetic phase diagram are indicative of comparably small entropy changes. Our quantitative analysis evidences that the evolution of the SkL phase, depending on the temperature, yields an entropy gain of $\Delta S \approx 100 - 150$ mJ/(mol K) while the entropy jumps at the transition out of the skyrmion phase by 300-600 mJ/(mol K). These values are by far larger than for the chiral magnet MnSi where latent heat at the phase boundaries only

Table 3.1: Relevant quantities and anomaly sizes at the phase boundaries of the skyrmion lattice phase, at $T = 4.3$ K, and in magnetic fields $B \parallel c$ which have been either directly extracted from the experimental data or were obtained by using thermodynamic relations as given in the text.

Transition	T (K)	B_c (T)	$\Delta(dL/L)$ (10^{-6})	Δm (μ_B/Gd)	$\partial B_c/\partial T$ (T/K)	ΔS_{calc} (mJ/mol K)	$\partial T_c/\partial p_i$ (K/GPa)	$\partial B_c/\partial p_i$ (mT/GPa)
IC-1 $\rightarrow$ A(SkL)	4.3±0.1	0.49±0.02	–10.8±1.1	1.0±0.1	–0.01	125±13	–6.1±0.9	–50±50
A(SkL) $\rightarrow$ IC-2	4.3±0.1	1.04±0.03	–2.4±0.3	1.0±0.1	–0.03	360±40	–0.47±0.07	–15±2

amount to a few mJ/(mole K) [90]. Uniaxial pressure along the c-axis significantly enhances the SkL phase as seen by the uniaxial pressure dependencies of the transition temperatures. Specifically, at 4 K there is a rapid decrease of the IC-1/IC-1' $\rightarrow$ A(SkL) transition temperature $\partial T_{\mathrm{in}}/\partial p_c \approx -6$ K/GPa, leading to an expansion of the A(SkL) phase towards lower temperatures under pressure. At the same time the temperature of the A(SkL) $\rightarrow$ IC-2 transition, i.e. exiting the SkL phase towards higher temperatures, changes by only $\partial T_{\mathrm{out}}/\partial p_c \approx -0.5$ K/GPa (see tables I and II). Enhancement of skyrmion lattice phases under pressure is also observed in other materials. In the insulating skyrmion system Cu_2OSeO_3, Levatić et al. report a dramatic enhancement of the skymion pocket under pressure by about 8 K at 0.6 GPa [91]. While in Gd_2PdSi_3 the SkL phase appears at lower temperatures, our results ($\partial T_{\mathrm{in}}/\partial p_c - \partial T_{\mathrm{out}}/\partial p_c$) imply about half of this effect. We also note similar findings to the ones reported at hand in the chiral magnet MnSi [92, 93] where uniaxial pressure along [001] yields a rapid decrease of the onset temperature of the skyrmion phase while the high temperature phase boundary shows a much smaller pressure dependence [1]. Recent theoretical studies by Hayami et al. investigated the influence of single-ion anisotropy on the formation and stability of the skyrmion lattice phase. They show that easy-axis anisotropies stabilize magnetic-field-induced skyrmion crystals in frustrated magnets [94] and easy-axis (easy-plane) anisotropy substantially increases (decreases) the stable field-range for a Skyrmion lattice. These findings suggest, that the pressure dependencies stabilizing the skyrmion lattice phase in Gd_2PdSi_3 may originate from small distortions in the local environment of Gd leading to an increase of the weak magnetic anisotropy of the Gd moments.

The transition from the depinned phase to the field-induced ferromagnetic phase is of a continuous type. It exhibits a jump in the magnetostriction coefficient $\Delta\lambda = -4.7(5) \cdot 10^{-5}/T$ (at 1.77 K) and in the derivative of the magnetization $\Delta\partial M/\partial B = -0.159(16)\mu_{\mathrm{B}}/(\mathrm{T\ Gd})$ (T = 1.9 K). Using an Ehrenfest relation, the uniaxial pressure dependence of the critical field can be expressed as $dB_{\mathrm{c}}/dp_i = \Delta\lambda/\Delta(dM/dB)$, which yields $dB_{\mathrm{c}}/dp_c = 1.9(5)$ T/GPa at 1.77 K, i.e. the depinned phase is stabilized under uniaxial pressure p_c. Similarly, using the anomaly values listed in Tab. S5, we find uniaxial pressure dependencies of the critical field between $-0.65(16)$ T/GPa (10 K) and $-0.50(8)$ T/GPa (14 K) at the continuous transition IC-2 to fiFM.

While Gd_2PdSi_3 shows only moderate frustration, magnetic entropy and length changes are observed up to about 2.7 T_{N1} (60 K), thereby implying the evolution of short range magnetic order in this temperature regime. Effects of fluctuations above

1 For MnSi, this also holds for pressure along [111] and [110]. From our data only uniaxial pressure effects $p \parallel c$ are accessible so that a comparison for the other directions cannot be made.

T_N in Gd_2PdSi_3 were observed before in resistivity measurements. Measurements on polycrystalline samples show a well-defined minimum around 45 K [95] which was also confirmed in single crystals [68]. A theoretical explanation of this behavior based on the RKKY-interaction in combination with frustration was given by Wang et al. [96]. Grüneisen scaling suggests that these precursor fluctuations are of the IC-1/IC-3 type. Both ordering phenomena are driven by the same dominating energy scale which differs from the one driving IC-1'. As expected for a Gd^{3+}-system, magnetoelastic coupling is moderate. It is, hence, somehow surprising that magnetostriction is large at high temperatures and displays pronounced effects up to 200 K. In addition, despite linear field dependence of the magnetization, magnetostriction does not follow a B^2-law below 200 K (see Fig. S6) as would be expected from the relation $dL_i/L_i = -1/2V\partial\chi_i/\partial p_i B^2$ in the paramagnetic regime [97]. Tentatively, magnetostriction above 100 K implies negative uniaxial pressure dependence, $\partial\chi/\partial p_c < 0$, of the magnetic susceptibility while $\partial\chi/\partial p_{a^*} > 0$. This observation suggests that antiferromagnetic exchange interactions are strengthened by uniaxial pressure along the c-axis and weakened upon application of $p \parallel a^*$. Notably, however, the long-range magnetic ordering temperatures do not follow this trend as $\partial T_N/\partial p_c < 0$ which further highlights the complex nature of magnetism in Gd_2PdSi_3.

3.5 Conclusions

For the first time, high-resolution dilatometry was used to study the interplay between magnetism and the lattice of single crystalline Gd_2PdSi_3. Strong magnetoelastic coupling and field effects up to high temperatures are found. Pronounced anomalies in the thermal expansion, magnetostriction and magnetization allow us to obtain the magnetic phase diagram. This yields in particular several novel phases for $B \parallel c$ while the B vs. T phase diagram for $B \parallel a^*$ has not yet been reported at all in the literature. Grüneisen analysis shows the onset of magnetic contributions well above T_{N1}, and the pressure dependencies of ordering phenomena are obtained. In particular, we find that uniaxial pressure strongly enhances the skyrmion lattice phase.

Acknowledgements

We thank I. Mazilu and Y. Xu for support in the crystal growth. We acknowledge financial support by BMBF via the project SpinFun (13XP5088) and by Deutsche Forschungsgemeinschaft (DFG) under Germany's Excellence Strategy EXC2181/1-390900948 (the Heidelberg STRUCTURES Excellence Cluster), through project KL 1824/13-1, and within the SFB 463.

Supplementary Material: Magnetoelastic Coupling and Phases in the Skyrmion Lattice Magnet Gd_2PdSi_3 Discovered by High-resolution Dilatometry

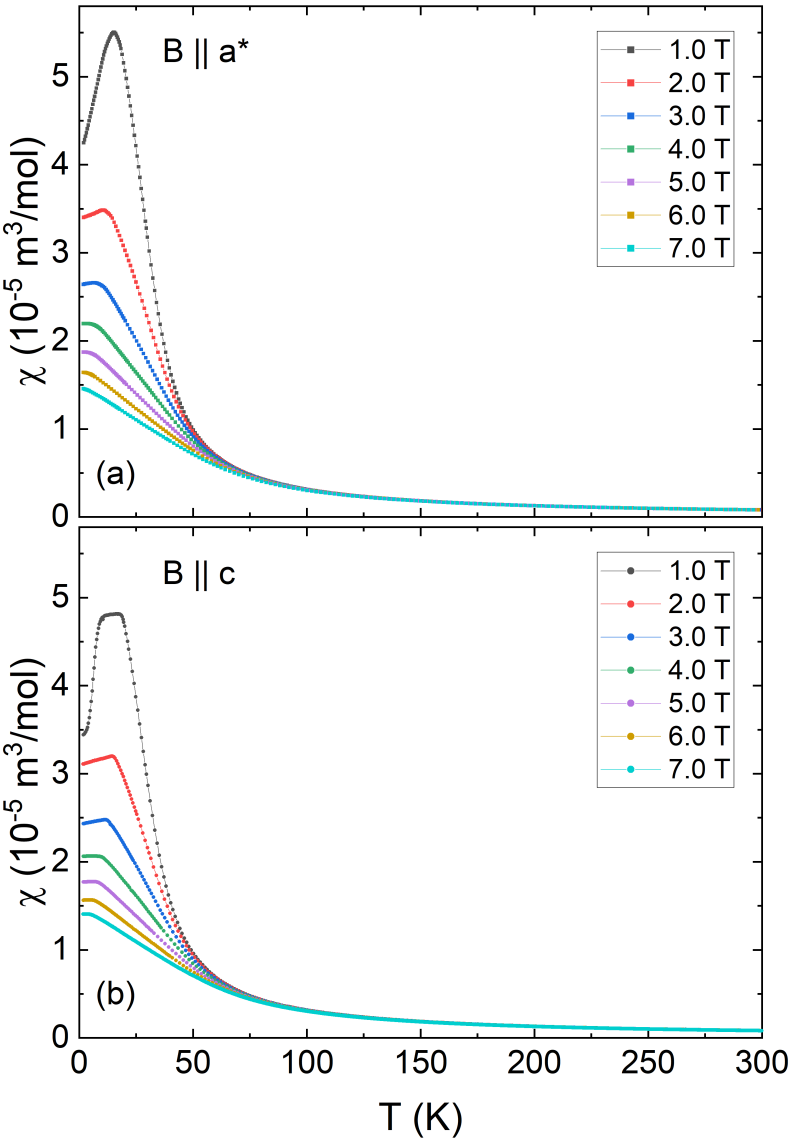

Figure S1: Static magnetic susceptibility $\chi = M/B$ for (a) $B \parallel a^*$ and (b) $B \parallel c$ (b).

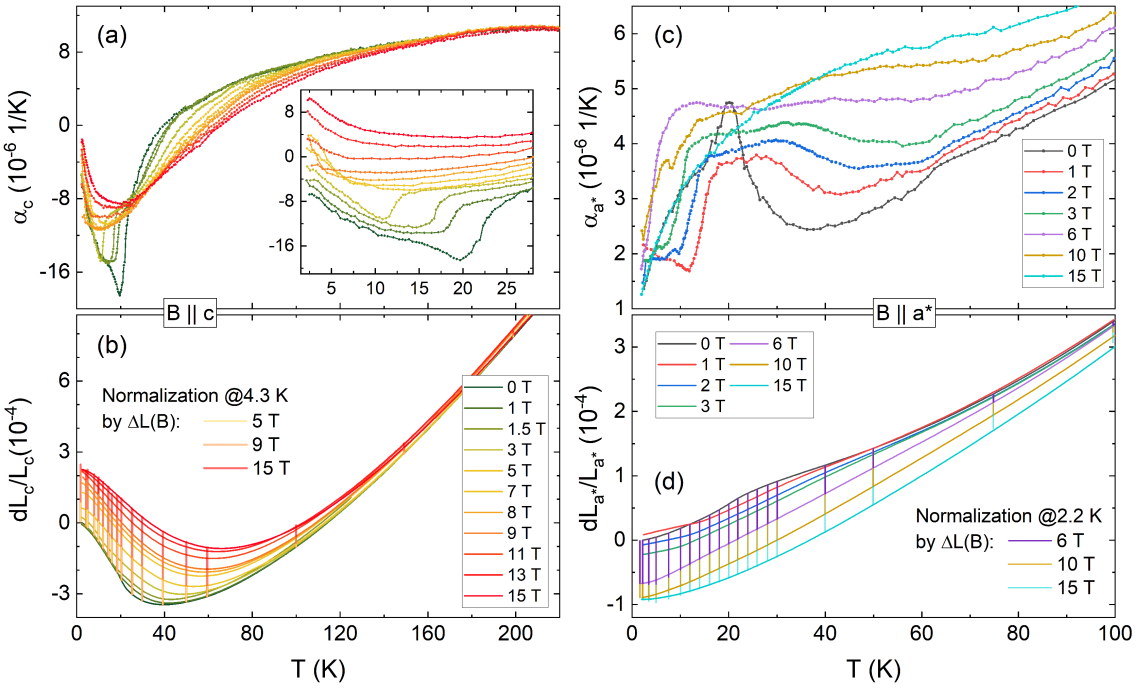

Figure S2: (a-b) Thermal expansion measurements up to 220 K for $B \parallel c$ in magnetic fields up to 15 T. (a) Thermal expansion coefficient α_c. The inset shows the magnified low temperature region with an offset of $1.2 \cdot 10^{-6}$ 1/K. (b) Relative length changes $dL_c(T)/L_c$. Vertical lines mark the changes $\Delta L(B)/L$ derived from magnetostriction measurements. The data at different fields are normalized by these changes at 4.3 K. (c-d) Thermal expansion measurements up to 100 K for $B \parallel a^*$ in magnetic fields up to 15 T. (c) Thermal expansion coefficient $\alpha_\perp$ offset by $2 \cdot 10^{-7}$ 1/K. (d) Relative length changes $dL_{a^*}(T)/L_{a^*}$. Vertical lines again mark the changes $\Delta L(B)/L$ taken from magnetostriction measurements. The data at different fields are offset and normalized by these changes at 2.2 K w.r.t. the zero-field data.

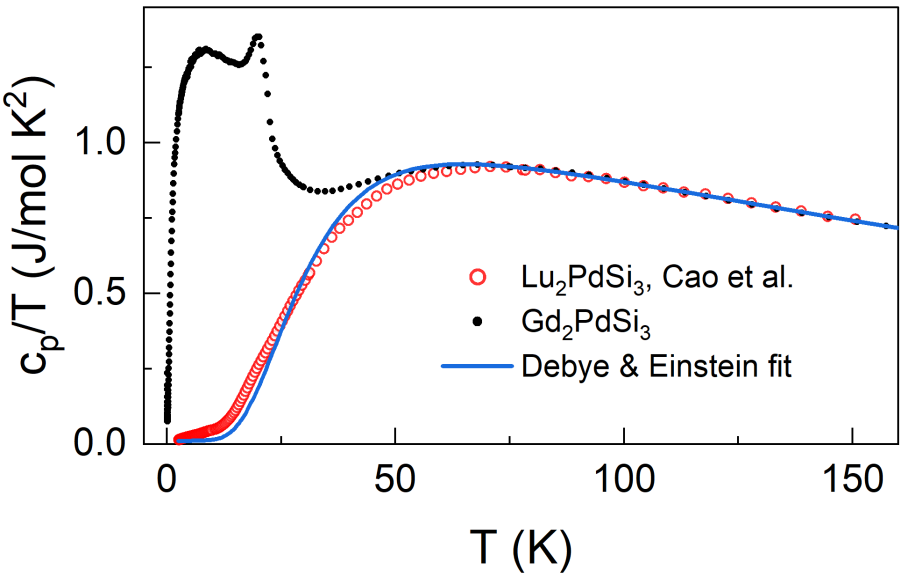

Figure S3: Comparison of the scaled Lu_2PdSi_3 specific heat c_p/T measured by Cao et al. [81] (red empty circles) with the Debye and Einstein fit (blue line). Note that the Lu_2PdSi_3 data was interpolated and therefore contains more data points than the published data.

Table S1: Relevant quantities and jumps, calculated changes of entropy, and calculated pressure dependencies for the discontinuous transition in magnetic field from IC-1/IC-1' → A(SkL) and IC-3 → IC-2 for the c-axis according to Eq. (3.7). The column of $\partial B_c/\partial T$ was calculated by taking the derivative of a polynomial fit to the values $B_c(T)$ for IC-1/IC-1' → A(SkL) and a linear fit (between between 18.39 K and 19 K as well as between 19 K and 21 K) for IC-3 → IC-2.

IC-1/IC-1' → A(SkL) – c-axis: Relevant quantities, entropy changes and uniaxial pressure dependencies							
T (K)	B_c (T)	$\Delta(dL/L)$ (10^{-6})	Δm (μ_B/Gd)	$\partial B_c/\partial T$ (T/K)	ΔS_{calc} (mJ/mol K)	$\partial T_c/\partial p_i$ (K/GPa)	$\partial B_c/\partial p_i$ (T/GPa)
1.77	0.52±0.02	–7.3±0.8	1.00±0.10	–0.01135	126±13	–4.1±0.6	–0.046±0.007
4.3	0.49±0.02	–10.8±1.1	0.99±0.10	–0.01133	125±13	–6.1±0.9	–0.069±0.010
5.01	0.48±0.02	–8.9±0.9	0.99±0.10	–0.01151	127±13	–4.9±0.7	–0.056±0.008
7.94	0.45±0.02	–8.4±0.9	0.95±0.10	–0.01318	140±14	–4.2±0.6	–0.056±0.008
9.83	0.42±0.02	–8.7±0.9	0.81±0.08	–0.01499	135±14	–4.6±0.7	– 0.068±0.010
9.99	0.42±0.02	–7.2±0.8	0.81±0.08	–0.01516	137±14	–3.7±0.6	–0.056±0.008
12.02	0.38±0.02	–7.0±0.7	0.75±0.08	–0.01783	149±15	–3.3±0.5	–0.059±0.009
14.35	0.34±0.02	–4.5±0.5	0.52±0.05	–0.02260	131±14	–2.4±0.4	–0.055±0.008
16	0.30±0.02	–2.4±0.3	0.40±0.04	–0.02505	110±11	–1.5±0.2	–0.038±0.006
IC-3 → IC-2 – c-axis: Relevant quantities, entropy changes and uniaxial pressure dependencies							
18.39	0.30±0.04	–9±2	0.24±0.03	–0.1	270±40	–2.3±0.6	–0.23±0.06
20.27	0.23±0.04	–3.8±0.4	0.21±0.05	-0.04	94±30	–2.9±0.8	–0.12±0.03

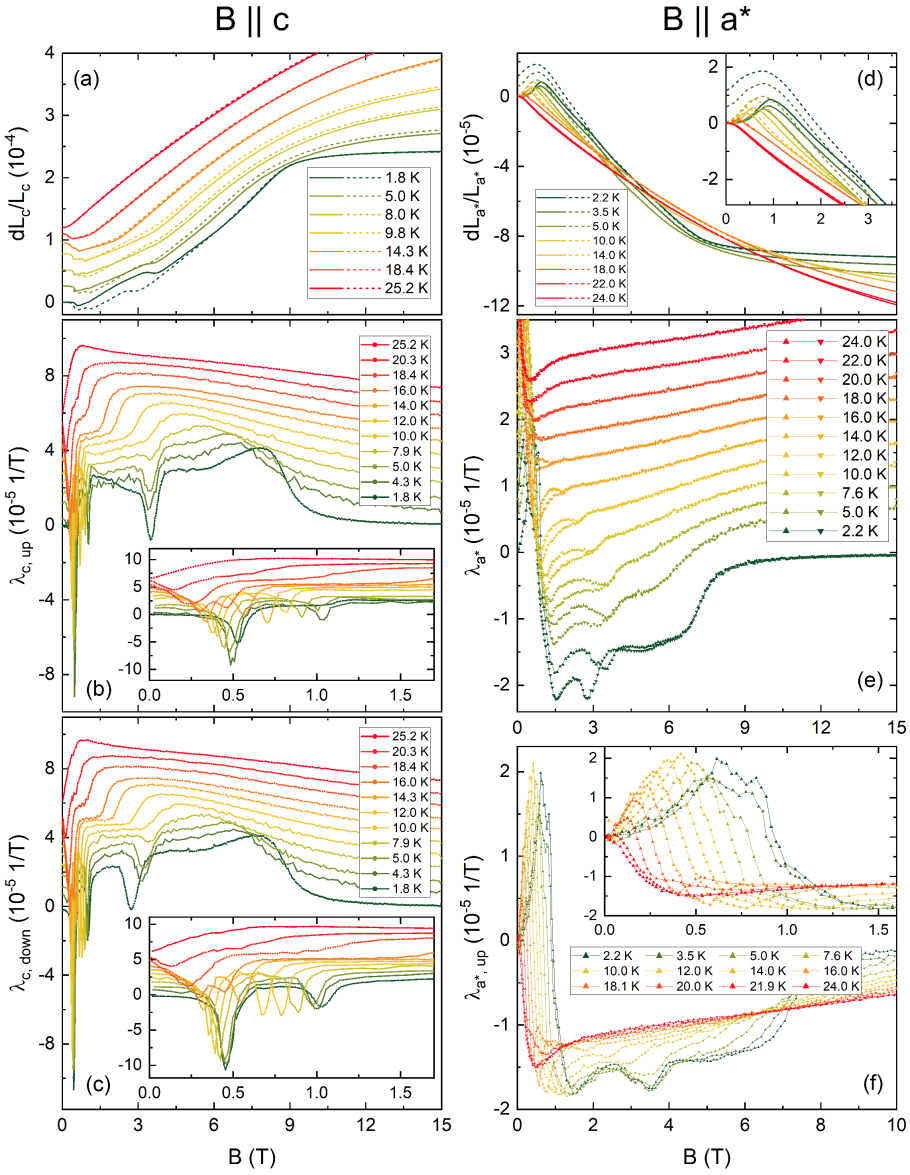

Figure S4: Magnetostriction measurements at temperatures from 1.7 K to 25 K for $B \parallel c$ (a-c) and $B \parallel a^*$ (d-f): The relative length change $dL(B)/L$ (a, d) and magnetostriction coefficient λ_i (b, c, e, f) are shown. Solid lines in (a, d) represent up-sweeps, dashed lines down-sweeps. Triangles pointing upwards in (d) mark up-sweeps, triangles pointing downwards mark down-sweeps. Data in (a-c, insets also) and (e) are shifted vertically for better visibility by: (a) different amounts, (b, c) $6 \cdot 10^{-6}$ 1/T, (e) $3.7 \cdot 10^{-6}$ 1/T (3.5 K data is omitted). Insets show magnifications of the low field regions.

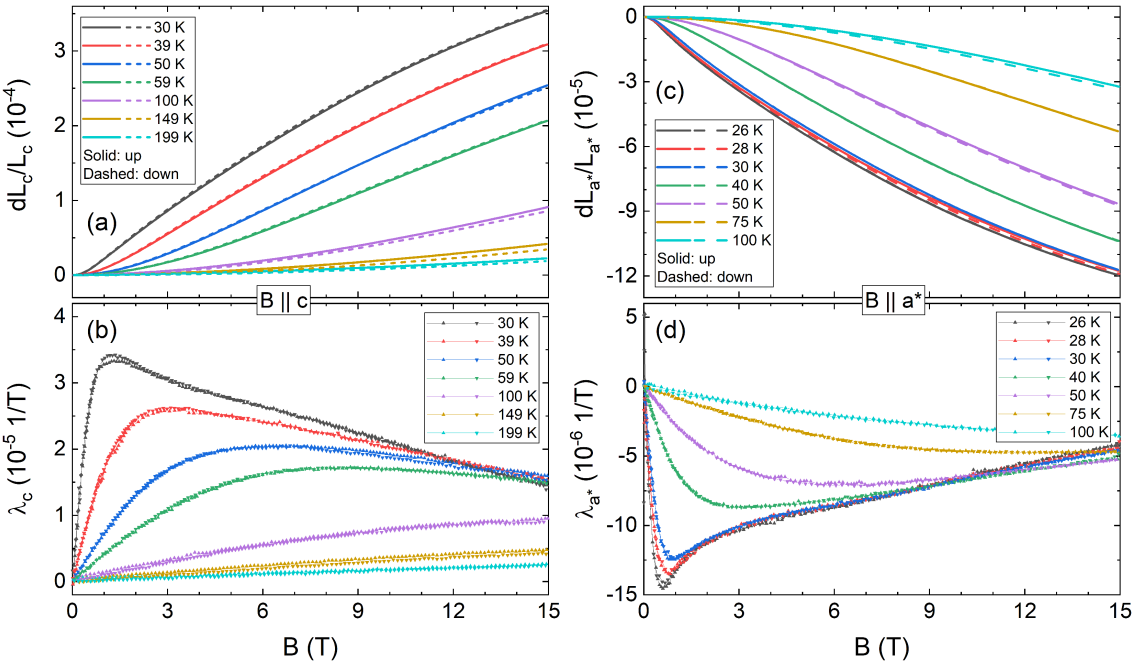

Figure S5: Magnetostriction measurements at temperatures above T_{N1} for $B \parallel c$ (a-b) and $B \parallel a^*$ (c-d): The relative length change $dL(B)/L$ (a, c) and magnetostriction coefficient λ_i (b, d) are shown. Solid lines in (a, c) represent up-sweeps, dashed lines down-sweeps. Triangles pointing upwards in (b, d) are up-sweeps, triangles pointing downwards mark down-sweeps.

Table S2: Relevant quantities and jumps, calculated changes of entropy, and calculated pressure dependencies for the discontinuous transition in magnetic field from A(SkL) to IC-2 for the c-axis according to Eq. (3.7). The column of $\partial B_c/\partial T$ was calculated by taking the derivative of a polynomial fit to the values $B_c(T)$.

A(SkL) → IC-2 – c-axis: Relevant quantities, entropy changes and uniaxial pressure dependencies							
T (K)	B_c (T)	$\Delta(dL/L)$ (10^{-6})	Δm (μ_B/Gd)	$\partial B_c/\partial T$ (T/K)	ΔS_{calc} (mJ/mol K)	$\partial T_c/\partial p_i$ (K/GPa)	$\partial B_c/\partial p_i$ (T/GPa)
1.77	1.11±0.03	0	0.95±0.10	–0.028	300±30	0	0
4.3	1.04±0.03	–2.4±0.3	1.01±0.11	–0.031	360±40	–0.47±0.07	–0.015±0.002
5.01	1.01±0.02	–1.4±0.2	1.00±0.10	–0.033	370±40	–0.27±0.04	–0.009±0.002
7.94	0.91±0.02	–2.5±0.3	0.99±0.10	–0.041	450±50	–0.40±0.06	–0.016±0.003
9.83	0.82±0.02	–5.1±0.5	0.98±0.10	–0.048	520±60	–0.69±0.10	–0.033±0.005
9.99	0.82±0.02	–2.9±0.3	0.98±0.10	–0.048	530±60	–0.39±0.06	–0.019±0.003
12.02	0.7±0.02	–5.9±0.6	0.93±0.10	–0.057	590±60	–0.70±0.10	–0.040±0.006
14.35	0.56±0.02	–5.9±0.6	0.75±0.08	–0.069	580±60	–0.72±0.11	–0.050±0.007
16	0.45±0.02	–4.0±0.4	0.66±0.07	–0.079	580±60	–0.49±0.07	–0.039±0.006
18.39	0.23±0.02			-0.095			

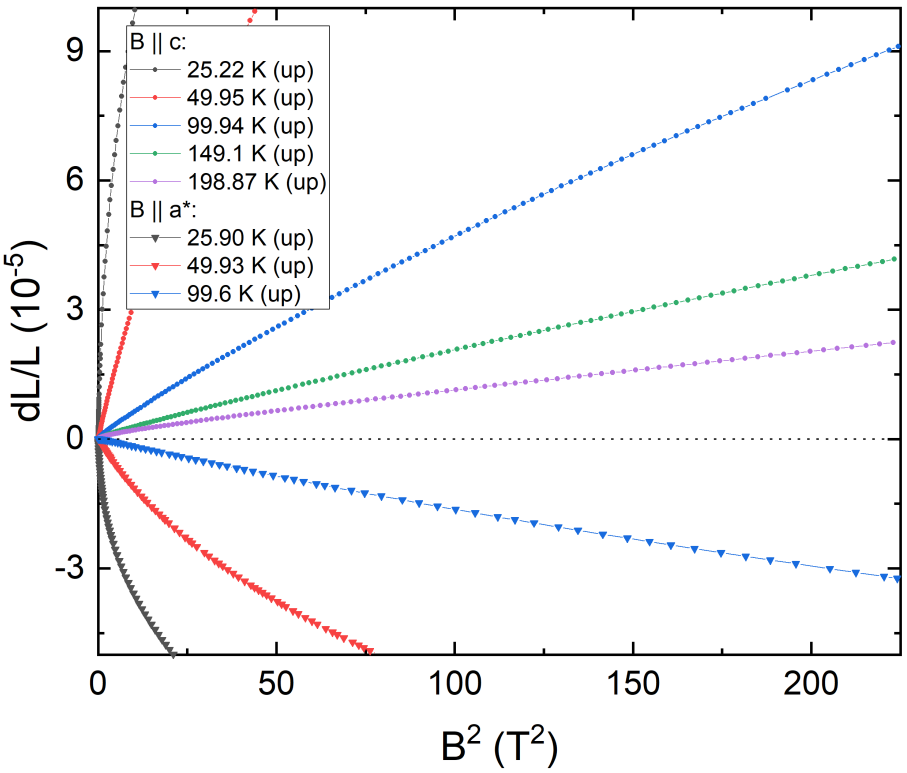

Figure S6: Relative length changes dL/L plotted vs. B^2. The uniaxial pressure dependence of the susceptibility is related to the magnetostriction by the Maxwell relation $\partial(dL/L)/\partial B = -\partial M/\partial p$. For a paramagnetic material with $M = \chi B$ we thus have $dL/L = -\frac{1}{2}\partial\chi/\partial p B^2$, i.e. $\partial\chi/\partial p$ is proportional to the slope in the above plot.

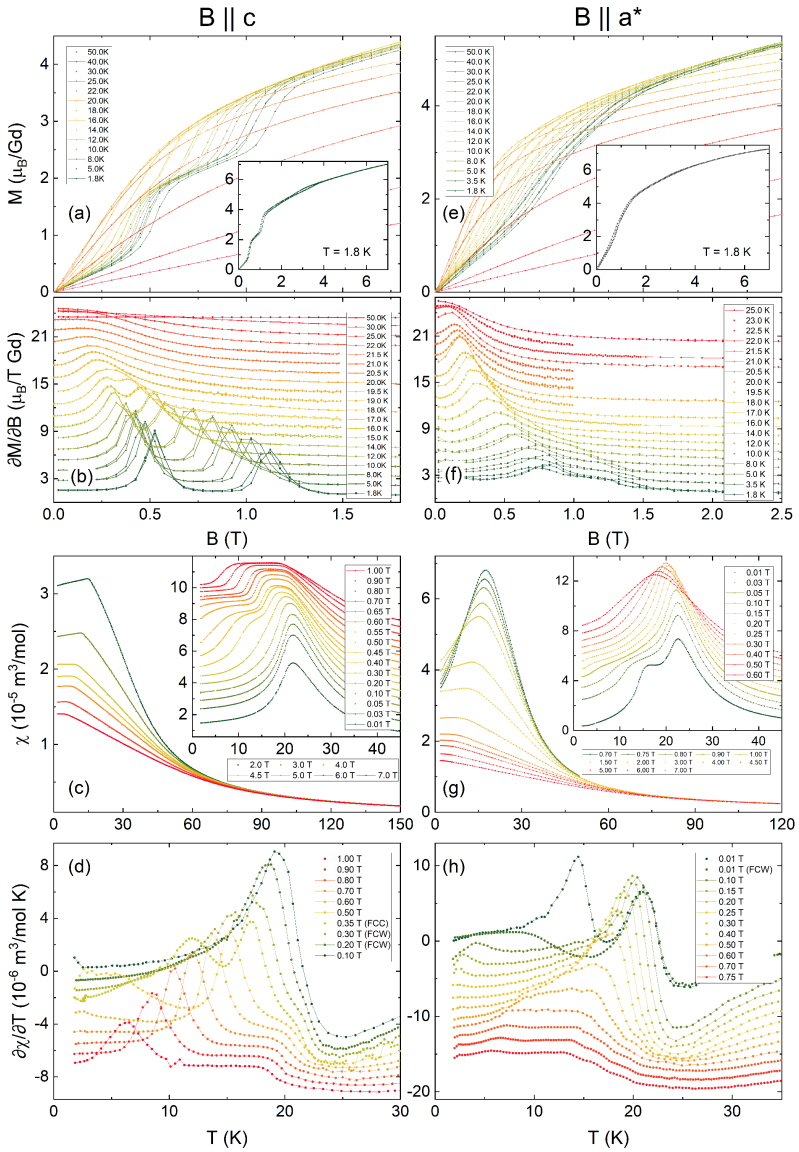

Figure S7: Measurements of the isothermal magnetization as well as the static magnetic susceptibility $\chi(T)$ and their derivatives for $B \parallel c$ (a-d) and $B \parallel a^*$ (e-h). $\chi(T)$ measurements were performed in a zero-field cooled manner unless stated otherwise (FCW: field-cooled warming, FCC: field-cooled cooling). Data are offset for better visibility by (b) 1.2 μ_B/(T Gd), (c, inset) $4.5 \cdot 10^{-6}$ m^3/mol, (d) $-8 \cdot 10^{-7}$ m^3/(mol K), (f) 1.1 μ_B/(T Gd), (g, inset) $5 \cdot 10^{-6}$ m^3/mol, and (h) $-1.4 \cdot 10^{-6}$ m^3/(mol K) starting with the data for $B = 0.10$ T.

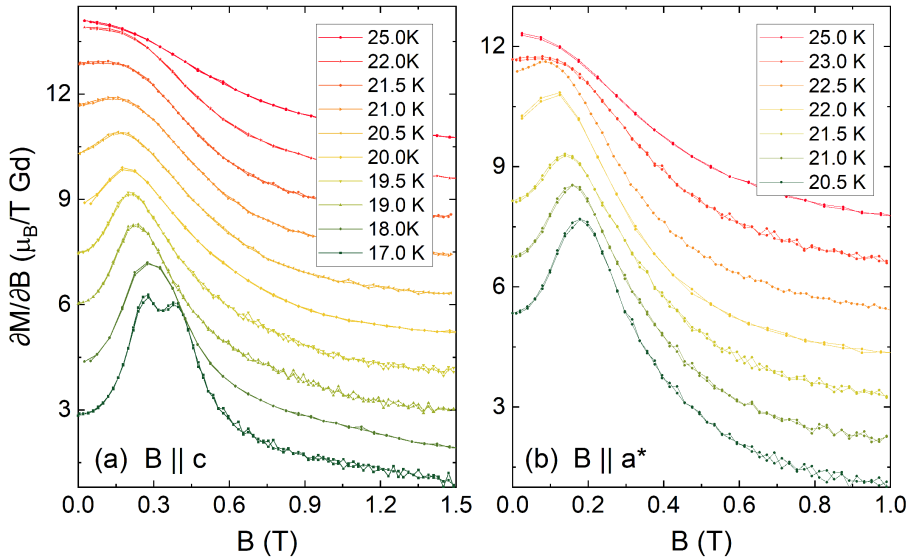

Figure S8: Close-up of the measurements of the magnetic susceptibility $\partial M/\partial B$ for $B \parallel c$ (a) and $B \parallel a^*$ (b) in the temperature regime of the IC-3 $\rightarrow$ IC-2 transition.

Table S3: Relevant quantities and jumps, calculated changes of entropy, and calculated pressure dependencies for the discontinuous transition in temperature from A(SkL) to IC-2 for the c-axis according to Eq. (3.7). The column of $\partial T/\partial B$ was calculated by taking the derivative of a polynomial fit to the values $T_c(B)$, including the values from 0 T to 0.3 T.

A(SkL) $\rightarrow$ IC-2 – c-axis: Relevant quantities						
B (T)	T_c (K)	Δ(dL/L) (10^{-6})	Δm (μ_B/Gd)	$\partial T_c/\partial B$ (K/T)	ΔS_{calc} (mJ/mol K)	dT_c/dp_i (K/GPa)
0	19.7±0.5		no SkL			
0.1	19.3±0.3		no SkL	–4.8		
0.2	18.8±0.5		no SkL	–8.1		
0.3	17.9±0.7		no SkL	–10.8		
0.4	16.4±0.4	–5.0±1.0	0.36±0.04	–13.0	310±40	–1.2±0.3
0.5	15.3±0.4	–7.4±1.0	0.54±0.04	–14.8	410±40	–1.3±0.2
0.6	13.6±0.3	–7.0±0.7	0.70±0.04	–16.0	490±30	–1.02±0.12
0.7	12.0±0.3	–5.1±0.5	0.77±0.04	–16.7	510±30	–0.70±0.08
0.8	10.4±0.3	–2.7±0.3	0.86±0.04	–17.0	560±30	–0.34±0.04
0.9	8.60±0.3	–1.3±0.1	0.91±0.04	–16.7	610±30	–0.15±0.02

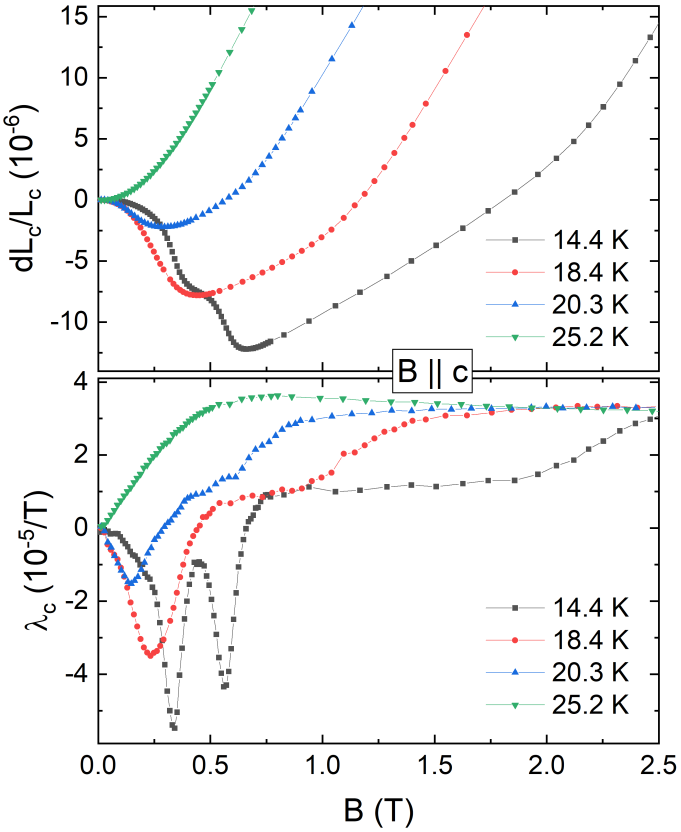

Figure S9: (a) Relative length changes dL_c/L_c and (b) magnetostriction coefficient λ_c in the low-field regime at temperatures below and above T_{N1} and T_{N2} for $B \parallel c$. Only up-sweeps are shown.

Table S4: Relevant quantities and jumps, calculated changes of entropy, and calculated pressure dependencies for the discontinuous transition in magnetic field from IC-2 to DP for the c-axis according to Eq. (3.7). The column of $\partial B_c/\partial T$ was calculated by taking the derivative of a polynomial fit to the values $B_c(T)$.

IC-2 → DP – c-axis: Relevant quantities, entropy changes and uniaxial pressure dependencies							
T (K)	B_c (T)	$\Delta(dL/L)$ (10^{-6})	Δm (μ_B/Gd)	$\partial B_c/\partial T$ (T/K)	ΔS_{calc} (mJ/mol K)	$\partial T_c/\partial p_i$ (K/GPa)	$\partial B_c/\partial p_i$ (T/GPa)
1.77	3.51±0.05	–17.1±1.7	0.08±0.03	–0.04±0.04	16±16	–80±80	–1.4±0.6
4.3	3.44±0.05	–12.2±2	0.08±0.04	–0.014±0.014	7±7	–130±130	–0.9±0.4
5.01	3.44±0.10	–11.8±0.4	0.07±0.03	–0.008±0.008	3±3	–250±250	–1.0±0.6
7.94	3.45±0.15	–6±3	0.044±0.018	0.018±0.009	-4±3	100±80	-0.9±0.6

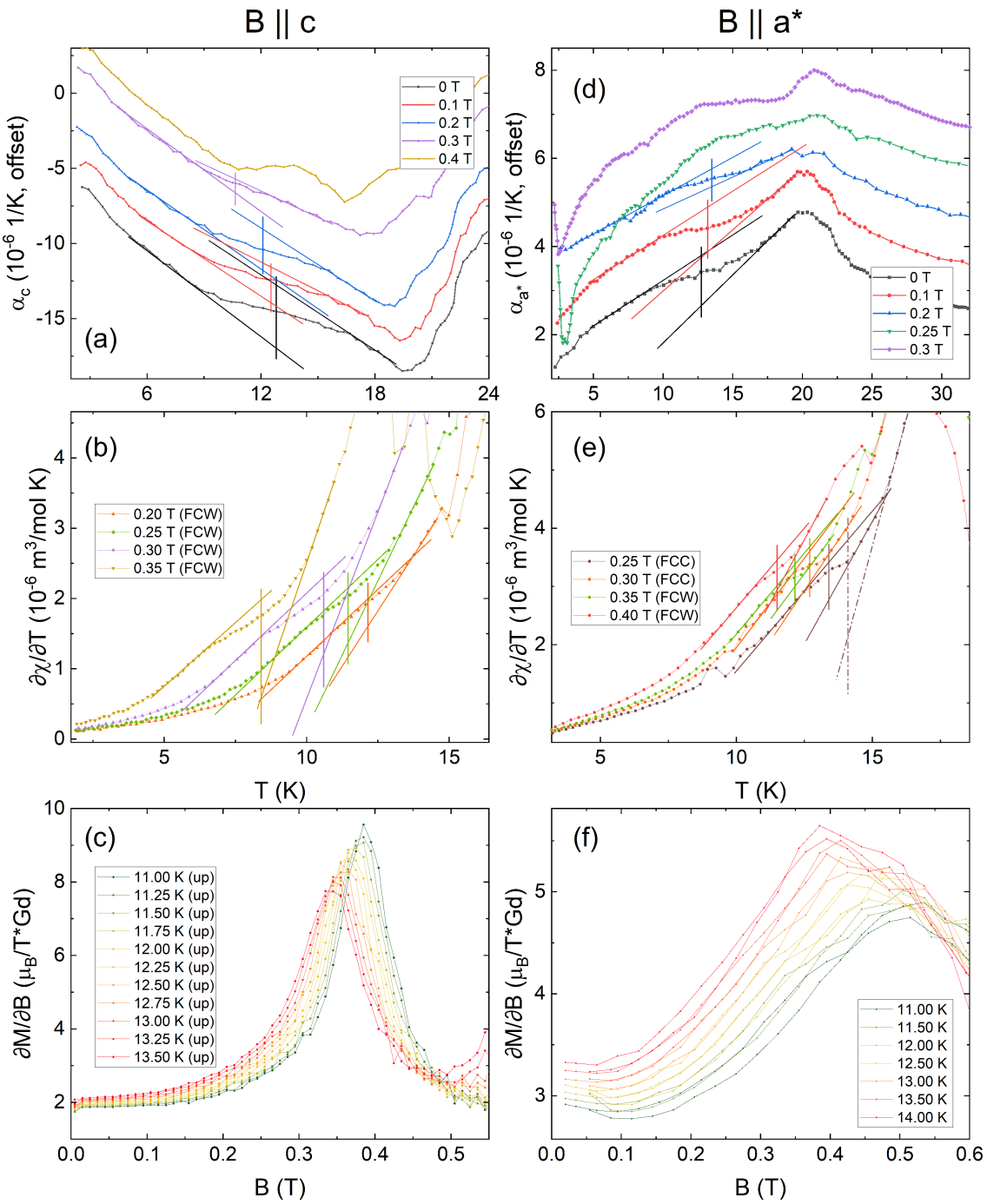

Figure S10: Extraction of T^* from thermal expansion (a, d), $\partial\chi/\partial T$ (b, e) and $\partial M/\partial B$ for $B \parallel c$ (a-c) and $B \parallel a^*$ (d-f). Vertical lines mark the position of T^* for the different measurements. Data in (a) and (d) are offset by $2 \cdot 10^{-6}$ 1/K and $1 \cdot 10^{-6}$ 1/K, respectively.

Table S5: Relevant quantities and jumps and calculated field and pressure dependencies for the continuous transition from IC-2 to the field-induced ferromagnetic (fiFM) phase for the *c*-axis according to Eq. (3.4), (3.5).

IC-2 → fiFM – *c*-axis: Relevant quantities, entropy changes and uniaxial pressure dependencies				
T (K)	B_c (T)	$\Delta\lambda$ (10^{-6}/T)	$\Delta(\partial M/\partial B)$ (μ_B/(T Gd))	$\partial B_c/\partial p_i$ (T/GPa)
9.99	3.7±0.1	15±2	–0.15±0.03	-0.7±0.2
12.02	3.0±0.1	17±2	–0.19±0.03	-0.6±0.2
14.35	2.3±0.1	19±2	–0.25±0.03	-0.5±0.1

Table S6: Relevant quantities and jumps and calculated field and pressure dependencies for the continuous transition from the depinned phase (DP) to the field-induced ferromagnetic (fiFM) phase for the *c*-axis according to Eq. (3.4), (3.5).

DP → fiFM – *c*-axis: Relevant quantities, entropy changes and uniaxial pressure dependencies				
T (K)	B_c (T)	$\Delta\lambda$ (10^{-5}/T)	$\Delta(\partial M/\partial B)$ (μ_B/(T Gd))	$\partial B_c/\partial p_i$ (T/GPa)
1.77	8.8±0.5	–4.7±1.0	–0.159±0.018	1.9±0.5
4.3	7.94±0.4	–1.9±1.0	–0.094±0.009	1.3±0.7
5.01	6.6±0.4	–1.4±1.0	–0.074±0.018	1.2±0.9
7.94	6.48±0.6	–0.7±0.4	–0.065±0.018	0.6±0.4

Table S7: Relevant quantities, jumps, and calculated field and pressure dependencies for the continuous transition at T^* from IC-1 to IC-1' for the *c*-axis according to Eq. (3.4), (3.5). Note that the c_p data was only measured at 0 T. The jumps in field B were scaled by the changes of the jumps in α_c, i.e., $\Delta c_p(B) = c_p(0) \cdot \Delta\alpha(B)/\Delta\alpha(0)$.

IC-1 → IC-1' – *c*-axis						
B (T)	T_c (K)	$\Delta\alpha_c$ (10^{-6})	Δc_p (J/mol K)	$\Delta(\partial M/\partial T)$ ($10^{-3}\mu_B$/f.u. K)	dT_c/dp_i (K/GPa)	dT_c/dB_i (K/T)
0	12.8±0.7	4.1±0.5	–2.7±0.5		–1.4±0.3	
0.2	12.15±0.5	2.7±0.4	–1.8±0.4	–5.6±1.4	–1.3±0.4	–0.037±0.013
0.25	11.45±0.5			–11±4		
0.3	10.6±0.5	0.9±0.3	–0.6±0.3	–16±6	–1.1±0.7	–0.28±0.18
0.35	8.4±0.5			–20±7		

Chapter 4

Magnetoelastic Coupling and Phase Diagram of the Buckled-Kagomé Antiferromagnet $Cu_3Bi(SeO_3)_2O_2Cl$

In this chapter a thorough investigation of the buckled-Kagomé antiferromagnetic $Cu_3Bi(SeO_3)_2O_2Cl$ using thermal expansion, magnetostriction and magnetization measurements is presented. Background information on physical phenomena, possible applications and structural properties of $Cu_3Bi(SeO_3)_2O_2Cl$ are given in the introduction. The experimental methods section then gives an overview of the samples used in the study along with information on basic characterization and orientation of the samples. This section is followed by the experimental results, which are directly discussed as they are presented, to facilitate keeping an overview over the different observed phenomena and their interpretation. The results and discussion section is divided into four sections. The first section focuses on the results of thermal expansion measurements in zero-field. This includes a Grüneisen analysis and an analysis of the critical scaling at the observed phase transitions. The following section presents the effects of a magnetic field in terms of thermal expansion and magnetostriction data. An emphasis in this section is on the phenomena observed for measurements along the c-axis with $B \parallel c$. In the third section magnetization measurements in fiedls up to 14 T are presented, from which the phase diagrams in the fourth and last section are constructed. Finally, a conclusion sums up the findings from this study on $Cu_3Bi(SeO_3)_2O_2Cl$.

4.1 Introduction

Since the revival of frustrated magnetism as a highly active research field in the 1990s [98], many Kagomé lattice compounds have been discovered, synthesized, and investigated extensively. The corner-sharing triangles of the Kagomé lattice provide a rich playground for geometric frustration [11, 99]. Classically, this geometric frustration can lead to macroscopic ground state degeneracies and branches of zero-energy excitations which prevent any long-range order down to the lowest temperatures [98, p. 208]. An ideal $S = 1/2$ Kagomé Heisenberg antiferromagnet

is one realization of a system in which this phenomenon, the so-called (quantum) spin liquid state, is expected. However, geometrically frustrated systems provide a much broader range of phenomena than only the spin liquid state. Among them are fractionalized magnetization plateaus, chiral and helical spin arrangements as well as spin glass, spin nematic, and spin ice behaviors [98].

In a number of geometrically frustrated systems such as $FeTe_2O_5Cl$ [100], $PbCu_3TeO_7$ [101], and $Ni_3V_2O_8$ multiferroic behavior has been found [102, 103]. Multiferroics are defined as systems which exhibit more than one of the primary ferroic properties – ferromagnetism, ferroelectricity and ferroelasticity – in the same phase [104]. From a technological perspective they are especially sought-after for controlling magnetism via electric fields. This comes with the promise of a substantially lower energy consumption than manipulating magnetic states via magnetic fields [105]. Possible applications range from ultra-low power logic-memory to radio- and high-frequency devices: electric field-tunable radio-frequency/microwave signal processing, magnetic field sensors, magnetoelectric random access memory (MERAM) and voltage-tunable magnetoresistance. An introduction to the field of multiferroics along with a basic overview is given in Refs. [106–108].

$Cu_3Bi(SeO_3)_2O_2Cl$, "the" francisite, after which the francisite family is named, crystallizes in a special realization of the Kagomé lattice [109] and exhibits multiferroic properties at low temperatures [16, 17]. What makes the francisite Kagomé lattice peculiar is a buckling of the Kagomé layers along the out-of-plane (c) direction (Fig. 4.1(a)). Cu^{2+} ($S = 1/2$) ions are the magnetic centers forming the Kagomé lattice in the ab-plane of $Cu_3Bi(SeO_3)_2O_2Cl$ (more often called CBSCl in the following) (Fig. 4.1(b)). They are situated at two different crystal sites, Cu1 and Cu2. Both Cu1 and Cu2 ions are found in a square planar coordination with Cu-O bond lengths of 1.933 Å to 1.978 Å. These plaquettes are non-parallel, as visible in Fig. 4.1(a) and (b). Along the c-axis Cu ions are connected by long Bi–O bonds with a bond length of about 2.8 Å (not shown in the figure). While the Bi^{3+} ions sit in tunnels along the a-axis (omitted in Fig. 4.1), stacked in line with the Cu2 ions along c, the Cl^- ions are situated in tunnels along the c-axis in the center of Cu1–Cu2 hexagons in the ab-plane (Fig. 4.1(b)). The stereochemically active Se^{4+} ions are situated in the same tunnels with the Cl ions.

The correct space group of CBSCl has been a matter of debate for several years. The latest reports assign the orthorhombic $Pmmn$ space group to the high temperature phase with an orthorhombic to orthorhombic structural phase transition at $T_S \approx 115$ K. The low-temperature phase is suggested to be the nonpolar, possibly antiferroelectric (AFE) [110], $Pcmn$ phase [16]. However, minor inclusions of a ferroelectric $P2_1mn$ phase may be present below T_S within the matrix of the major AFE phase [110]. The magnetic structure of CBSCl at 2 K has been determined by

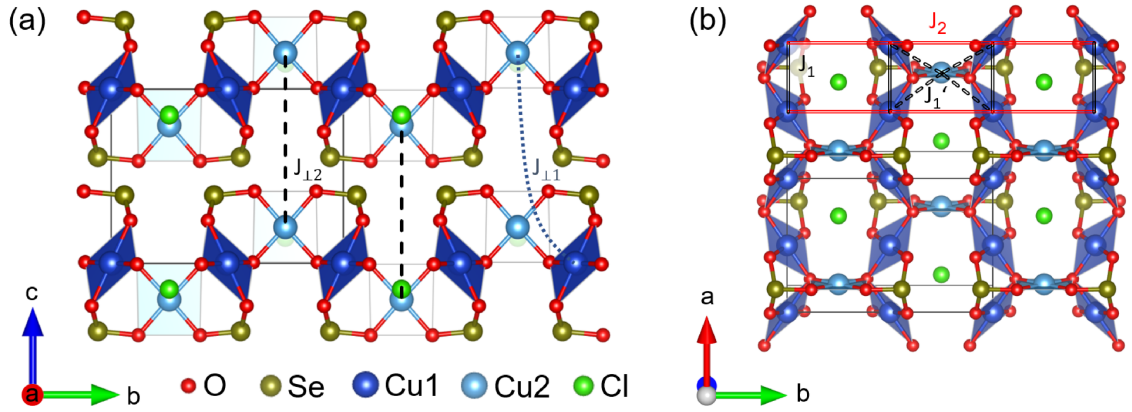

Figure 4.1: Crystal structure of $Cu_3Bi(SeO_3)_2O_2Cl$ for the (a) *bc*-plane and (b) *ab*-plane. Thin black lines mark the non-magnetic high temperature orthorhombic *Pmmn* unit cell. Black, red and blue lines mark different exchange couplings. Bi ions are omitted for clarity and (b) is slightly tilted forward for better visibility.

neutron diffraction experiments [16]. Layers within the *ab*-plane show a ferromagnetic alignment of canted Cu magnetic moments, with antiferromagnetic alignment along the *c*-axis. The Cu moments are confined to the *bc*-plane. Cu2 spins are aligned strictly (anti)parallel with the *c*-axis, whereas the most probable refinement for the Cu1 canting angle yields a canting towards the *b*-axis of 59(4)°. Calculations by Rousochatzakis et al. [15] and Nikolaev et al. [111] yielded large exchange couplings between the Cu spins with ferromagnetic nearest neighbor interactions on the order of −70 K to −80 K, and antiferromagnetic next-nearest neighbor interactions on the order of 60 K. Furthermore, linear magnetoelectric coupling has been found in CBSCl [16] and, most recenctly, the structural transition at T_S has been assigned to an archetypal soft-mode-driven antipolar transition [112]. Besides, controllable broadband absorption linked to a mixed phase has been reported for the isostructural compound $Cu_3Bi(SeO_3)_2O_2Br$ (CBSBr) [113]. CBSBr exhibits physical properties almost identical to those of CBSCl – with one major difference being the absence of the structural phase transition. Therefore, these properties may also be expected to be present in CBSCl.

4.2 Experimental Methods

Single crystals of $Cu_3Bi(SeO_3)_2O_2Cl$ were grown by the chemical vapor transport method (for details see supplemental material of Ref. [110]) by the group of Prof. A. Vasiliev from the National University of Science and Technology (MISiS) and Lomonosow Moscow State University . The magnetization in magnetic fields up to 7 T was studied in a Magnetic Properties Measurement System (MPMS3, Quantum

Design). For in-plane angular measurements a rotatable sample holder was used, with the sample c-axis aligned with the rotational axis, i.e., perpendicular to the magnetic field. Measurements up to 14 T were performed in a Physical Properties Measurement System (PPMS-14, Quantum Design) using the Vibrating Sample Magnetometry (VSM) option. Specific heat measurements were performed by Maria Markina on a PPMS calorimeter using a relaxation method on a single crystal of $m = 1.8$ mg (2 K-100 K).

The measurements performed in the frame of this work were performed on a set of different crystals. Measurements along the c-axis, both magnetization and dilatometry, were performed on a crystal of $m = 7.03(5)$ mg of dimensions $1.3 \times 2.45 \times 0.76$ mm^3 (Fig. 4.2(c)). a- and b-axis dilatometric experiments were performed on an elongated hexagonal-like crystal of $m = 7.76(5)$ mg of $2.30 \times 1.80 \times 0.58$ mm^3 (Fig. 4.2(b)), while in-plane magnetization measurements up to 7 T were performed on a very small crystal of $m = 0.6(5)$ mg and roughly $1 \times 1 \times 0.12$ mm^3 (see Fig. 4.2(a)). Further magnetization measurements with $B \parallel a, b$ up to 14 T were performed on a large crystal of $2.5 \times 2.0 \times 0.6$ mm^3 with $m = 8.88(5)$ mg. The a-axis dilatometry measurements shown in the appendix were performed on a crystal with $l = 1.10$ mm along the a-axis.

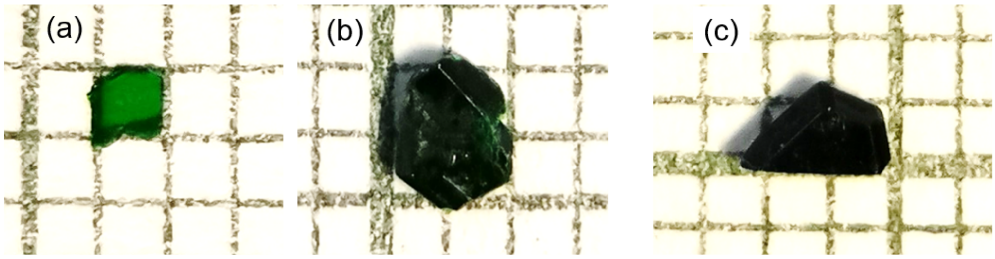

Figure 4.2: (a-c) Single crystals of $Cu_3Bi(SeO_3)_2O_2Cl$ as described in the text and used for different measurements.

The single-crystals were oriented using a Laue X-Ray Diffraction (XRD) setup prior to the experiments (Fig. 4.3(a-c)). Furthermore, an angular dependence of the in-plane magnetization was recorded at $T = 2$ K and $B = 5$ T on the small and very thin crystal of $m = 0.60(5)$ mg (Fig. 4.2(a)) in order to determine the hard and easy in-plane axes (Fig. 4.3(d)). The mounting in the rotating sample holder for the MPMS measurements assured that magnetic fields were applied perpendicular to the c-axis and possible tilting was negligible. The measurements show a two-fold symmetry with minima at around 35° and 215° and maxima at 125° and 305°. The minima mark the hard axis, which is assumed to be the a-axis according to calculations by Rousochatzakis et al. [15], whereas maxima mark the easy in-plane direction, i.e., the b-axis.

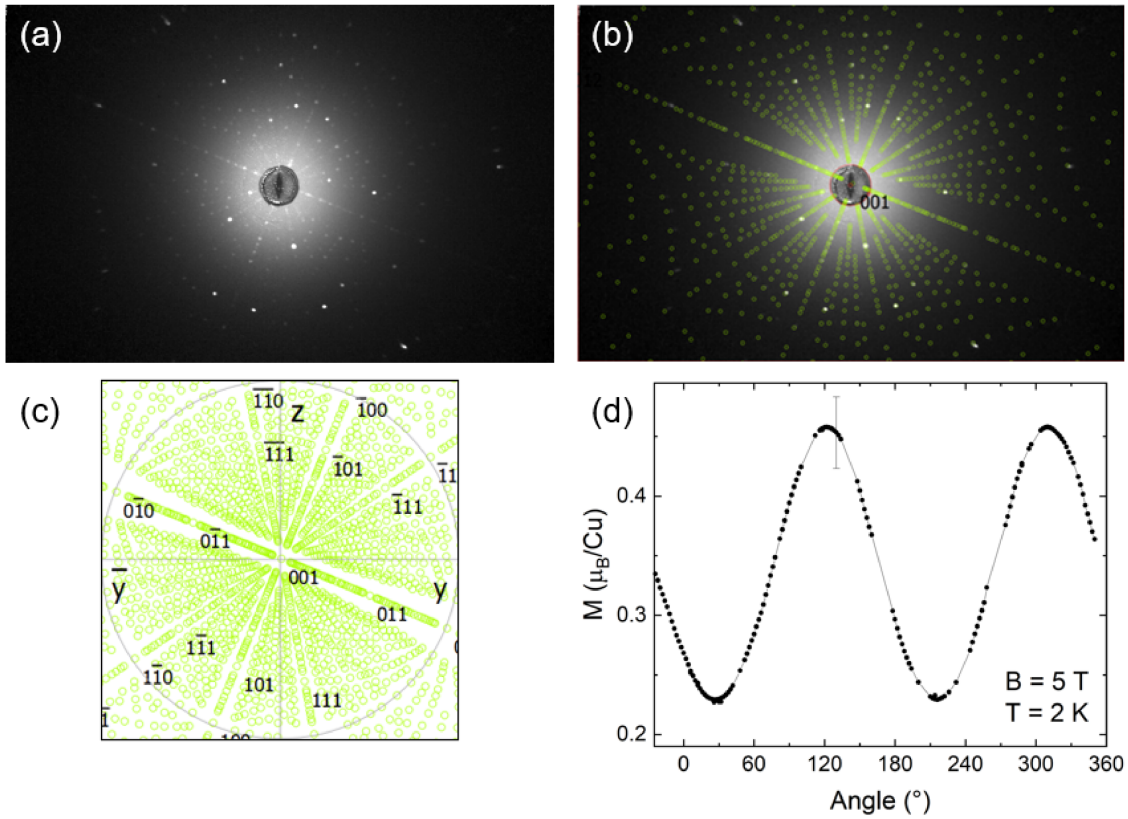

Figure 4.3: Orienting the $Cu_3Bi(SeO_3)_2O_2Cl$ samples: (a) Exemplary Laue XRD image (b) with corresponding orientation and (c) a wider stereographic projection. (d) In-plane angular dependence of the magnetization at 2 K and 5 T. The error bar is representative for all data points.

Thermal expansion measurements were performed at temperatures between 2 K and 300 K in magnetic fields up to 15 T, applied along the direction of the measured length changes, and the linear thermal expansion coefficients $\alpha_i = 1/L_i \cdot dL_i(T)/dT$ were derived. Unless specified otherwise, the measurements were performed in a zero-field-cooled manner, i.e., cooling to the lowest temperatures at B = 0 , ramping the field to the desired value and subsequently measuring the warming sweep. In addition, the field-induced length changes $dL_i(B_i)$ were measured at various fixed temperatures between 1.7 K and 200 K in magnetic fields up to 15 T. The longitudinal magnetostriction coefficient $\lambda_i = 1/L_i \cdot dL_i(B_i)/dB_i$ was derived from $dL_i(B_i)$.

4.3 Results and Discussion

4.3.1 Thermal Expansion at B = 0

Thermal expansion measurements in zero-field show pronounced anomalies at $T_S = 120.7(5)$ K and $T_N = 26.4(3)$ K (Fig. 4.4). Both anomalies appear as clear kinks in the relative length changes (Fig. 4.4(b)), i.e., signaling continuous phase transitions. The magnitudes and signs of the anomalies differ for all three axes, indicating a strong anisotropy of the uniaxial pressure dependence of the corresponding ordering phenomena already in zero-field. The length changes at temperatures between T_S

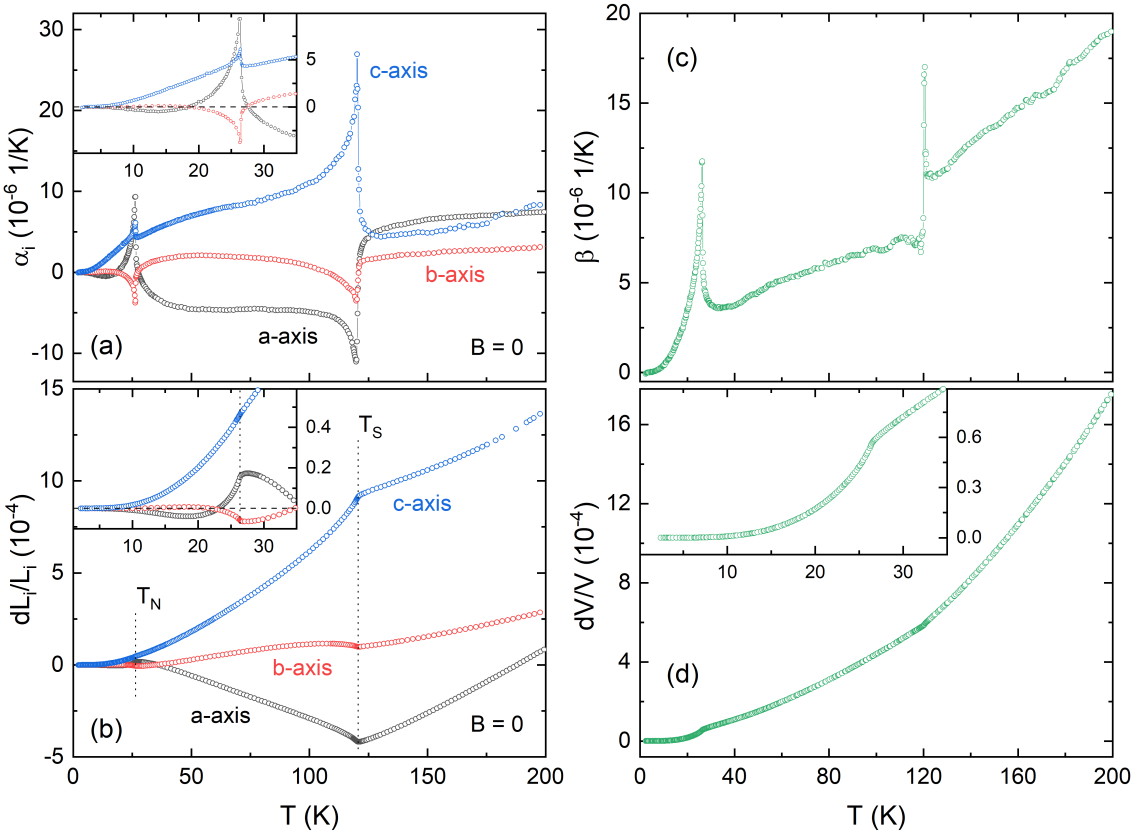

Figure 4.4: (a) Thermal expansion coefficients α_i and (b) relative length changes dL_i/L_i in zero-field for the crystallographic a-, b-, and c-axis of $Cu_3Bi(SeO_3)_2O_2Cl$. Insets show a magnification of the low temperature regime around T_N with zero y-values indicated by horizontal dashed lines. Vertical dotted lines in (b) mark T_N and T_S. (c) Volume expansion coefficient β and (c) relative volume changes dV/V in zero-field calculated from adding α_i and subsequent integration to obtain dV/V.

and T_N are also highly anisotropic. While the a-axis elongates linearly towards T_N, the c-axis shrinks about twice as fast. The changes of the b-axis in this temperature window, as for the whole measured temperature regime, are small compared to

the other axes. Below T_S the b-axis slightly elongates until about 107 K and then contracts down to T_N.

By adding up the α_i for the a-, b-, and c-axis the volume expansion coefficient β is obtained (Fig. 4.4(c)). Integrating β yields the relative volume changes (Fig. 4.4(d)). A positive jump with an additional peak on top of it at T_S, and a positive peak at T_N mark the structural and magnetic phase transitions in the volume, respectively, indicating positive pressure dependencies for both transitions.

In the following sections the antiferromagnetic phase transition at T_N is investigated, especially by means of a Grüneisen analysis and critical scaling analysis of the spontaneous strain. Subsequently, the structural transition at T_S is discussed.

The Antiferromagnetic Transition at T_N

The strong lattice changes related to the phase transition at T_N provide evidence for magnetoelastic coupling in CBSCl. These changes are highly anisotropic, with the c-axis lattice changes being the smallest, whereas the b-axis anomaly, which is opposite in sign, has a peak height in α_b of about twice the size. The changes along the a-axis are again much stronger. The peak in α_a is positive and two to three times larger than for the b-axis. Note also that the a-axis shows a negative thermal expansion with a minimum around 14 K. This behavior is discussed in more detail below. The lattice changes observed by the dilatometric measurements fit very well with the changes in lattice parameter obtained from X-ray Diffraction (XRD) measurements by Pregelj et al. [114].

Both qualitative and quantitative results on the pressure dependence of the phase transitions can be drawn from a Grüneisen analysis, i.e., comparing the specific heat and thermal expansion data. A first impression is obtained by simply dividing α_i by c_p to obtain Γ_i (Fig. 4.5). This includes no assumptions about magnetic or other contributions to the lattice changes and specific heat, and yields a number of instructive observations: (1) Above T_S the Grüneisen ratio is approximately constant for all axes as well as for the volume, implying that the competition between interactions is fully resolved at these high temperatures and a single dominating energy scale remains. (2) Below T_S all axes show different behavior, while the volume Grüneisen ratio is nearly constant, only starting to rise significantly below 40 K towards a peak at T_N. The strong anisotropy seen in the pure zero-field thermal expansion data is reflected here. (3) At the phase transitions the anomalies in thermal expansion are much more pronounced than in the specific heat, which leads to significant peaks in Γ_i. The c-axis around T_N is an exception in this respect, where only a small anomaly is visible in Γ_c.

For further quantitative analysis a phononic background is subtracted. For this

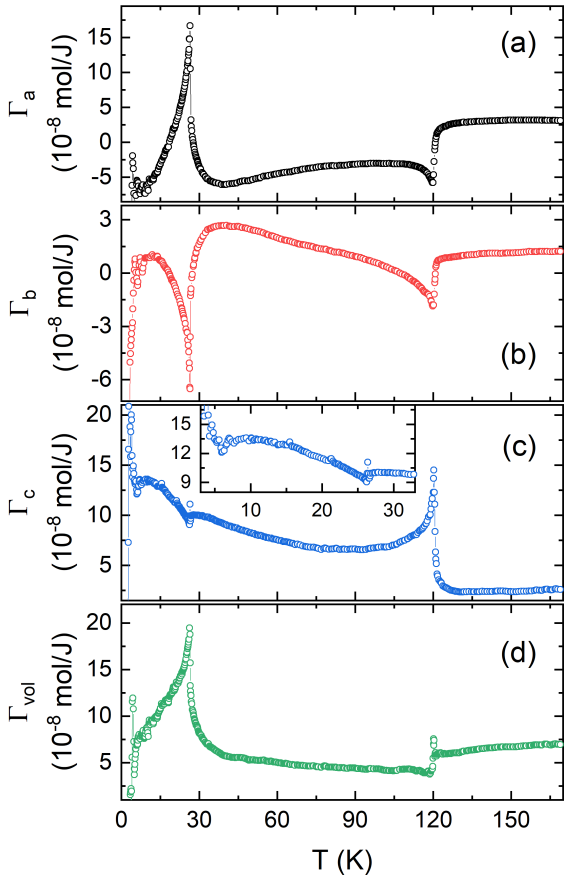

Figure 4.5: Grüneisen ratio $\Gamma_i = \alpha_i/c_p$ for all axes (a-c) and the volume (d) obtained as described in the text. Note that the c-axis thermal expansion data was shifted by –0.15 K prior to division by c_p for better overlap with the c_p data at T_N.

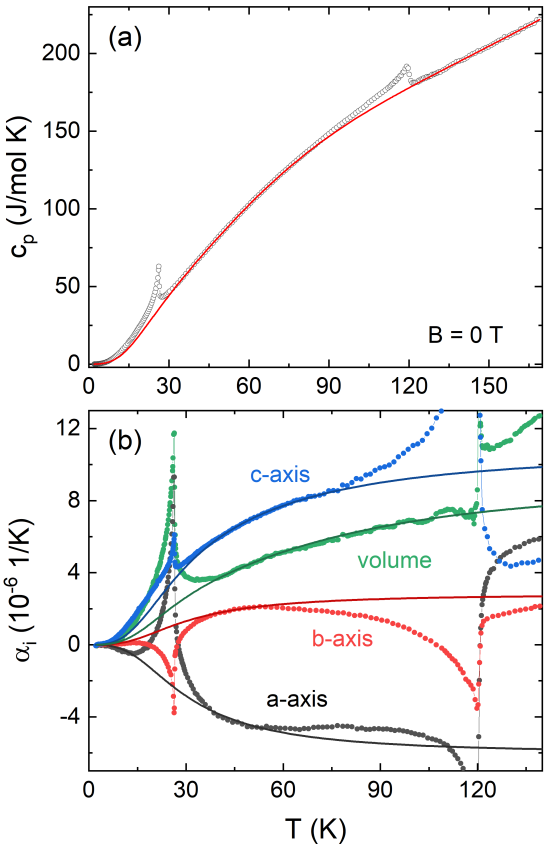

Figure 4.6: Phononic background fits (lines) to (a) the specific heat [115] and (b) the low temperature thermal expansion data (circles) in zero-field as explained in the text.

purpose both thermal expansion and specific heat are fitted by Debye and Einstein contributions according to

$$c_p^{ph} = n_{D1} D\left(\frac{T}{\Theta_{D1}}\right) + n_{D2} D\left(\frac{T}{\Theta_{D2}}\right) + n_E E\left(\frac{T}{\Theta_E}\right), \tag{4.1}$$

where $n_{D1,2}$ and n_E are constants, and $D(T/\Theta_{D1,2})$ and $E(T/\Theta_E)$ are the Debye and Einstein functions with the Debye and Einstein temperatures $\Theta_{D1,2}$ and Θ_E. A fit to the specific heat below the onset of T_S, at 35 K to 93 K, yields $n_{D1} = 3.25$, $n_{D2} = 6.14$ and $n_E = 12.1$ with $\Theta_{D1} = 127$ K, $\Theta_{D2} = 377$ K and $\Theta_E = 1063$ K. These Debye and Einstein temperatures are then used to fit the thermal expansion data in the range

from 35 K to 60 K. Due to the high value of the Einstein temperature, however, the contribution of Einstein modes to the thermal expansion below 100 K is negligible. Therefore, and in order to reduce the number of free parameters, the Einstein mode is omitted for the thermal expansion fit. The resulting background fits are shown in Fig. 4.6. The fits for the c-axis and volume describe the data very well – the c-axis up to about 80 K and the volume up to T_S – while the a- and b-axis only coincide with the data in a narrow temperature range, roughly between 40 K and 54 K.

Subtracting the background yields the magnetic contributions to the specific heat and thermal expansion coefficient. The comparison of magnetic contributions $\alpha_{i,\mathrm{mag}}$ and $c_{\mathrm{p,mag}}$ as shown in Fig. 4.7(a-d) evidences an onset of magnetic contributions, i.e., effects of short-range correlations, at 35 K to 40 K for both $\alpha_{i,\mathrm{mag}}$ and $c_{\mathrm{p,mag}}$. Scaling the $\alpha_{i,\mathrm{mag}}$ ordinates appropriately, a very good overlap at T_N, between 23 K and 27 K, is obtained for all axes and the volume, implying a single dominant energy scale in this narrow temperature window. Above 27 K, the overlap is reasonable but not perfect for the a-axis and the volume, while for the b-axis a different scaling factor can be used to yield a perfect overlap. More significantly, below 23 K both the specific heat and the c-axis thermal expansion coefficient show a shoulder-like anomaly around 15 K which is neither visible in the in-plane data nor in the volume. This anomaly will be discussed below, together with data measured in non-zero applied magnetic field.

The magnetic Grüneisen ratios in Fig. 4.7(e-h) emphasize the different behavior: the a- and b-axis qualitatively show a similar evolution of $\Gamma_{i,\mathrm{mag}}$ with temperature, but of opposite sign, whereas $\Gamma_{\mathrm{c,mag}}$ evolves differently. It assumes an approximately constant value up to 15 K before it decreases, reaches a minimum at T_N, and then increases again. The low temperature regimes for the in-plane $\Gamma_{\mathrm{a,mag}}$ and $\Gamma_{\mathrm{b,mag}}$ are also roughly constant, but only up to about 10 K before they increase or decrease, respectively. Both reach a plateau above 22 K and exhibit a jump to a different constant value above T_N. Γ_{vol} is constant from 6 K to 10 K, then gradually increases, reaches a plateau at 21 K and continues to increase above T_N.

As noted in the previous chapter on Gd_2PdSi_3 (Sec. 3.3.1), for a constant Grüneisen ratio the uniaxial pressure dependence of a dominating energy scale J can be calculated according to

$$\Gamma_i = \frac{\alpha_i}{c_p} = \frac{1}{T_N V_m}\frac{\partial S/\partial p_i}{\partial S/\partial T} = \frac{1}{V_m}\frac{\partial \ln T_N}{\partial p_i} = \frac{1}{V_m}\frac{\partial \ln J}{\partial p_i}, \tag{4.2}$$

where the dominant energy scale is directly related to the transition temperature T_N. Considering only magnetic contributions, the pressure dependence of T_N is then

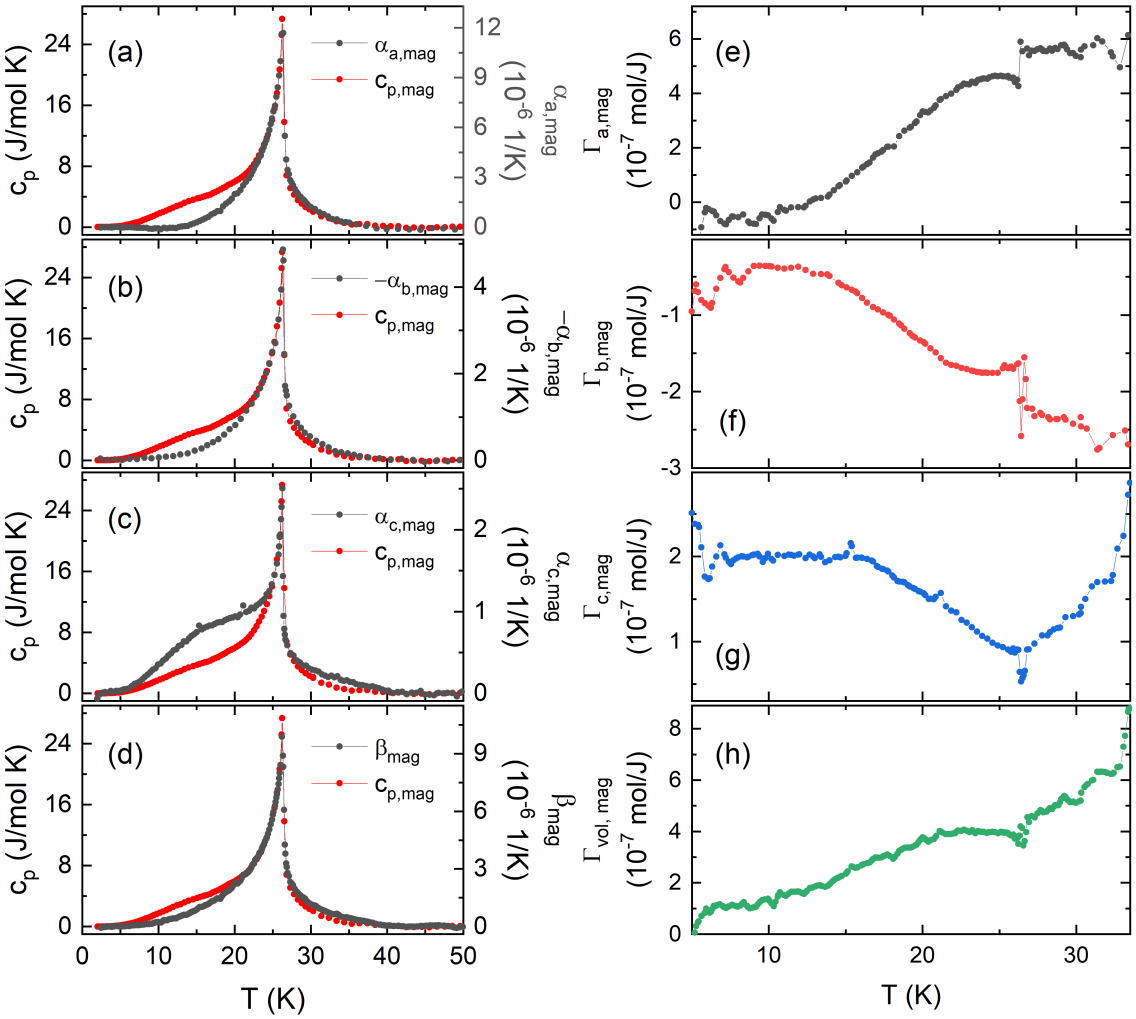

Figure 4.7: Comparison of the magnetic contributions to the specific heat (red circles, left ordinates) and thermal expansion coefficient (black circles, right ordinates) along the (a) *a*-axis, (b) *b*-axis, (c) *c*-axis, and (d) for the volume expansion. (e-h) Magnetic Grüneisen ratio $\Gamma_{i,\mathrm{mag}} = \alpha_{i,\mathrm{mag}}/c_{\mathrm{p,mag}}$ for (a-c) all axes and (d) the volume obtained as described in the text. Note that the *c*-axis thermal expansion data was shifted by –0.15 K for better overlap with the $c_{\mathrm{p,mag}}$ data at T_{N}.

determined by

$$\frac{\partial T_{\mathrm{N}}}{\partial p_i} = V_{\mathrm{m}} T_{\mathrm{N}} \Gamma_{i,\mathrm{mag}}, \tag{4.3}$$

where $V_{\mathrm{m}} = 1.333 \cdot 10^{-4}$ m^3/mol is the molar volume and the index i indicates a linear direction or the volume. The values of $\Gamma_{i,\mathrm{mag}}$ and resulting pressure dependencies are listed in Tab. 4.1. The a- and c-axis show positive uniaxial pressure dependencies of 1.8(4) K/GPa and 0.33(10) K/GPa, whereas T_{N} decreases under uniaxial pressure along the b-axis by about $-0.62(15)$ K/GPa ($-0.8(2)$ K/GPa if the data are brought to overlap for $T > T_{\mathrm{N}}$ instead of $T < T_{\mathrm{N}}$). For hydrostatic pressure an increase of T_{N} by about 1.4(3) K/GPa is expected. This matches very well with the linear increase of about 1 K/GPa obtained on polycrystalline CBSCl samples in pressures up to 1.3 GPa by Wu et al. [17].

Table 4.1: Pressure dependence of the transition temperatures calculated from the magnetic Grüneisen ratios $\Gamma_{i,\mathrm{mag}}$ at T_{N}, as well as from the jumps $\Delta\alpha_i$ and Δc_{p} at T_{S} for all crystallographic axes. The value dT_{S}/dp for the volume is calculated as the sum of all three axes.

	$\Gamma_{i,\mathrm{mag}}$ (10^{-7} mol/J)	$\partial T_{\mathrm{N}}/\partial p_i$ (K/GPa)	Γ_i (10^{-7} mol/J)	$\partial T_{\mathrm{S}}/\partial p_i$ (K/GPa)
a-axis	5.0	1.8±0.4	–11.9	–19±6
b-axis	–1.8	–0.62±0.15	–3.5	–5.7±1.1
c-axis	0.93	0.33±0.10	16.9	27±3
volume	4.0	1.4±0.3	–	2.3±1.0

The magnetic interactions in CBSCl have been calculated [15, 111] as well as investigated experimentally by inelastic neutron scattering studies [16]. According to these studies, strong ferromagnetic (FM) nearest-neighbor (NN) exchange couplings (J_1 and J_1') and antiferromagentic (AFM) next-nearest neighbor (NNN) exchange interactions (J_2) are present in the ab-plane of CBSCl giving rise to a canted AFM spin configuration. Dzyaloshinskii-Moriya (DM) interactions lift an infinite ground state degeneracy and select the uniform canted phase already at the classical level [15] The FM couplings are $J_1 = -76$ K ($J_1' = -70$ K) for the Cu1–Cu1 (Cu1–Cu2) NN exchange couplings, whereas the strength of the AFM NNN Cu1–Cu1 interactions has been calculated to be $J_2 = 55$ K [15]. Besides, both FM and AFM interlayer couplings are present: $J_{\perp 1} = -0.4$ K (FM) between Cu1 and Cu2 spins in adjacent layers along c; and $J_{\perp 2}$ between Cu2 spins. The strong anisotropy observed in the thermal expansion data and Grüneisen ratios evidences the different uniaxial pressure dependence of these exchange couplings along the three crystallographic axes. While the FM NN exchange pathways J_1 lie along the a-axis and J_1' diagonally

in the ab-plane, the AFM NNN couplings J_2 lie along the b-axis. As the results in Tab. 4.1 imply, pressure along the a-axis strengthens the overall antiferromagnetic interactions, thereby increasing T_N, while pressure along b leads to a decrease of T_N, i.e., strengthening overall FM interactions.

Uniaxial pressure applied along the a-axis presumably leads to a decrease of the Cu1–O–Cu1 bond angle and an increase in the Cu1–O–Cu2 bond angle. For Cu–O–Cu bridging angles close to 90° the Goodenough-Kanamori-Anderson rules suggest a ferromagnetic exchange interaction. Calculations of the angle dependence of the Cu–O–Cu exchange interaction in $CuGeO_3$ suggest a FM–AFM crossover for bridging angles around 96°–98° [116]. As Rousochatzakis et al. pointed out [15], the FM couplings in francisites may extend to much higher bridging angles due to the twisted geometry of the CuO_4 plaquettes. This was also observed in the Kagomé mineral kapellasite [117] and in other Cu^{2+}-based quantum magnets [118]. A qualitatively similar change in bond angles as expected for pressure along the a-axis was observed for Te substitution in the Se site of CBSCl [17]. The Te substitution leads to an anisotropic change of lattice parameters. The in-plane lattice parameters increase, by 0.65% for the a-axis and 1.09% for the b-axis at 60% Te doping, whereas the c-axis lattice parameter slightly decreases by −0.21%. Because the elongation of the b-axis is stronger than of the a-axis, the room temperature Cu1–O–Cu1 (Cu1–O–Cu2) bond angles decrease (increase) from 111.936(1)° to 111.0(9)° (−0.83%) (113.194(0)° to 115.0(6)°, 1.6%), while T_N increases strongly by about 5 K [17]. This is in line with the positive uniaxial pressure dependence of T_N found above for the a-axis.

The results at hand show that uniaxial pressure along the b-axis is expected to have an inverse effect on the Cu1–O–Cu1 and Cu1–O–Cu2 bond angles compared to pressure along the a-axis. This is in agreement with the opposite sign of $\partial T_N/\partial p_b$, i.e., $\partial T_N/\partial p_b < 0$, signaling an overall strengthening of FM interactions by application of pressure along b.

The dominant interlayer couplings $J_{\perp,1}$ (Cu1–Cu2) and $J_{\perp,2}$ (Cu2–Cu2) (dashed lines in Fig. 4.1(a)) were determined by Rousochatzakis et al. as FM $J_{\perp,1} = -0.4$ K and AFM $J_{\perp,2} = 2$ K, respectively [15]. Applying uniaxial pressure along c leads to an increase in T_N (Tab. 4.1), i.e., strengthening of the AFM coupling $J_{\perp,2}$ between Cu2 spins with respect to $J_{\perp,1}$.

The Antiferromagnetic Transition at T_N: Critical Scaling

In order to investigate the scaling behavior of the thermal expansion in the vicinity of T_N, the spontaneous strain $\varepsilon_{i,\mathrm{mag}} = (\Delta L_i/L_i)_{\mathrm{mag}}$ which is related to the onset of long-range magnetic order is derived by integrating $\alpha_{i,\mathrm{mag}}$ with respect to temperature. For better comparability the $\varepsilon_{i,\mathrm{mag}}$ are normalized by their value at lowest temperatures, $\varepsilon_{i,0}$, as shown in Fig. 4.8. Notably, the a- and b-axis exhibit a very similar behavior,

whereas the c-axis differs strongly below T_N. The increase in spontaneous strain along the c-axis is much slower and suppressed below T_N with respect to the in-plane directions. This behavior is probably caused by competing interactions along the c-axis and possibly hints at two competing order parameters in this temperature regime. Moreover, the spontaneous strains $\varepsilon_{i,\mathrm{mag}}/\varepsilon_{i,0}$ show an order-parameter-like evolution: The values are zero above T_N, increase steeply below, and subsequently reach a saturation value. This order-parameter-like behavior suggests that a quantitative analysis of the data with a power law

$$\frac{\varepsilon_{i,\mathrm{mag}}}{\varepsilon_{i,0}} = A \cdot |T - T_\mathrm{N}|^{\beta_{\mathrm{c},i}} \tag{4.4}$$

will yield valuable information on the phases by means of the critical exponent β_c. The temperature window from 22.8 K to 25.8 K as indicated in Fig. 4.8 was used for the fits. The resulting exponents – despite the qualitatively different c-axis behavior – are very similar, $\beta_{\mathrm{c,a}} = 0.38(3)$. $\beta_{\mathrm{c,b}} = 0.35(3)$, and $\beta_{\mathrm{c,c}} = 0.35(3)$. In

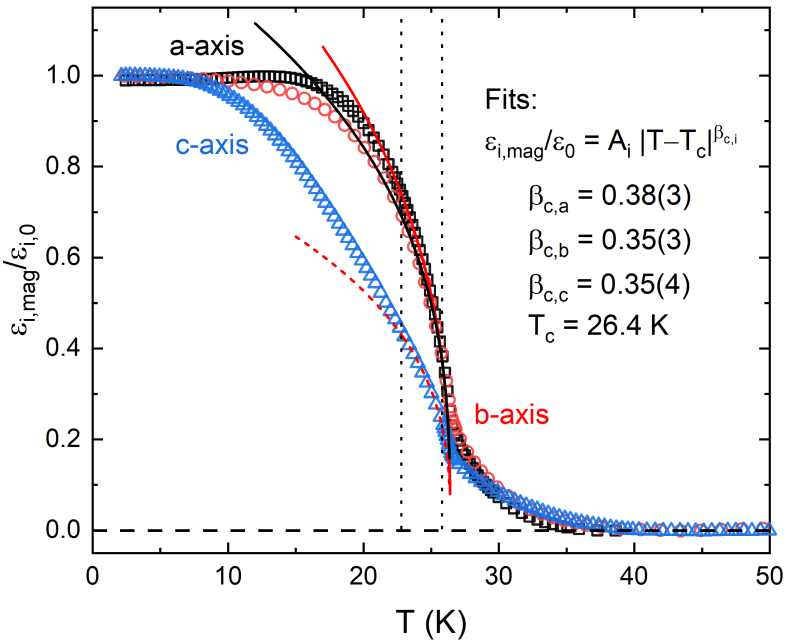

Figure 4.8: Spontaneous strain $\varepsilon_{i,\mathrm{mag}} = \Delta L_i/Li$ related to T_N normalized to the value at lowest temperatures. Critical exponent fits for the a-, b-, and c-axis are marked by red, black and dashed red lines, respectively. Vertical dotted lines indicate the temperature regime used for the fits. Horizontal dashed line indicates zero spontaneous strain.

order to relate the exponents found above to one of the known critical exponents, an assumption has to be made about the relation between β_c and an order parameter which describes the transition from the paramagnetic to the antiferromagnetic phase.

If a linear relation between the spontaneous strain and the order parameter Q is assumed, $\beta_{\mathrm{c,i}}$ corresponds to the critical exponents reported for different models (see Tab. 1.4). Within error bars the values then correspond to the 3D XY ($d = 3, D = 2$, $\beta_{\mathrm{c}} \approx 0.345$) and the 3D Heisenberg model ($d = 3, D = 3$, $\beta_{\mathrm{c}} \approx 0.365$). This finding is in line with previous experimental reports and calculations on CBSCl. Although for the brother compound CBSBr, Pregelj et al. claimed a 2D XY character, with $\beta_{\mathrm{c}} \leq 0.23$ obtained from neutron diffraction measurements near $T_{\mathrm{N}} = 27.4$ K [114], the effective 3D spin model by Rousochatzakis et al. describes many of the properties of $Cu_3Bi(SeO_3)O_2X$ (X = Cl, Br) by Heisenberg spins together with Dzyaloshinskii-Moriya (DM) interactions and symmetric anisotropic exchange interactions. While Rousochatzakis et al. found the symmetric anisotropic exchange interactions from their calculations to be too small to play any appreciable role in the magnetism of the francisites, Constable et al. found them necessary to satisfactorily simulate the spin-wave spectra from inelastic neutron scattering experiments [16]. As mentioned above, the strength of the interlayer couplings $J_{\perp,1}$ (Cu1–Cu2) and $J_{\perp,2}$ (Cu2–Cu2) was determined by Rousochatzakis et al. as -0.4 K (ferromagnetic) and 2 K (antiferromagnetic), respectively [15]. These numbers are small, but still on the order of 3% of the largest intralayer couplings and therefore not small enough for a pure two-dimensional behavior. In conclusion, the data in this work support the presence of 3D magnetic behavior in $Cu_3Bi(SeO_3)_2O_2Cl$ at low temperatures.

The Structural Phase Transition

The structural phase transition at T_{S} not only shows a λ-like behavior in α_i, indicating strong fluctuations and a second order phase transition, but it also shows a clear jump on top of the λ-like feature in α_{a} and α_{c} (Fig. 4.4(a)). For α_{c} the λ-peak is very pronounced and positive, while it is weaker and negative for α_{b} and α_{a}. The total jump heights in α_i of $\Delta\alpha_{\mathrm{a}} = 1.78(8) \cdot 10^{-5}$/K, $\Delta\alpha_{\mathrm{b}} = 5.3(3) \cdot 10^{-6}$/K, and $\Delta\alpha_{\mathrm{c}} = -2.53(8) \cdot 10^{-5}$/K were determined using an area conserving interpolation shown in Fig. 4.9(a-c). The transition temperatures related to this interpolation are 121.0(3) K, 120.7(3) K and 121.1(3) K, respectively. The jump heights reflect the strong anisotropy present in the system. Notably, above T_{S} the thermal expansion coefficient along the b-axis essentially assumes the value it had before the fluctuations around T_{S} set in, while there are significant jumps in α_{a} and α_{c}. Above T_{S} all axes show a small, roughly linear increase in α_i, with absolute values $2\ \alpha_{\mathrm{b}} \approx \alpha_{\mathrm{c}} \approx \alpha_{\mathrm{a}}$. The specific heat of CBSCl also shows an anomaly at T_{S} (Fig. 4.6(a) and 4.9(d)). For an entropy-conserving interpolation the jump size in c_{p}/T was extracted, amounting to $\Delta c_{\mathrm{p}}/T = -0.125(8)$ J/(mol K^2) at $T_{\mathrm{S}} = 120.2(2)$ K, which translates to $\Delta c_{\mathrm{p}} = -15(1)$ J/(mol K).

From the jump heights in thermal expansion and specific heat the uniaxial pressure dependence of T_{S} can be derived using the Ehrenfest relation via the Grüneisen ratio,

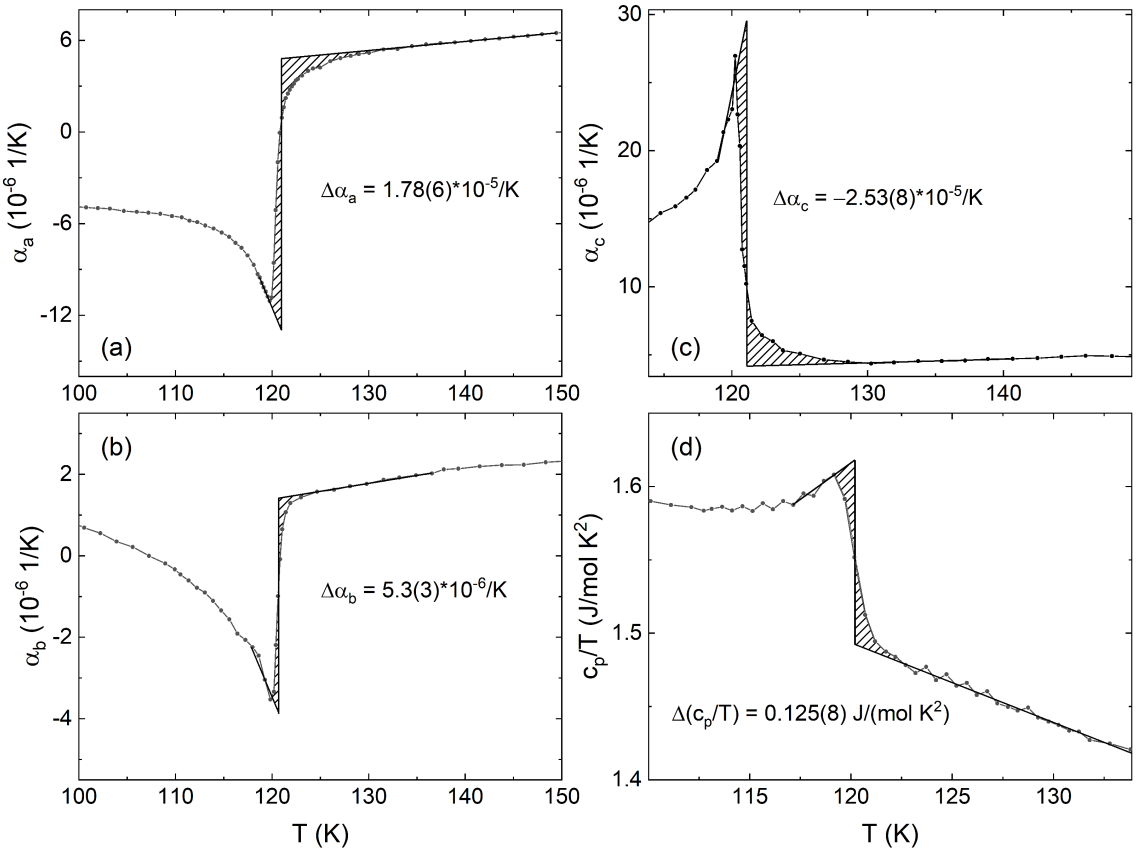

Figure 4.9: Determination of the jump heights in (a-c) thermal expansion coefficient and (d) specific heat by an area-conserving interpolation as described in the text.

similarly as before for T_{N}, but now considering the jumps in α_i and $\mathrm{c_p}$:

$$\Gamma_i = \frac{\Delta\alpha_i}{\Delta c_{\mathrm{p}}} = \frac{1}{TV_{\mathrm{m}}}\frac{\partial S/\partial p_i}{\partial S/\partial T}. \tag{4.5}$$

The pressure dependence of T_{S} is then determined by

$$\frac{\partial T_{\mathrm{S}}}{\partial p_i} = V_{\mathrm{m}} T_{\mathrm{S}} \Gamma_i, \tag{4.6}$$

where $V_{\mathrm{m}} = 1.333 \cdot 10^{-4}$ m^3/mol is the molar volume and the index i indicates a linear direction or the volume. The resulting uniaxial pressure dependencies are large for the a- and c-axis, $\partial T_{\mathrm{S}}/\partial p_a = -23(6)$ K/GPa and $\partial T_{\mathrm{S}}/\partial p_c = 27(3)$ K/GPa, while $\partial T_{\mathrm{S}}/\partial p_b = -6.7(1.0)$ K/GPa is much smaller. Adding up the uniaxial pressure dependence for the three axes yields a hydrostatic pressure dependence of $dT/dp = 2.3(1.5)$ K/GPa. The results including the Grüneisen ratios are also summarized in

Tab. 4.1.

To investigate further the behavior of the thermal expansion coefficient around T_S the spontaneous strain $\varepsilon_i = \Delta L_i/L_i$ was extracted. For the extraction of ε_i linear as well as second- and third-order polynomial functions were fitted to the relative length changes between 126 K and 200 K, in order to test the differences in fitting parameters arising from the different backgrounds. The fits and resulting spontaneous strains are shown in the appendix (Fig. B.1). Power-law fits according to

$$\varepsilon = A \cdot |T - T_S|^p \tag{4.7}$$

were performed on all resulting spontaneous strain data, in the range from 115 K to 119.6 K. The fit results are summarized in Tab. 4.2 and the spontaneous strain of each of the axes is shown in Fig. 4.10. A number of observations can be made from the plot and fit results: (1) The general behavior of the three axes is very similar. (2) The a- and c-axis show the same critical exponent $p \approx 0.71(2)$ (averaged over the different fits), but their strains are of opposite sign. (3) While the qualitative behavior of the axes is similar, the strain along the b-axis at T_S is smaller by a factor of four and its corresponding critical exponent $p \approx 0.77(2)$ is slightly higher compared to the other two axes.

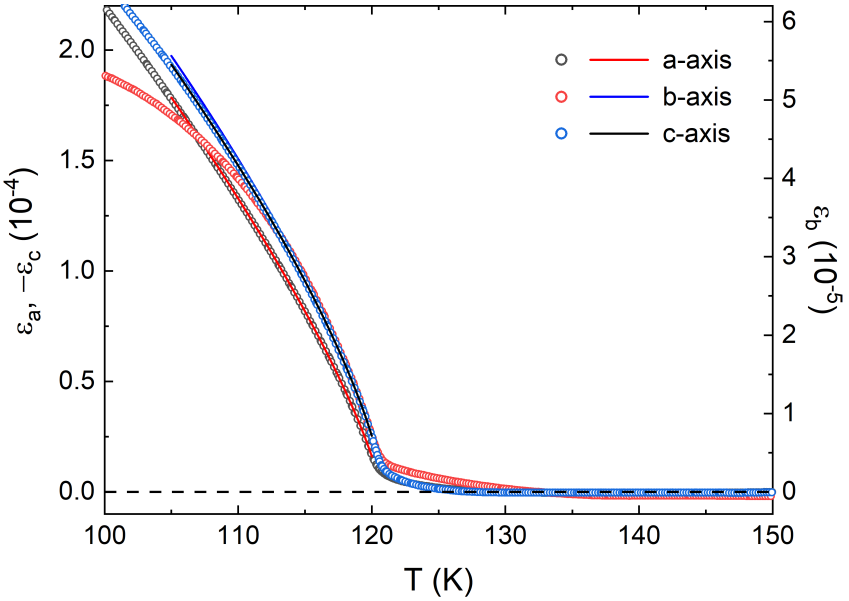

Figure 4.10: Spontaneous strain ε_i at T_S and power-law fitting. The left (right) ordinate refers to the a- and c-axis (b-axis). Second- (third-)order polynomials were subtracted from the b- and c-axis (a-axis) dL_i/L_i data to obtain the spontaneous strain around T_S as described in the text. Power-law fits are indicated by solid lines and the horizontal dashed line indicates zero spontaneous strain. Note the negative sign of ε_c.

Table 4.2: Power law function fit parameters for different backgrounds subtracted from dL_i/L_i to obtain the spontaneous strain ε. All fits were performed in the temperature regime from 115 K to 119.6 K, i.e., in the vicinity of the phase transition.

Fitting results for the spontaneous strain at T_S $\varepsilon = A\|T - T_S\|^p$			
Axis & Background	T_S (K)	A (10^{-5})	p
a-axis			
2nd order polynomial	120.92	2.68(1)	0.713(2)
3rd order polynomial	120.81	2.61(2)	0.715(1)
b-axis			
2nd order polynomial	120.99	2.323(4)	0.773(1)
3rd order polynomial	120.69	2.136(6)	0.771(2)
c-axis			
linear	120.42	0.639(3)	0.716(3)
2nd order polynomial	120.90	0.771(7)	0.714(4)
3rd order polynomial	120.55	0.686(7)	0.712(5)

For a qualitative impression the linear thermal expansion coefficients α_i, plotted against the reduced temperature $t = |(T - T_S)/T_S$ on a logarithmic scale, are shown in Fig. 4.11. The results for $t \lessapprox 0.03$ are very sensitive to the choice of T_S. Changing T_S by about 0.1 K–0.2 K, however, does not change the qualitative behavior. The values of T_S chosen for the data in Fig. 4.11 are $T_{S,a} = 119.95$ K, $T_{S,b} = 120.15$ K, and $T_{S,c} = 120.22$ K. Two distinct linear regimes become visible in this plot, as marked by straight lines in Fig. 4.11. The behavior very close to T_S probably shows a critical slowing down, originating here from the softening of the phonon mode which drives the structural phase transition [112]. Critical slowing down sets in around 0.01 t for the a- and c-axis, and around 0.03 t for the b-axis, i.e., in a temperature window of 1 K–4 K around T_S.

The nature of the phase transition at T_S was debated for some time. Initial hints to its existence were discovered by Millet et al. [119] by a change of slope in the inverse static susceptibility. Miller et al. found 16 additional phonon modes below 115 K but were not able to resolve a new structure [120]. They suggested a loss of centro-symmetry by a second-order transition to the polar orthorhombic $Pm2_1n$ or $P2_1mn$ space groups. A study of high-resolution synchrotron powder diffraction and density functional calculations of lattice dynamics by Prishchenko et al. found the nonpolar $Pcmn$ space group to be lowest in energy for both CBSCl and CBSBr [121]. Especially, they uncovered structural instabilities in the lattice leading to an antiferroelectric distortion in CBSCl below 115 K and suggested a residual disorder scenario as the driving force for the transition. The distortion was found to involve cooperative

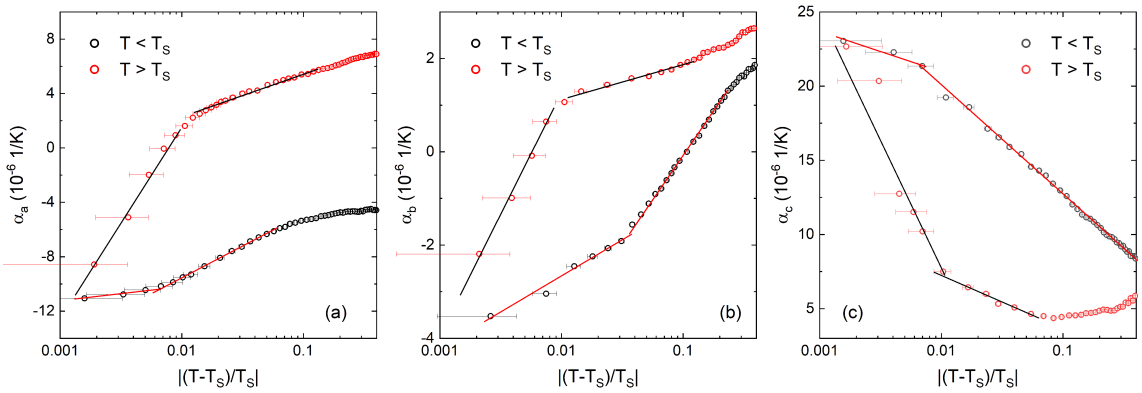

Figure 4.11: Logarithmic scaling of thermal expansion data around T_S. Lines are guides to the eye.

displacements along the a-axis of Cu and Cl atoms, originating from the optimization of interatomic distances of the weakly bonded halogen atoms [121]. The Cu2–Cl distance was found to shorten from 3.205 Å in the undistorted structure to 2.782(6) Å in the distorted structure. Neutron diffraction studies by Constable et al. confirmed the structural transition from the $Pmmn$ phase to the $Pcmn$ phase with a doubling of the c cell parameter [16]. Additionally, their dielectric measurements revealed an antiferroelectric phase below T_S and a linear magnetoelectric coupling below T_N. Most recently a publication by Milesi-Brault et al. described the structural transition at T_S as a rare archetype of a transition driven by a soft antipolar phonon mode [112]. They were able to track this phonon mode on both sides of T_S with a linear behavior of the squared phonon energy according to the classical theory of soft-mode-driven transitions [122, 123]. Furthermore, they concluded from the slope $\partial E^2/\partial T$ that a phenomenological description of the transition by means of a Landau model should include at least the sixth order term $cQ^6/6$. At the same time they acknowledged the complexity of the transition and the fact that the simple image of the transition as being driven by the antipolar displacements of Cl ions is only an approximation.

The results presented here give direct evidence of the strong fluctuations well below T_S as seen in the thermal expansion coefficients. To relate the critical exponents extracted from the spontaneous strain to a universality class of the observed second order transition, a physical model is needed to clarify the relation between strain and the order parameter Q of the transition. This is beyond the scope of this work and will be a future task to be performed by the author. It shall be noted, however, that for a possible relation $\varepsilon \sim Q^2$ the critical exponent $\beta_c = 0.5p$ would be 0.35(1) and 0.39(2) for the a- and c- as well as the b-axis, respectively. These values fit to the 3D XY model ($d = 3, D = 2$, $\beta_c = 0.345$) and the 3D Heisenberg model ($d = 3, D = 3$, $\beta_c = 0.365$) and are also close to the 3D Ising model ($d = 3, D = 1$, $\beta_c = 0.325$), i.e.,

showing three-dimensional ordering.

4.3.2 Thermal Expansion and Magnetostriction at B $\neq$ 0

Fig. 4.12 shows the effect of an applied magnetic field of B = 15 T on the thermal expansion. From highest temperatures to the structural phase transition at T_S no field effect is observed for any of the axes. For the *c*-axis, the 0 T and 15 T data coincide also below T_S to about 27 K. Below 27 K a small and positive field effect on the order of $\Delta L_c/L_c = 1 \cdot 10^{-5}$ is visible, but no anomaly indicating a phase transition remains. The scenario for the in-plane directions differs strongly: Significant field effects become visible around 100 K. For the *b*-axis (with $B \parallel b$) a positive field effect is observed. No phase transition is observed at B = 15 T and the length change from 0 T to 15 T at the lowest temperatures amounts to $\Delta L_b/L_b = 4.1 \cdot 10^{-5}$. The *a*-axis, in contrast to *b* and *c*, shrinks upon application of a magnetic field and shows a broad peak in α_a around 22 K. Due to this peak the length change in field at the lowest temperatures is much larger than for the other axes, $\Delta L_a/L_a \approx -3.1 \cdot 10^{-4}$. In summary, the *c*-axis shows only a minor field effect at low temperatures, whereas a substantial field effect is visible below the structural phase transition at T_S for the in-plane directions. The transition temperature T_S itself is unchanged by an applied magnetic field, i.e., the structural changes are not coupled to magnetic phenomena.

In order to trace the evolution of the phase transition at T_N in an applied magnetic field, thermal expansion and magnetostriction as well as magnetization measurements were performed for all axes.

$B \parallel c$: Field-Induced Mixed Phase Behavior

The thermal expansion of the *c*-axis in fields between 0 T and 1 T in comparison to the Fisher specific heat [124] derived from the static susceptibility χ_c are presented in Fig. 4.13. The field dependence of the transition at T_N in zero-field is clearly visible and qualitatively identical in both α_c and $\partial(\chi_c T)/\partial T$. The peak heights increase from 0 T to 0.5 T and then broaden substantially in higher fields, extending over a range of 10 K (from 3.2 K to 13 K) at 0.8 T. Especially, above 0.4 T the behavior starts to look more like two subsequent phase transitions rather than a single broad transition, i.e., with an intermediate phase of enhanced thermal expansion. At 0.9 T no sign of a phase transition remains.

A similar one-to-one correspondence as observed between the thermal expansion and static susceptibility data is also observed between the magnetostriction and isothermal magnetization (Fig. 4.14): At 2.3 K (2.0 K for $M(B)$) a sharp step is observed in the up-sweeps of both magnetization and magnetostriction. This step extends from 0.80 T to 0.86 T where a plateau is reached. The down-sweep shows considerable hysteresis and an almost instantaneous jump at $B \approx 0.76$ T of negligible

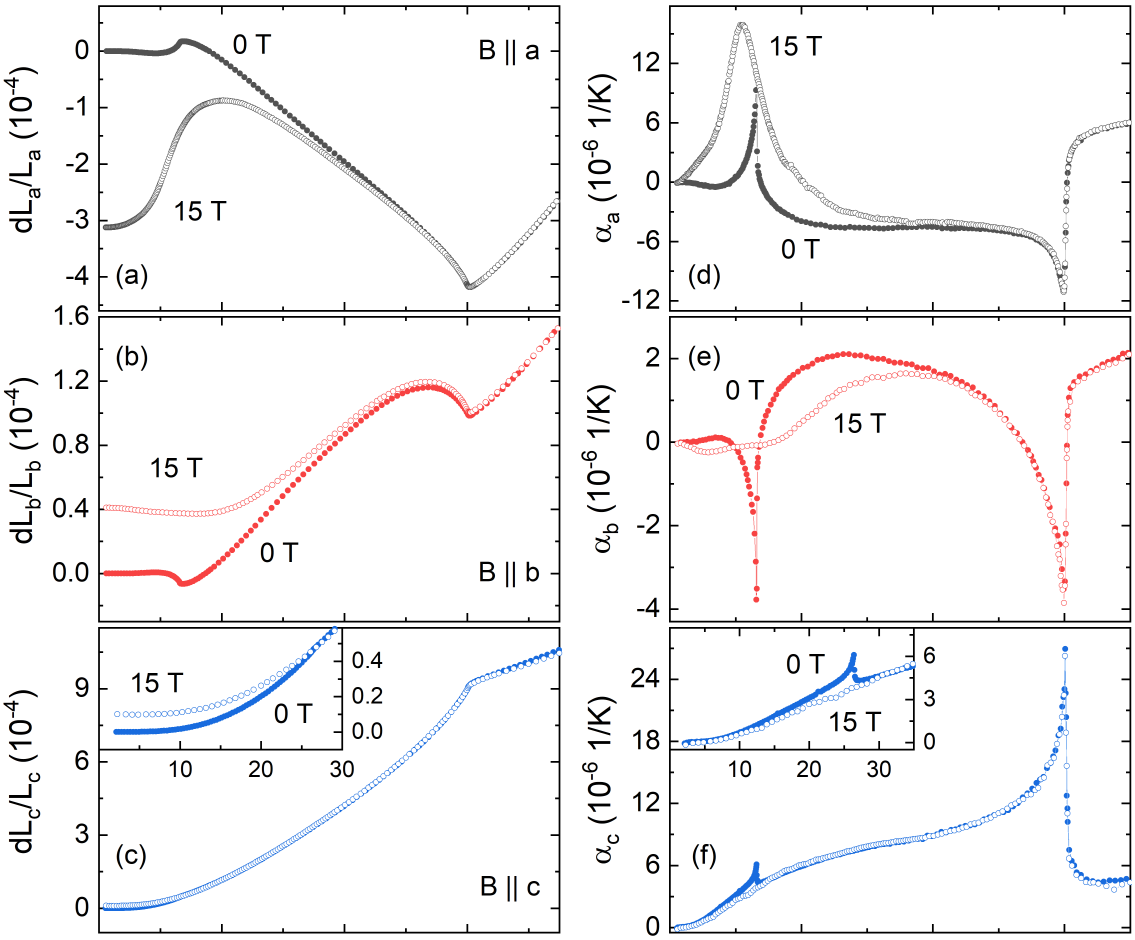

Figure 4.12: Comparison of relative length changes dL_i/L_i (a-c) and thermal expansion coefficients α_i (d-f) in zero-field (closed circles) and B = 15 T (open circles). Insets in (c) and (f) show a magnification of the low temperature window.

width. At higher temperatures the hysteresis decreases and vanishes above 20 K. In Fig. 4.14(c) and (d) the hysteresis regions are colored for better visibility, with the magnetostriction down-sweeps shifted up by 6 mT to correct for the remanent field of the superconducting magnet in the thermal expansion setup. Notably, the hysteresis does not extend over the complete step-like transition. The data between 10 K and 20 K show that the hysteresis is related to the upper boundary of the transition, and a jump in magnetization and magnetostriction to a linear behavior is observed. Below 10 K the hysteresis is larger than the width of the step, such that no linear behavior but only an abrupt jump is observed in the down-sweeps. Note that the magnetostriction is fully reversible. This suggests a well-ordered ground state as well as a high single crystal quality with few defects which could lead to the creation of antiferromagnetic domains.

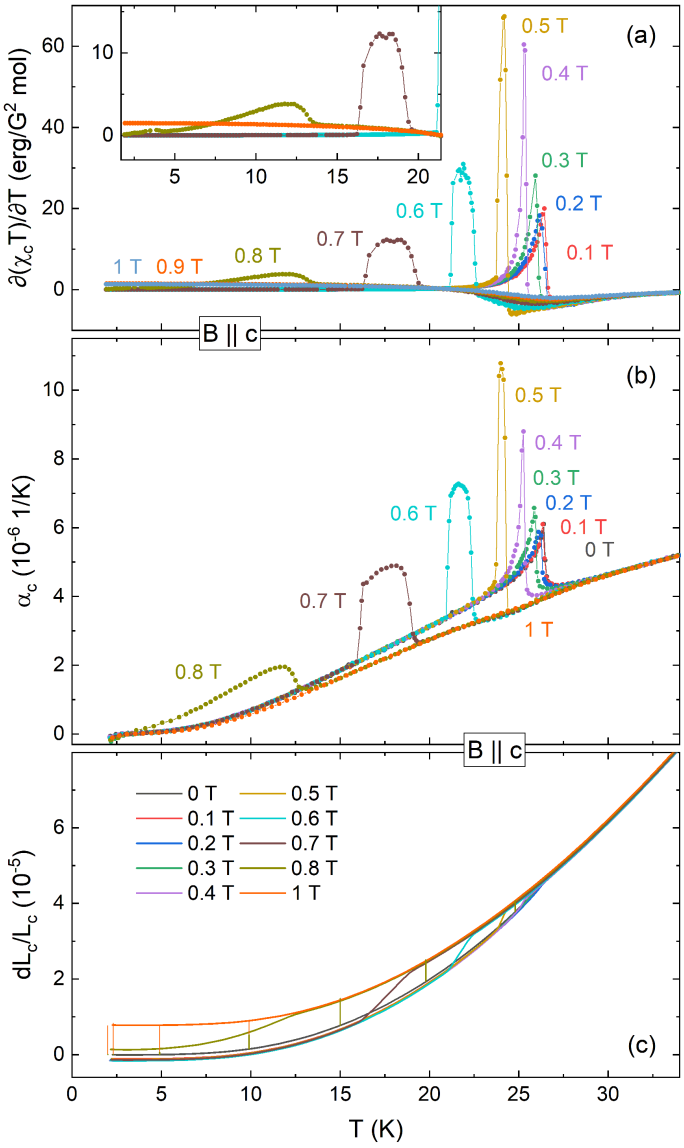

Figure 4.13: (a) Fisher's specific heat calculated from the static magnetic susceptibility, (b) thermal expansion coefficient, and (c) relative length changes for $B \parallel c$ for B = 0 to B = 1 T. The inset in (a) presents a magnification of the low temperature region. Vertical bars in (c) mark the relative length changes $\Delta L(B)$ from 0 T to 0.8 T and 1 T, respectively, obtained from magnetostriction measurements.

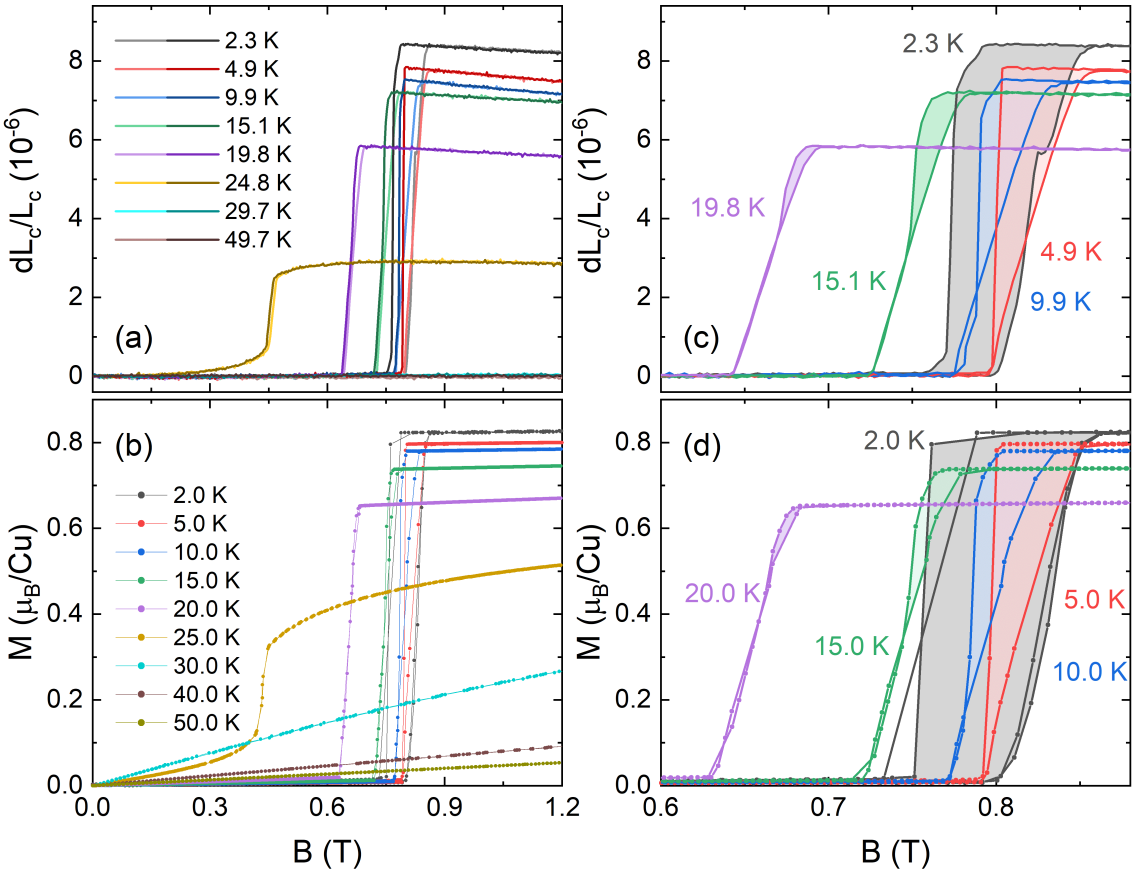

Figure 4.14: Comparison of relative length changes $dL_c(B)/L_c(0)$ (a, c) and isothermal magnetization (b, d) for $B \parallel c$. Note that (c) and (d) show a magnification of the transition region and only data for selected temperatures. Hysteresis is marked by colored areas. Magnetostriction down-sweeps in (c) are shifted by 6 mT to correct for the remanent field of the magnet.

The behavior described here both in field and temperature is related to the mixed antiferromagnetic (AFM)/ferromagnetic(FM) phase which was predicted from theory and observed in experiments for metamagnets before [113, 125, 126]. Wyatt observed a linear increase in $M(H)$ between $H_a = 4$ kOe and 6.8 kOe on the cubic lattice of $Dy_3Al_5O_{12}$ with H_0 applied along one of the high symmetry axes [125]. He also found a clear and simple explanation of this effect: Below a critical magnetic field H_a the spins are aligned antiferromagnetically with zero demagnetizing field. For $H_0 > H_a$, i.e., above the spin-flip field, the AFM couplings will be broken and a field-induced ferromagnetic alignment is expected. However, in the field-induced ferromagnetic phase there will be a large demagnetizing field H_d. If the spin-flip occurred all at once in the whole sample, the resulting internal field would be $H_{int} = H_0 - N \cdot M_S$, with the demagnetizing factor N and the saturation magnetization M_S. Since for $H_0 > H_a$

with $H_0 < H_a + N \cdot M_S$ one gets $H_{int} < H_a$, the transition would not occur at all. At the same time the material cannot exist in an unmagnetized state for $H_0 > H_a$. Therefore, in an external field range $H_a < H_0 < H_a + N \cdot M_S$ the antiferromagnetic alignment will be partially broken, and the sample is in a mixed phase state with well-defined regions of parallel and antiparallel phases with an average magnetization $\bar{M}$. The ratio of the amounts of the two phases will then adjust automatically in any external field so that the internal field is $H_{int} = H_a = H_0 - N \cdot \bar{M}$ for $H_a < H_0 < H_a + N \cdot M_S$. While H_0 increases linearly in the mixed phase, so does the average magnetization with slope $1/N$.

To use another terminology: in the mixed phase the increasing external field leads to the creation of ferromagnetic domains (and destruction of antiferromagnetic order) along the *c*-axis, which produce an increasing demagnetizing field and average magnetization until saturation is reached. Stryjewski and Giordano also described this behavior as typical for metamagnets [126]. More recent experiments on antiferromagnetically coupled multilayers studied the creation, morphology, and magnetization of the so-called metamagnetic domains [127, 128]. More importantly, the mixed phase behavior has been studied in detail employing neutron scattering, muon spin relaxation, specific heat, ac and dc magnetization measurements, as well as electron magnetic resonance in the CBSCl brother compound $Cu_3Bi(SeO_3)_2O_2Br$ (CBSBr). In the mixed phase of CBSBr broadband absorption for excitations extending over at least ten decades of frequency was found, opening an exciting potential for technological applications [113]. The data in this work confirm the presence of the mixed phase also in CBSCl, making it also interesting for a number of applications related to broadband microwave absorption such as microwave filters, signal-to-noise enhancers, optical signal processing, electromagnetic interference shielding etc. with potential electric or magnetic field control [113].

Also in CBSBr, a hysteresis behavior of the upper boundary of the mixed phase analogous to the one desribed for CBSCl here was found in electron spin resonance (ESR) experiments [129]. However, in CBSBr the hysteresis at 5 K only extends to about 1/3 of the mixed phase, while for CBSCl at 5 K it extends almost over the entire mixed phase.

Connecting the process described for the mixed phase above to the thermal expansion data, the increased thermal expansion can be ascribed to the breaking of the antiferromagnetic coupling as temperature increases, and the concomitant creation of ferromagnetic domains until saturation is reached. Also the linear magnetostriction in the mixed phase is expected to arise from a linear process of successively flipping the AFM coupled layers, i.e., the creation of ferromagnetic domains which increase in size/number with increasing field.

$B \parallel c$: Linear Magnetoelastic Coupling

As seen in the previous section both the positions and relative heights of the magnetization and magnetostriction jumps at the metamagnetic transition for different temperatures match very well with each other (Fig. 4.14). Normalizing the jump heights in magnetization and relative length changes by their value at 2 K emphasizes the proportionality $\Delta M \sim \Delta L_c$ between the jumps, with $\Delta M/(\Delta L/L) = 1.1(1) \cdot 10^5 \mu_B/\mathrm{Cu}$ (Fig. 4.15).

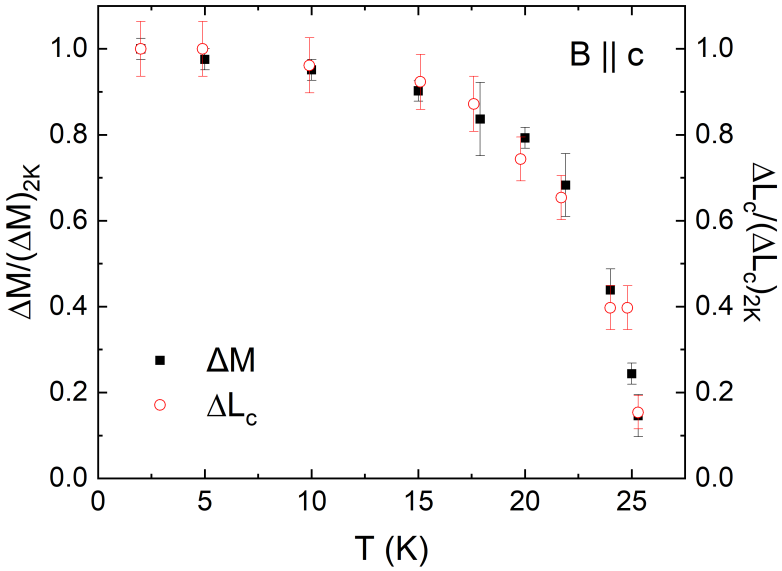

Figure 4.15: Comparison of jumps in magnetization (left ordinate) and relative length changes (right ordinate) normalized by their value at 2 K.

This proportionality means that the magnetization and magnetostriction couple to the order parameter Q related to the antiferromagnetic (AFM) to ferromagnetic (FM)/paramagnetic (PM) transition in the same way. Notably, this coupling is gone above T_N, i.e., in the paramagnetic phase: the magnetization at 30 K shows a clear linear increase, whereas the magnetostriction at the same temperature is virtually zero. Furthermore, the magnetostriction at 24.8 K is also non-zero below the jump at 0.45 T. Therefore, the similar behavior in magnetization and magnetostriction is not limited to the region of linear increase but is present in magnetic fields below this region as well. Considering the discussion of the mixed phase in the last section, the non-zero magnetostriction and magnetization at 24.8 K, near T_N, can be understood by breaking the AFM alignment of the stacked francisite layers along the c-axis below H_a due to thermal excitations. Above T_N no AFM alignment and thus no creation of FM domains takes place, and hence magnetostriction is zero. Since in the mixed phase the internal magnetic field $H_{\mathrm{int}} = H_0 - H_d$ is expected to rise linearly, the observed behavior does not only imply a linear dependence $L(H) \sim M(H)$ but

also a linear magnetoelastic coupling $L(H_{\mathrm{int}})\ H_{\mathrm{int}}$ which can be described by a linear magnetostriction coefficient d as $dL/L = d \cdot H_{\mathrm{int}}$. One could for simplicity state that there is a linear magnetoelastic coupling in the mixed phase, but this would ignore the data at 24.8 K below B_c as well as the observed hysteresis. I consider it thus more accurate to state that a linear magnetoelastic coupling in CBSCl exists with respect to the internal field.

The phenomenon of linear magnetoelastic coupling was investigated extensively in the late 1950s and early 1960s, both in ferro- and antiferromagnetic materials. According to Zvezdin et al., linear magnetostriction was first observed in CoF_2 by Borovik-Romanov and co-workers [130]. Among many others, antiferromagnetic examples include hematite (α-Fe_2O_3) [131], dysprosium orthoferrite [130] ($DyFeO_3$), and more recently the multiferroic $TbMnO_3$ [132]. In all of these compounds linear magnetostriction is closely related to the presence of antiferromagnetic domains. Moreover, Birss and Anderson worked out a list of 35 magnetic crystal classes in which linear magnetostriction is expected as a dominant effect from symmetry considerations [133]. The magnetic point group of CBSCl, $mm'm$, is not among the point groups in which a linear magnetostriction is expected to be dominant. This does not mean, however, that it may not, as observed, be dominant. In addition to the linear magnetoelastic coupling, Constable et al. argued that $mm'm$ is also compatible with a linear magnetoelectric coupling [16]. And indeed, a linear magnetoelectric coupling was shown experimentally by Wu et al. [17]. They measured the electric polarization in CBSCl in an applied magnetic field up to 4 T with $B \parallel c$ at 10 K, showing a linear behavior above the spin-flip transition. However, the behavior of the polarization in the mixed phase can not be derived from the data by Wu et al. because the magnetic field scale on which the data is presented is too large to see it. It would be interesting to see the electric polarization in the AFM phase and the mixed phase region with increasing and decreasing magnetic field in greater detail to draw conclusions about the multiferroic behavior of CBSCl, especially the relation between the linear magnetoelastic and magnetoelectric couplings.

Quantitative Analysis of the Phase Boundaries for $B \parallel c$

For a quantitative analysis the Clausius-Clapeyron equation and related equations [9] are used to investigate the pressure dependence of the AFM to FM phase boundary for both temperature and field sweeps:

$$\left(\frac{\partial T_c}{\partial p_i}\right)_B = V_\mathrm{m}\frac{\frac{\Delta L_i}{L_i}}{\Delta S} \tag{4.8}$$

$$\left(\frac{\partial T_c}{\partial B_i}\right)_p = -\frac{\Delta m_i}{\Delta S} = -\frac{\Delta(M_i \cdot V)}{\Delta S} \tag{4.9}$$

$$\left(\frac{\partial B_c}{\partial p_i}\right)_T = V_\mathrm{m}\frac{\frac{\Delta L_i}{L_i}}{\Delta m_i} \tag{4.10}$$

The change in entropy related to the transition is also calculated. To enable this analysis, the mixed phase which is discussed above as an intermediate phase is treated in this analysis as one phase transition region, i.e., the transition is treated as a first order transition. All results are shown in Tab. 4.3.

At the lowest temperatures the calculated change in entropy related to the phase transition at B_c is $\Delta S_\mathrm{calc} = 30(14)$ mJ/(mol K). As the phase transition shifts to lower fields at higher temperatures this value increases, reaching about 300 mJ/(mol K) at 25 K. In contrast, the uniaxial pressure dependence $\partial T_\mathrm{N}/\partial p_\mathrm{c}$ is very large and positive, 34(16) K/GPa at 2 K, due to the nearly flat phase boundary at lowest temperatures. As the critical field decreases with temperature, this number decreases strongly. At 15 K (25 K) it decreases to 6.0(1.5) K/GPa (1.3(4) K/GPa) and approaches the zero-field value of 0.33(10) K/GPa. Lastly, the uniaxial pressure dependence of the critical field along c is also positive. Even though the absolute values are small, on the order of $\partial B_\mathrm{c}/\partial p_\mathrm{c} = 80(10)$ mT/GPa, the relative pressure dependencies $\partial ln(B_\mathrm{c})/\partial p$ are around 10(1)% due to the small critical field. In summary, uniaxial pressure along the c-axis stabilizes the antiferromagnetic order both in temperature and in field. In terms of exchange interactions, this means an increase in the antiferromagnetic interlayer coupling $J_{\perp,2}$ between Cu2 spins and/or weakening of the ferromagnetic $J_{\perp,1}$ between Cu1 and Cu2 by an applied uniaxial pressure as also observed in the zero-field data.

a- & b-axis: In-Field Thermal Expansion

In contrast to studies on the c-axis, in-plane measurements along the a- and b-axis pose a veritable challenge. Due to the plate-like sample geometry aligning the single crystals along their crystallographic axes yields large error bars. A small tilting of 5° to 10° away from the desired axis is easily possible for the a- and b-axis. In an

Table 4.3: Jump heights, calculated changes in entropy, field and pressure dependencies for the discontinuous transition in magnetic field from AFM to FM for $B \parallel c$ according to Eq. (4.8). The quantity $\partial B_c/\partial T$ was calculated by taking the derivative of two polynomial fits in different temperature regimes to the values $B_c(T)$ in the phase diagram.

AFM → FM – c-axis: Extracted and calculated quantities									
T (K)	B_c (T)	Sweep	$\Delta L_c/L_c$ (10^{-6})	ΔM (μ_B/Cu)	$\partial B_c/\partial T$ (mT/K)	ΔS_{calc} (mJ/mol K)	$\partial T_N/\partial p$ (K/GPa)	$\partial B_c/\partial p$ (mT/GPa)	$\partial \ln(B_c)/\partial p$ (%/GPa)
2.0±0.1	0.82	B	7.8±0.5	0.82±0.02	–2.2±1.0	30±14	34±16	76±6	9.3±0.7
5.0±0.1	0.81	B	7.8±0.5	0.8±0.02	–2.2±1.0	29±14	35±17	78±6	9.6±0.7
10.0±0.2	0.80	B	7.5±0.5	0.78±0.02	–7±3	90±40	11±5	77±6	9.6±0.7
15.0±0.2	0.75	B	7.2±0.5	0.74±0.02	–13±3	160±40	6.0±1.5	77±6	10.4±0.8
17.9±0.4	0.70	T	6.8±0.5	0.69±0.07	–17±3	200±40	4.6±1.0	79±10	11.3±1.4
20.0±0.2	0.66	B	5.8±0.4	0.65±0.02	–27±8	290±90	2.6±0.8	71±6	10.8±0.9
21.9±0.3	0.60	T	5.1±0.4	0.56±0.06	–38±8	360±90	1.9±0.5	72±10	12.1±1.6
24.0±0.2	0.50	T	3.1±0.4	0.36±0.04	–60±20	360±130	1.1±0.5	69±12	14±3
25.0±0.2	0.44	B	3.1±0.4	0.20±0.02	–94±20	320±80	1.3±0.4	120±20	28±5
25.3±0.2	0.40	T	1.2±0.3	0.12±0.04	–142±30	280±120	0.6±0.3	80±40	20±9

applied magnetic field such seemingly small misalignment yields a finite effective field along the other axes, and respective changes of the resulting magnetic phase diagrams are significant. (see appendix, e.g., Figs. B.2 and B.4).

At the lowest temperatures the magnetostriction of the a- and b-axis exhibits very strong anomalies in λ with peak heights on the order of 10^4/T. For the a-axis, a step-like negative jump is observed in $dL_a(B)$ with a subsequent linear behavior, while a gradual rise in $dL_b(B)$ dominates at the b-axis. At temperatures of 10 K and below this rise turns into a jump-like behavior. Furthermore, for the a-axis λ_a shows a broad transition reminiscent of the mixed phase of the c-axis. The critical fields at around 2 K are $B_{c,a} \approx 5.6$ T and $B_{c,b} \approx 6.5$ T. While the latter is close to the saturation field determined by magnetization measurements presented below (7.1 T), the a-axis is expected to show no abrupt transition but a simple saturating behavior at fields around 15 T or higher [15]. For both axes, measurements on several crystals were performed to reproduce the observed features. Even though the qualitative behavior in field was similar – positive and negative magnetostriction for the a- and b-axis, respectively, as well as the jumps for $B \parallel a$ and a gradual rise for $B \parallel b$ – the critical fields differed widely, from 5.5 T to 7.5 T for the a-axis and 4.5 T to 6.5 T for the b-axis. Furthermore, two transitions were visible in several cases, especially for $B \parallel b$. In one case this can be explained by contact twinning, as reported by Pring et al. [109]. For the other cases a quick calculation shows that the strong peaks in λ_a and λ_b are explained well by a tilt of the crystal towards the c-axis. For magnetic fields B_{exp} applied at an angle α with respect to the c-axis such tilting yields an effective field $B_{c,eff} = B_{exp} \cdot \sin\alpha$ along the c-axis. If this field reaches $B_{exp} > B_c \approx 0.8\ T$, the metamagnetic transition is triggered. For $B_{c,a} = 5.6$ T and

$B_{c,b} = 6.5$ T as mentioned above, this yields a tilting of about 8° and 7°, respectively. This tilt towards c also explains the mixed phase behavior and its width visible in the a-axis data. Due to this tilting, the in-plane thermal expansion and magnetostriction measurements by themselves cannot be used either to construct the phase diagram or to analyze the phase transitions in field for $B \parallel a, b$. Therefore, magnetization data presented below clarify which of the observed anomalies originate purely from the a- or b-axis, and which anomalies originate from a combined effect due to the tilting towards the c-axis. Selected thermal expansion and magnetostriction measurements are shown in the appendix (Figs. B.2 to B.5).

Excitations in the Long-Range Ordered Phase

Finally, an inspection of the broad shoulder at about 15 K which was observed in $c_{p,mag}$ and $\alpha_{c,mag}$ (Fig. 4.7) is in order. To determine its field dependence the phononic background which was used for the zero-field specific heat data (Fig. 4.6) was also subtracted from c_p measurements in fields of 3 T, 5 T and 7 T with $B \parallel c$. For the thermal expansion data $\alpha_{c,mag}$ at 1 T and 15 T was also extracted. To emphasize the features in the background corrected data, $c_{p,mag}/T$ and $\alpha_{c,mag}/T$ are plotted in Fig. 4.16. In the specific heat data two features become clearly distinguishable at $B > B_c$. The first anomaly remains constant at about 15 K in increasing field, only slightly decreasing in intensity. The second feature broadens and shifts to higher fields from 27.4 K at 3 T to 33.4 K at 7 T. Similar observations can be made for $\alpha_{c,mag}/T$: a peak around 15 K remains up to highest fields, whereas a second feature is seen at 1 T around 28 K. At 15 T this feature is not distinguishable from the broad high temperature tail of the peak at 15 K.

The anomaly at higher temperatures in thermal expansion and specific heat can readily be assigned to the crossover from the field-induced ferromagnetic phase to the paramagnetic phase. In fact, the shoulder in $\alpha_{c,mag}$ at 1 T hints at a peak at about 27 K. This fits perfectly with the crossover line in the c-axis phase diagram shown below (Fig. 4.22).

The origin of the field-independent 15 K anomaly, on the other hand, can not be definitely determined. A Schottky anomaly can be ruled out, because it would shift in an applied magnetic field. Furthermore, plotting $\alpha_{c,mag}/T^{3/2}$ vs. $T^{3/2}$ (Fig. 4.16(b) inset) shows a linear behavior, i.e., $\alpha_{c,mag}\ T^3$, with a negative offset. While the offset is related to ferromagnetic magnons – $\alpha_{FM}\ c_{p,FM}\ T^{3/2}$ – this linear behavior signals either phononic or antiferromagnetic magnonic contributions. In the ferromagnetic phase above the critical field no AFM magnons can be present, therefore the linear rise suggests a phononic origin of the 15 K anomaly.

Several observations have been reported in the AFM and FM phases for $B \parallel c$ in CBSCl, which may be related to the anomaly: Infrared reflection and transmission

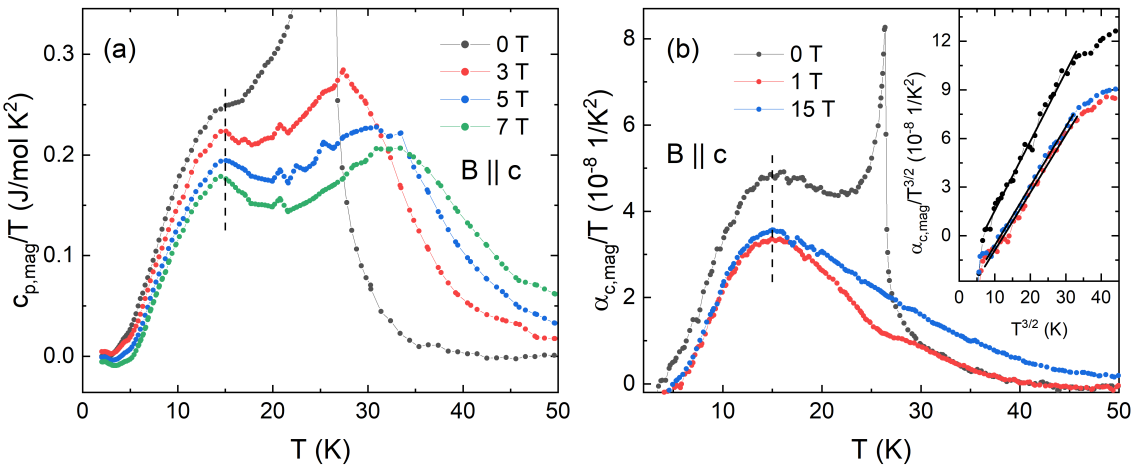

Figure 4.16: Contributions after subtracting a phononic background as explained in the text to (a) the specific heat in fields up to 7 T and (b) the thermal expansion in zero-field as well as at B = 1 T and 15 T for $B \parallel c$. Vertical dashed lines at 15 K mark the peak position. The inset in (b) shows $\alpha_{c,mag}/T^{3/2}$ vs. $T^{3/2}$. Black lines represent linear fits to the data.

studies by Miller et al. found two low-frequency phonon excitations at 5 K [120]. One of them, at 33.1 cm^{-1} ($\approx$ 48 K), is visible in zero-field and only shifts slightly, to about 35 cm^{-1} in fields $B \parallel c$ of 10 T. For $B \perp c$ the resonance frequency of this phonon mode decreases. Miller et al. tentatively assigned this phonon branch to magnon excitations, based on their analysis of previously reported oscillator strengths of magnons and electromagnons. The second phonon excitation at 5 K was only observed for $B \parallel c$ in the ferromagnetic phase, with a frequency of 10.5 cm^{-1} ($\approx$ 15.1 K) at 1 T [120]. This phonon shifts linearly in an applied magnetic field, up to about 16 cm^{-1} (23 K) at 7 T.

Constable et al. reported a global spin gap of 1.57 meV (18.2 K) [16]. This fits with the temperature scale of the anomaly and would suggest a relation to magnonic excitations. The presence in zero-field, i.e., in the AFM phase, would then be explained by ferromagnetic spin-waves within the ferromagnetically coupled layers.

Lastly, Wang et al. observed two resonances at 1.23 meV (14.3 K) and 1.28 meV (14.8 K) in CBSBr in time-domain THz spectra at 3.9 K [134]. They also performed electron spin resonance (ESR) measurements which suggest that these two resonances are of magnetic origin and shift to higher frequencies in higher magnetic fields. However, a flat, i.e., field-independent, resonance would not be seen by spectroscopic field-sweeps around 300 GHz. Frequency sweeps at different magnetic fields would be necessary to observe such a resonance.

In conclusion, low-energy optical phonons, potentially coupled to magnon excitations,

seem to be the cause for the anomalies observed around 15 K.

4.3.3 Magnetization Measurements

Magnetization measurements along the a-axis (corresponding to 215° in Fig. 4.3(d)), the b-axis (315°), and in-between both axes (260°, not shown) were performed in order to investigate the in-plane phase diagram of CBSCl. The results of the measurements, together with the magnetization measurements of the c-axis, are briefly presented in the following paragraphs.

Fig. 4.17(a) shows a comparison of the isothermal magnetization at 2 K up to 7 T for all three crystal axes. For $B \parallel c$ the magnetization jumps at the metamagnetic transition to a value of 0.82 μ_B/Cu, while the in-plane directions show no transition up to 7 T. M_b, however, shows an increasing slope above 4 T after an initially linear rise, while M_a increases linearly up to the highest measured field. The slopes of the magnetization curves are 0.045(3) μ_B/(T Cu), 0.089(3) μ_B/(T Cu), and 0.009(2) μ_B/(T Cu) for the a-, b-, and c-axis, respectively.

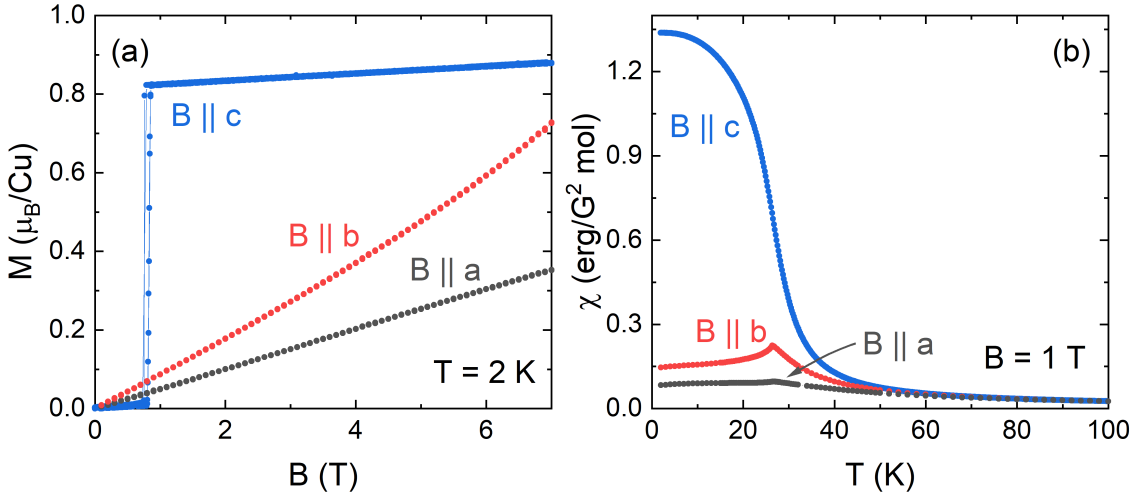

Figure 4.17: (a) Isothermal magnetization at T = 2 K and (b) static magnetic susceptibility $\chi = M/H$ at $B = 1$ T for $B \parallel a$ (black), $B \parallel b$ (red), and $B \parallel c$ (blue). Errors bars are on the order of the size of the data points.

Nikolaev et al. calculated the slopes of the magnetization curves for the tilted Cu1 spins for the a- and c-axis. They obtained $\partial M_a/\partial B = 0.15$ μ_B/T (0.044 μ_B/T) and $\partial M_c/\partial B = 0.0073$ μ_B/T (0.0061 μ_B/T) from the conventional local-density approximation including spin-orbit coupling, and Hartree Fock (HF) calculations (results in parentheses) [111]. These values, especially from the Hartree Fock calculations, agree with the values obtained in this work within experimental error bars. Furthermore, Nikolaev et al. calculated the work W_b done by the magnetic field $B \parallel b$ when spins

are fully polarized in field as $W_\mathrm{b} = 2.2\ \mu_\mathrm{B}$T. Integrating M_b from 0 T to 7 T at 2 K yields $W_\mathrm{b,exp} = 2.26\ \mu_\mathrm{B}$T, which is in good agreement with the calculations and indicates that the spins are nearly fully polarized at 7 T. An overview of the theoretical and experimental results is given in Tab. 4.4.

Table 4.4: Experimental results from magnetization measurements in comparison to the theoretical results by Nikolaev et al. [111].

	$\partial M_\mathrm{a}/\partial B$ (μ_B/T)	$\partial M_\mathrm{b}/\partial B$ (μ_B/T)	$\partial M_\mathrm{c}/\partial B$ (μ_B/T)	$\mathrm{W_b}$ (μ_BT)
This work	0.045(3)	0.089(3)	0.009(2)	2.26
LDA+SO [111]	0.15	-	0.0073	-
Hartree Fock [111]	0.044	-	0.0061	2.2

The isothermal magnetization for all axes and at various temperatures is shown in Fig. 4.18. For $B \parallel a$ no sign of a phase transition is seen at low temperatures (Fig. 4.18(a) and (b)). Only at 20 K and 25 K a peak in the susceptibility is observed. For $B \parallel b$, at 2 K a clear kink is visible in the magnetization at 7.1 T (Fig. 4.18(c) and (d)) analogous to the behavior predicted [15] and observed [114] in $Cu_3Bi(SeO_3)_2O_2Br$. At higher temperatures this peak shifts to lower fields while retaining its characteristic shape. The features for $B \parallel c$ (Fig. 4.18(e) and (f)) were discussed in detail before and are not mentioned further here.

The static magnetic susceptibility at B = 1 T visualizes the strong anisotropy for the three axes once more (Fig. 4.17(b)). The evolution of the phase transition in χ_i and $\partial(\chi_i T)/\partial T$ in fields up to 14 T (1 T for $B \parallel c$) for the different axes is presented in Fig. 4.19. Measurements up to 6 T for the *a*- and 7 T for the *b*-axis were performed in an MPMS3 on a very small crystal ($m = 0.60(5)$ mg, thus with a large error bar), and measurements up to 14 T in a PPMS-14 (sample with $m = 8.88(5)$ mg). While the *a*-axis shows only minor shifts with increasing field (26.3 K at 1 T to 20.0 K at 14 T), the *b*-axis shows a strong suppression in field, to 7.7 K at 7 T, with no transition visible at higher fields.

With this knowledge on the in-plane magnetization, a small feature observed in the magnetostriction of CBSCl stands out (Fig. 4.20). While the large peaks related to the metamagnetic transition are very prominent, a small additional anomaly in λ_b is visible at slightly higher fields. The position of this feature corresponds exactly to the peaks in the *b*-axis susceptibility $\partial M/\partial B$. Therefore, the transition towards saturation is visible in the magnetostriction data for $B \parallel b$, but along with a much larger peak from triggering the metamagnetic transition while measuring along *b* due to a small effective magnetic field along *c*.

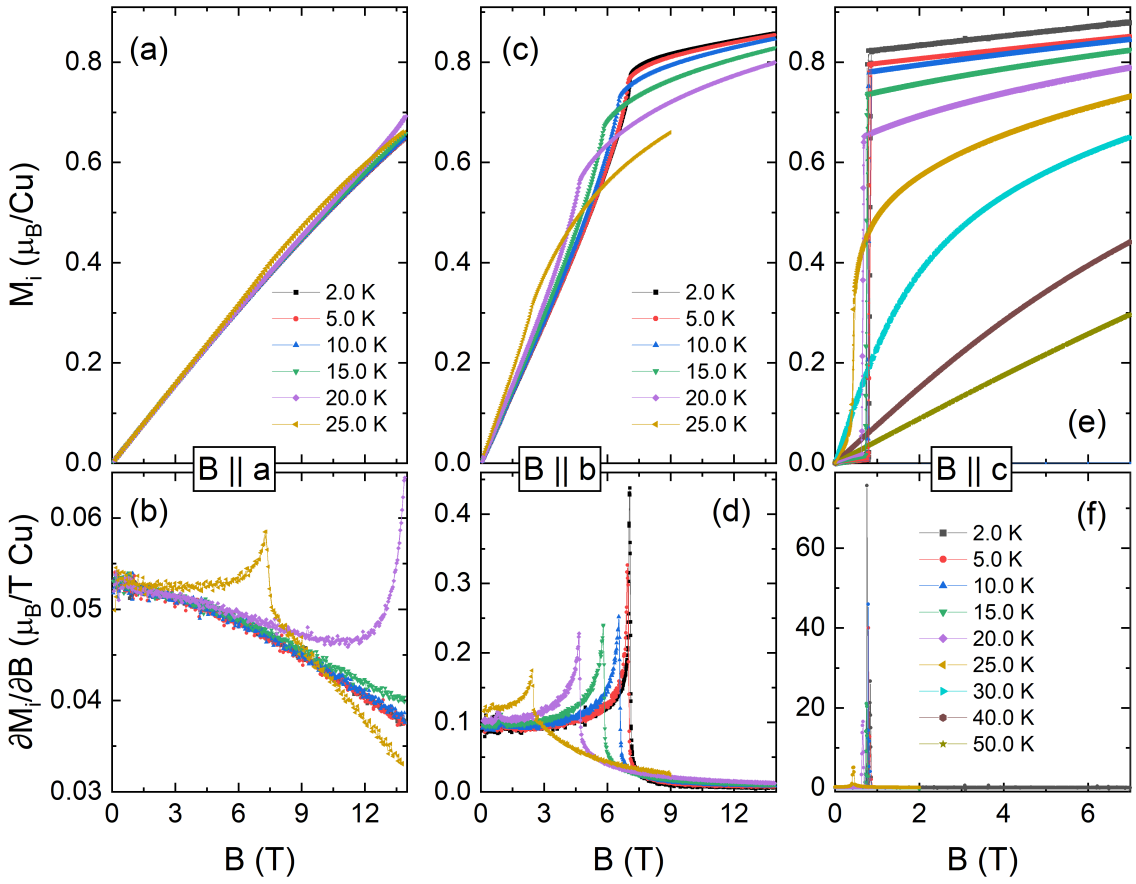

Figure 4.18: Isothermal magnetization and magnetic susceptibility $\partial M_i/\partial B$ at low temperatures for (a, b) $B \parallel a$, (c, d) $B \parallel b$ and (e, f) $B \parallel c$.

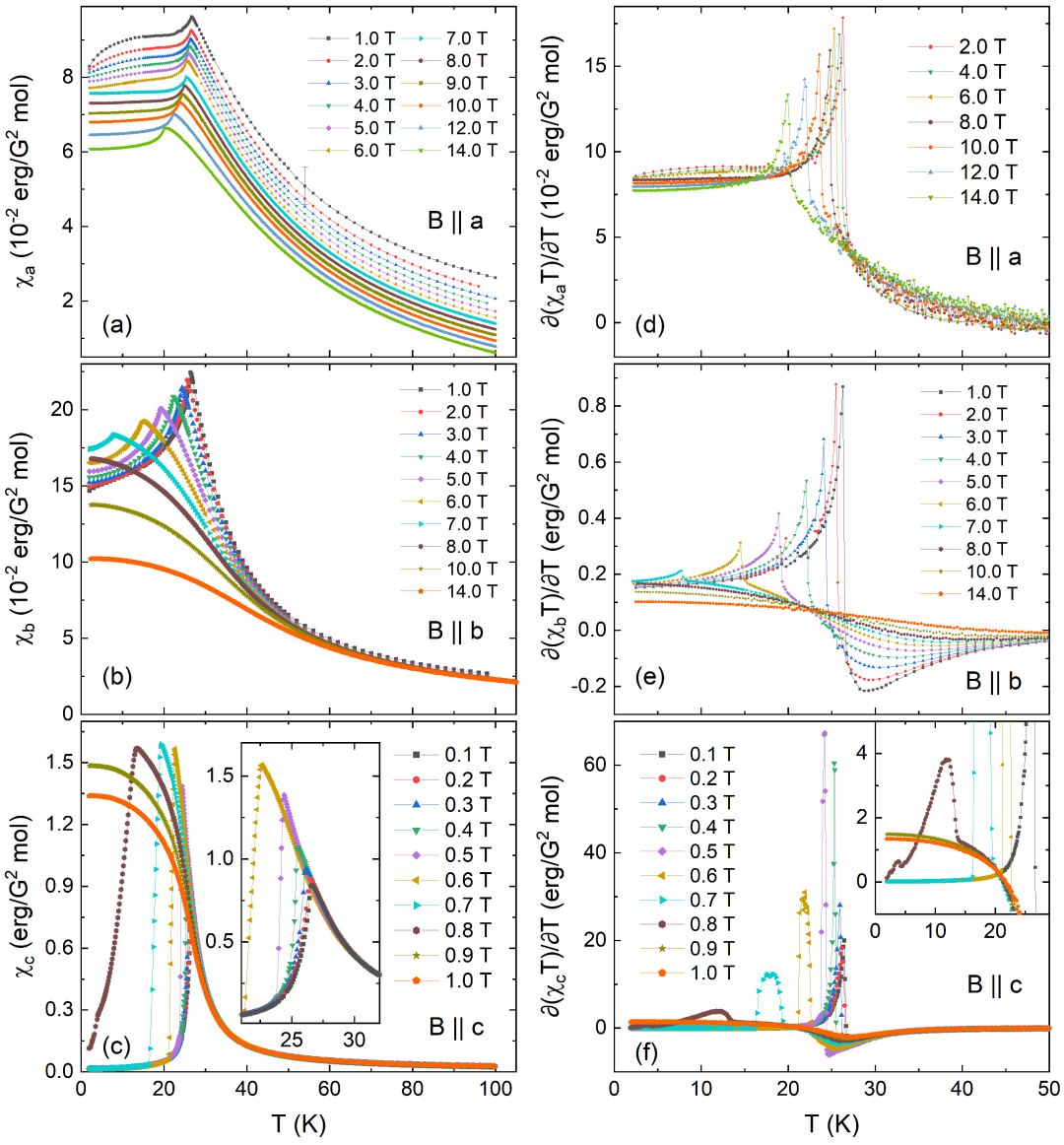

Figure 4.19: Static magnetic susceptibility $\chi = M/H$ and derived Fisher's specific heat in magnetic fields up to 14 T for $B \parallel a$ (a, d), $B \parallel b$ (b, e), and $B \parallel c$ (c, f). Data up to 6 T in (a, d) and up to 7 T (b, e) were measured in the MPMS3, data at higher fields up to 14 T in the PPMS. The inset in (c) shows a magnification for fields up to 0.6 T around T_N. The inset in (f) shows a magnification of the low temperature region. Data in (a) are offset by $-1.5 \cdot 10^{-3}$ erg/(G^2 mol).

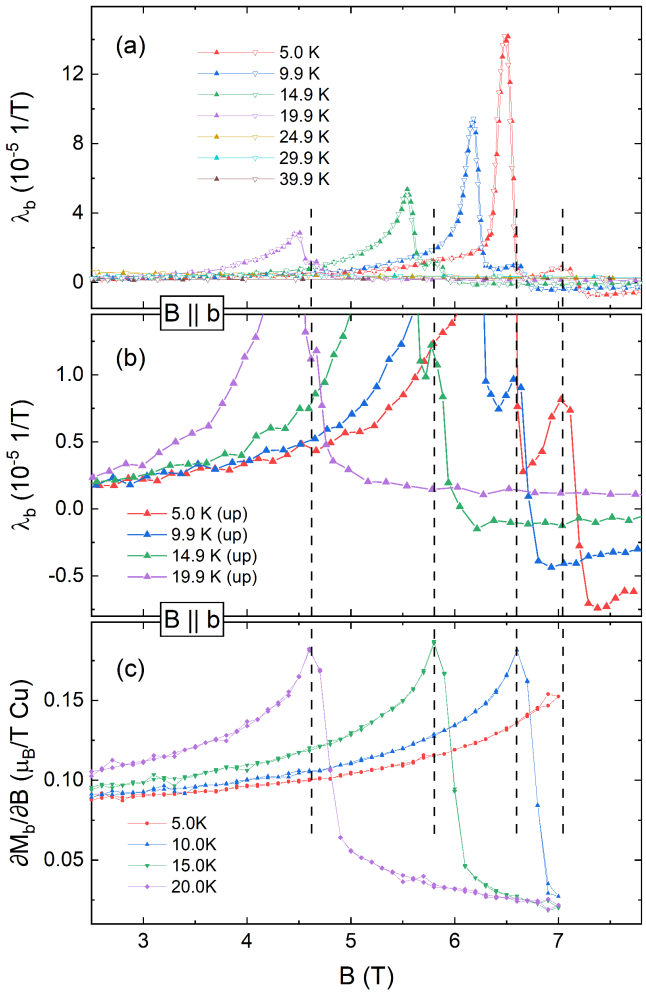

Figure 4.20: Comparison of magnetostriction coefficient λ_b (a, c) and isothermal magnetic susceptibility $\partial M/\partial B$ (b) for $B \parallel b$. Vertical lines in (b) and (c) mark the critical fields observed in both quantities.

4.3.4 Phase Diagrams

From the in-plane magnetization measurements the low temperature phase diagrams for the a- and b-axis are constructed and presented in Fig. 4.21. The b-axis shows a transition from the antiferromagnetic (AFM) phase to the field-polarized phase at $B_{c,b} = 7.1(2)$ T, and an extrapolation of the a-axis data, by simply stretching the b-axis phase boundary along the magnetic field axis, yields $B_{c,a} = 20.6(5)$ T. Calculations of the magnetization process in CBSCl yielded saturation fields of 5.8 T ($B \parallel b$) and 17 T ($B \parallel a$), which are both lower than the experimentally observed fields, but close to them [111]. In comparison, the brother compound $Cu_3Bi(SeO_3)_2O_2Br$ shows a saturation along the b-axis at a similar field, about 7 T, whereas $B_{c,a}$ is nearly 40% higher than the value of 15 T in CBSBr which was also obtained by extrapolation [114].

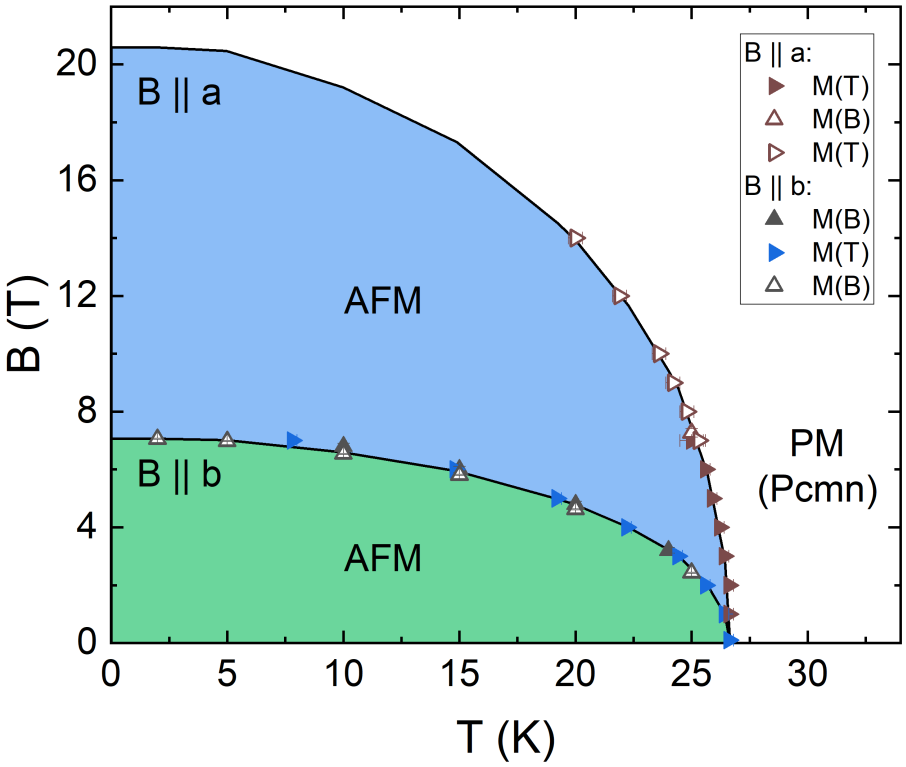

Figure 4.21: Low-temperature magnetic phase diagram for $B \parallel a$ (blue area) and $B \parallel b$ (green area) constructed from magnetization measurements. Closed (open) markers refer to measurements in the MMPS (PPMS). Extrapolation: The blue area is obtained by scaling the green area along the y-axis to match the markers for $B \parallel a$ up to 14 T.

The c-axis phase diagram in Fig. 4.22 is constructed from the peaks, and left and right flanks where the mixed phase sets in, in α_c and λ_c as well as peaks in the susceptibility

in field and temperature. The points marking the crossover between the field-induced FM and PM phases are extracted from the minimum in $\partial\chi_c/\partial T$. Qualitatively, this phase diagram is identical to the CBSBr phase diagram for $B \parallel c$ [113], however, the critical field is slightly higher and T_N lower compared to $Cu_3Bi(SeO_3)_2O_2Br$ ($T_N = 27.4$ K).

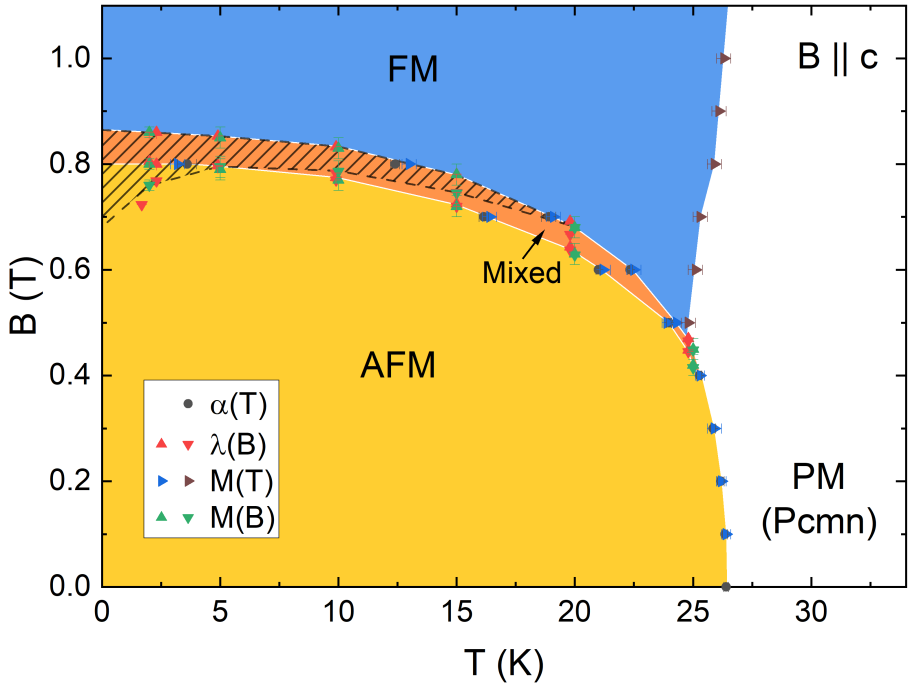

Figure 4.22: Low-temperature magnetic phase diagram in fields up to 1 T for $B \parallel c$ constructed from magnetization and dilatometric measurements as indicated in the legend and mentioned in the text. The shaded region displays the hysteresis visible in magnetization and magnetostriction down-sweeps, with the dashed lines indicating down-sweep phase boundaries. Where hysteresis and the mixed phase overlap, white lines indicate phase boundaries obtained from up-sweep data.

4.4 Conclusion

The multiferroic buckled-Kagomé francisite $Cu_3Bi(SeO_3)_2O_2Cl$ is investigated by thermal expansion, magnetostriction, magnetization and specific heat measurements. Strong fluctuations persist in a large temperature range below the structural phase transition at $T_S = 120.7(5)$ K, with critical exponents of $2\beta_c = 0.71(2)$ at T_S for the a- and c-axis as well as 0.77(2) for the b-axis. Large uniaxial pressure dependencies are found for T_S, in contrast to a moderate hydrostatic pressure dependence of $dT/dp = 2.3(1.5)$ K/GPa. The spontaneous strain around the antiferromagnetic transition at $T_N = 26.4$ K, with critical exponents of $\beta_c = 0.35(4)$ (b- and c-axis) and $\beta_c = 0.38(3)$ (a-axis), is in the range of the 3D XY and 3D Heisenberg models and suggests a 3D magnetic ordering. The c-axis was studied in detail below T_N. A field-induced mixed phase behavior above 0.4 T was uncovered, analogous to the related francisite $Cu_3Bi(SeO_3)_2O_2Br$. In this mixed phase, linear magnetoelastic coupling is present for $B \parallel c$. Uniaxial and hydrostatic pressure dependencies of T_N are small, ranging from $-0.62(15)$ K/GPa for $p \parallel b$ and 0.33(10) K/GPa for $p \parallel c$ to 1.8 K/GPa for $p \parallel a$, with a hydrostatic pressure dependence $dT_N/dp = 1.4(3)$ K/GPa. The pressure dependence of the critical field, as well as the change in entropy at the antiferromagnetic (AFM) to ferromagnetic/paramagnetic phase boundary, are derived using thermodynamic relations, revealing a stabilization of the AFM phase under applied pressure $p \parallel c$. For the a- and b-axis the phase diagram is derived from magnetization measurements, with critical fields of $B_{c,a} = 20.6$ T (obtained by extrapolation) and $B_{c,b} = 7.1$. The c-axis phase diagram is constructed from the thermal expansion, magnetostriction and magnetization data, showing a critical field of $B_{c,c} = 0.8$ T at 2 K.

Many aspects of the physics of $Cu_3Bi(SeO_3)_2O_2Cl$ are well understood, including theoretical models for the relevant magnetic interactions. This study adds a thermodynamic analysis, especially of the effects of uniaxial pressure, the magnetic phase diagrams of the a- and b-axis, and a detailed high-resolution study of lattice changes with temperature and especially in applied magnetic fields, which to this point were missing.

Chapter 5

Dilatometric Studies of the Ferromagnetic Semiconducting Van der Waals Compound $Cr_2Ge_2Te_6$

In this chapter the experimental results on $Cr_2Ge_2Te_6$ are presented and discussed. An introduction on $Cr_2Ge_2Te_6$ is followed by a note on experimental details and especially the necessary signal corrections. Then the experimental results are presented along with their discussion, before a conclusion sums up the insights gained in this chapter. The presentation of results is divided into three main sections. The main focus of the first – and by far largest – section is on data obtained from thermal expansion, complemented by specific heat data where needed for the thermodynamic analysis. Zero-field thermal expansion is presented first, followed by a brief paragraph describing the effect of an applied magnetic field of 15 T. The following subsection discusses the Grüneisen parameters of the zero-field data, from which the uniaxial pressure dependence of the critical temperature is derived. Subsequently, magnetic contributions to the thermal expansion coefficient in an applied magnetic field are discussed, followed by a critical scaling analysis of both the thermal expansion coefficient and of the strain resulting from the magnetic contribution to the thermal expansion. In the second section magnetostriction measurements are presented in conjunction with isothermal magnetization data. From these results the uniaxial pressure dependence of the magnetization in $Cr_2Ge_2Te_6$ is derived. The final section contains the phase diagrams for the measured directions.

5.1 Introduction

In early 2017, long-range magnetic order in pristine 2D crystals – down to the bilayer in $Cr_2Ge_2Te_6$ [20] and the monolayer in CrI_3 [135] – was first observed. Research into two-dimensional (2D) materials had already been rapidly growing after the first production of single-layer graphene [136]. This ground-breaking discovery further spurred research into quasi-2D layered van der Waals (vdW) materials. Previously, extrinsically-induced magnetic responses had been studied in thin films, whereas the new magnetic 2D materials offer the advantages that they decouple from

substrates, allow electrical control, are mechanically flexible, and open to chemical functionalization [25]. Quasi-2D layered vdW materials are interesting both from a fundamental point of view and from an applications perspective: on the fundamental side, they open up the opportunity to study ground states, fundamental excitations and magnon dynamics in 2D magnets [25]; on the applications side, new roads to sensing, computing, and data storage can be envisioned with atomically thin magneto-optical and magnetoelectric devices for ultracompact spintronics or on-chip optical communications. Recent examples of steps towards $Cr_2Ge_2Te_6$-based applications include the realization of a $Cr_2Ge_2Te_6$-based phase-change random access memory (PCRAM) [137] and efficient switching of the magnetization by spin-orbit torque as a step towards spintronic devices [138].

$Cr_2Ge_2Te_6$ crystallizes in the trigonal space group $R\bar{3}$ (No. 148) and belongs to the class of layered van der Waals (vdW) transition metal trichalcogenides (TMTC). The edge-sharing transition metal chalcogenide octahedra form a honeycomb network (indicated in red in Fig. 5.1(b)). These honeycomb layers are stacked onto each other in an ABC-stacking with a van der Waals (vdW) gap along the crystallographic c-axis (Fig. 5.1(a) and (b)) [139]. In its bulk form $Cr_2Ge_2Te_6$ is a quasi-2D ferromagnetic semiconductor, with T_C= 65 K [140, 141], and has been shown to retain its ferromagnetic property at least down to the bilayer [20]. This key feature of low-dimensional magnetism at non-zero temperature arises from the presence of a magnetic anisotropy, circumventing the effects of the Mermin-Wagner theorem [18] which forbids long-range order at non-zero temperatures for isotropic spins in low dimensions ($D \leq 2$) due to gapless magnonic fluctuations. Anisotropy leads to the opening of a gap in the magnon density of states and thus allows for static long-range order to form. At zero external pressure $Cr_2Ge_2Te_6$ shows a uniaxial magnetic anisotropy with the magnetic easy-axis along the crystallographic c-axis [21, 140, 141]. This anisotropy is presumably caused by spin-orbit coupling of the Cr ions in connection to the underlying crystallographic lattice as well as off-site spin-orbit coupling effects between Cr and Te ions [22, 141].

Furthermore, $Cr_2Ge_2Te_6$ shows an anisotropic temperature dependence of the lattice as shown by Carteaux et al. [139]. Down to 100 K the lattice parameters a and c shrink monotonously. However, around 100 K the a-axis starts to increase towards lower temperatures while the c-axis shrinks further. The increase of the a-parameter leads to a value of 6.820 Å at 5 K which is larger than 6.812 Å at 270 K. This indicates that $Cr_2Ge_2Te_6$ has a strong magnetostriction effect, i.e., a coupling between the onset of ferromagnetic interactions and the anisotropic behavior of the underlying lattice. So far, no detailed thermal expansion and magnetostriction studies have been reported for $Cr_2Ge_2Te_6$ to explore the magnetoelastic coupling, which motivates the high-resolution thermal expansion and magnetostriction measurements in this chapter.

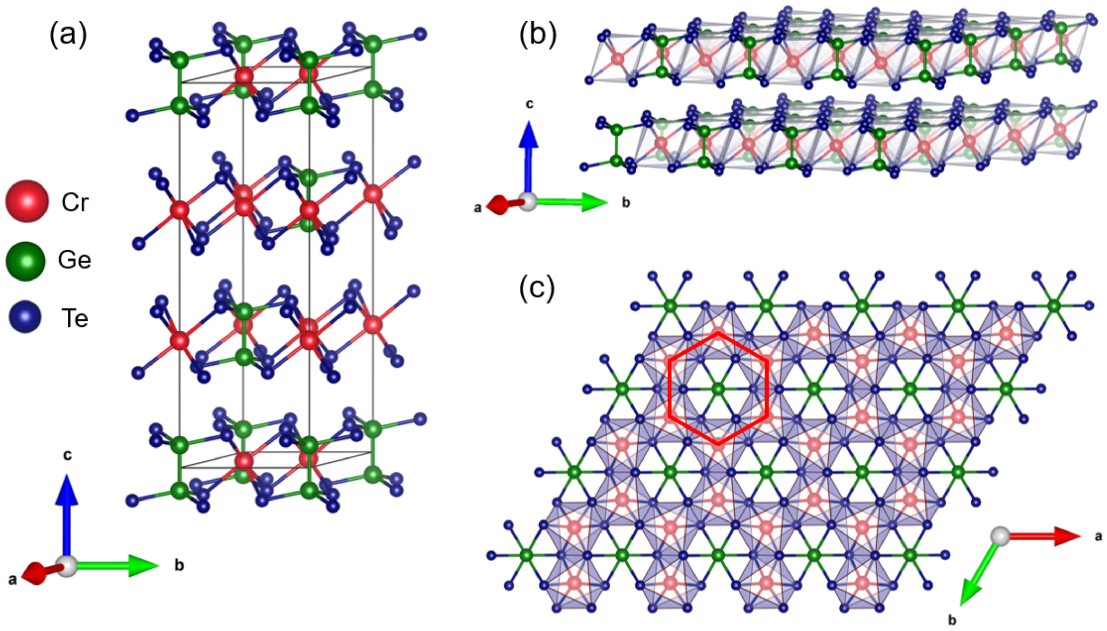

Figure 5.1: Crystal structure of $Cr_2Ge_2Te_6$ in the space group $R\bar{3}$ (no. 148) as reported in Ref. [139]. (a) Unit cell of $Cr_2Ge_2Te_6$. (b) Van der Waals layers and stacking along the c-axis with Cr octahedra shown. (c) View onto the ab-plane with the honeycomb network indicated by the red hexagon.

5.2 Experimental Details

Single crystals of $Cr_2Ge_2Te_6$ were grown by the self-flux technique by Dr. Aswartham in Dresden at the Leibniz Institute for Solid State and Materials Research and were characterized in detail as reported in Refs. [140, 141]. The crystals measured in this study had a length of 0.255 mm along the c-axis (see Fig. 5.2(c)) and 1.292 mm along the in-plane direction, respectively. For zero-field measurements the mini-dilatometer was used, whereas measurements in zero-field and an applied magnetic field were performed in the standard dilatometer. Uniaxial relative length changes $dL_i(T)/L_i$ and the linear thermal expansion coefficients $\alpha_i = 1/L_i \cdot dL_i(T)/dT$ were studied at temperatures between 2 K and 300 K in magnetic fields up to 15 T. Magnetic fields were applied along the direction of the measured length changes $i = c, \perp c$, i.e., along the in-plane and cross-plane directions. In addition, the field-induced length changes $dL_i(B_i)$ were measured at various fixed temperatures between 2 K and 204 K in magnetic fields up to 15 T. The longitudinal magnetostriction coefficient $\lambda_i(B,T) = 1/L_i(0,T) \cdot dL_i(B_i)/dB_i$ was derived from $dL_i(B_i)$ at different fixed temperatures. Measurements of the isothermal magnetization were performed on a thin sample with a dimensions of $2.0 \times 1.3 \times 0.235$ mm^3 and a mass of $m = 3.27(5)$ mg. The measured magnetization was corrected for the demagnetizing

field using demagnetization factors of $N = 0.746$ for $B \parallel c$ and $N = 0.099$ for $B \perp c$ (Fig. 5.2(a) and (b)). Further correction factors due to the sample geometry were obtained based on the experimental data of a square nickel film [142]. To extract correction factors for the side lengths of 2.0 mm and 1.3 mm a square of equal area with a side length of 1.65 mm was assumed. For measurements with $B \parallel c$, along the thin direction, power-law fits to the data provided in Ref. [142] for vibration amplitudes of 1.0 mm to 5.0 mm yielded the correction factor f at 1.65 mm at different amplitudes. A linear interpolation of these data points resulted in $f = 1.086$ for the amplitude of 1.8 mm at which all measurements were performed. For a vertical alignment of the sample, with $L = 1.3$ mm and $B \perp c$, third-order polynomial fits were applied to extract f at different vibration amplitudes. A linear interpolation of the resulting values for the different amplitudes yielded $f = 1.061$ for an amplitude of 1.8 mm. The effect of the corrections is shown in Fig. 5.2(d).

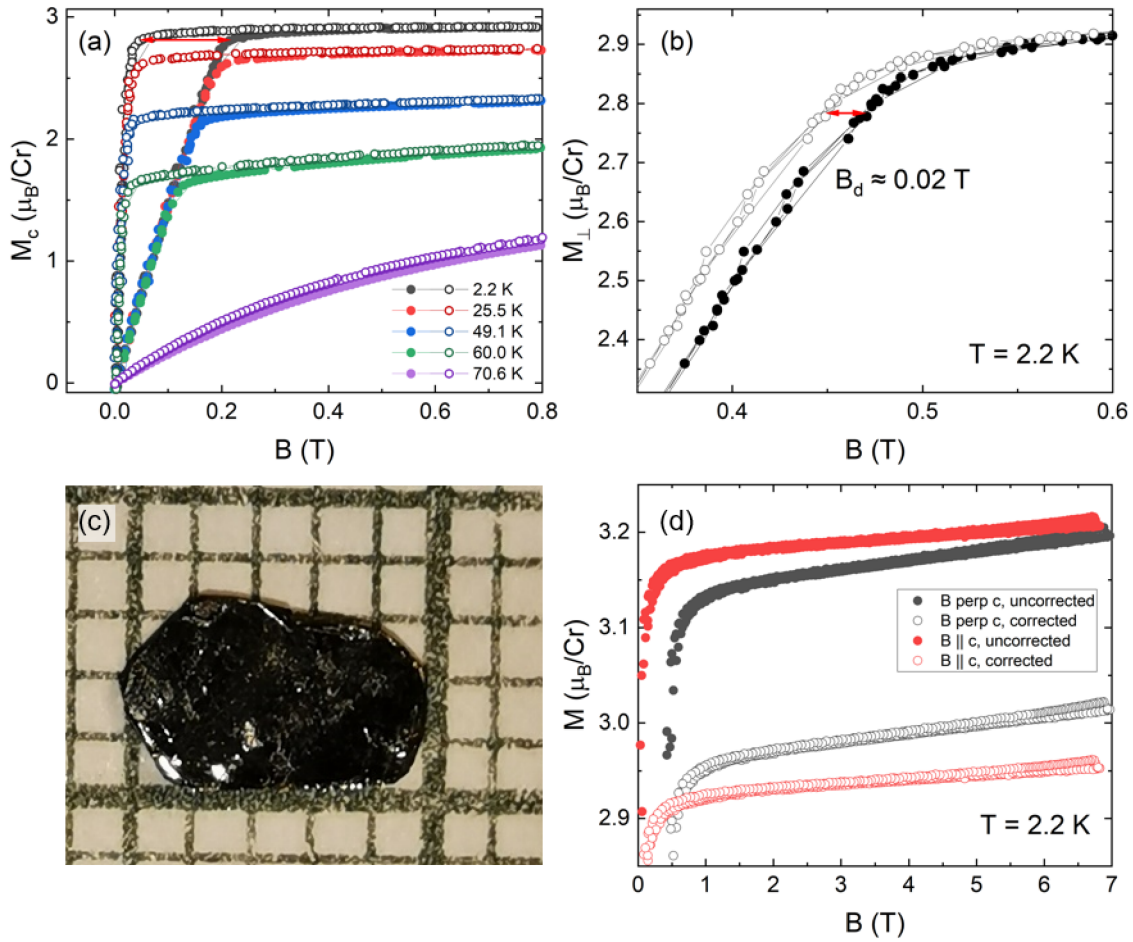

Figure 5.2: (a, b) Demagnetization factor correction with (a) $N = 0.746$ for $B \parallel c$ and (b) $N = 0.099$ for $B \perp c$. Red horizontal arrows give an impression of the demagnetization field. (c) $Cr_2Ge_2Te_6$ sample used for the c-axis thermal expansion measurements in the Standard-dilatometer. (d) Example for the effect of the magnetization correction due to sample geometry. Closed (open) symbols mark the uncorrected (corrected) data in (a), (b) and (d).

5.3 Results and Discussion

5.3.1 Thermal Expansion

Zero-field

Thermal expansion measurements shown in Fig. 5.3 display strong magnetoelastic coupling in $Cr_2Ge_2Te_6$. In zero magnetic field, the onset of long-range ferromagnetic order is associated with pronounced kinks in dL_i/L_i, $i = c, \perp c$, and corresponding peaks in the thermal expansion coefficients at $T_C = 64.7(4)$ K (in-plane) and

$T_C = 65.3(4)$ K (c-axis). The origin of this difference is discussed below after the calculation of the uniaxial pressure dependence for the two axes. While the anomalies evidence a continuous phase transition, their signs imply opposite pressure dependence for uniaxial pressure applied in-plane ($\perp c$) and cross-plane ($\parallel c$), respectively. Note that the anomalies extend from the lowest temperatures up to at least 100 K. This is associated with negative in-plane thermal expansion up to nearly 95 K while α_c is positive in the whole temperature regime under study. Note further, however, that due to the softness of the samples in-plane length changes were difficult to measure and hence possess larger errors than cross-plane data. In particular, different mounting of the sample yielded a smaller anomaly in $\alpha_\perp$ while negative thermal expansion extended to around 70 K only. Negative thermal expansion up to 95 K, however, fits very well with the observations of Carteaux et al. mentioned in the introduction, who found an increase in the a-axis lattice parameter, i.e., in-plane, below 100 K [139].

High-Field Behavior at $B = 15\ T$

Applying an external magnetic field of 15 T yields two distinct field-induced effects on the length changes up to at least 200 K as shown by Fig. 5.3 (red lines and symbols). The data in (a) are shifted vertically to coincide at highest temperatures, exposing a field effect at 15 T which starts between 210 K and 250 K. Vertical lines in Fig. 5.3 display experimentally determined magnetostriction $(L(15T) - L(0))/L(0)$ at various temperatures, thereby confirming the magnetic field effect. A field effect up to high temperatures is seen especially well in the thermal expansion coefficient in Fig. 5.3(b). The deviation between the 0 T and 15 T data following their overlap at high temperatures marks its onset. Besides, the peak in the thermal expansion coefficients shifts to higher temperatures with applied field for both directions, to 90 K for $B \perp c$ and 103 K for $B \parallel c$, and broadens substantially. For $B \parallel c$, the data imply shrinking of the c-axis for 30 K $\lesssim T \lesssim$ 210 K in an applied field of 15 T with respect to zero-field, while magnetostriction is very small outside this temperature regime. In contrast, magnetostriction is positive for $B \perp c$ but changes sign at $\sim$ 37 K (see inset of Fig. 5.3a).

Grüneisen Scaling and High-Temperature Correlations at $B = 0$

In order to estimate non-phononic contributions to the thermal expansion of $Cr_2Ge_2Te_6$, the high temperature regime is fitted by means of a Debye approximation

$$\begin{aligned} \alpha_{ph} &= \gamma \cdot c_{ph}^{D}(T) \\ &= \gamma \cdot 9 \cdot n_D \cdot k_B \left(\frac{T}{\Theta_D}\right)^3 \cdot \int_0^{\Theta_D/T} \frac{x^4 e^x}{(e^x - 1)^2} dx \end{aligned} \tag{5.1}$$

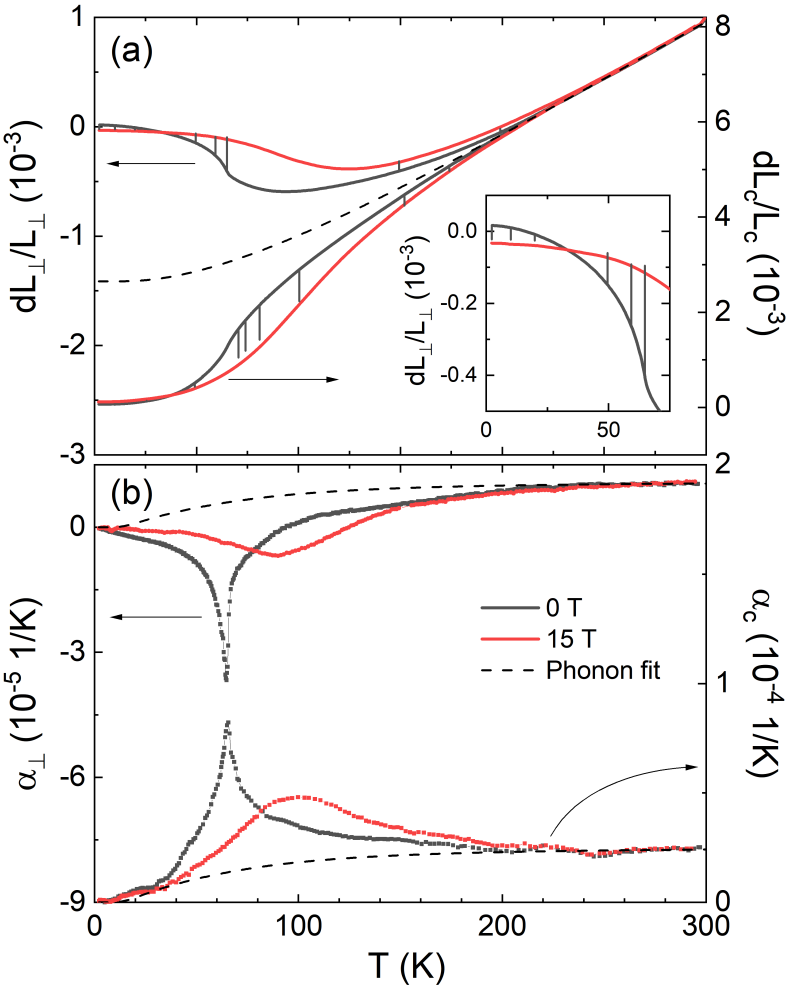

Figure 5.3: (a) Relative length changes in zero-field and at $B = 15$ T for $B \perp c$ (left axis) and $B \parallel c$ (right axis) and (b) corresponding thermal expansion coefficients. Dashed lines show the estimated phonon background (see the text). For (a), ordinates have been scaled to obtain good overlap of both zero field data and phonon background above 220 K. 15-Tesla data have been shifted with respect to the measured magnetostriction at 150 K ($B \parallel c$) and to overlap at high temperatures ($B \perp c$). Vertical lines indicate the length changes between 0 T and 15 T obtained from magnetostriction measurements at selected temperatures. Inset in (a) highlights the low-temperature behavior of $dL_\perp(T)$

where γ is an effective Grüneisen parameter on the order of 10^{-7} used to scale the phonon specific heat c_{ph}^{D} to the thermal expansion, n_D is the number of atoms in the unit cell, k_B the Boltzmann constant and Θ_D the Debye temperature. A fit of the specific heat yields a Debye temperature of $\Theta_D = 241$ K and $n_D = 9.85$ which is very close to 10, as expected for the 10 atoms in the unit cell. The resulting thermal expansion backgrounds using $\gamma_c \approx 1.0 \cdot 10^{-7}$ and $\gamma_\perp \approx 4.5 \cdot 10^{-8}$ are shown as dashed lines in Fig. 5.3. In Fig. 5.4 the specific heat with the phononic background fit is presented along with the specific heat of $In_2Ge_2Te_6$ (blue circles). The latter lies both above (low temperatures) and below (high temperatures) the specific heat of $Cr_2Ge_2Te_6$. A scaling of the data with the ratio of In and Cr masses did not resolve the problem, therefore the Debye background fit was preferred to the non-magnetic analog for background subtraction.

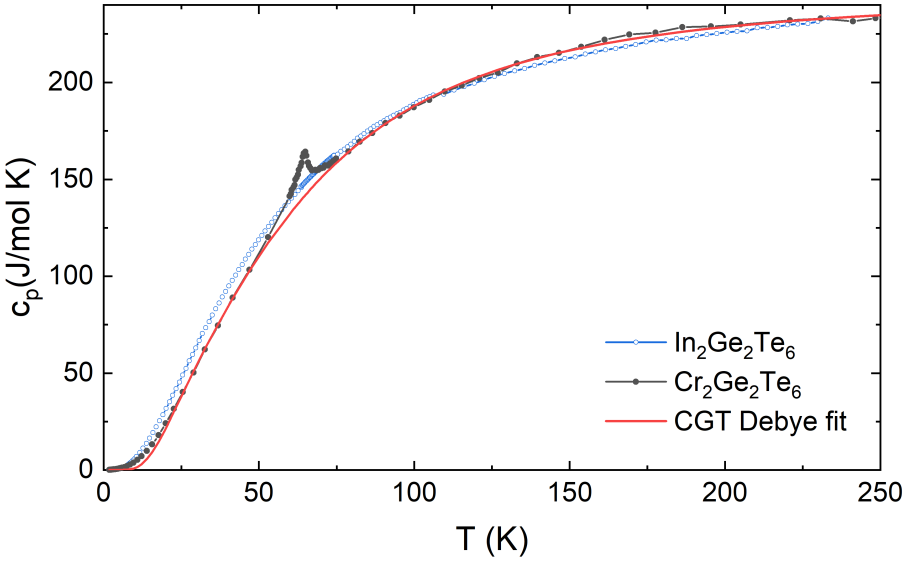

Figure 5.4: Specific heat of $Cr_2Ge_2Te_6$ (black circles) and $In_2Ge_2Te_6$ (blue circles) [143] as well the Debye background fit (red line) as described in the text.

The data in Fig. 5.3 (dashed lines) show that above roughly 220 K thermal expansion is described well by the phonon background. Upon cooling non-phononic thermal expansion evolves, which is anisotropic in nature. This non-phonon behavior is attributed to magnetic degrees of freedom. Note that the associated entropy changes are very small at high temperatures so that a reliable estimate of magnetic entropy changes is impossible. Lin et al. did publish a magnetic specific heat of $Cr_2Ge_2Te_6$ [144], but the background function they subtracted to obtain it is highly disputable. The Grüneisen ratio $\gamma_i = \alpha_i / c_p$ in Fig. 5.5, however, confirms the presence of an additional degree of freedom below about 220 K as also evidenced by anisotropy in α_i. Specifically, while an approximately constant $\gamma(T)$ at high

temperatures implies the presence of only one dominant, phonon, energy scale [83, 84], the progressive evolution of a competing degree of freedom, i.e., that of magnetic fluctuations, is clearly confirmed by the data.

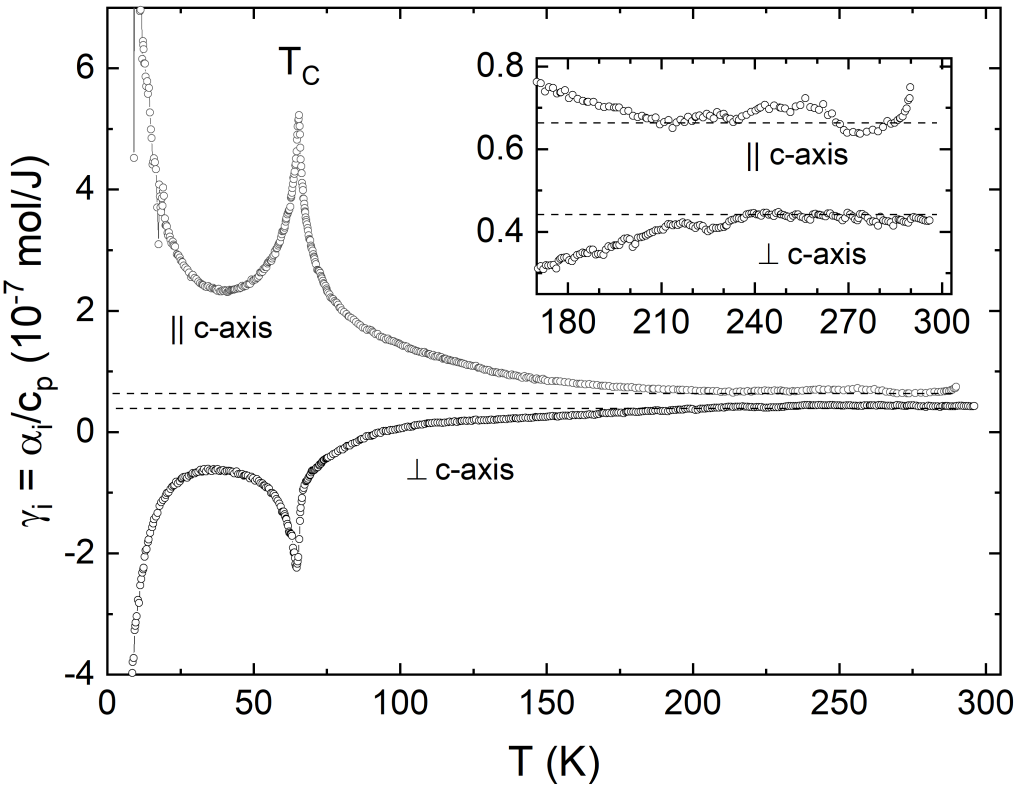

Figure 5.5: Ratio of thermal expansion coefficients and specific heat $\gamma_i = \alpha_i/c_p$, with zero-field thermal expansion data from the mini-dilatometer (see appendix, Fig. C.1). Inset: High-temperature behavior. Dashed lines are guide to the eye.

Magnetic correlations up to high temperature are a key feature in $Cr_2Ge_2Te_6$ and the isostructural compound $Cr_2Si_2Te_6$. Most importantly, these features imply the presence of 2D correlations up to high temperatures. For $Cr_2Ge_2Te_6$ correlations up to 160 K were deduced by Sun et al. from the deviation of a Curie-Weiss fit to the static magnetic susceptibility and a concomitant broadening of the X-band electron spin resonance (ESR) intensity for both in-plane and cross-plane crystal directions [145]. Such deviations from a purely paramagnetic behavior in X-band ESR spectra at least up to 100 K were also noted by Zeisner et al. [140] (Fig. 5.15). Additionally, angle-resolved photoemission spectroscopy (ARPES) spectra of $Cr_2Ge_2Te_6$ at 150 K, at more than two times T_C, were better described by calculations for the ferromagnetic state than for the paramagnetic state [146]. The magnetic fluctuations seen in the Grüneisen ratio therefore provide the first macroscopic measurement of high temperature correlations and the related quasi-2D behavior in $Cr_2Ge_2Te_6$.

Similar van der Waals compounds, such as the ferromagnetic (FM) and antiferromagnetic (AFM) semiconductors $Cr_2Si_2Te_6$ (FM), $MnPSe_3$ (AFM), and $MnPS_3$ (AFM), also show characteristic short-range correlations up to high temperatures [147, 148]. For $Cr_2Si_2Te_6$ static and dynamic in-plane magnetic correlations were observed in neutron diffraction and inelastic neutron scattering experiments at least up to 300 K [147], similarly to $MnPSe_3$ and $MnPS_3$ where magnetic excitations were visible up to 200 K, the highest measured temperatures [148]. Such high-temperature behavior was repeatedly interpreted as pointing to low-dimensional exchange interactions with the presence of in-plane correlations to high temperatures [147, 148].

Grüneisen analysis allows not only a qualitative but also a quantitative analysis. A reliable quantitative analysis of the thermal expansion and specific heat data is possible due to the large size of the anomalies. Therefore, the Debye background obtained above is subtracted from the thermal expansion and specific heat, respectively. For the thermal expansion it is scaled to the high-temperature regime of $\alpha_\perp$ and α_c. The resulting magnetic contributions are plotted together such that the peaks around T_C have a maximal overlap. From the ratio of the ordinates in Fig. 5.6 the magnetic Grüneisen ratio $\gamma_{i,\mathrm{mag}} = \alpha_{mag}/c_{p,mag}$ is obtained. This yields $\gamma_{c,\mathrm{mag}} \approx 2.3$ mol/MJ and $\gamma_{\perp,\mathrm{mag}} \approx -1.4$ mol/MJ in the regime of 10 K around the ferromagnetic transition. Using the Ehrenfest relation, the obtained values of γ_i yield the uniaxial pressure

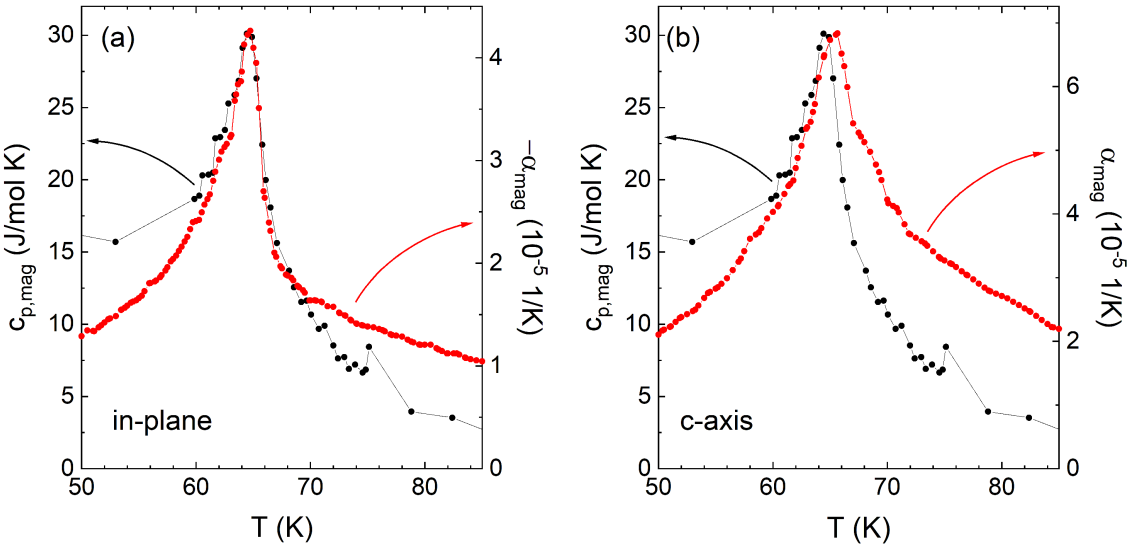

Figure 5.6: Comparison of $\alpha_{i,\mathrm{mag}}$ (red symbols) and $c_{p,\mathrm{mag}}$ (black symbols) at B = 0 T for the in-plane direction (a) and the c-axis (b) yielding the Grüneisen parameters $\gamma_\perp = 1.4$ mol/MJ and $\gamma_c = 2.3$ mol/MJ.

dependence of the ordering temperatures, i.e., $\partial T_C/\partial p_i = T_C V_m \gamma_{i,\mathrm{mag}}$. The results deduced using the molar volume $V_m = 5 \cdot 10^{-4}$ m^3/mol are $\partial T_C/\partial p_c = 74(10)$ K/GPa and $\partial T_C/\partial p_\perp = -45(10)$ K/GPa. The hydrostatic pressure dependence can be

inferred as $dT_C/dp = 2 \cdot \partial T_C/\partial p_\perp + \partial T_C/\partial p_c = -16$ K/GPa. Notably, the behavior for $\alpha_{c,mag}$ and $\alpha_{\perp c,mag}$ is very different around T_C (Fig. 5.6): while $\alpha_{c,mag}$ shows a rather symmetric behavior around T_C, $\alpha_{\perp c,mag}$ and $c_{p,mag}$ show an asymmetric behavior. This difference may be related to the pressure applied perpendicular to the van der Waals gap for α_c, which is absent for $\alpha_{\perp c}$ and c_p. The forces employed by the setup unto the sample are on the order of 0.2(1) N for the in-plane measurements and 0.8(2) N for measurements along the c-axis. With surface areas of few mm^2 for the c-axis and few tenths of a mm^2 for the in-plane measurements, this leads to pressures on the order of hundreds of kPa (c-axis) to few MPa ($\perp c$) applied onto the sample surfaces. Considering the pressure dependence calculated above, this would lead to shifts in T_C up to 0.1 K at most, i.e., it cannot account for the difference of about 0.6 K of T_C for the two measured directions. A small thermal gradient is an alternative possible explanation for the difference in T_C, i.e., cross-plane thermal conductivity along c would need to be lower than the in-plane, $\perp c$, thermal conductivity, which has been observed in van-der-Waals compounds before [149–151]. However, the difference in T_C may also simply arise from the use of two different samples with different thickness and slightly different stacking defects.

The effects of pressure on $Cr_2Ge_2Te_6$ have been investigated in several publications, both experimentally and based on calculations [152–154]. In all of these works the effect of hydrostatic pressure was studied, and a decrease in T_C with applied pressure was unambiguously identified. Also, the resulting behavior was explained by the decrease of Cr–Cr and Cr–Te bond lengths and an increase in Cr–Te–Cr bond angle away from 90° [153].

The numbers derived above describe the initial pressure dependence, i.e., for $p \to 0$, and should thus be compared to the initial pressure dependence in other measurements. Both Sun et al. [152] and Fumega et al. [154] observed an initial drop of T_C of -14 K/GPa, in the range from 0 GPa to 0.25 GPa, and from 0 GPa to 0.1 GPa, respectively. This corresponds well to $dT/dp = -16$ K/GPa derived from thermal expansion and specific heat above. Sakurai et al. found a hydrostatic pressure dependence of -3.8 K/GPa [153], but from only two data points in a much larger pressure range, from 0 GPa to 1.3 GPa. This cannot resolve the initial steeper drop in T_C observed in the other reports. However, it is in line with ≈ -4 K/GPa between two data points at 0 GPa and 1 GPa found in one of the other reports [154]. Fumega et al. also investigated the effect of hydrostatic pressure on the exchange couplings J_{in} and J_{out} in $Cr_2Ge_2Te_6$, using a simplified spin model with respect to other publications. J_{in} is the sum of two exchange contributions, the direct Cr–Cr exchange across the octahedral edge, which is antiferromagnetic (AF) between two half-filled t_{2g} bands, and the indirect Cr–Te–Cr superexchange at approximately 90-degrees. This indirect superexchange, according to Goodenough-Kanamori-Anderson rules, can be either FM or AF, depending on the extent of the delocalization and

correlation superexchange effects [154, 155]. J_{out}, on the other hand, is the inter-plane exchange coupling between Cr–Cr neighbors. In the calculations by Fumega et al. J_{out} increases from 12 K at 0 GPa to about 29 K at 5.6 GPa hydrostatic pressure, while J_{in} decreases from about 28 K to 20 K in the same pressure regime, with a steeper initial change, by about 35%/GPa for J_{out} and −10%/GPa for J_{in}. At pressures above 7 GPa a transition to a metallic state, potentially together with a structural phase transition, was predicted [154]. Ge et al. and Dong et al. found a semiconductor to metal transition at about 14 GPa [156, 157]. The change in coupling strengths J_{in} and J_{out} observed for hydrostatic pressure suggests that similar effects may be the cause for the uniaxial cross-plane ($\parallel c$) and in-plane ($\perp c$) pressure dependence. Uniaxial cross-plane pressure may lead to an increase in J_{out} and a stabilization of ferromagnetism, whereas uniaxial in-plane pressure may induce a decrease in J_{in}, thereby weakening ferromagnetic interactions and leading to a suppression of T_{C}. This simplified picture lends itself as an explanation but calculations will be necessary to actually test the effect of uniaxial pressure on bond angles and exchange coupling strengths.

A comparison of the pressure effects in $Cr_2Ge_2Te_6$ to the isostructural compounds CrI_3 and VI_3 is surprising. Although being of similar magnitude, the hydrostatic pressure dependence is positive, i.e., of opposite sign than for $Cr_2Ge_2Te_6$ [158, 159]. Moreover, the initial effect of uniaxial pressure in CrI_3 shows the same positive cross-plane ($\parallel c$) and negative in-plane ($\perp c$) behavior, but is almost two magnitudes smaller than for $Cr_2Ge_2Te_6$ [160]. Such large uniaxial pressure effects are very welcome for device applications, e.g., for sensing, data storage or computing, because they enable control of the transition temperature, especially enhancing T_{C} with the goal of room temperature applications. The feasibility of such T_{C}-enhancement in $Cr_2Ge_2Te_6$ has been shown by Wang et al., with electrochemical intercalation of organic molecules in the van der Waals gap leading to an enhancement of T_{C} to 208 K, three times the value of pristine $Cr_2Ge_2Te_6$ [161]. Besides, they found a concomitant change of the magnetic easy-axis direction from the c-axis direction to the ab-plane.

The uniaxial and hydrostatic pressure dependence in $Cr_2Ge_2Te_6$ may thus not only be discussed in terms of varying exchange interaction strengths, but also in terms of a pressure-dependent magnetic anisotropy, especially a pressure dependence of the intrinsic magnetocrystalline anisotropy. Magnetocrystalline anisotropy can arise from a coupling of the magnetic spins to the lattice via the crystal electric field and spin-orbit coupling. If this is the case, pressure-induced lattice distortions will also have an effect on the magnetocrystalline anisotropy. For $Cr_2Ge_2Te_6$ a uniaxial magnetic anisotropy has been reported, along with investigations of its temperature dependence [141, 145, 162]. In principle, the magnetocrystalline anisotropy is a material constant and therefore independent of temperature or applied magnetic

field. On a macroscopic level, however, many ferromagnets, e.g., Fe, Co, and Ni, exhibit a temperature dependence of the magnetocrystalline anisotropy constant. This behavior can be understood in the frame of the theory laid out by Zener [163], by the effect of temperature fluctuations on the anisotropy of the magnetization. Selter et al. suggested that the uniaxial anisotropy along the c-axis is responsible for the low-temperature magnetic phase seen for $B \perp c$. They described the change in magnetization direction in an applied magnetic field on this basis, with moments pointing along the c-axis in zero-field and gradually rotating towards the in-plane direction as a field $B \perp c$ is applied. Studies of the hydrostatic pressure dependence of the magnetic anisotropy in $Cr_2Ge_2Te_6$ by Lin et al. claimed a reorientation from a uniaxial anisotropy to an easy-plane anisotropy in the ab-plane between 1.0 GPa and 1.5 GPa [22]. Contrasting this study, Sakurai et al. found no reorientation of the magnetic anisotropy under hydrostatic pressure up to 2.5 GPa [153]. They did find evidence for a significant decrease of the magnetocrystalline anisotropy energy constant of $Cr_2Ge_2Te_6$ upon application of hydrostatic pressure, along with a suppression of T_C, but no sign change in the anisotropy constant was found [153]. In contrast, an increase in T_C is expected if the uniaxial anisotropy is enhanced by (uniaxial) pressure. With this in mind, the positive uniaxial pressure dependence of T_C for $p \parallel c$ suggests an enhancement of the uniaxial anisotropy, while the decrease in T_C for $p \perp c$ suggests it weakens for pressure applied along the in-plane direction, just as for hydrostatic pressure.

Magnetic Contributions to the Thermal Expansion for $B > 0$

The magnetic contribution to the thermal expansion for $B > 0$ is obtained by subtracting the zero-field phonon background from the thermal expansion coefficient at different fields. By integrating $\alpha_{i,\mathrm{mag}}$ ($i = c, \perp c$) with respect to temperature the spontaneous strain $\varepsilon_{\mathrm{mag}} = (dL/L)_{\mathrm{mag}}$ related to the evolution of ferromagnetic order is obtained. Fig. 5.7 shows both the zero-field data and the evolution of $\alpha_{i,\mathrm{mag}}$ in various magnetic fields for $B \parallel c$ (top) and $B \perp c$ (bottom). The main findings are: (1) a broadening of the anomaly at T_C and shift of the extrema towards higher temperatures with higher fields. The length changes at low temperatures related to magnetism therefore decrease with increasing field, whereas the thermal expansion is enhanced at higher temperatures. For $B = 15$ T, the extrema are shifted by about 30 K with respect to T_C in zero-field, indicating a moderate stabilization of ferromagnetism. The magnetic entropy is expected to shift accordingly. (2) The overall magnetic length changes are approximately independent of the magnetic field except for the above-mentioned sign change of magnetostriction $dL_\perp(B)$ below $\sim$37 K. Furthermore, for $B \leq 15$ T the enhanced thermal expansion at higher temperatures does not significantly affect the high-temperature onset of magnetic length changes. Magnetic contributions for both directions extend up to about 220 K,

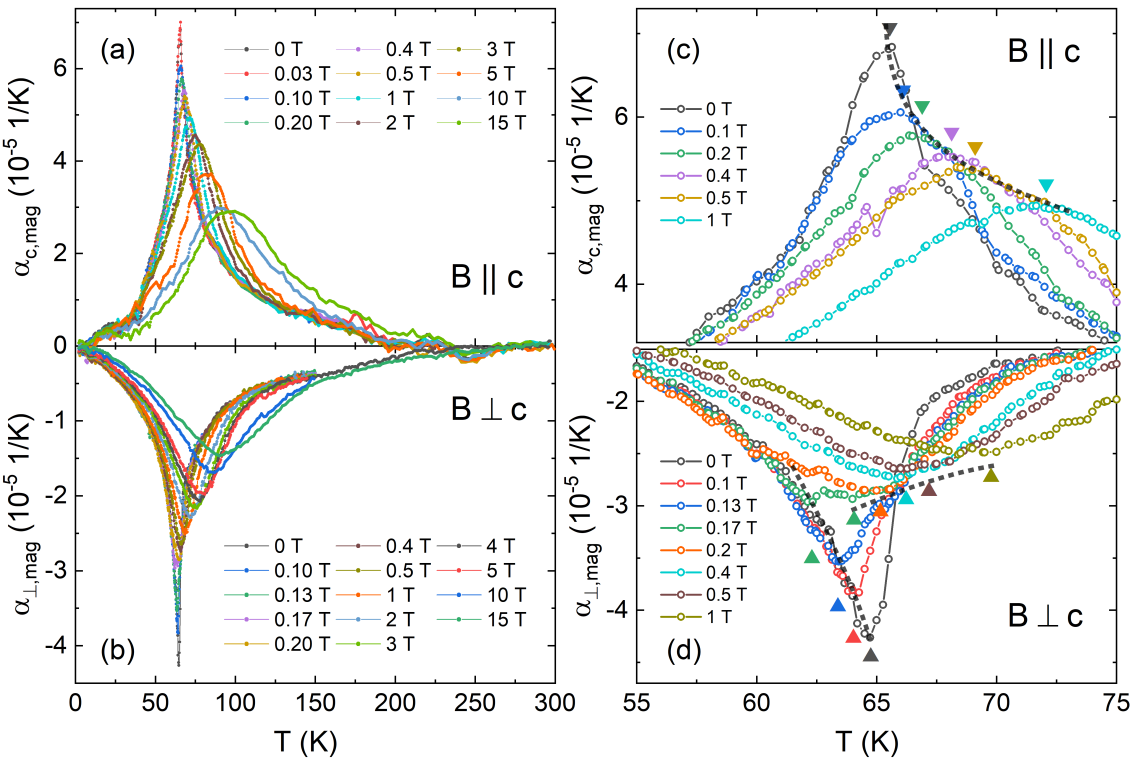

Figure 5.7: Magnetic contribution to the thermal expansion coefficient, $\alpha_{i,\mathrm{mag}}$, $i = c, \perp$, in various magnetic fields up to 15 T. Colored triangles in (c) and (d) mark the peak positions while dashed lines illustrate the general trend of the transition temperatures.

nearly independently of the magnitude of the applied field. (3) In contrast to the general trend in magnetic fields, small fields below 0.2 T yield a suppression of the anomaly for $B \perp c$ as highlighted in Fig. 5.7(c) and (d). The extrema are marked by colored triangles (same colors as the corresponding data) and the dashed lines illustrate their field dependence. For fields up to 0.17 T the peak in $\alpha_\perp$ first shifts to lower temperatures, at which point the peak flattens at the top, indicating a splitting into two peaks, one shifting to higher and one to lower temperatures. However, no two single peaks are clearly distinguishable in the data at a given field, which can be attributed to the large width of the overall peak. For $B \parallel c$, the peak in α_c shifts to higher temperatures in increasing fields, with no suppression at small fields. Selter et al. recently published the specific heat in small magnetic fields [141]. The behavior observed in the thermal expansion exactly matches their findings (Fig. 5.8).

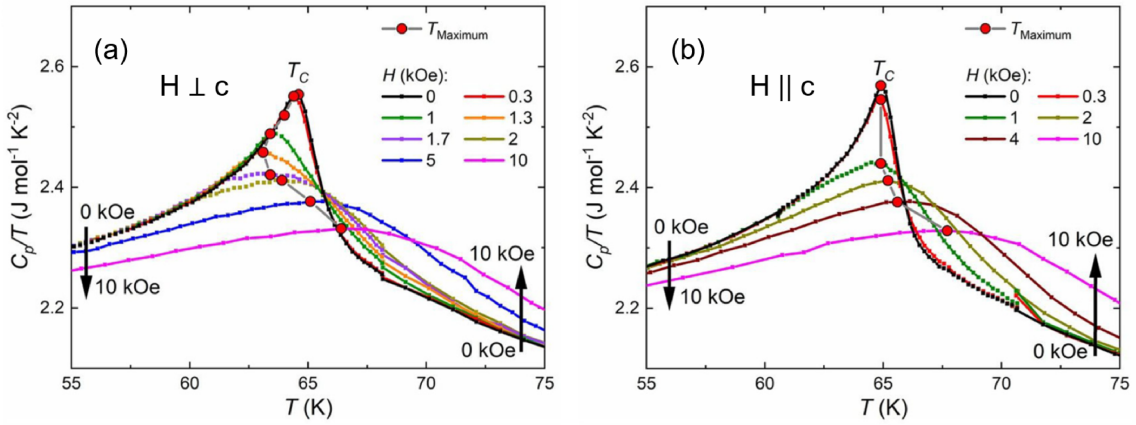

Figure 5.8: c_p/T as a function of temperature under different magnetic fields applied along (a) the hard magnetization plane and (b) the easy magnetization axis c. Taken from [141].

Critical Scaling Analysis

The nature of the spin ordering in $Cr_2Ge_2Te_6$ has been discussed by a large number of studies focusing on an analysis of critical exponents in recent years [144, 145, 164–169]. In this section, the critical behavior of the thermal expansion coefficient and relative length changes in the vicinity of T_C is studied. The behavior of $\alpha_{i,\mathrm{mag}}$ and α_i with respect to the reduced temperature $t = |T - T_C|/T_C$ is investigated and critical exponents are obtained from fits to $\varepsilon_{\mathrm{mag}} = (\Delta L/L)_{\mathrm{mag}}$ near T_C, both in zero-field and for $B > 0$.

An analysis of critical exponents is only valid close to the investigated phase transition. It is not clear, however, how large the temperature window above and/or below T_C should be for reliable results. Moreover, as will be seen in this section, the exponent β_c varies strongly depending on the chosen temperature interval. The uncertainties in such an analysis are therefore large and the resulting values have to be taken with caution.

Fig. 5.9 shows the magnetic contributions to the thermal expansion coefficient for selected fields for both $B \parallel c$ (Fig. 5.9(a-b)) and $B \perp c$ (Fig. 5.9(c-f)) plotted against the reduced temperature t on a logarithmic scale. This scale is chosen because for critical exponents $\alpha_\pm$ close to $\alpha_\pm = 0$ a logarithmic divergence is expected as explained in the theory section (Sec. 1.2.2). For each plot T_C was adjusted carefully around the temperature corresponding to the peak in $\alpha_{i,\mathrm{mag}}$, to obtain a maximal overlap for $T > T_C$ and $T < T_C$ where possible. The values chosen as T_C are shown in the figure.

Zero-field data for $\alpha_{c,\mathrm{mag}}$ and $\alpha_{\perp c,\mathrm{mag}}$ show distinctly different behavior (Fig. 5.9(a)

and (c)). For $\alpha_{\mathrm{c,mag}}$ the data overlap perfectly within error bars for $t < 0.1$, and show a linear regime, i.e., logarithmic scaling. This is a strong indication for 2D Ising spins as the overlap of the data shows that $\alpha_- = \alpha_+$ and logarithmic scaling indicates $\alpha_\pm \approx 0$. The behavior of $\alpha_{\perp\mathrm{c,mag}}$, on the other hand, clearly differs for $T > T_\mathrm{C}$ and $T < T_\mathrm{C}$. Although such behavior could originate from the phononic background, data for $B \geq 1$ T up to 5 T show a very good overlap to values of t of above 0.35. Notably, at 5 T the data scale for $t < 0.45$ with $T_\mathrm{C} = 77.8$ K, i.e., within 35 K above and below T_C. Moreover, the $\alpha_{\perp,\mathrm{mag}}$ data for $T < T_\mathrm{C}$ show linear behavior nearly to $t = 1$, i.e., logarithmic scaling down to lowest temperatures. Very close to the phase transition logarithmic scaling breaks down and $\alpha_{i,\mathrm{mag}}$ becomes nearly constant. This behavior is presumably related to a critical slowing down.

The very large temperature window for which logarithmic divergence applies is illustrated in Fig. 5.10. Red lines show logarithmic fits

$$\alpha_i = a - b \cdot \ln\left(|T - T_\mathrm{C}|\right) \tag{5.2}$$

to the zero-field thermal expansion coefficients, where $b = \alpha_\pm \cdot \mathrm{const}$. The temperature window for the fitting was 42 K to 64 K (65.2 K to 120 K) for $T < T_\mathrm{C}$ ($T > T_\mathrm{C}$) for the in-plane data, and 2.3 K to 64.1 K (66 K to 148 K) for the c-axis. For the c-axis logarithmic scaling applies from the lowest temperatures to about 120 K – or even 200 K within experimental error bars. The fits to $\alpha_\perp$ show a similar behavior with a good overlap of the fit from about 240 K down to 45 K. A logarithmic divergence at the critical temperature T_C was calculated by Onsager for the specific heat of a two-dimensional (2D) Ising model [19]. As stated in the theory section (Sec. 1.2.2), the mean-field model also exhibits $\alpha_\pm = 0$, with the difference from the 2D Ising model that a discontinuity in $\alpha_\pm$ is expected. Fitting the zero-field thermal expansion coefficients with the same parameter b above and below T_C does not work well, suggesting that a mean-field model may describe the data better than the 2D Ising model.

Souza et al. proposed a different approach to determining critical exponents from thermal expansion coefficients which also relies on the close relation between thermal expansion and specific heat [170]. From thermodynamic considerations, especially using the Ehrenfest equation, Souza et al. concluded that if the specific heat $c_\mathrm{p}^* \equiv c_\mathrm{p} - a - bT$ can be superimposed with $\eta\alpha T$, where η is a constant with units of J/(mol K), αT diverges with the same critical exponent as c_p. These assumptions are analogous to the assumptions implied for the Grüneisen analysis in Sec. 5.3.1. For the logarithmic divergence in this section $c_\mathrm{p} \sim \alpha$ was assumed instead of $c_\mathrm{p} \sim \alpha T$. Moreover, η is related to the pressure dependence of the critical temperature by $dT_\mathrm{C}/dp = V_\mathrm{m}/\eta$, with the molar volume V_m. For the uniaxial pressure dependence derived from the Grüneisen analysis this yields $\eta_\mathrm{c} = 6.757 \cdot 10^3$ J/(mol K) and

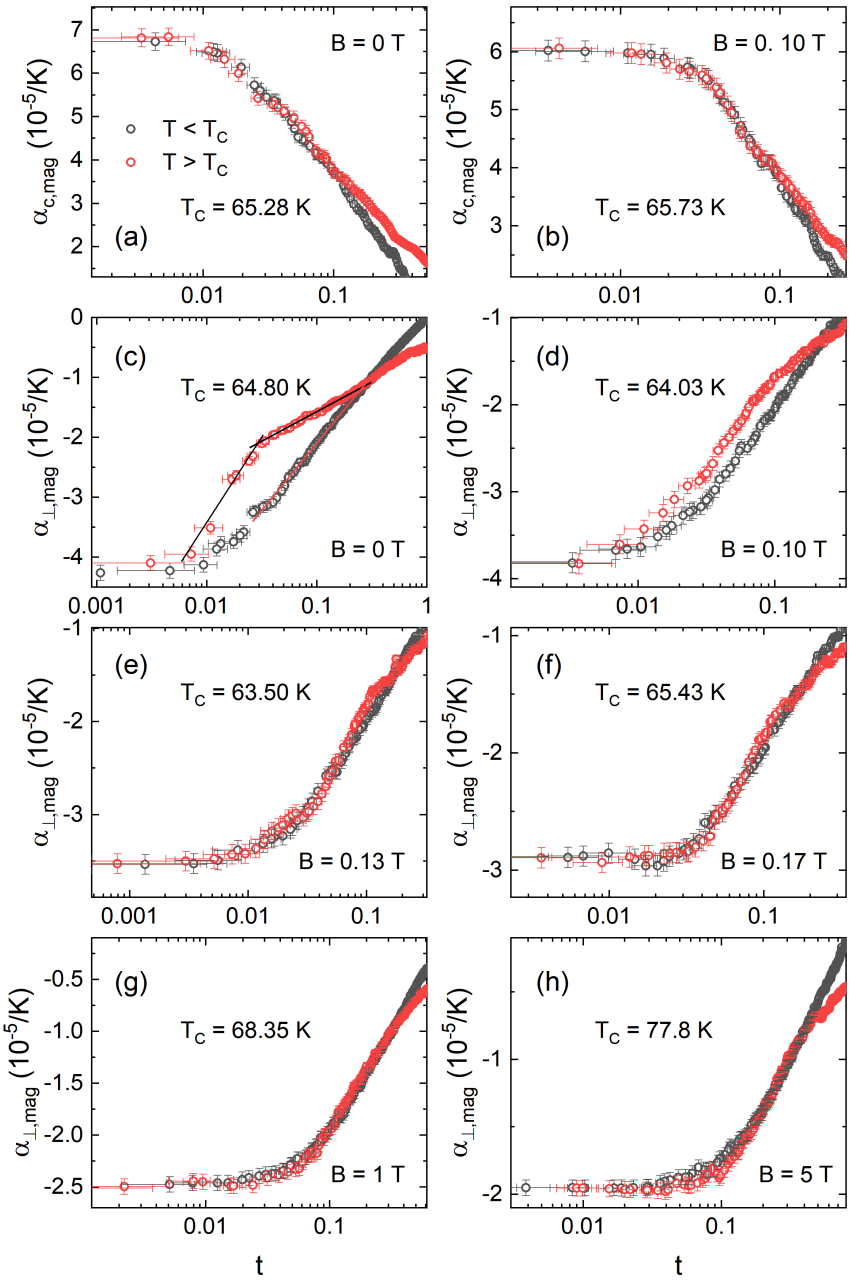

Figure 5.9: Magnetic contributions to α_i for selected fields for (a-b) $B \parallel c$, and (c-f) $B \perp c$, with respect to the reduced temperature t on a logarithmic scale. Black (red) circles mark data for $T < T_C$ ($T > T_C$). Corresponding values for T_C are shown in the figures. Lines in (c) are a guide to the eye.

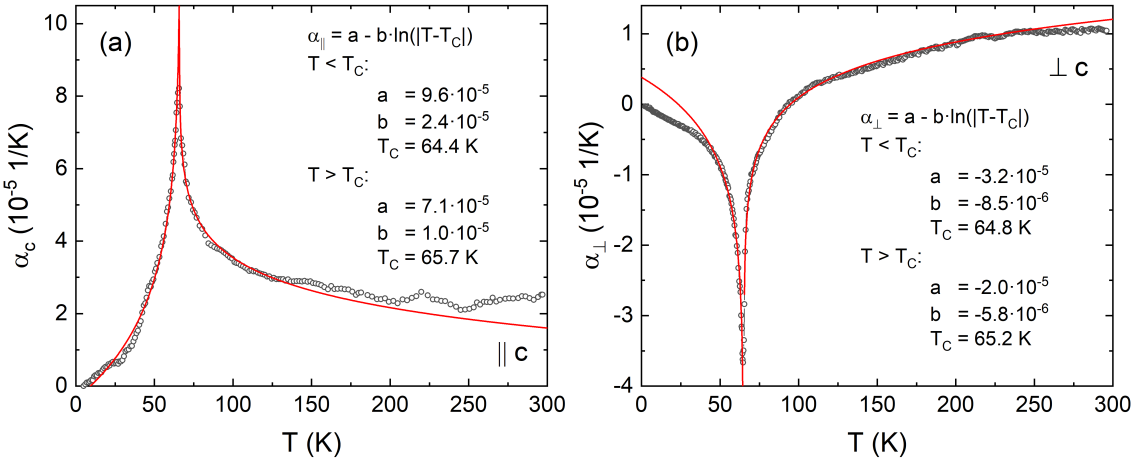

Figure 5.10: Logarithmic fits to the zero-field thermal expansion coefficient for (a) the c-axis and (b) the in-plane direction. Fit results are indicated in the plot. Fit ranges are given in the text.

$\eta_{\perp} = -1.111 \cdot 10^4$ J/(mol K). Including both a constant and a linear background, the canonical expression for critical behavior which is employed in the following is

$$\eta_i \alpha_i T \simeq \frac{A_{\pm}}{\alpha} |t|^{-\alpha} (1 + E_{\pm} |t|^{\chi}) + B + Dt, \tag{5.3}$$

where $\chi = 0.5$ and $t \equiv (T - T_C)/T_C$ is again the reduced temperature [171]. The plus-minus subscripts denote quantities which are potentially different above (+) and below (−) T_C. $\eta_i \alpha_i T$ is shown together with c_p* in Fig. 5.11(a). Here, instead of a constant and a linear term, a polynomial background was subtracted from c_p to obtain c_p*. As for the Grüneisen analysis, the scaled in-plane thermal expansion and the specific heat c_p* overlap, while $\eta_c \alpha_c T$ shows a similar behavior around T_C but slightly higher values and a different behavior for temperatures above T_C. Fits according to Eq. 5.3 are presented in Fig. 5.11(b). For these fits, T_C was fixed to 65.3 K (64.7 K) for the c-axis (in-plane) as well as $B = 0$. The applied temperature window for the fits was from 53 K to 88.5 K (67.9 K), respectively, i.e., including temperatures both above and below T_C. Separate fits for $T < T_C$ and $T > T_C$ were also preformed, as well as fits to $\alpha_{i,\mathrm{mag}}$ (both not shown). The fits in Fig. 5.11(b) yield $\alpha_{\pm} = 0.041(7)$, $A = 1.3(2)$, $D = 31.3(9)$, $E = -1.10(4)$ for the c-axis and $\alpha_{\pm} = 7.5 \cdot 10^{-7} \pm 0.011$, $A = 2.3 \cdot 10^{-5} \pm 0.34$, $D = -72 \pm 8$, $E = -2.9(1)$ with large interdependencies between the fit parameters. Indicated errors are of statistical nature. Fits to $\alpha_{\perp,\mathrm{mag}}$ yielded $0.03 < \alpha_{\pm} < 0.14$, for different temperature windows and different combinations of fixing the fit parameters to zero or a fixed value.

Considering these results, a number of conclusions can be drawn: (1) The critical exponent $\alpha_{\pm}$ varies widely depending on the temperature window. (2) Within its

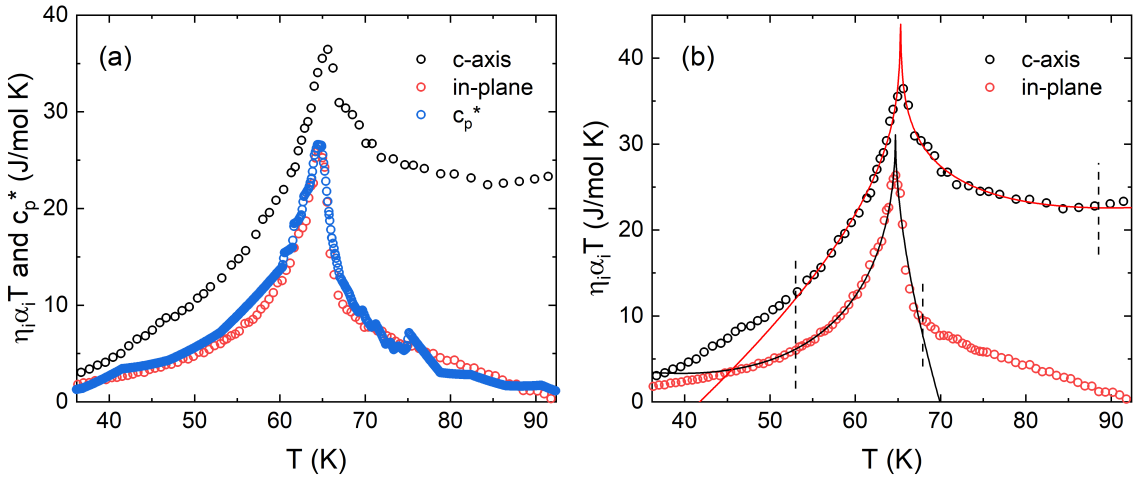

Figure 5.11: (a) Scaling of $\eta_i\alpha_i T$ and c_p*. (b) Critical fits to the scaled zero-field thermal expansion coefficient $\eta_i\alpha_i T$ for the c-axis (red line) and the in-plane direction (black line). Fit results are discussed in the text. Fit ranges are indicated by vertical bars. The lower boundary applies for both fits.

variation $\alpha_\pm$ is always positive and small, namely, $0 \leq \alpha_\pm < 0.15$. (3) A small and positive $\alpha_\pm$ is in line with calculations for the 3D Ising model ($\alpha \approx 0.11$), but also with the 2D Ising model and mean field theory ($\alpha = 0$) (see Tab. 1.4 and Ref. [41]).

A further quantitative analysis can be performed using the spontaneous strain ε_mag, which shows an order-parameter-like behavior below T_C. Above T_C ε_mag does not, unlike the francisite in the previous chapter, assume a constant value due to the short-range magnetic correlations up to high temperatures. However, the behavior below T_C is reminiscent of an order parameter, with a steep rise and subsequent transition to a saturation value at lowest temperatures. A comparison of the spontaneous strain to the intensity of the magnetic (1 0 1) Bragg peak as measured by neutron diffraction [139] confirms its relation to the magnetic order parameter (Fig. 5.12). In order to account for the different T_C of the neutron diffraction and thermal expansion data the temperature axes have been scaled. The evolution of the in-plane $\varepsilon_{\perp,\mathrm{mag}}$ coincides with the neutron intensity evolution over the whole temperature window below T_C, whereas for the c-axis the data do not overlap well below 40 K. This may suggest an additional effect at low temperatures for the c-axis.

The spontaneous strain represents a secondary order parameter, in contrast to the primary order parameter Q of a system. For a paramagnetic to ferromagnetic transition the magnetization normalized to the saturation magnetization, M/M_S, is an order parameter. The relationship between the spontaneous strain ε and Q may be described by a Ginzburg-Landau expansion of the free energy density F. Assuming a coupling between the order parameter and the lattice strains enables to derive the

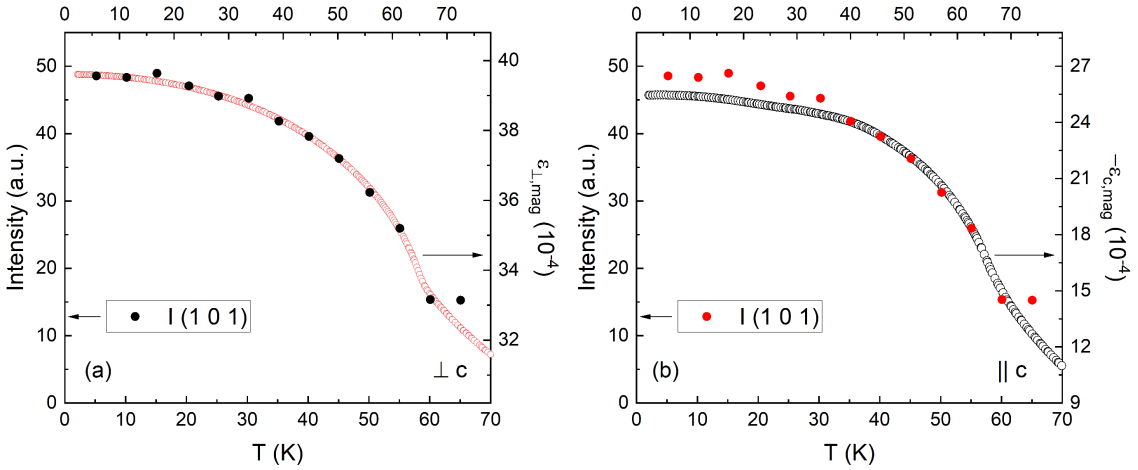

Figure 5.12: Neutron intensity for the (1 0 1) Bragg peak in comparison to the spontaneous strain $\varepsilon_{i,\mathrm{mag}} = (dL_i/L_i)_{\mathrm{mag}}$ in zero-field. Neutron intensities taken from [139].

relationship between ε and Q in thermal equilibrium without external stress, i.e., from $\partial F/\partial\varepsilon = 0$ (see, e.g., Ref. [172]). Here, $\varepsilon_{i,\mathrm{mag}}$ evolves in the same manner as the neutron scattering Bragg peak intensity. Since this intensity has been shown to follow a $|T - T_\mathrm{C}|^{2\beta_\mathrm{c}}$-behavior near T_C in both ferro- and antiferromagnetic systems [173, 174], the zero-field and $B > 0$ data are fitted with $\varepsilon_{i,\mathrm{mag}} = \varepsilon_0 + A \cdot |T - T_\mathrm{C}|^{2\beta_\mathrm{c}}$. Fits to $\varepsilon_{i,\mathrm{mag}}$ in the vicinity of T_C, from 57 K to 64 K, yield $2\beta_\mathrm{c} = 0.66(8)$ and $2\beta_\mathrm{c} = 0.67(8)$ for the zero-field c-axis and in-plane data, respectively (Fig. 5.13). To obtain the values T_C was fixed to 65.3 K (c-axis) and 64.7 K (in-plane) and values 0.4 K above and below to observe the changes in the critical exponent. Furthermore, different temperature windows were applied for the fits to test the resulting variation of β_c. The relatively large error bars reflect these variations. [1]

Strictly speaking the critical exponents as introduced in Sec. 1.2.2 are only valid in zero-field. Nonetheless, in order to trace the evolution of β_c in field, the spontaneous strain for $B > 0$ was fitted in the same way as the zero-field data, for both $B \perp c$ and $B \parallel c$. The fits yield values of $0.65 < 2\beta_\mathrm{c} < 0.72$ and $0.62 < 2\beta_\mathrm{c} < 0.68$, respectively, indicating that the phase transition does not change its nature in an applied magnetic field. In Fig. 5.14(a) and (b) the resulting critical exponents are displayed along with the exponents expected for different physical models (horizontal dashed lines). For the 2D Ising model one would expect $2\beta_\mathrm{c} = 0.25$, which is well below the obtained values (Tab. 1.4). Due to the large error bars the physical

1 A fit to $\varepsilon_{i,\mathrm{mag}}$ in a very large temperature window from 31.5 K to 64 K fields $2\beta_\mathrm{c} = 0.43$, i.e., $\beta_\mathrm{c} = 0.215$. With the choice of a smaller window close to T_C β_c assumes higher values.

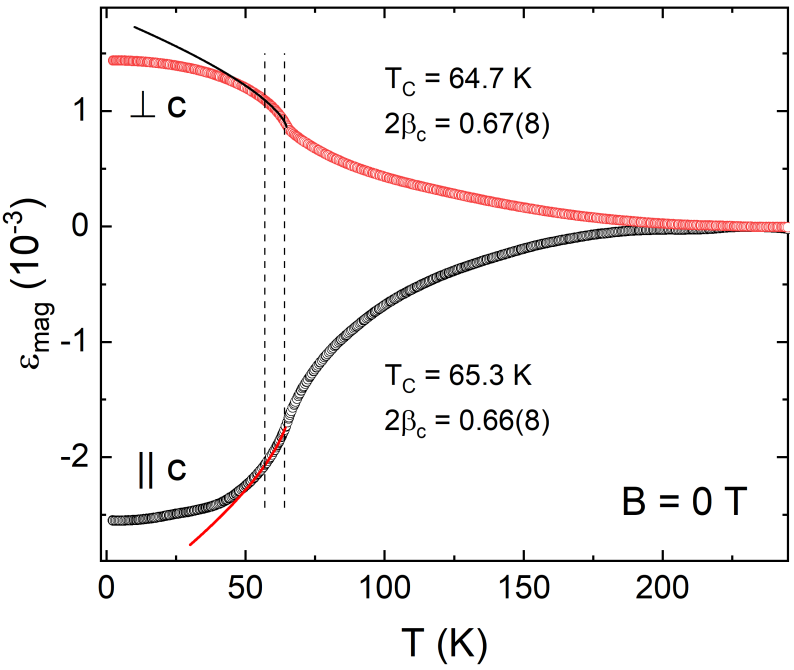

Figure 5.13: Spontaneous strain $\varepsilon_{\mathrm{mag}} = (dL_i/L_i)_{\mathrm{mag}}$ in zero-field. Vertical lines indicate the temperature regime, 57 K to 64 K, used for the fits.

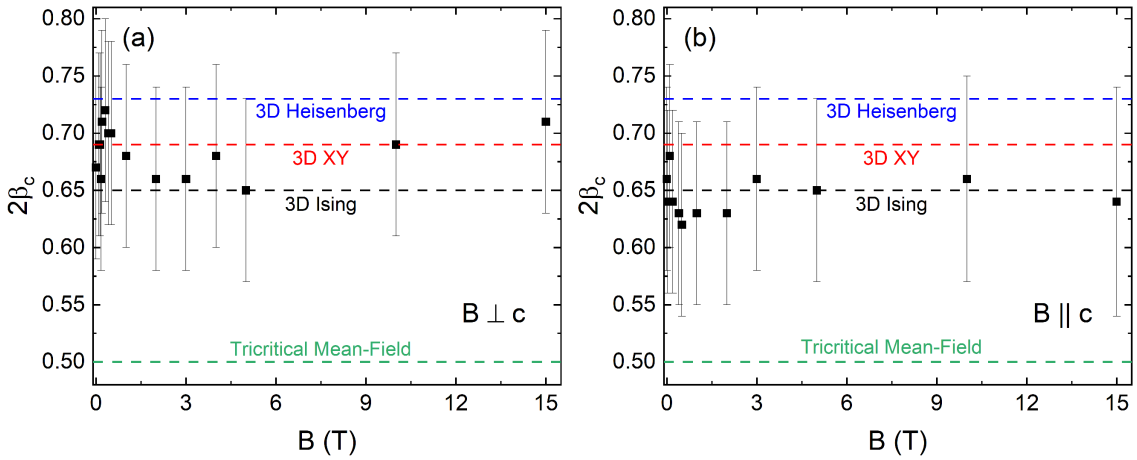

Figure 5.14: Critical exponents extracted from $\varepsilon_{i,\mathrm{mag}}$ for (a) $B \perp c$ and (b) $B \parallel c$ as described in the text. Horizontal dashed lines indicate the expectations for different physical models.

model which applies for the ferromagnetic phase in $Cr_2Ge_2Te_6$ cannot be determined unambiguously from the critical behavior of the spontaneous strain near T_C. However, approximately the determined critical exponents lie closest to the value expected for the three-dimensional Ising model.

As alluded to at the beginning of this section, the critical behavior around T_C in $Cr_2Ge_2Te_6$ has been studied by different groups, mostly based on isothermal magnetization measurements. Tab. 5.1 presents an overview of these results. Significantly, the experimentally-derived critical exponents vary widely. Results for the critical exponent β_c, which was also studied above, fall in the range $0.177 \leq \beta_c \leq 0.35$, spanning the range of values close to the 2D Ising model ($\beta_c = 0.125$) almost up to the 3D Heisenberg model ($\beta_c = 0.365$). Lin et al. considered that, due to its smaller van der Waals gap and larger cleavage energy as compared to $Cr_2Si_2Te_6$, $Cr_2Ge_2Te_6$ may be close to a tricritical point, i.e., a change from second-order to first-order behavior of the phase transition. This smaller van der Waals gap and larger cleavage energy may lead to a transition from 2D to 3D magnetism [144]. Some authors came to the conclusion that $Cr_2Ge_2Te_6$ cannot be described by any single theory model [145].

In contrast to arguments for 3D behavior in $Cr_2Ge_2Te_6$, the presence of quasi-2D magnetism in bulk $Cr_2Ge_2Te_6$ has been supported by different experimental techniques: On a microscopic level measurements of the angular dependence of the electron spin resonance (ESR) linewidth suggest the intrinsic 2D nature of magnetism [140] (Fig. 5.15). On the macroscopic level the small entropy related to the peak in the specific heat at T_C of about 2 J/(mol K) has been interpreted as an indication of 2D magnetism, with entropy shifted to higher temperatures due to magnetic fluctuations [141]. The full magnetic entropy expected for an $S = 3/2$ system would be about ten times higher, i.e., $S_{mag} = 2R \ln(2 \cdot 3/2 + 1) = 23.05$ J/(mol K). Furthermore, the Curie-Weiss temperatures observed for $Cr_2Ge_2Te_6$ are well above T_C, around 90 K–100 K [140, 141], whereas usually $\Theta_{CW} \gtrsim T_C$ in ferromagnets exhibiting three-dimensional magnetic order. This suppression of T_C has also been attributed to two-dimensional behavior [141].

In the isostructural compound $Cr_2Si_2Te_6$ Cr spins exhibit a weak single-ion anisotropy, on the order of 25μeV, originating from a small distortion of the surrounding Te octahedra [147]. In this compound 2D-Ising behavior of the Cr spins was observed with values of $\beta_c = 0.17$[175] and more recently $\beta_c = 0.151(2)$ [147], along with strong in-plane 2D correlations up to 300 K [147]. At the same time 3D magnetic order below $T_C = 31$ K was suggested, with results from inelastic neutron scattering experiments pointing to Heisenberg-like spins [147]. Furthermore, a transition from 2D to 3D behavior was unveiled by high-multipole nonlinear optical polarimetry [176]. This transition was reported at $T_{3D} \sim 60$ K, whereas the onset of 2D correlations

Table 5.1: Critical exponents determined from experiments on $Cr_2Ge_2Te_6$ as reported in different works. Abbreviations of the methods used to extract the exponents: Modified Arrott plot (MAP), Kouvel-Fisher plot (KFP), critical isotherm (CI), relative cooling power (RCP). $\Delta S_M^{\max}$ is the maximum of the magnetic specific heat calculated from magnetization measurements.
[a]: First-principles calculations, exponent derived from calculated magnetization

Critical exponents from different works on $Cr_2Ge_2Te_6$								
Ref.	Method	T_C (K)	β_c	γ	δ	n	l	m
[144]	MAP	67.9	0.242	0.985	5.07			
[164]	MAP	62.7	0.196	1.32	7.73			
[164]	KFP	62.7	0.2	1.28	7.4			
[164]	CI	62.7			7.96			
[165]	$\Delta S_M^{\max}$ & RCP	66.4	0.177	1.746	10.869			
[166]	$\Delta S_M^{\max}$ & RCP	65.6				0.61	1.21	
[166]	MAP	65.6	0.242	0.985	5.07			
[166]	KF	65.6	0.24	1	5.167			
[145]	χ_{ac}	62.8	0.35	1.43	5.24			
[167]	$\Delta S_M^{\max}$ & RCP	62.7				0.51	1.13	1.13
[167]	MAP	62.7	0.196	1.32	7.7	0.47	1.13	1.135
[167]	KF	62.7	0.2	1.28	7.4	0.46	1.135	1.129
[167]	CI	62.7			7.73		1.129	
[169]	CI	65.5	0.221	1.42	7.29			
[168]	calc.[a]	103	0.341					
This work	ε_{mag}	64.7	0.33					

was observed already at around $T_{2D} \sim 110$ K, well below T_C. Structural distortions observed at T_{2D} and T_{3D} were attributed to ionic displacements along different totally symmetric normal-mode coordinates, consistent with an onset of interlayer and intralayer spin correlations, respectively [176]. It is surprising, then, that the critical exponent exhibits a value corresponding to 2D Ising spins in a temperature range in which 3D correlations are present.

A similar transition from 2D to 3D magnetism may very well also be present in $Cr_2Ge_2Te_6$. The spin correlations visible as an onset of magnetic strain (Fig. 5.13) and a deviation from constant Grüneisen scaling (Fig. 5.5) around 200 K can then be interpreted as signs of 2D spin correlations, whereas 3D correlations are expected to evolve at lower temperatures. Where this transition from 2D to 3D behavior takes place cannot be derived from the macroscopic measurements presented in this work. Sensitive microscopic techniques such as NMR or high-multipole nonlinear optical polarimetry will be required to answer this open question.

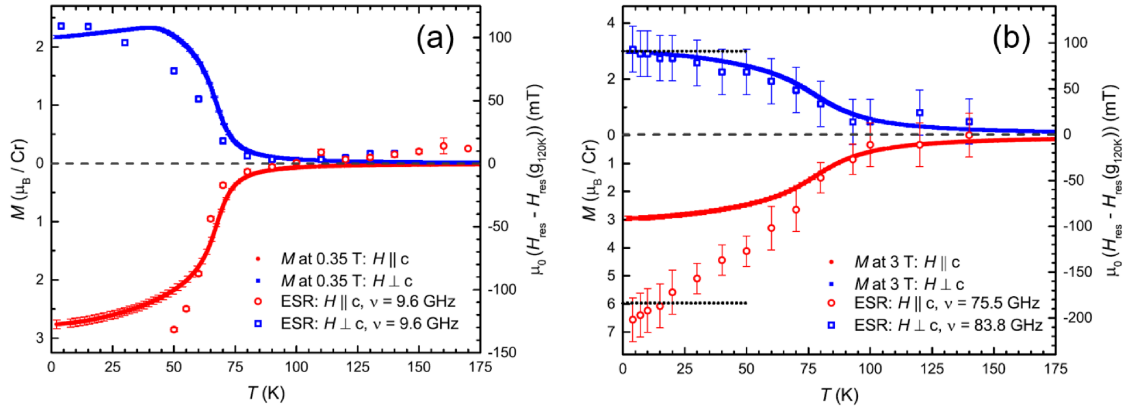

Figure 5.15: Resonance shift δH (right ordinates) as a function of temperature at a microwave frequency ν of (a) 9.6 GHz and (b) at higher frequencies for $B \parallel c$ and $B \perp c$, respectively (open symbols), together with the temperature dependence of the static magnetization $M(T)$ (left ordinates) for the respective field orientations (closed symbols). For better visibility, error bars for static magnetization are shown only for every tenth data point. A vertical gray line (dashed) indicates the zero shift of an ideal paramagnet. The black dotted line on panel (b) denotes the shift at 4 K obtained from the analysis of the frequency dependent FMR data (see the text). Taken from [140].

5.3.2 Magnetostriction and Magnetization

The in-plane magnetostriction at about 2 K exhibits a jump at a critical field of $B_c = 0.47\ T$, which separates two distinctly different regimes (Fig. 5.16): In the low-field region below B_c a negative magnetostriction with a quadratic behavior $dL_\perp/L_\perp \sim -B^2$ is visible, i.e., a linear behavior in $\lambda_\perp$ with a negative slope. Around B_c a kink is visible in $dL_\perp/L_\perp$ which translates to a sharp jump in $\lambda_\perp$, signaling a second order phase transition. In the second regime, i.e., above B_c, magnetostriction is nearly zero. Considering the magnetization data in Fig. 5.17(d-f) the squared-in-field magnetostriction is linked to a rotation of the magnetic moments towards the in-plane direction of the applied magnetic field. As saturation is reached, i.e., $M \parallel B$, the magnetostriction coefficient drops to nearly zero.

Magnetostriction data for different temperatures up to 70 K are presented in Fig. 5.17(a-c) in direct comparison to the isothermal magnetization at the same temperatures (Fig. 5.17(d-f)). Magnetostriction data at higher temperatures up to T_C display the same qualitative behavior as at 2 K, with magnetostriction above B_c increasing significantly as the temperature is increased to higher temperatures above 40 K (Fig. 5.17(a-c)). Furthermore, as expected from thermodynamic relations, the jump in $\lambda_\perp$ is seen as a jump in the magnetic susceptibility $\partial M_\perp/\partial B$ (Fig. 5.17(c) and (d)). Moreover, Fig. 5.17(b) and (c) show $\lambda_\perp$ diverging around B_c as the temperature

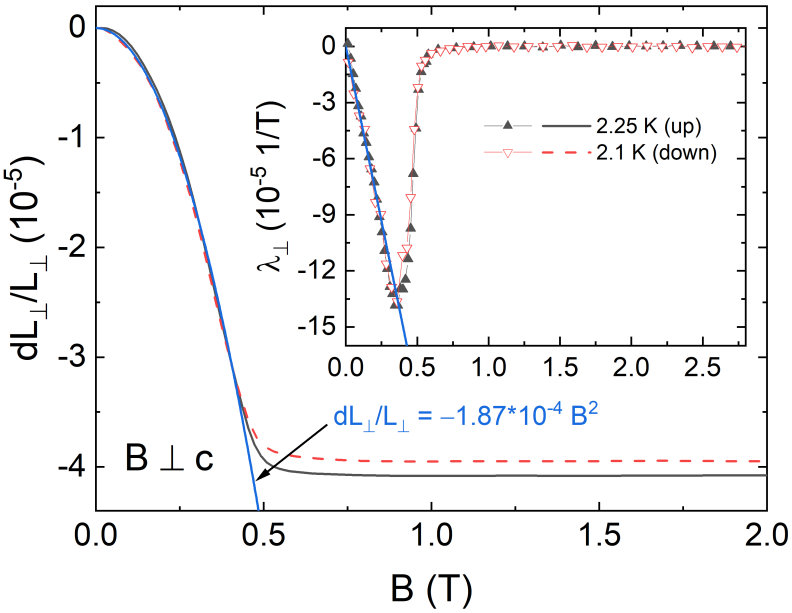

Figure 5.16: Relative length changes $dL_\perp(B)/L_\perp$ of $Cr_2Ge_2Te_6$ at T $\approx$ 2 K. Inset: Magnetostriction coefficient $\lambda_\perp$. Up- (down-) sweeps are marked by black (red) and filled (open) symbols. Blue lines show a fit to $dL_\perp(B)/L_\perp$ in low fields as indicated in the plot.

approaches T_C.

The magnetostriction for $B \parallel c$ below T_C is of opposite sign (Fig. 5.18(a) and (b)). In conjunction with the isothermal magnetization data for $B \parallel c$ (Fig. 5.18(c) and (d)) a number of observations can be made: (1) The magnetostriction is negative and a continuous behavior is observed in $dL(B)$ without any anomalies, i.e., there is no phase transition up to 15 T. (2) As T approaches T_C the magnitude of magnetostriction also rises strongly. (3) Around T_C the magnetostriction shows a strong hysteresis between up- and down-sweeps, which is not visible for $B \perp c$ nor in the magnetization. The absence of hysteresis in the magnetization data suggests a merely structural origin. Considering the weak bonding of the van der Waals layers this hysteresis may arise from small rearrangements of the van der Waals layers when the sample shrinks as the magnetic field decreases. (4) The magnetic susceptibility $\partial M_c/\partial B$ (Fig. 5.18(d)) also rises strongly as the temperature approaches T_C both from above and from below. Note that the magnetic field of the magnetostriction data is not corrected for the demagnetization field which would yields a shift of about -0.2 T for $T < T_C$ (see Fig. 5.2).

Increasing the temperatures above T_C leads to a gradual decrease of magnetostriction for both $B \perp c$ (Fig. 5.19(a) and (b)) and $B \parallel c$ (Fig. 5.19(c) and (d)). The qualitative behavior for the two directions is similar but again of opposite sign. λ_i reaches a

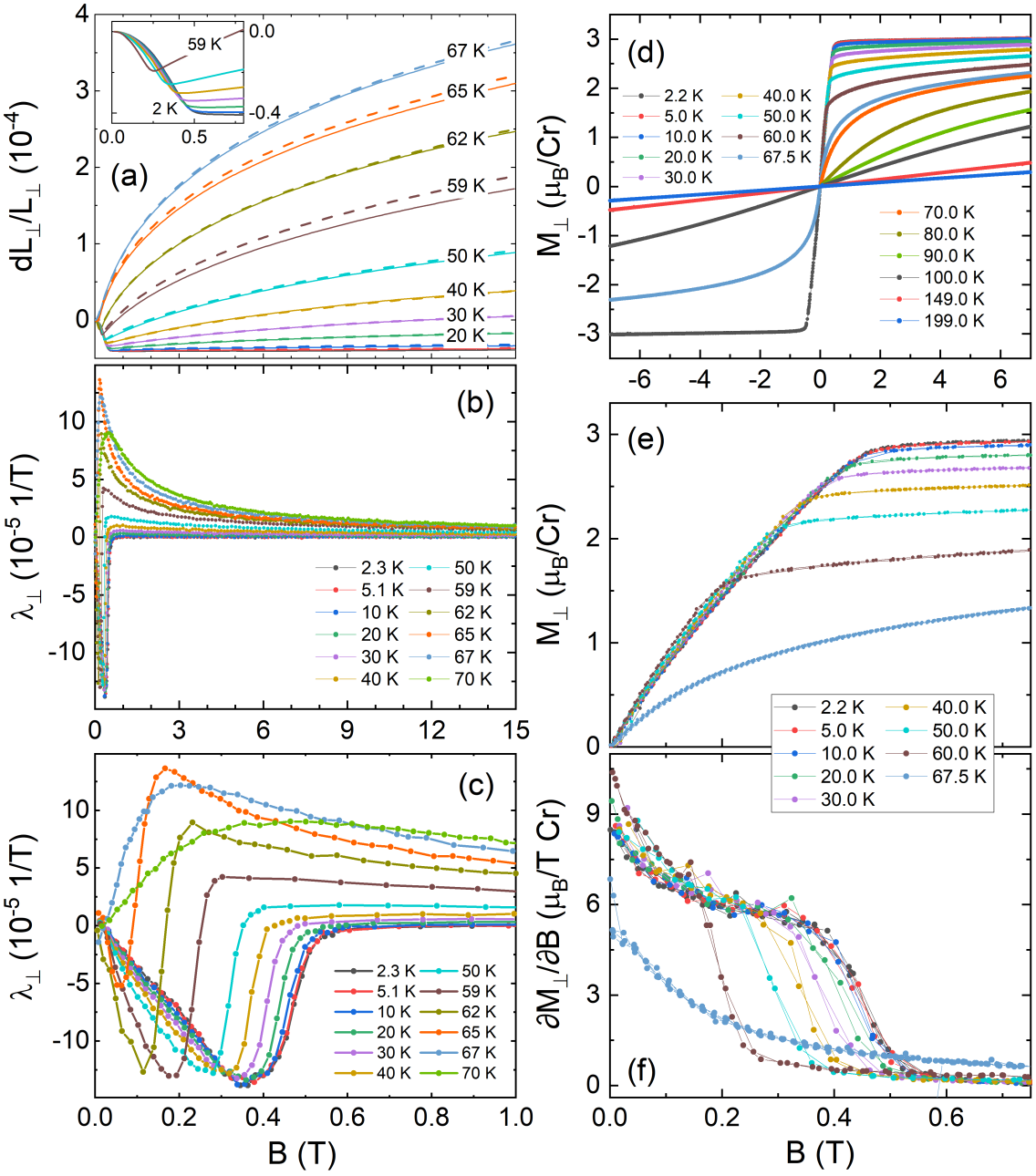

Figure 5.17: (a) Magnetostriction $dL_\perp/L_\perp$, (b-c) magnetostriction coefficients $\lambda_\perp$, (d-e) isothermal magnetization, and (f) magnetic susceptibility for different temperatures. Solid (dashed) lines in (a) represent up- (down-)sweeps of magnetic field $B \perp c$. The inset in (a) shows magnetostriction up-sweeps at low fields between 2.3 K and 59 K.

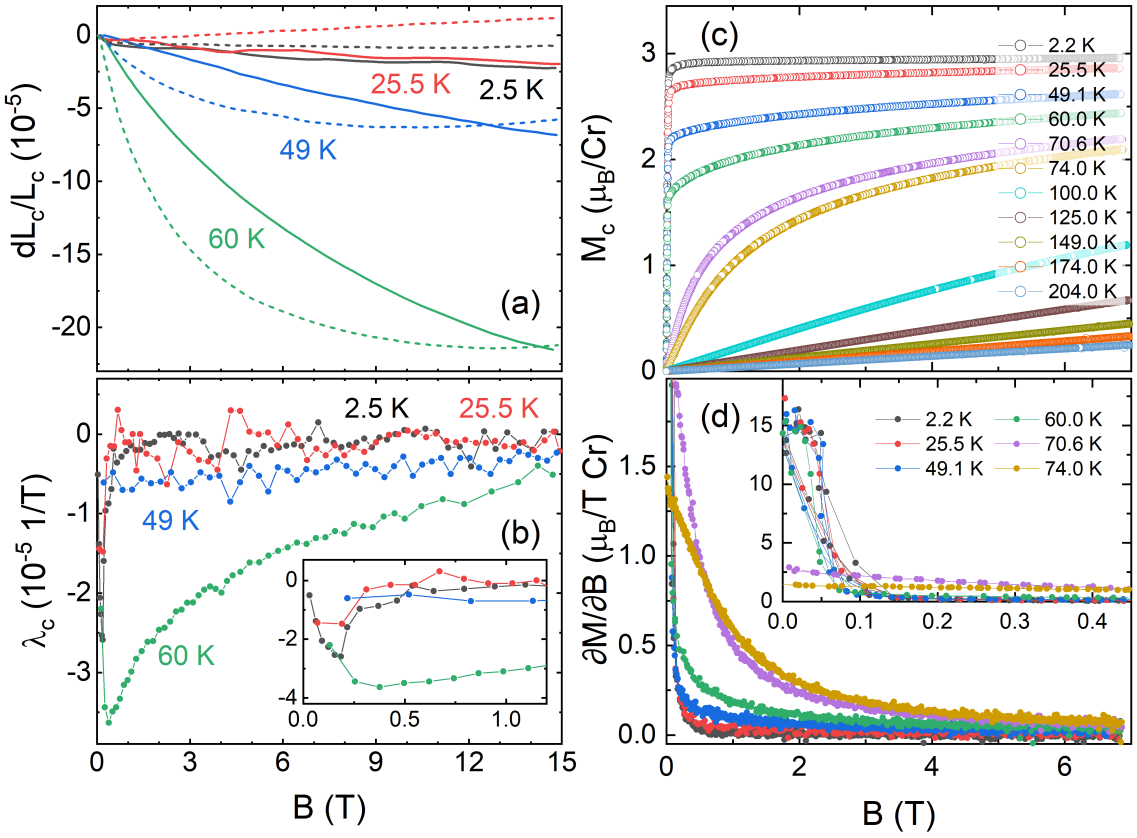

Figure 5.18: (a) Magnetostrictive length changes dL_c/L_c and (b) corresponding magnetostriction coefficients (up-sweeps only) λ_c at temperatures below T_C. (c) Isothermal magnetization and (d) magnetic susceptibility for different temperatures below and above T_C. Solid (dashed) lines in (a) represent up- (down-)sweeps of magnetic field $B \parallel c$. Insets in (b) and (d) show magnifications of the low-field region.

peak at low fields and temperatures close to T_C, i.e., at 70 K. This peak broadens and shifts to higher fields as temperature is increased. Two major differences are visible between the in-plane and cross-plane directions: (a) The magnitude of $dL_c(B)$ is larger by a factor of roughly 1.5 and (b) the hysteresis visible for $B \parallel c$ up to 125 K is absent for $B \perp c$.

Before turning to a quantitative analysis of the magnetostriction and magnetization data, a qualitative conclusion concerning the magnetostriction in $Cr_2Ge_2Te_6$ shall be drawn. As shown in the theory section (Sec. 1.1.3), the magnetostriction coefficient represents a measure for the pressure dependence of the magnetization M at constant temperature

$$\lambda_i = -\left.\frac{\partial M_i}{\partial p_i}\right|_T . \tag{5.4}$$

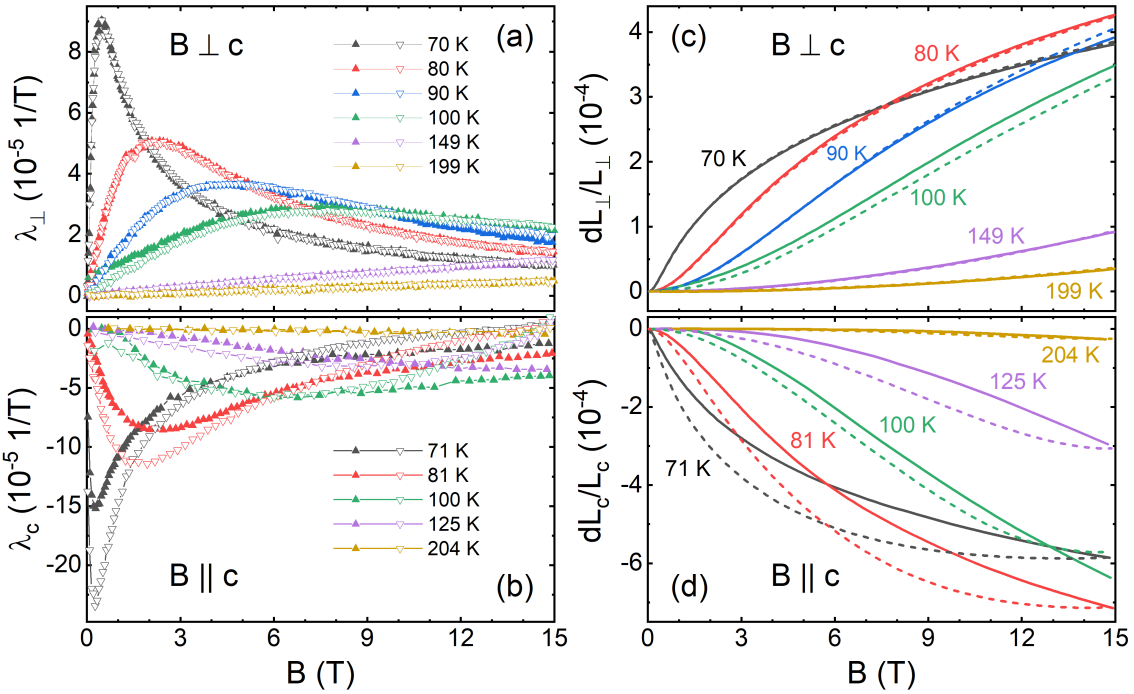

Figure 5.19: Magnetostriction coefficients λ_i for different temperatures above T_C for (a) $B \perp c$ and (b) $B \parallel c$. Filled (open) symbols indicate up- (down-)sweeps of the magnetic field. (c) and (d) show the corresponding relative length changes. Solid (dashed) lines indicate up- (down-)sweeps.

The magnetostriction data show that uniaxial pressure along the c-axis leads to an increase in magnetization $M \parallel c$, whereas pressure applied perpendicular to the c-axis and for $B > B_c$ causes a decrease of the in-plane magnetization. At temperatures below T_C at magnetic fields $B < B_c$ in-plane stress also causes an increase in magnetization, with a sign change of $\partial M_\perp / \partial p_\perp$ at B_c. As the temperature rises towards T_C the magnitude of the pressure dependence increases for both axes, i.e., the magnetization becomes more susceptible to a change in pressure near T_C. This behavior is in line with the uniaxial pressure dependence of T_C obtained in the Grüneisen analysis above. The strongly negative dependence of T_C for uniaxial pressure applied along the in-plane direction leads to a shift of the paramagnetic phase to lower temperatures, so a decrease in magnetization is expected. Analogously, the phase boundary of the ferromagnetic phase shifts to higher temperatures for $p \parallel c$, such that at a constant temperature magnetization is expected to increase under uniaxial pressure. These findings are in line with a strengthening (weakening) of the uniaxial anisotropy constant for $p \parallel c$ ($p \perp c$) as stated above.

A quantitative evaluation of the pressure dependence of the magnetization, or equivalently the static magnetic susceptibility, shows pronounced peaks near T_C,

with values $\partial \ln(\chi_c)/\partial p_c$ close to $\pm 1000\%$/GPa (Fig. 5.20). Furthermore, for $B \perp c$ a strong rise in $\partial \ln(\chi_\perp)/\partial p_\perp$ only occurs above 50 K.

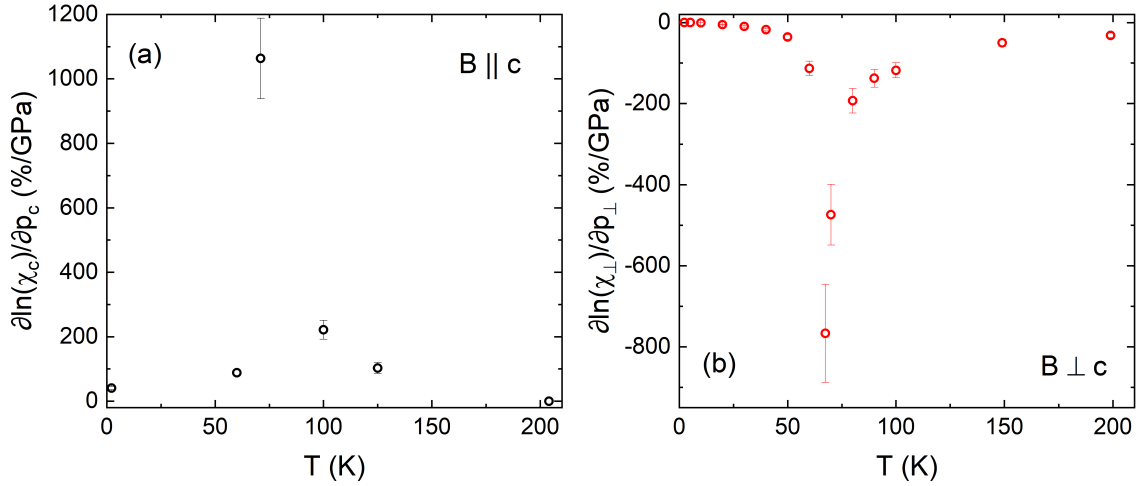

Figure 5.20: Uniaxial pressure dependence of the static magnetic suscetibility, $\partial \ln(\chi_i)/\partial p_i$, for (a) $B \parallel c$ and (b) $B \perp c$. Values up to 100 K were calculated from the maximum value of $\lambda_\perp$ and the magnetization at the corresponding field. Values at 125 K and above were calculated from λ_i at 15 T and a linear extrapolation of the isothermal magnetization up to this field.

From the quadratic-in-field behavior of the magnetostriction at low fields a temperature-dependent coupling constant $a(T)$ is obtained (Fig. 5.21). At 2 K it assumes a value of $-1.87 \cdot 10^{-4}/\mathrm{B}^2$ and increases in magnitude as the temperature is increased towards T_C, leading to a stronger magnetostriction effect at higher temperatures approaching T_C, in line with the increase in the pressure dependence of the magnetization discussed in the previous section. Moreover, the isothermal magnetization also shows a more rapid increase at low fields as temperature is increased towards T_C (Fig. 5.17(e) and (f)). This behavior can be linked to the evolution of the effective uniaxial anisotropy constant $K_{\mathrm{U,eff}}$ with temperature [141, 162]. As temperature increases, $K_{\mathrm{U,eff}}$ decreases and it becomes easier to rotate the magnetic moments towards the in-plane direction. Hence the coupling constant $a(T)$ increases. It therefore seems to be inversely linked to $K_{\mathrm{U,eff}}$.

To obtain the uniaxial pressure dependence of the critical field from the jumps in $\lambda_\perp$ and $\partial M/\partial B$ an Ehrenfest-like relation can be applied:

$$\left(\frac{\partial \mathrm{B_c}}{\partial p_\perp}\right)_\mathrm{T} = \frac{\Delta\lambda}{\Delta\left(\frac{\partial M}{\partial B}\right)_\mathrm{T}} \tag{5.5}$$

where $p_\perp$ is the uniaxial pressure, $\Delta\lambda$ the jump height in λ at the transition,

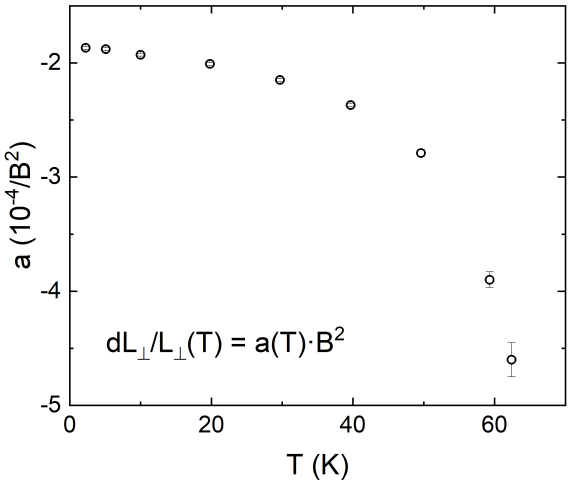

Figure 5.21: Coupling constant $a(T)$ extracted from square field dependence $dL_\perp(B)/L_\perp = a(T) \cdot B^2$ of the magnetostriction for $B \perp c$ at low fields. Error bars at low temperatures are about the size of the circles.

$\Delta(\partial \mathrm{M}/\partial \mathrm{B})$ the jump in the derivative of M(B) at B_c.

The analysis yields a strong uniaxial pressure dependence of the critical magnetic field of $\partial B_\mathrm{c}/\partial p_\perp = -3.7(6)$ T/GPa. This value remains approximately constant up to 60 K and implies that the low-temperature and high-field ferromagnetic phase is stabilized under an applied pressure $p \perp c$. Furthermore, uniaxial pressures $p \perp c$ on the order of 0.1 GPa are expected to be sufficient to suppress the low-temperature phase completely . The negative sign of $\partial B_\mathrm{c}/\partial p_\perp$ is in line with $\partial M_\perp/\partial p_\perp > 0$ above B_c and with $\partial M_\perp/\partial p_\perp < 0$ below B_c. This also agrees to a weakening of the uniaxial magnetic anisotropy along c. An overview of the extracted jump sizes and resulting pressure dependencies is given in Tab. 5.2.

In the magnetostriction data short-range correlations up to 150 K are also visible. Fig. 5.22 shows the high-temperature magnetostriction with a quadratic scaling of the x-coordinate. A system in the fully paramagnetic regime should yield a quadratic relationship $\Delta L(B)/L \sim B^2$ [97]. In Fig. 5.22 non-quadratic behavior is still visible at 149 K, indicating finite short-range correlations, while at 199 K fully paramagnetic behavior has set in.

In summary, the magnetostriction data in conjunction with measurements of the isothermal magnetization provide valuable insights into the magnetoelastic coupling in $Cr_2Ge_2Te_6$. A rotation of the magnetic moments leads to the negative quadratic-in-field magnetostriction for the in-plane direction, with a clear change in behavior as the moments are fully aligned with the applied magnetic field. The temperature dependence of the coupling correlates with the decrease of the effective uniaxial

Table 5.2: Temperatures, jump sizes and resulting calculated pressure dependence of B_c as well as change in bulk modulus $\Delta\kappa$ derived from an Ehrenfest-like thermodynamic analysis according to Eq. 5.5.

$B \perp c$: FM $(M \angle B) \rightarrow$ FM $(M \parallel B)$				
T (K) $\lambda_\perp$	$\Delta\lambda_\perp$ (10^{-5}/T)	T (K) $M(B)$	$\Delta(\partial M_\perp/\partial B)$ (μ_B/Cr)	$(\partial B_c/\partial p)_T$ (T/GPa)
2.25	19.3	2.2	–4.62	–3.7(6)
5.1	18.7	5	–4.60	–3.6(6)
10.0	19.0	10	–4.51	–3.8(6)
19.8	18.6	20	–4.49	–3.7(6)
29.7	17.9	30	–4.65	–3.5(5)
39.7	18.7	40	–4.82	–3.3(5)
49.6	24.1	50	–5.21	–3.2(5)
59.3	27.8	60	–5.42	–4.0(6)

anisotropy constant $K_{U,eff}$. Lastly, the derived uniaxial pressure dependence of the magnetization is strongly enhanced near T_C, in agreement with the large uniaxial pressure dependence of T_C.

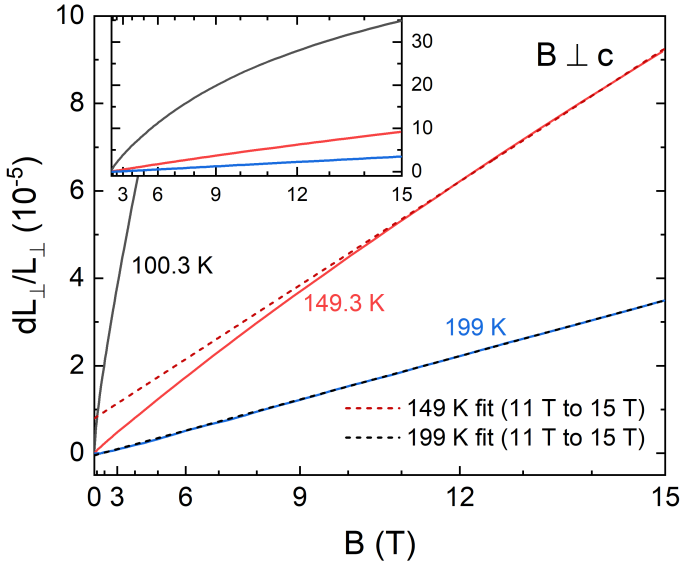

Figure 5.22: Magnetostriction dL/L at 100 K and above with a quadratic scaling of the x-coordinate. Dashed lines indicate linear fits in the range from 11 T to 15 T.

5.3.3 Phase Diagrams

Thermal expansion, magnetostriction and magnetization data presented above are used to construct the magnetic B vs. T phase diagrams for $B \parallel c$ and $B \perp c$ (Fig. 5.23). Overall trends in the phase diagram are visualized by color coding obtained from the magnetic contribution to the thermal expansion ($B \parallel c$, Fig. 5.23(a)) and the magnetostriction coefficients $\lambda_\perp$ ($B \perp c$, Fig. 5.23(b)) while extrema in α and λ are used to show the field and temperature dependencies of thermodynamic anomalies.

For $B \parallel c$ only a single phase transition, separating the paramagnetic (PM) high-temperature and ferromagnetic (FM) low-temperature phase is seen (Fig. 5.23(a)). The peaks in α_c (for low fields see Fig. 5.7(c)) mark the transition temperature (black triangles). Positions of the broad peaks in λ_c, which display a small hysteresis, are also shown (smaller red triangles). These peaks in λ_c signal a change of bending of the $dL(B)$ curves from right- to left-bending and are attributed to the crossover from para- to ferromagnetism. A horizontal red arrow in Fig. 5.23(a) visualizes the effect of uniaxial pressure $p \parallel c$ on the phase boundary, i.e., a stabilization of the low-temperature ferromagnetic phase. The pressure dependence of the magnetization is also indicated for the FM and PM phase.

For the in-plane direction an additional phase is seen in the magnetization and magnetostriction measurements. The magnetic fields corresponding to half the jump height in $\lambda_\perp$ and $\partial M_\perp/\partial B_\perp$ are marked in Fig. 5.23(b) by brown triangles and red diamonds, respectively. Upwards- (downwards-)pointing triangles signal magnetostriction up- (down-)sweeps. Black triangles again mark the peaks in $\alpha_\perp$, as shown for low fields in Fig. 5.7(d). The low-field phase has been described by Selter et al. as a phase where the magnetic moment initially points along the c-axis, i.e., along the direction of the uniaxial anisotropy, and is rotated gradually towards the direction of the applied field as B increases [141]. The phase transition at 0.44 T (2 K) then marks the saturation field. As shown above and illustrated by the red arrows in Fig. 5.23(b) uniaxial pressure $p \perp c$ suppresses T_C and B_c, destabilizing the low-field FM phase with respect to the PM and high-field FM phases. The phase diagrams presented here agree with those presented by Selter et al. from specific heat and $M(T)$ measurements [141].

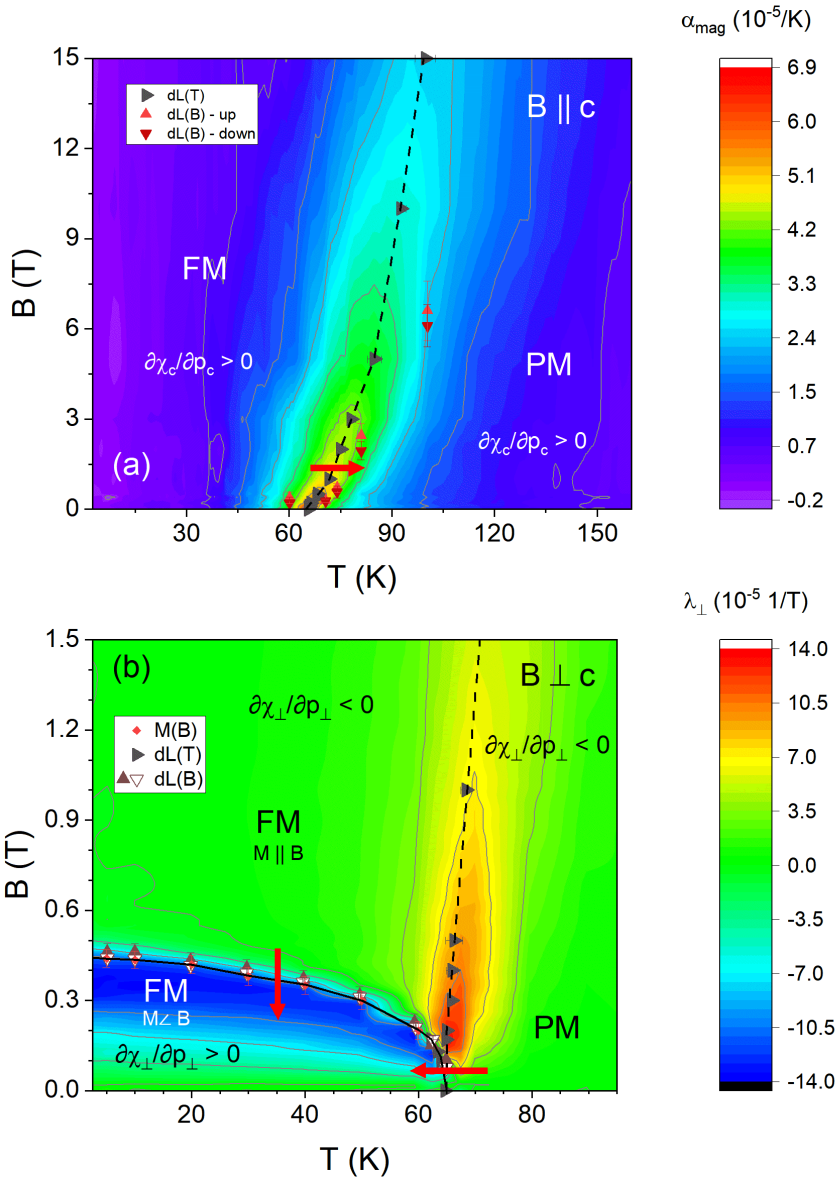

Figure 5.23: Magnetic phase diagram for (a) $B \parallel c$ and (b) $B \perp c$. Colors in (a) show $\alpha_{c,mag}$, in (b) $\lambda_\perp$. Symbols show anomalies detected in thermal expansion, magnetostriction and magnetization as described in the text. Red arrows indicate the uniaxial pressure dependence of the transition temperature or critical field for $p \parallel B$. The uniaxial pressure dependence of the static magnetic susceptibility is also indicated. Grey lines are contour lines.

5.4 Conclusion

The quasi-2D layered van der Waals compound $Cr_2Ge_2Te_6$ has been studied by high-resolution thermal expansion and magnetostriction, supported by magnetization and specific heat measurements. The Grüneisen parameter in zero-field reveals correlations up to 200 K, which are interpreted as a sign of 2D spin correlations. Such correlations have also been observed in related layered van der Waals compounds. A Grüneisen analysis uncovers large uniaxial pressure dependencies of opposite sign, $\partial T_C/\partial p_c = 74$ K/GPa and $\partial T_C/\partial p_\perp = -45$ K/GPa, and a moderate initial hydrostatic pressure dependence $dT/dp_{p\to 0} = -16$ K/GPa. An analysis of the critical scaling in the vicinity of T_C tentatively suggests a one-dimensional order parameter, i.e., 2D or 3D Ising spins. Applying a magnetic field of 15 T yields a strong enhancement of T_C and field effects up to high temperatures of about 200 K. For fields $B \perp c$ a negative quadratic-in-field magnetostriction is observed in the low-temperature and low-field phase. The coupling constant of this behavior correlates with the observed decrease of the effective uniaxial magnetic anisotropy constant. A calculation of the pressure dependence of the critical field from thermodynamic relations shows that the high-field phase is stabilized under pressure $p \perp c$. Furthermore, $Cr_2Ge_2Te_6$ exhibits a very large effect of pressure on the static magnetic susceptibility near T_C. This is in agreement with the strong effect of uniaxial pressure on T_C.

A possible explanation of the derived pressure dependencies is an enhancement (weakening) of the uniaxial magnetic anisotropy for uniaxial pressure applied along the stacking direction (*ab*-plane) of the van der Waals layers.

The large pressure effects and quasi-2D nature of magnetism in $Cr_2Ge_2Te_6$ present an intriguing playground for $Cr_2Ge_2Te_6$-based technological applications, bringing into reach room-temperature ferromagnetism in 2D materials. Chemically engineering this material holds the promise of expanding the toolkit of the semiconductor industry by adding the functionalities of intrinsic magnetism.

Chapter 6

Summary

In this work high-resolution thermal expansion and magnetostriction measurements on the correlated electron systems Gd_2PdSi_3, $Cu_3Bi(SeO_3)_2O_2Cl$, and $Cr_2Ge_2Te_6$ are presented. The investigated temperature window spans from 1.8 K to 300 K and magnetic fields up to 15 T are applied. The thermal expansion and magnetostriction are measured using a capacitive dilatometry setup which measures the absolute value of the capacitance with a resolution of 10^{-6} pF. This allows the detection of relative length changes on the order of $\Delta L/L \approx 10^{-8}$ to 10^{-9}, well below the resolution of X-ray or neutron diffraction techniques. In combination with magnetization and specific heat measurements both magnetic and structural phase transitions are investigated.

In the skyrmion-hosting intermetallic Gd_2PdSi_3 large spins of $S = 7/2$ are arranged on a triangular lattice. A delicate interplay of indirect exchange coupling mediated by the conduction electrons, i.e., the Rudermann-Kittel-Kasuya-Yosida (RKKY) interaction, dipole-dipole interactions and geometric frustration leads to complex incommensurate spin arrangements and the competition between nearly degenerate phases. A positive Curie-Weiss temperature and at the same time antiferromagnetic order are further signs of the strong competition between ferromagnetic and antiferromagnetic interactions in Gd_2PdSi_3, which result in a complex phase diagram. One of these phases is a field-induced skyrmion lattice phase, one of the first skyrmion phases found on a centrosymmetric lattice where Dzyaloshinskii-Moriya interactions are absent and other competing interactions are at the basis of the canted spin arrangement. Thermal expansion measurements of Gd_2PdSi_3 show magnetoelastic effects associated with incommensurate antiferromagnetic order at $T_{N1} = 22.3$ K and $T_{N2} = 19.7$ K, confirming the presence of two phase transitions around 20 K. Moreover, Grüneisen scaling unveils the evolution of an additional competing energy scale at T^* which was not seen in previous studies of this material. The nature of this weak phase transition can not be determined from thermodynamic measurements, but its presence is confirmed by measurements of the static magnetic susceptibility, although the signatures are weak. Detailed neutron diffraction and inelastic neutron

scattering studies, or other microscopic measurements of similar sensitivity, will be necessary to further elucidate the nature of the changes at T^*. Besides the changes at T^*, a Grüneisen analysis shows the onset of magnetic correlations around 60 K, well above T_N, and a weak uniaxial pressure dependence of the transition temperatures, $\partial T_{N,1}/\partial p_c = -1.3$ K/GPa and $\partial T_{N,1}/\partial p_{a^*} = 0.3$ K/GPa. In an applied magnetic field the correlation region extends significantly and strong field effects on the lattice are visible up to 200 K (150 K) for $B \parallel c$ ($B \parallel a^*$, i.e. $B \perp c$). The phase transitions show pronounced anomalies in the magnetostriction coefficient for $B \parallel c$, whereas they are much weaker and less well-defined for $B \parallel a^*$. It was previously believed that the IC-2 phase in Gd_2PdSi_3 extends to zero-field between T_{N1} and T_{N2}. In contrast, magnetization and magnetostriction measurements signal the presence of an additional phase boundary which separates the small pocket between T_{N1} and T_{N2} from the IC-2 phase, although their spin arrangements may be very similar. Analyzing the thermodynamic properties of the phase boundaries surrounding the skyrmion lattice phase shows that this phase is strongly enhanced by uniaxial pressure, similar to results for other skyrmion phases such as in Cu_2OSeO_3 and MnSi.

The physics of the multiferroic buckled-Kagomé francisite $Cu_3Bi(SeO_3)_2O_2Cl$ (CBSCl) is very different from Gd_2PdSi_3. Not only is it an insulator, such that there are no mechanisms involving interactions with conduction electrons, but in contrast to the nearly isotropic Gd spins, the Cu $S = 1/2$ spins show highly anisotropic behavior at low temperatures. In zero-field two phase transitions are detected by thermal expansion measurements between 2 K and 300 K: A structural phase transition at $T_S = 120.7(5)$ K, with critical exponents of $2\beta = 0.71(2)$ at T_S for the a- and c-axis as well as 0.77(2) for the b-axis, and an antiferromagnetic phase transition at $T_N = 26.4(3)$ K. The structural phase transition is unique to CBSCl among the francisites, owing to the small Cl ions which can move easily in the hexagonal channels in the lattice in contrast to bigger Br and I halide ions in other francisite compounds. The nature of this structural phase transition, a cooperative displacement of Cu and Cl ions introducing an antiferroelectric phase, is well studied both experimentally and from theoretical calculations. Grüneisen analysis reveals a large uniaxial pressure dependence of T_S, with $\partial T_S/\partial p_a = -19(6)$ K/GPa, $\partial T_S/\partial p_b = -5.7(1.1)$ K/GPa, and $\partial T_S/\partial p_c = 27(3)$ K/GPa, in contrast to a moderate hydrostatic pressure dependence of $dT_S/dp = 2.3(1.5)$ K/GPa. For the antiferromagnetic transition at $T_N = 26.4$ K, critical exponents of $\beta = 0.35(4)$ (b- and c-axis) and $\beta = 0.38(3)$ (a-axis), are obtained for power-law fits to the spontaneous strain, in the range of the 3D XY and 3D Heisenberg models, suggesting a three-dimensional order parameter and lattice dimensionality, $d = 3$ and $D = 3$. Uniaxial and hydrostatic pressure dependencies of T_N and the critical field, as well as the change in entropy at the antiferromagnetic (AFM) to ferromagnetic (FM)/paramagnetic (PM) phase boundaries for $B \parallel c$, are derived from thermodynamic relations. The analysis shows

that the AFM phase is stabilized for uniaxial pressure $p \parallel c, a$ whereas $p \parallel b$ stabilizes the PM phase. From magnetization measurements the magnetic phase diagrams for the a- and b-axis are constructed. Critical fields of $B_{\mathrm{c,a}} = 20.6$ T (obtained by extrapolation) and $B_{\mathrm{c,b}} = 7.1$ are observed at 2 K, slightly higher than previous calculations. The low-field AFM phase for $B \parallel c$ is especially interesting, holding the potential for technological applications which use the broadband absorption discovered in the phase transition window. Applying of a magnetic field $B \parallel c$ triggers the metamagnetic transition, a spin-flip of the antiferromagnetic layers to a ferromagnetic alignment, at a small critical field $B_{\mathrm{c,c}} = 0.8$ T. The transition region exhibits a mixed phase behavior above 0.4 T, analogous to the related francisite $Cu_3Bi(SeO_3)_2O_2Br$. In the mixed phase, a linear increase is observed in the magnetization $M(B)$ and magnetostriction $dL(B)$, i.e., a linear magnetoelastic coupling is present for $B \parallel c$. Different theoretical calculations have shown that many of the aspects of the magnetism in $Cu_3Bi(SeO_3)_2O_2Cl$ are well understood, e.g., observed spin-wave excitations have been modelled successfully. The present work adds a detailed high-resolution study of the lattice changes in CBSCl, in zero-temperature and especially in an applied magnetic field. The magnetic phase diagrams in the ab-plane have not been reported previously and the thermodynamic analysis provides insights into the effects of uniaxial pressure on the phase boundaries of CBSCl which had been missing to this point.

The quasi-two-dimensional (2D) layered van der Waals compound $Cr_2Ge_2Te_6$ is in the focus of much current research due to the discovery that it retains ferromagnetism down to the bilayer. In the bulk form it is a ferromagnetic semiconductor with $T_{\mathrm{C}} \approx 65$ K and promising both for investigating fundamental physics such as two-dimensional excitations, and for novel technological applications. The magnetocrystalline anisotropy in quasi-2D materials is also of great interest to the scientific community, for if it can be controlled purposefully, transition temperatures can be engineered and large-scale technological applications are within reach. Zero-field thermal expansion measurements of $Cr_2Ge_2Te_6$ reveal magnetic contributions to the thermal expansion up to 200 K. Results from Electron Spin Resonance experiments on $Cr_2Ge_2Te_6$ have shown deviations from paramagnetic behavior up to about 150 K before. Similar correlations have also been observed in related layered van der Waals compounds, and are interpreted as a sign of short-range 2D spin correlations up to high temperatures. An analysis of the critical behavior in the vicinity of T_{C} tentatively suggests a one-dimensional order parameter, i.e., 2D or 3D Ising spins, with a logarithmic divergence of α_i. However, the critical exponents have to be taken with caution, because they show large error bars and a clear distinction between the exponents for Ising, XY, and Heisenberg models is not possible. Importantly, $Cr_2Ge_2Te_6$ shows very large effects of uniaxial pressure on T_{C}. A Grüneisen analysis yields $\partial T_{\mathrm{C}}/\partial p_{\mathrm{c}} = 74$ K/GPa and $\partial T_{\mathrm{C}}/\partial p_{\perp} = -45$ K/GPa, i.e.,

a strong enhancement for pressure perpendicular to the van der Waals layers, and a strong suppression of T_C for in-plane stress. A moderate initial hydrostatic pressure dependence $dT/dp_{p\to 0} = -16$ K/GPa is in line with other reports. Applying a large magnetic field of 15 T yields a strong enhancement of T_C and field effects on the lattice up to high temperatures of about 200 K for both the cross-plane and in-plane directions. For fields $B \perp c$ a negative quadratic-in-field magnetostriction is observed in the low-temperature and low-field phase, with an increasingly negative coupling constant as the temperature is increased towards T_C. The pressure dependence of the critical field is calculated and shows that the high-field phase is stabilized under pressure $p \perp c$. Furthermore, the pressure dependence of the static magnetic susceptibility near T_C is found to be very large as a result of the large uniaxial pressure dependence of T_C itself. The derived pressure dependencies can be explained by an enhancement of the uniaxial magnetic anisotropy for uniaxial pressure applied along the stacking-direction of van der Waals layers. Uniaxial pressure along the *ab*-plane, in contrast, weakens the uniaxial magnetic anisotropy. The large pressure effects and quasi-2D nature of magnetism in $Cr_2Ge_2Te_6$ present an intriguing playground for $Cr_2Ge_2Te_6$-based technological applications, bringing room temperature ferromagnetism in 2D materials into reach. For further investigations of a possible transition from 2D to 3D behavior in $Cr_2Ge_2Te_6$ measurements using highly sensitive microscopic techniques such as the high-multipole nonlinear optical polarimetry used on $Cr_2Si_2Te_6$ will be necessary.

The electronic properties of the three compounds investigated in this work, a metal, a semiconductor and an insulator, are extremely different. What joins them, however, are the presence of spin-lattice coupling and critical phenomena at continuous phase transitions as well as the competition between different degrees of freedom. The thermodynamic methods applied in this work reveal these competing interactions as well as the effects of pressure on the different phases, especially by analyzing the Grüneisen parameter of the different systems. The unparalleled resolution of capacitance dilatometry thereby proves valuable in detecting even weak phase transitions and analyzing critical behavior.

List of Publications

1. D. Rout, S. R. Mudi, M. Hoffmann, **S. Spachmann**, R. Klingeler, and S. Singh:
   Structural and physical properties of trilayer nickelates $R_4Ni_3O_{10}$ (R = La, Pr, and Nd)
   Physical Review B 102, 195144 (2020).
2. R. Ohlendorf, **S. Spachmann**, L. Fischer, K. Dey, D. Brunt, G. Balakrishnan, O. A. Petrenko, and R. Klingeler:
   Magnetoelastic coupling and Grüneisen scaling in NdB_4
   Physical Review B 103, 104424 (2021).
3. S. Tripathi, S. Vaidya, N. Ahmed, E. Andreasen Klahn, H. Cao, L. Spillecke, C. Koo, **S. Spachmann**, R. Klingeler, G. Rajaraman, J. Overgaard, and M. Shanmugam:
   Structure-property correlation in stabilizing axial magnetic anisotropy in octahedral Co(II) complexes
   Cell Reports Physical Science 2, 100404 (2021).
4. **S. Spachmann**, A. Elghandour, M. Frontzek, W. Löser, and R. Klingeler:
   Magnetoelastic Coupling and Phases in the Skyrmion Lattice Magnet Gd_2PdSi_3 Discovered by High-resolution Dilatometry
   Physical Review B (accepted) (2021).
5. E. S. Kozlyakova, A. Moskin, P. S. Berdonosov, V. V. Gapontsev, S. V. Streltsov, Y. Skourski, **S. Spachmann**, A. Elghandour, R. Klingeler, and A. N. Vasiliev:
   Quasi-1D XY antiferromagnet $Sr_2Ni(SeO_3)_2Cl_2$ at Sakai-Takahashi phase diagram
   Submitted to Scientific Reports (2021).

Bibliography

1. C. Broholm, R. J. Cava, S. A. Kivelson, D. G. Nocera, M. R. Norman, and T. Senthil, Science **367**, 10.1126/science.aay0668 (2020).
2. J. M. Kosterlitz and D. J. Thouless, Journal of Physics C: Solid State Physics **5**, L124–L126 (1972).
3. V. L. Berezinskii, Sov. Phys. JETP **34**, 610–616 (1972).
4. J. M. Kosterlitz and D. J. Thouless, Journal of Physics C: Solid State Physics **6**, 1181–1203 (1973).
5. F. D. M. Haldane, Physics Letters A **93**, 464–468 (1983).
6. A. Vasiliev, O. Volkova, E. Zvereva, and M. Markina, npj Quantum Materials **3**, 18 (2018).
7. D. I. Khomskii, *Transition metal compounds* (Cambridge University Press, 2014).
8. P. Fazekas, *Lecture Notes on Electron Correlation and Magnetism*, Vol. Volume 5 (World Scientific, 1999), p. 796.
9. T. H. K. Barron and G. K. White, *Heat capacity and thermal expansion at low temperatures* (1999).
10. A. Fert, N. Reyren, and V. Cros, Nature Reviews Materials **2**, 17031 (2017).
11. A. P. Ramirez, Annual Review of Materials Science **24**, 453–480 (1994).
12. B. A. Trump, S. M. Koohpayeh, K. J. T. Livi, J.-J. Wen, K. E. Arpino, Q. M. Ramasse, R. Brydson, M. Feygenson, H. Takeda, M. Takigawa, K. Kimura, S. Nakatsuji, C. L. Broholm, and T. M. McQueen, Nature Communications **9**, 2619 (2018).
13. Z.-Y. Pan, C.-D. Cao, X.-J. Bai, R.-B. Song, J.-B. Zheng, and L.-B. Duan, Chinese Physics B **22**, 056102 (2013).
14. T. Kurumaji, T. Nakajima, M. Hirschberger, A. Kikkawa, Y. Yamasaki, H. Sagayama, H. Nakao, Y. Taguchi, T. Arima, and Y. Tokura, Science **365**, 914–918 (2019).

15. I. Rousochatzakis, J. Richter, R. Zinke, and A. A. Tsirlin, Physical Review B **91**, 024416 (2015).
16. E. Constable, S. Raymond, S. Petit, E. Ressouche, F. Bourdarot, J. Debray, M. Josse, O. Fabelo, H. Berger, S. de Brion, and V. Simonet, Physical Review B **96**, 014413 (2017).
17. H. C. Wu, W. J. Tseng, P. Y. Yang, K. D. Chandrasekhar, H. Berger, and H. D. Yang, Journal of Physics D: Applied Physics **50**, 265002 (2017).
18. N. D. Mermin and H. Wagner, Physical Review Letters **17**, 1133–1136 (1966).
19. L. Onsager, Physical Review **65**, 117–149 (1944).
20. C. Gong, L. Li, Z. Li, H. Ji, A. Stern, Y. Xia, T. Cao, W. Bao, C. Wang, Y. Wang, Z. Q. Qiu, R. J. Cava, S. G. Louie, J. Xia, and X. Zhang, Nature **546**, 265–269 (2017).
21. X. Zhang, Y. Zhao, Q. Song, S. Jia, J. Shi, and W. Han, Japanese Journal of Applied Physics **55**, 033001 (2016).
22. Z. Lin, M. Lohmann, Z. A. Ali, C. Tang, J. Li, W. Xing, J. Zhong, S. Jia, W. Han, S. Coh, W. Beyermann, and J. Shi, Physical Review Materials **2**, 051004 (2018).
23. K. Everschor-Sitte, J. Masell, R. M. Reeve, and M. Kläui, Journal of Applied Physics **124**, 240901 (2018).
24. N. A. Spaldin, Proceedings of the Royal Society A: Mathematical, Physical and Engineering Sciences **476**, 20190542 (2020).
25. C. Gong and X. Zhang, Science **363**, `10.1126/science.aav4450` (2019).
26. R. Küchler, T. Bauer, M. Brando, and F. Steglich, Review of Scientific Instruments **83**, 095102 (2012).
27. S. J. Blundell and K. M. Blundell, *Concepts in thermal physics* (Oxford University Press, Oxford, 2006).
28. S. Blundell, *Magnetism in condensed matter*, Oxford Master Series in Condensed Matter Physics (Oxford University Press, 2003).
29. T. Vojta, Annalen der Physik **9**, 403–440 (2000).
30. J.-C. Zhao, MRS Bulletin **34**, 92–94 (2009).
31. Wikipedia, *Thermodynamic Square – Wikipedia, The Free Encyclopedia*, English, [Online; accessed April 29, 2021], `https://en.wikipedia.org/wiki/Thermodynamic_square`.
32. L. T. Klauder, American Journal of Physics **36**, 556–557 (1968).
33. R. F. Fox, Journal of Chemical Education **53**, 441 (1976).

34. J. M. Phillips, Journal of Chemical Education **64**, 674 (1987).
35. E. Grüneisen, Annalen der Physik **344**, 257–306 (1912).
36. R. Gross and A. Marx, *Festkörperphysik*, Third Edition, De Gruyter Online (De Gruyter, Berlin, 2018).
37. L. P. Kadanoff, Physics Physique Fizika **2**, 263–272 (1966).
38. B. Widom, The Journal of Chemical Physics **43**, 3892–3897 (1965).
39. R. B. Griffiths, Physical Review Letters **24**, 1479–1482 (1970).
40. S. Blundell, *Magnetism in condensed matter*, 2003.
41. A. Pelissetto and E. Vicari, Physics Reports **368**, 549–727 (2002).
42. J. C. Le Guillou and J. Zinn-Justin, Physical Review B **21**, 3976–3998 (1980).
43. T. H. K. Barron, J. G. Collins, and G. K. White, Advances in Physics **29**, 609–730 (1980).
44. N. Kabeya, K. Imura, K. Deguchi, and N. K. Sato, Journal of the Physical Society of Japan **80**, SA098 (2011).
45. J. Clay and F. Van Der Maesen, Physica **15**, 467–480 (1949).
46. R. Pott and R. Schefzyk, Journal of Physics E: Scientific Instruments **16**, 444–449 (1983).
47. R. Küchler, A. Wörl, P. Gegenwart, M. Berben, B. Bryant, and S. Wiedmann, Review of Scientific Instruments **88**, 083903 (2017).
48. Andeen-Hagerling Inc., *AH 2550A 1 kHz Ultra-Precision Capacitance Bridge*, (Jan. 5, 2021) `http://www.andeen-hagerling.com/ah2550a.htm`.
49. B. Tran, 'Thermal expansion and magnetostriction studies on R2PdSi3 (R = Ho, Dy) single crystals', Master Thesis (Ruprecht-Karls-Universität, Heidelberg, 2016).
50. F. R. Kroeger and C. A. Swenson, Journal of Applied Physics **48**, 853–864 (1977).
51. S. Krippendorf, 'Installation und kalibration eines neuen kapazitätsdilatometers und untersuchung von LiFePO4-einkristallen', Master Thesis (Ruprecht-Karls-Universität, Heidelberg, 2016).
52. M. Hoffmann, 'High-resolution capacitance dilatometry studies on transition metal oxides', Master Thesis (Ruprecht-Karls-Universität, Heidelberg, 2020).
53. S. Spachmann, A. Elghandour, M. Frontzek, W. Löser, and R. Klingeler, Physical Review B (accepted) (2021).

54. R.-D. Hoffmann and R. Pöttgen, Zeitschrift für Kristallographie - Crystalline Materials **216**, 127–145 (2001).

55. S. Majumdar and E. V. Sampathkumaran, Physical Review B **63**, 172407 (2001).

56. S. Majumdar, E. V. Sampathkumaran, P. L. Paulose, H. Bitterlich, W. Löser, and G. Behr, Physical Review B **62**, 14207–14211 (2000).

57. S. Majumdar, H. Bitterlich, G. Behr, W. Löser, P. L. Paulose, and E. V. Sampathkumaran, Physical Review B **64**, 012418 (2001).

58. P. L. Paulose, E. V. Sampathkumaran, H. Bitterlich, G. Behr, and W. Löser, Physical Review B **67**, 212401 (2003).

59. C. D. Cao, R. Klingeler, H. Vinzelberg, N. Leps, W. Löser, G. Behr, F. Muranyi, V. Kataev, and B. Büchner, Physical Review B **82**, 134446 (2010).

60. M. Hirschberger, T. Nakajima, M. Kriener, T. Kurumaji, L. Spitz, S. Gao, A. Kikkawa, Y. Yamasaki, H. Sagayama, H. Nakao, S. Ohira-Kawamura, Y. Taguchi, T. H. Arima, and Y. Tokura, Physical Review B **101**, 220401(R) (2020).

61. S. Majumdar, M. Mahesh Kumar, R. Mallik, and E. Sampathkumaran, Solid State Communications **110**, 509–514 (1999).

62. S. R. Saha, H. Sugawara, T. D. Matsuda, Y. Aoki, H. Sato, and E. V. Sampathkumaran, Physical Review B **62**, 425–429 (2000).

63. S. Majumdar, E. V. Sampathkumaran, S. Berger, M. Della Mea, H. Michor, E. Bauer, M. Brando, J. Hemberger, and A. Loidl, Solid State Communications **121**, 665–668 (2002).

64. D. Kaczorowski and H. Noel, Journal of Physics: Condensed Matter **5**, 9185–9195 (1993).

65. C. Tien, L. Luo, and J. S. Hwang, Physical Review B **56**, 11710–11714 (1997).

66. D. X. Li, A. Dönni, Y. Kimura, Y. Shiokawa, Y. Homma, Y. Haga, E. Yamamoto, T. Honma, and Y. Onuki, Journal of Physics: Condensed Matter **11**, 8263–8274 (1999).

67. D. X. Li, S. Nimori, Y. Shiokawa, Y. Haga, E. Yamamoto, and Y. Onuki, Physical Review B **68**, 012413 (2003).

68. S. R. Saha, H. Sugawara, T. D. Matsuda, H. Sato, R. Mallik, and E. V. Sampathkumaran, Physical Review B **60**, 12162–12165 (1999).

69. M. Hirschberger, L. Spitz, T. Nomoto, T. Kurumaji, S. Gao, J. Masell, T. Nakajima, A. Kikkawa, Y. Yamasaki, H. Sagayama, H. Nakao, Y. Taguchi, R. Arita, T. H. Arima, and Y. Tokura, Physical Review Letters **125**, 076602 (2020).

70. A. Szytuła, M. Hofmann, B. Penc, M. Ślaski, S. Majumdar, E. V. Sampathkumaran, and A. Zygmunt, Journal of Magnetism and Magnetic Materials **202**, 365–375 (1999).

71. F. Tang, M. Frontzek, J. Dshemuchadse, T. Leisegang, M. Zschornak, R. Mietrach, J.-U. Hoffmann, W. Löser, S. Gemming, D. C. Meyer, and M. Loewenhaupt, Physical Review B **84**, 104105 (2011).

72. F. Tang, P. Link, M. Frontzek, A. Schneidewind, W. Löser, and M. Loewenhaupt, Journal of Physics: Conference Series **251**, 012004 (2010).

73. M. Frontzek, 'Magnetic properties of R2PdSi3 (R = heavy rare earth) compounds', Ph.D. Thesis (Technische Universität Dresden, 2009).

74. M. Smidman, C. Ritter, D. T. Adroja, S. Rayaprol, T. Basu, E. V. Sampathkumaran, and A. D. Hillier, Physical Review B **100**, 134423 (2019).

75. K. Mukherjee, T. Basu, K. K. Iyer, and E. V. Sampathkumaran, Physical Review B **84**, 184415 (2011).

76. H. Zhang, Q. Huang, L. Hao, J. Yang, K. Noordhoek, S. Pandey, H. Zhou, and J. Liu, arXiv (2020).

77. I. Mazilu, 'Einkristallzüchtung und Konstitutionsuntersuchungen von magnetisch geordneten Seltenerd-Übergangsmetallverbindungen', Ph.D. Thesis (Technische Universität Darmstadt, 2006).

78. Y. Xu, M. Frontzek, I. Mazilu, W. Löser, G. Behr, B. Büchner, and L. Liu, Journal of Crystal Growth **318**, 942–946 (2011).

79. D. S. Inosov, D. V. Evtushinsky, A. Koitzsch, V. B. Zabolotnyy, S. V. Borisenko, A. A. Kordyuk, M. Frontzek, M. Loewenhaupt, W. Löser, I. Mazilu, H. Bitterlich, G. Behr, J.-U. Hoffmann, R. Follath, and B. Büchner, Physical Review Letters **102**, 046401 (2009).

80. J. Werner, W. Hergett, M. Gertig, J. Park, C. Koo, and R. Klingeler, Physical Review B **95**, 214414 (2017).

81. C. Cao, C. G. F. Blum, T. Ritschel, S. Rodan, L. Giebeler, D. Bombor, S. Wurmehl, and W. Löser, CrystEngComm **15**, 9052–9056 (2013).

82. A. Tari, *The specific heat of matter at low temperatures* (Published by Imperial College Press and distributed by World Scientific Publishing Co., 2003).

83. P. Gegenwart, Rep. Prog. Phys. **79**, 114502 (2016).

84. R. Klingeler, J. Geck, S. Arumugam, N. Tristan, P. Reutler, B. Büchner, L. Pinsard-Gaudart, and A. Revcolevschi, Physical Review B **73**, 214432 (2006).

85. V. M. Kalita, A. F. Lozenko, and S. M. Ryabchenko, Low Temperature Physics **26**, 489–493 (2000).

86. V. M. Kalita, A. F. Lozenko, and P. A. Trotsenko, Low Temperature Physics **28**, 263–266 (2002).

87. K. Dey, S. Sauerland, B. Ouladdiaf, K. Beauvois, H. Wadepohl, and R. Klingeler, Physical Review B **103**, 134438 (2021).

88. M. Hirschberger et al., Nature Communications **10**, 1–9 (2019).

89. R. Klingeler, B. Büchner, S.-W. Cheong, and M. Hücker, Physical Review B **72**, 104424 (2005).

90. A. Bauer, M. Garst, and C. Pfleiderer, Physical Review Letters **110**, 177207 (2013).

91. I. Levatić, P. Popčević, V. Šurija, A. Kruchkov, H. Berger, A. Magrez, J. S. White, H. M. Rønnow, and I. Živković, eng, Scientific reports **6**, 21347 (2016).

92. A. Chacon, A. Bauer, T. Adams, F. Rucker, G. Brandl, R. Georgii, M. Garst, and C. Pfleiderer, Physical Review Letters **115**, 267202 (2015).

93. Y. Nii, T. Nakajima, A. Kikkawa, Y. Yamasaki, K. Ohishi, J. Suzuki, Y. Taguchi, T. Arima, Y. Tokura, and Y. Iwasa, Nature Communications **6**, 8539 (2015).

94. S. Hayami, S.-Z. Lin, and C. D. Batista, Physical Review B **93**, 184413 (2016).

95. R. Mallik, E. V. Sampathkumaran, M. Strecker, and G. Wortmann, Europhysics Letters **41**, 315–320 (1998).

96. Z. Wang, K. Barros, G.-W. Chern, D. L. Maslov, and C. D. Batista, Physical Review Letters **117**, 206601 (2016).

97. N. Johannsen, A. Vasiliev, A. Oosawa, H. Tanaka, and T. Lorenz, Physical Review Letters **95**, 017205 (2005).

98. C. Lacroix, P. Mendels, and F. Mila, eds., *Introduction to Frustrated Magnetism*, 1st ed., Vol. 164, Springer Series in Solid-State Sciences (Springer-Verlag Berlin Heidelberg, 2011).

99. P. Mendels and F. Bert, Comptes Rendus Physique **17**, Physique de la matière condensée au XXIe siècle: l'héritage de Jacques Friedel, 455–470 (2016).

100. M. Pregelj, A. Zorko, O. Zaharko, P. Jeglič, Z. Kutnjak, Z. Jagličić, S. Jazbec, H. Luetkens, A. D. Hillier, H. Berger, and D. Arčon, Physical Review B **88**, 224421 (2013).

101. K. Yoo, B. Koteswararao, J. Kang, A. Shahee, W. Nam, F. F. Balakirev, V. S. Zapf, N. Harrison, A. Guda, N. Ter-Oganessian, and K. H. Kim, npj Quantum Materials **3**, 1–9 (2018).

102. I. Cabrera, M. Kenzelmann, G. Lawes, Y. Chen, W. C. Chen, R. Erwin, T. R. Gentile, J. B. Leão, J. W. Lynn, N. Rogado, R. J. Cava, and C. Broholm, Physical Review Letters **103**, 087201 (2009).

103. Q. Zhang, W. Knafo, P. Adelmann, P. Schweiss, K. Grube, N. Qureshi, T. Wolf, H. v. Löhneysen, and C. Meingast, Physical Review B **84**, 184429 (2011).

104. N. A. Spaldin and M. Fiebig, Science **309**, 391–392 (2005).

105. S. Manipatruni, D. E. Nikonov, and I. A. Young, Nature Physics **14**, 338–343 (2018).

106. D. Khomskii, Physics **2**, 10.1103/physics.2.20 (2009).

107. M. Fiebig, T. Lottermoser, D. Meier, and M. Trassin, Nature Reviews Materials **1**, 16046 (2016).

108. N. A. Spaldin and R. Ramesh, Nature Materials **18**, 203–212 (2019).

109. A. Pring, B. M. Gatehouse, and W. D. Birch, American Mineralogist **75**, 1421–1425 (1990).

110. V. Gnezdilov, Y. Pashkevich, P. Lemmens, V. Kurnosov, P. Berdonosov, V. Dolgikh, E. Kuznetsova, V. Pryadun, K. Zakharov, and A. Vasiliev, Physical Review B **96**, 115144 (2017).

111. S. A. Nikolaev, V. V. Mazurenko, A. A. Tsirlin, and V. G. Mazurenko, Physical Review B **94**, 144412 (2016).

112. C. Milesi-Brault, C. Toulouse, E. Constable, H. Aramberri, V. Simonet, S. de Brion, H. Berger, L. Paolasini, A. Bosak, J. Íñiguez, and M. Guennou, Physical Review Letters **124**, 097603 (2020).

113. M. Pregelj, O. Zaharko, A. Zorko, M. Gomilšek, O. Sendetskyi, A. Günther, M. Ozerov, S. A. Zvyagin, H. Luetkens, C. Baines, V. Tsurkan, and A. Loidl, Advanced Functional Materials **25**, 3634–3640 (2015).

114. M. Pregelj, O. Zaharko, A. Günther, A. Loidl, V. Tsurkan, and S. Guerrero, Physical Review B **86**, 144409 (2012).

115. M. Markina, *Private communication.*

116. M. Braden, G. Wilkendorf, J. Lorenzana, M. Ain, G. J. McIntyre, M. Behruzi, G. Heger, G. Dhalenne, and A. Revcolevschi, Physical Review B **54**, 1105–1116 (1996).

117. B. Fåk, E. Kermarrec, L. Messio, B. Bernu, C. Lhuillier, F. Bert, P. Mendels, B. Koteswararao, F. Bouquet, J. Ollivier, A. D. Hillier, A. Amato, R. H. Colman, and A. S. Wills, Physical Review Letters **109**, 037208 (2012).

118. R. Nath, A. A. Tsirlin, P. Khuntia, O. Janson, T. Förster, M. Padmanabhan, J. Li, Y. Skourski, M. Baenitz, H. Rosner, and I. Rousochatzakis, Physical Review B **87**, 214417 (2013).

119. P. Millet, B. Bastide, V. Pashchenko, S. Gnatchenko, V. Gapon, Y. Ksari, and A. Stepanov, J. Mater. Chem. **11**, 1152–1157 (2001).

120. K. H. Miller, P. W. Stephens, C. Martin, E. Constable, R. A. Lewis, H. Berger, G. L. Carr, and D. B. Tanner, Physical Review B **86**, 174104 (2012).

121. D. A. Prishchenko, A. A. Tsirlin, V. Tsurkan, A. Loidl, A. Jesche, and V. G. Mazurenko, Physical Review B **95**, 064102 (2017).

122. R. Blinc and B. Žekš, *Soft modes in ferroelectrics and antiferroelectrics*, 1st ed., Vol. 13, Series of monographs on selected topics in solid state physics (American Elsevier Publishing Company, 1974).

123. G. Venkataraman, Bulletin of Materials Science **1**, 129–170 (1979).

124. M. E. Fisher, The Philosophical Magazine: A Journal of Theoretical Experimental and Applied Physics **7**, 1731–1743 (1962).

125. A. F. G. Wyatt, Journal of Physics C: Solid State Physics **1**, 684–686 (1968).

126. E. Stryjewski and N. Giordano, Advances in Physics **26**, 487–650 (1977).

127. O. Hellwig, A. Berger, J. B. Kortright, and E. E. Fullerton, Journal of Magnetism and Magnetic Materials **319**, 13–55 (2007).

128. N. S. Kiselev, C. Bran, U. Wolff, L. Schultz, A. N. Bogdanov, O. Hellwig, V. Neu, and U. K. Rößler, Physical Review B **81**, 054409 (2010).

129. A. Zorko, M. Gomilšek, M. Pregelj, M. Ozerov, S. A. Zvyagin, A. Ozarowski, V. Tsurkan, A. Loidl, and O. Zaharko, AIP Advances **6**, 056210 (2016).

130. A. K. Zvezdin, I. Zorin, A. M. Kadomtseva, I. B. Krynetskii, A. S. Moskvin, and A. A. Mukhin, Zhurnal Eksperimental'noi i Teoreticheskoi Fiziki **88**, 1098–1102 (1985).

131. R. A. M. Scott and J. C. Anderson, Journal of Applied Physics **37**, 234–237 (1966).

132. N. Aliouane, D. N. Argyriou, J. Strempfer, I. Zegkinoglou, S. Landsgesell, and M. v. Zimmermann, Physical Review B **73**, 020102 (2006).

133. R. R. Birss and J. C. Anderson, Proceedings of the Physical Society **81**, 1139–1140 (1963).

134. Z. Wang, M. Schmidt, Y. Goncharov, V. Tsurkan, H.-A. Krug von Nidda, A. Loidl, and J. Deisenhofer, Physical Review B **86**, 174411 (2012).

135. B. Huang, G. Clark, E. Navarro-Moratalla, D. R. Klein, R. Cheng, K. L. Seyler, D. Zhong, E. Schmidgall, M. A. McGuire, D. H. Cobden, W. Yao, D. Xiao, P. Jarillo-Herrero, and X. Xu, Nature **546**, 270–273 (2017).

136. K. S. Novoselov, A. K. Geim, S. V. Morozov, D. Jiang, Y. Zhang, S. V. Dubonos, I. V. Grigorieva, and A. A. Firsov, Science **306**, 666–669 (2004).

137. S. Hatayama, Y. Sutou, S. Shindo, Y. Saito, Y.-H. Song, D. Ando, and J. Koike, ACS Applied Materials & Interfaces **10**, 2725–2734 (2018).

138. V. Ostwal, T. Shen, and J. Appenzeller, Advanced Materials **32**, 1906021 (2020).

139. V. Carteaux, D. Brunet, G. Ouvrard, and G. Andre, Journal of Physics: Condensed Matter **7**, 69–87 (1995).

140. J. Zeisner, A. Alfonsov, S. Selter, S. Aswartham, M. P. Ghimire, M. Richter, J. van den Brink, B. Büchner, and V. Kataev, Physical Review B **99**, 165109 (2019).

141. S. Selter, G. Bastien, A. U. B. Wolter, S. Aswartham, and B. Büchner, Physical Review B **101**, 014440 (2020).

142. Quantum Design, SQUID-VSM Application Note 1500-015 ((Quantum Design, 2010)).

143. A. Elghandour, *Private communication.*

144. G. T. Lin, H. L. Zhuang, X. Luo, B. J. Liu, F. C. Chen, J. Yan, Y. Sun, J. Zhou, W. J. Lu, P. Tong, Z. G. Sheng, Z. Qu, W. H. Song, X. B. Zhu, and Y. P. Sun, Physical Review B **95**, 245212 (2017).

145. Y. Sun, W. Tong, and X. Luo, Phys. Chem. Chem. Phys. **21**, 25220–25225 (2019).

146. M. Suzuki, B. Gao, K. Koshiishi, S. Nakata, K. Hagiwara, C. Lin, Y. X. Wan, H. Kumigashira, K. Ono, S. Kang, S. Kang, J. Yu, M. Kobayashi, S.-W. Cheong, and A. Fujimori, Physical Review B **99**, 161401 (2019).

147. T. J. Williams, A. A. Aczel, M. D. Lumsden, S. E. Nagler, M. B. Stone, J.-Q. Yan, and D. Mandrus, Physical Review B **92**, 144404 (2015).

148. S. Calder, A. V. Haglund, A. I. Kolesnikov, and D. Mandrus, Physical Review B **103**, 024414 (2021).

149. X. Qian, P. Jiang, P. Yu, X. Gu, Z. Liu, and R. Yang, Applied Physics Letters **112**, 241901 (2018).

150. Z.-Y. Ong and M.-H. Bae, 2D Materials **6**, 032005 (2019).

151. S. Chen, A. Sood, E. Pop, K. E. Goodson, and D. Donadio, 2D Materials **6**, 025033 (2019).

152. Y. Sun, R. C. Xiao, G. T. Lin, R. R. Zhang, L. S. Ling, Z. W. Ma, X. Luo, W. J. Lu, Y. P. Sun, and Z. G. Sheng, Applied Physics Letters **112**, 072409 (2018).

153. T. Sakurai, B. Rubrecht, L. T. Corredor, R. Takehara, M. Yasutani, J. Zeisner, A. Alfonsov, S. Selter, S. Aswartham, A. U. B. Wolter, B. Büchner, H. Ohta, and V. Kataev, Physical Review B **103**, 024404 (2021).

154. A. O. Fumega, S. Blanco-Canosa, H. Babu-Vasili, P. Gargiani, H. Li, J.-S. Zhou, F. Rivadulla, and V. Pardo, J. Mater. Chem. C **8**, 13582–13589 (2020).

155. J. B. Goodenough, *Magnetism and the chemical bond* (Interscience Publishers. New York, London, 1963).

156. W. Ge, K. Xu, W. Xia, Z. Yu, H. Wang, X. Liu, J. Zhao, X. Wang, N. Yu, Z. Zou, Z. Yan, L. Wang, M. Xu, and Y. Guo, Journal of Alloys and Compounds **819**, 153368 (2020).

157. E. Dong, B. Liu, Q. Dong, X. Shi, X. Ma, R. Liu, X. Zhu, X. Luo, X. Li, Y. Li, Q. Li, and B. Liu, Physica B: Condensed Matter **595**, 412344 (2020).

158. S. Mondal, M. Kannan, M. Das, L. Govindaraj, R. Singha, B. Satpati, S. Arumugam, and P. Mandal, Physical Review B **99**, 180407 (2019).

159. S. Son, M. J. Coak, N. Lee, J. Kim, T. Y. Kim, H. Hamidov, H. Cho, C. Liu, D. M. Jarvis, P. A. C. Brown, J. H. Kim, C.-H. Park, D. I. Khomskii, S. S. Saxena, and J.-G. Park, Physical Review B **99**, 041402 (2019).

160. J. Arneth, M. Jonak, S. Spachmann, M. Abdel-Hafiez, and R. Klingeler, *Uniaxial pressure effects in the two-dimensional van-der-waals ferromagnet CrI3*.

161. L. Wang, B. Tran, M. He, C. Meingast, M. Abdel-Hafiez, C. Cao, H. Bitterlich, W. Löser, and R. Klingeler, Journal of the Physical Society of Japan **88**, 094709 (2019).

162. S. Khan, C. W. Zollitsch, D. M. Arroo, H. Cheng, I. Verzhbitskiy, A. Sud, Y. P. Feng, G. Eda, and H. Kurebayashi, Physical Review B **100**, 134437 (2019).

163. C. Zener, Physical Review **96**, 1335–1337 (1954).

164. Y. Liu and C. Petrovic, Physical Review B **96**, 054406 (2017).

165. W. Liu, Y. Dai, Y.-E. Yang, J. Fan, L. Pi, L. Zhang, and Y. Zhang, Physical Review B **98**, 214420 (2018).

166. Y. Sun and X. Luo, physica status solidi (b) **256**, 1900052 (2019).

167. Y. Liu and C. Petrovic, Physical Review Materials **3**, 014001 (2019).

168. S. Tiwari, M. L. Van de Put, B. Sorée, and W. G. Vandenberghe, Physical Review B **103**, 014432 (2021).

169. Z. Li, D.-H. Xu, X. Li, L. H.-J., X. Xi, Y.-C. Yu, and W. Wang, arXiv (2021).

170. J. A. Souza, Y.-K. Yu, J. J. Neumeier, H. Terashita, and R. F. Jardim, Physical Review Letters **94**, 207209 (2005).

171. B. D. White, W. M. Pätzold, and J. J. Neumeier, Physical Review B **82**, 094439 (2010).

172. T. Lorenz, U. Ammerahl, T. Auweiler, B. Büchner, A. Revcolevschi, and G. Dhalenne, Physical Review B **55**, 5914–5928 (1997).

173. J. W. Lynn, L. Vasiliu-Doloc, and M. A. Subramanian, Physical Review Letters **80**, 4582–4585 (1998).

174. A. Singh, A. Senyshyn, H. Fuess, T. Chatterji, and D. Pandey, Physical Review B **83**, 054406 (2011).

175. V. Carteaux, F. Moussa, and M. Spiesser, Europhysics Letters **29**, 251 (1995).

176. A. Ron, E. Zoghlin, L. Balents, S. D. Wilson, and D. Hsieh, Nature Communications **10**, 1654 (2019).

177. S. Sauerland, 'Dilatometrische studien zur elektronischen nematizität und magneto-elastischen kopplung in eisenbasierten supraleitern und magnetoelektrika', PhD Thesis (Ruprecht-Karls-Universität, Heidelberg, 2020).

178. C. Romero-Muñiz, R. Tamura, S. Tanaka, and V. Franco, Physical Review B **94**, 134401 (2016).

A Mini-Dilatometer Reference Measurements

Fig. A.1 shows thermal expansion reference measurements for the mini-dilatometer on high-purity aluminum samples. Copper samples for cell effect measurements were of similar lengths (1.016 mm and 1.993 mm) as the aluminum samples (1.080 mm, 1.913 mm, and 1.992 mm). Related measurements were performed within few days up to at most three months. Reference measurements for the standard-dilatometer are shown in Ref. [177].

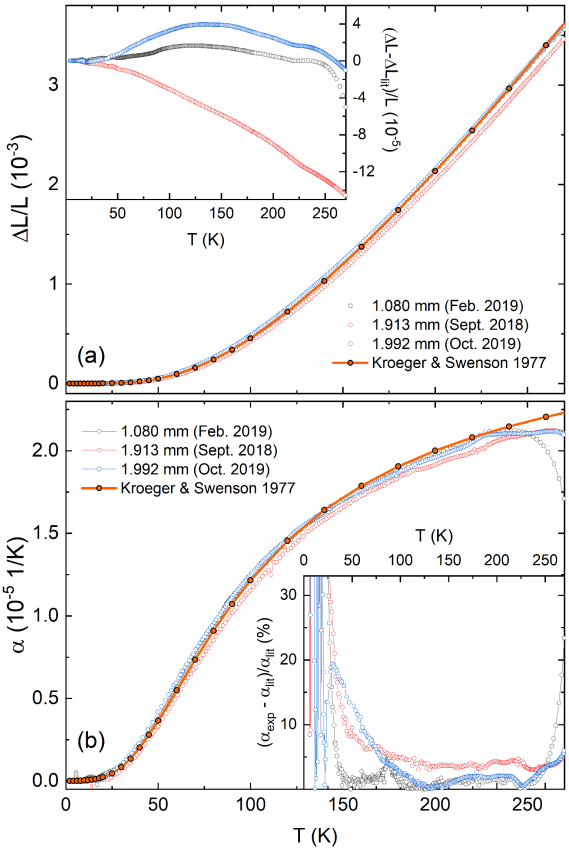

Figure A.1: Selected thermal expansion reference measurements on high-purity aluminum of different lengths in comparison to Ref. [50]. (a) Relative length changes $\Delta L/L$ and (b) thermal expansion coefficient α. Insets in (a) and (b) show absolute and relative deviations from $(\Delta L/L)_{\mathrm{lit}}$ and α_{lit}, respectively.

B $Cu_3Bi(SeO_3)_2O_2Cl$: Additional Figures

B.1 Critical Scaling at T_S: Background Subtraction

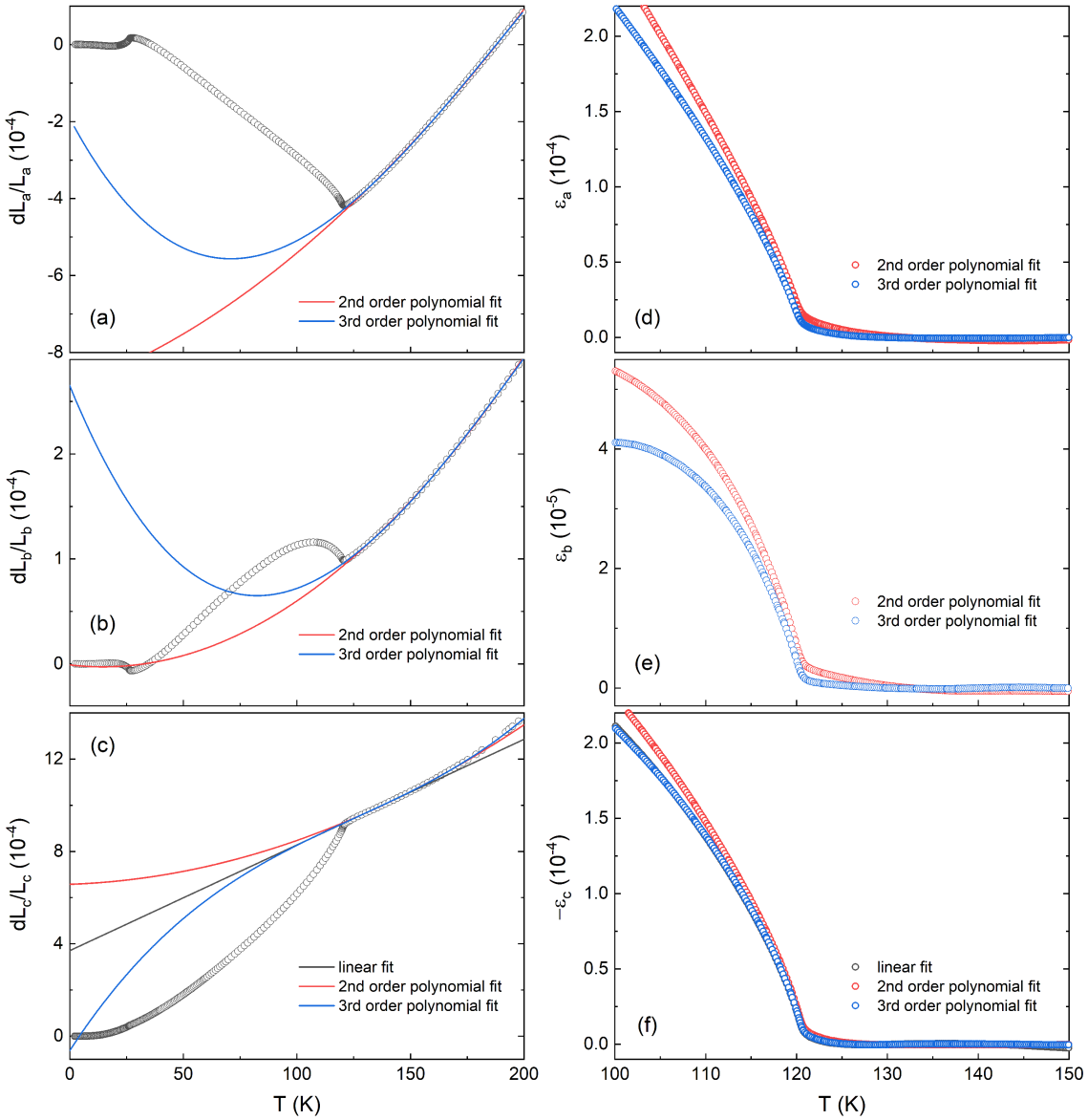

Figure B.1: (a-c) Different background fits to the dL_i/L_i data and (d-f) resulting spontaneous strain in $Cu_3Bi(SeO_3)_2O_2Cl$ around T_S.

B.2 In-Plane Thermal Expansion for $B \neq 0$

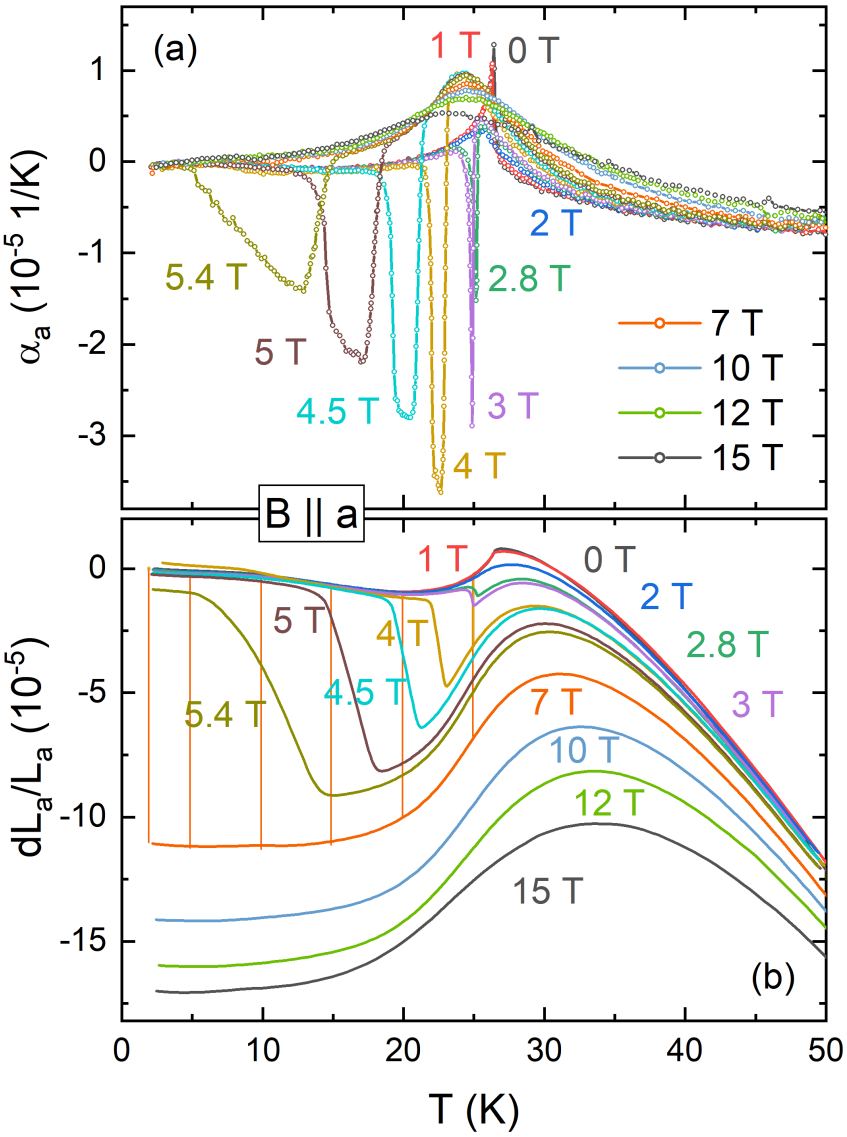

Figure B.2: (a) Thermal expansion coefficient and (b) relative length changes of $Cu_3Bi(SeO_3)_2O_2Cl$ for $B \parallel a$ at low temperatures and in fields up to 15 T. Vertical lines indicate $\Delta L(B)$ from 0 T to 7 T obtained from magnetostriction sweeps.

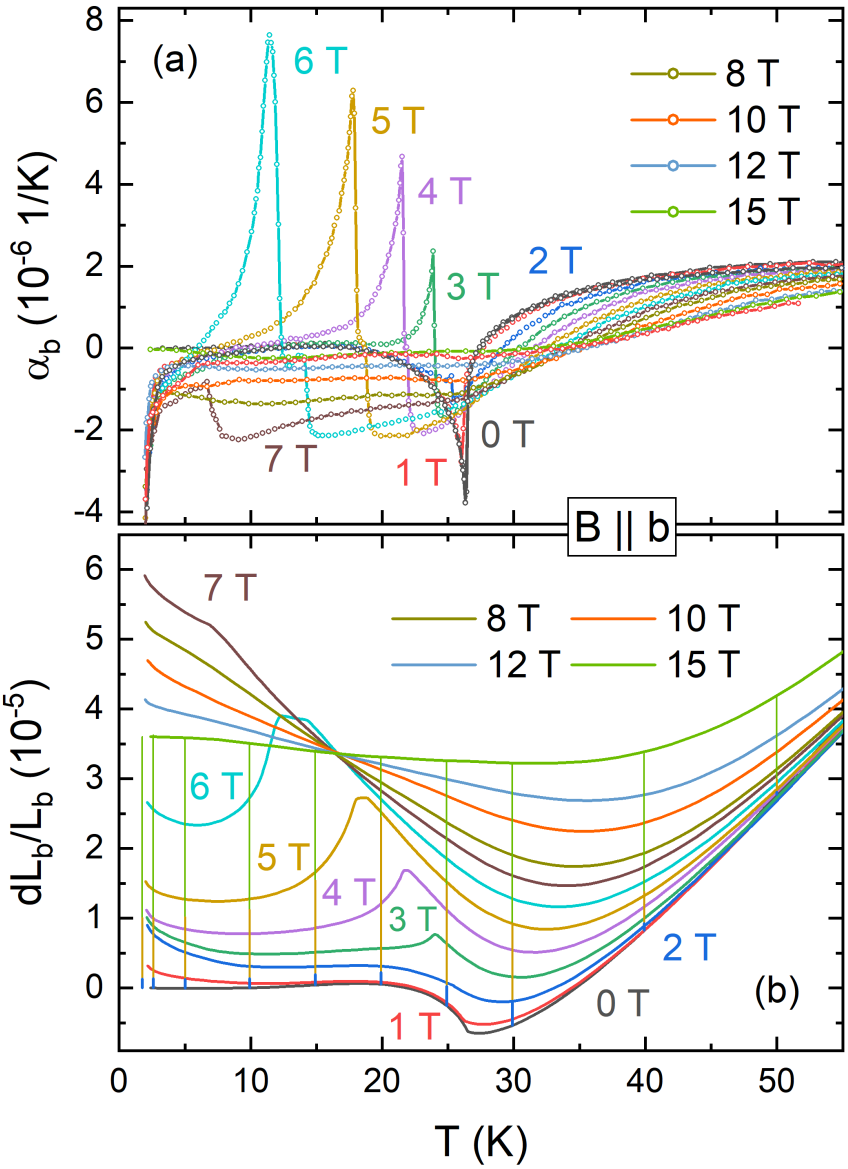

Figure B.3: (a) Thermal expansion coefficient and (b) relative length changes of $Cu_3Bi(SeO_3)_2O_2Cl$ for $B \parallel b$ at low temperatures and in fields up to 15 T. Vertical lines indicate $\Delta L(B)$ from 0 T to 2 T (blue), 5 T (brown) and 15 T (light green) obtained from magnetostriction sweeps.

B.3 In-Plane Magnetostriction

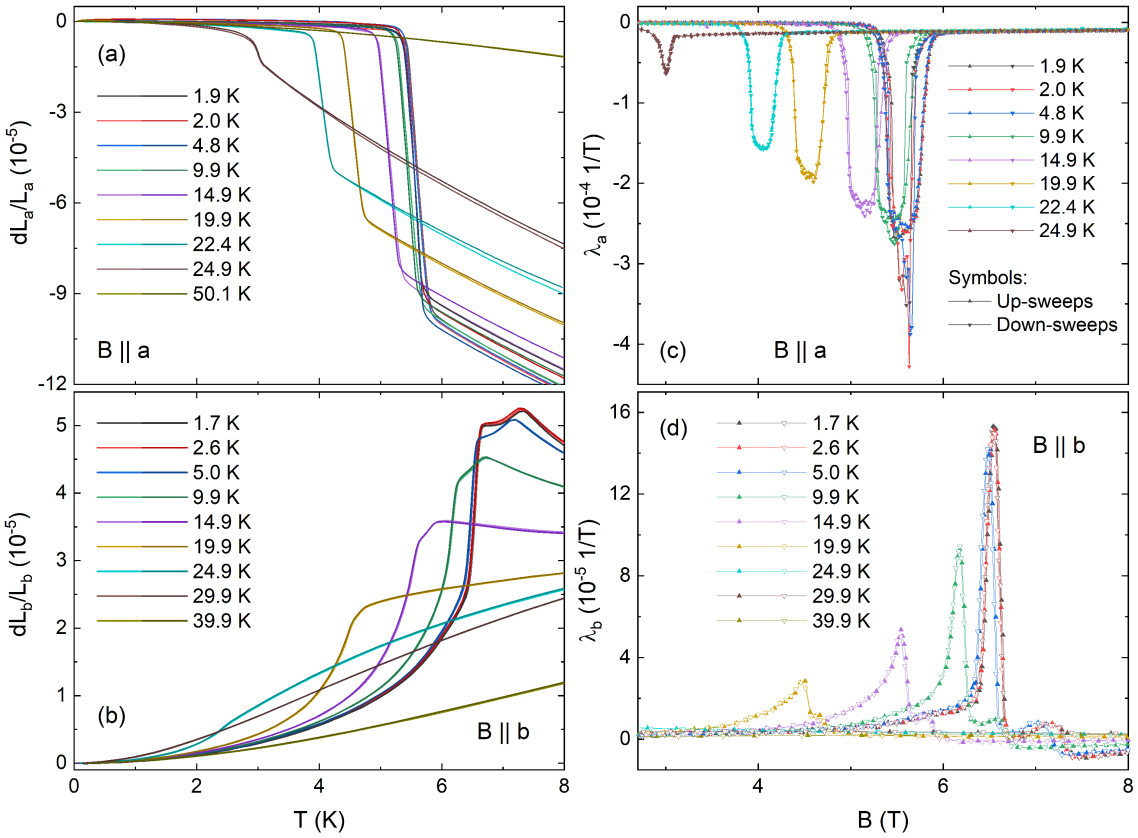

Figure B.4: (a-b) Magnetostrictive length changes $dL(B)/L(0)$ and (c-d) magnetostriction coefficient (c-d) of $Cu_3Bi(SeO_3)_2O_2Cl$ for $B \parallel a$ (a, c) and $B \parallel b$ (b, d) at temperatures up to 50 K. Closed (open) symbols signify up- (down-)sweeps.

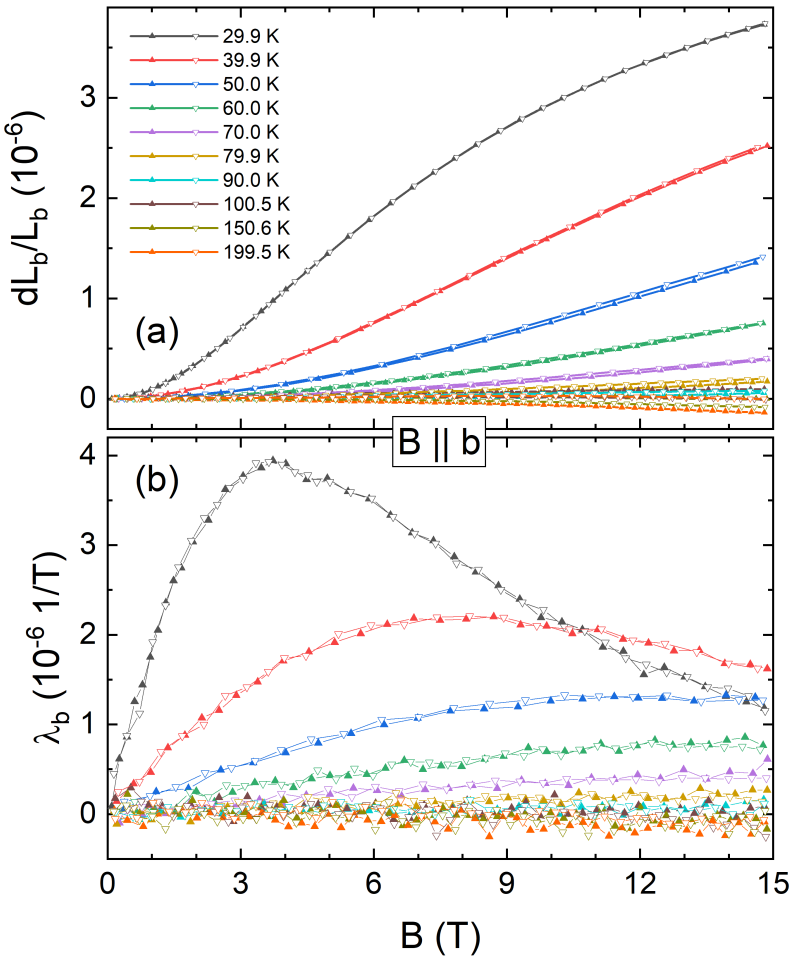

Figure B.5: (a) Magnetostrictive length changes $dL(B)/L(0)$ and (b) magnetostriction coefficients of $Cu_3Bi(SeO_3)_2O_2Cl$ for $B \parallel b$ at temperatures above T_N. Closed (open) symbols signify up- (down-)sweeps.

C $Cr_2Ge_2Te_6$: Additional Figures

C.1 Zero-Field Thermal Expansion – Mini-Dilatometer Data

Since measurements in applied magnetic field were only performed in the standard-dilatometer, thermal expansion data shown in the chapter on $Cr_2Ge_2Te_6$ (Ch. 5) are mainly from this dilatometer. However, zero-field thermal expansion measurements in the mini-dilatometer were of better quality, especially for the c-axis. These data are shown in Fig. C.1 in comparison to the standard-dilatometer zero-field data. The mini-dilatometer data set was used for the Grüneisen ratio Γ_i in Fig. 5.5.

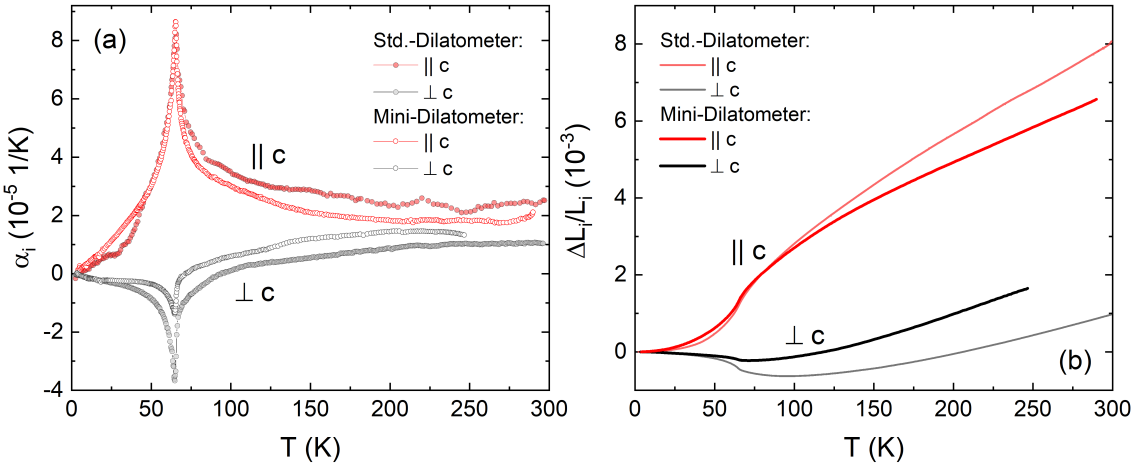

Figure C.1: Comparison of (a) thermal expansion coefficient and (b) relative length changes of $Cr_2Ge_2Te_6$ in zero-field as measured in the standard-dilatometer (closed circles in (a)) and the mini-dilatometer (open circles in (a)) on different samples.

C.2 Critical Scaling: $\mu\alpha_{\mathrm{mag}}T$

Logarithmic fits to the scaled magnetic contribution of the zero-field thermal expansion coefficient $\eta_i\alpha_{i,\mathrm{mag}}T$ are shown in Fig. C.2. Fit parameters are indicated in the graph. The data underscore the large temperature regime of logarithmic behavior already seen in Fig. 5.10.

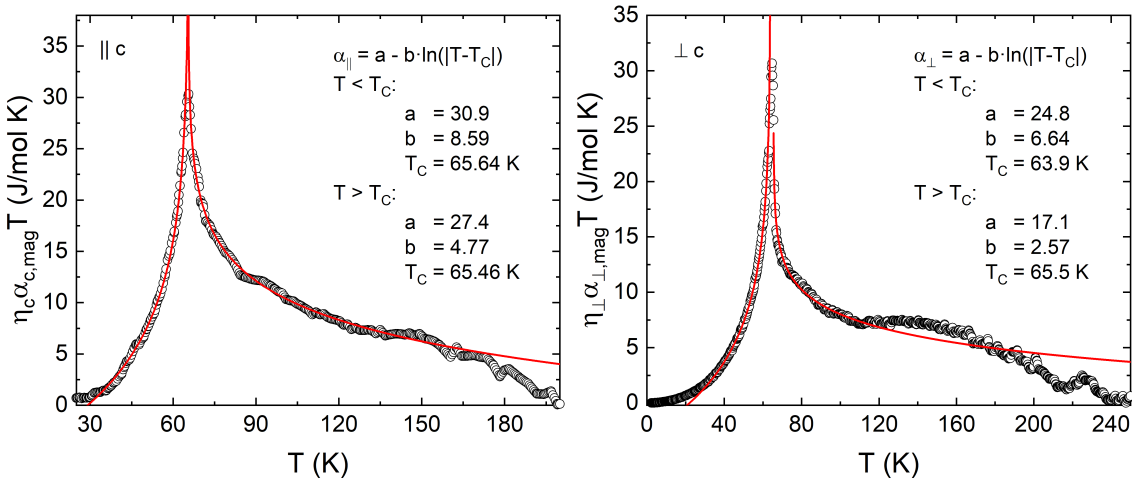

Figure C.2: Logarithmic fits to the scaled magnetic contribution of the zero-field thermal expansion coefficient $\eta_i\alpha_{i,\mathrm{mag}}T$ of $Cr_2Ge_2Te_6$.

C.3 Critical Scaling: Critical Fits to $\alpha_{i,\mathrm{mag}}$

Fig. C.3 shows the spontaneous strain $\varepsilon_{\mathrm{mag}}$ in magnetic fields $B \geq 0$ for both $B \parallel c$ and $B \perp c$ along with critical fits $\varepsilon_{i,\mathrm{mag}} = \varepsilon_0 + A \cdot |T - T_\mathrm{C}|^{2\beta_\mathrm{c}}$. Critical exponents β_c resulting from the fits are shown in Fig. 5.14.

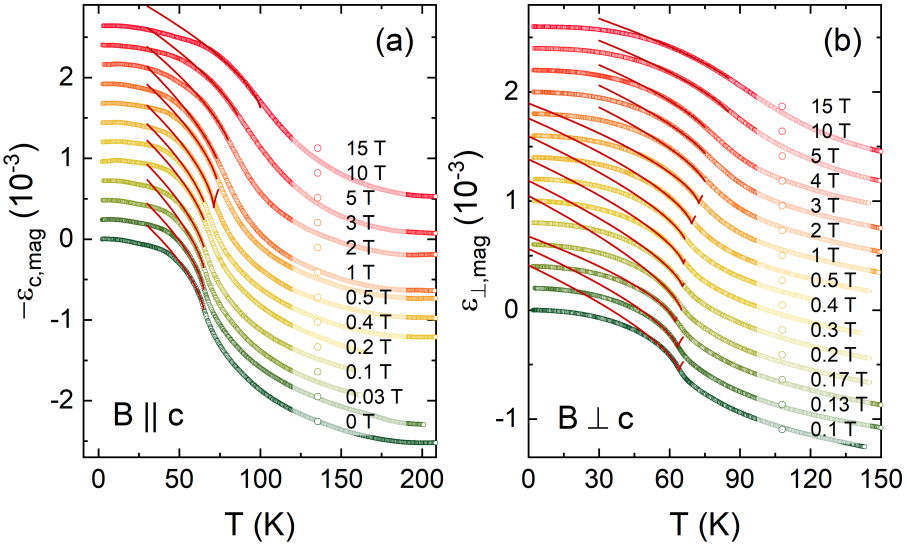

Figure C.3: Spontaneous strain $\varepsilon_{\mathrm{mag}}$ of $Cr_2Ge_2Te_6$ in magnetic fields $B \geq 0$ for (a) $B \parallel c$ and (b) $B \perp c$.

C.4 Universal Scaling of α_{mag}

A study of the magnetic entropy $\Delta S_{\mathrm{M}}(T,B)$ of $Cr_2Ge_2Te_6$ by Sun and Luo showed that under different magnetic fields up to 4.5 T $\Delta S_{\mathrm{M}}(T,B)$ can be scaled into a single curve independent of external field and temperature [166]. Such scaling behavior for continuous phase transitions has been observed experimentally in a wide range of materials and the limits of scaling, independent of the applied physical model such as a mean-field or 3D Ising model, were recently studied [178].

A similar scaling behavior as for the magnetic entropy can also be observed for the magnetic contribution to the thermal expansion coefficient (Fig. C.4 and Fig. C.5). For this purpose the $\alpha_{i,\mathrm{mag}}$ data at different fields are normalized to their respective peak value. Furthermore, the temperature above and below T_{C} is re-scaled independently:

$$\theta = \begin{cases} \frac{T_{\mathrm{C}}-T}{T_{r1}-T_{\mathrm{C}}}, & T \leq T_{\mathrm{C}} \\ \frac{T-T_{\mathrm{C}}}{T_{r2}-T_{\mathrm{C}}}, & T \geq T_{\mathrm{C}} \end{cases}$$

where T_{r1} and T_{r2} are scaling constants and in general arbitrary. For $B \parallel c$ the data were scaled to the data at 0.2 T, i.e., $T_{r1}(0.2\ T) = 0$ and $T_{r2}(0.2\ T) = 0$, whereas data for $B \perp c$ are normalized to the zero-field data. The zero-field data for both axes shows a much enhanced peak and was therefore not normalized to its peak value, but in a way to match with the data in applied magnetic field. Data from 0.5 T to 15 T for $B \parallel c$ can be scaled very well for $T < T_{\mathrm{C}}$ and up to about $\Theta = 0.07$ for $T > T_{\mathrm{C}}$ (Fig. C.4(a)). For $B \perp c$ data in the same field range scale well from about $\Theta = -0.08$ to $\Theta = 0.06$ (Fig. C.4(c)). T_{r1} and T_{r2} show a similar behavior as T_{r1} and T_{r2} for the magnetic entropy in [166].

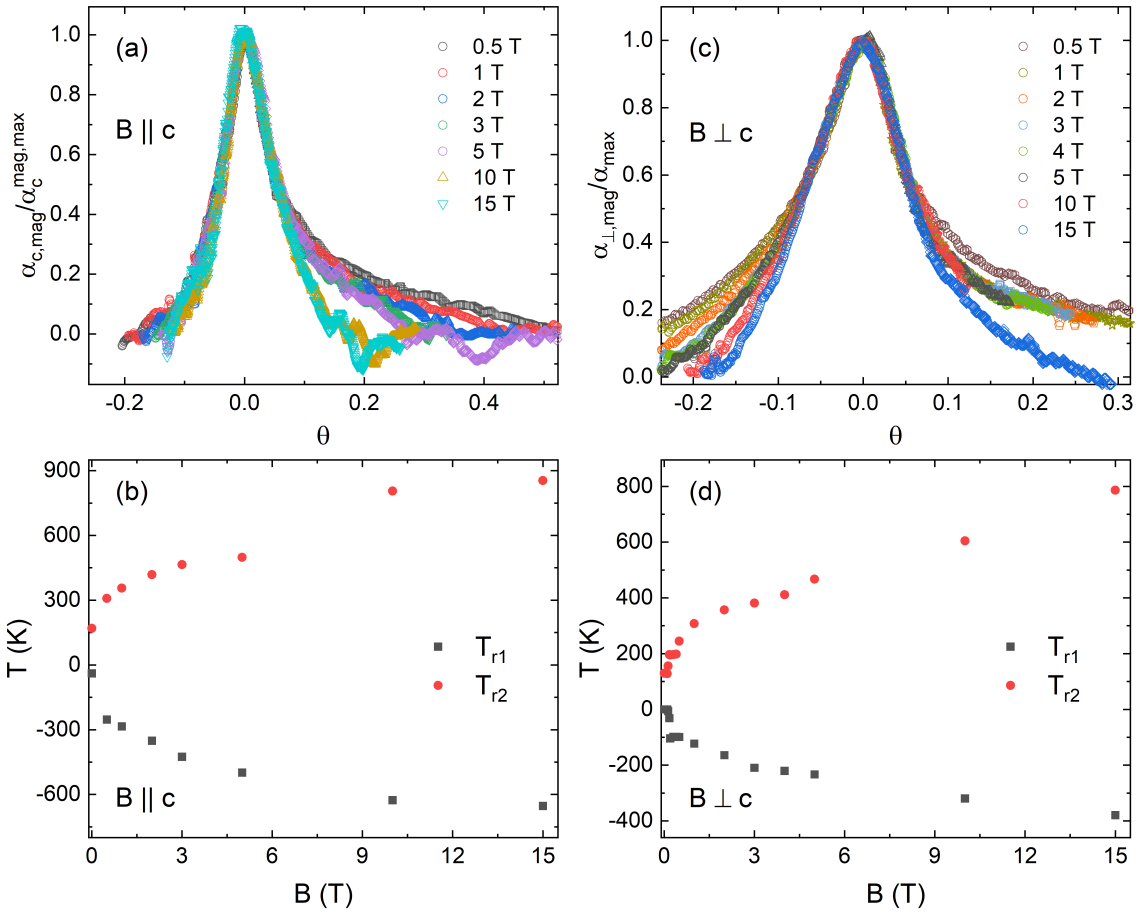

Figure C.4: Universal scaling behavior of $\alpha_{i,\mathrm{mag}}$ in $Cr_2Ge_2Te_6$ with scaling constants T_{r1} and T_{r2} for (a,b) $B \parallel c$ and (c,d) $B \perp c$.

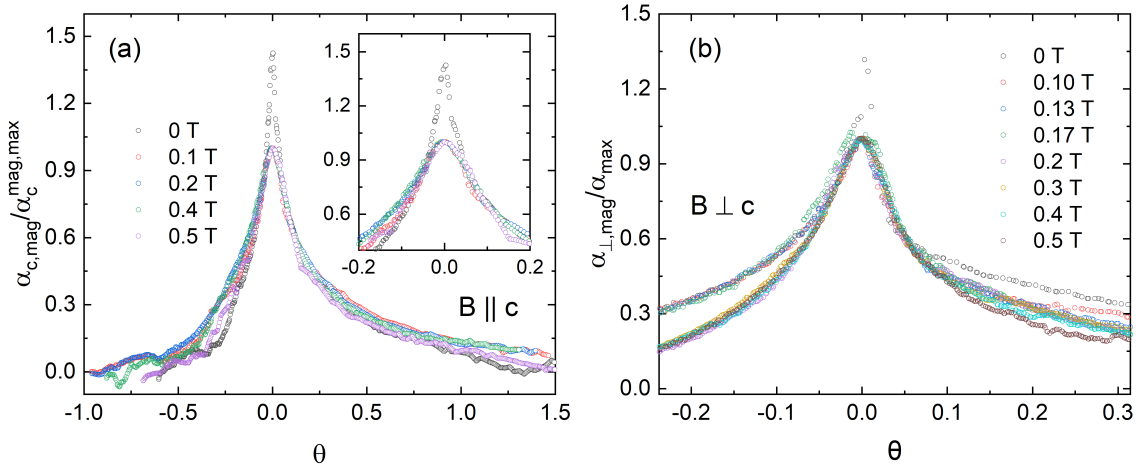

Figure C.5: Universal scaling behavior of $\alpha_{i,\mathrm{mag}}$ in $Cr_2Ge_2Te_6$ at low magnetic fields.

Acknowledgments

At this point I want to extend my thanks to the large number of people who made this work possible.

First and foremost I want to thank Prof. Dr. Rüdiger Klingeler who gave me the opportunity to work on these interesting materials. Thank you for your open door, the many enlightening discussions, and the helpful feedback on my work. I enjoyed learning from the way you think about experimental results and integrating your approaches into my own thinking. Thank you for your support, your trust and your honesty.

My gratitude also goes to Prof. Dr. Maurits Haverkort for taking on the role of second referee.

I want to thank Dr. Wolfgang Löser, Prof. Dr. Alexander Vasiliev, and Dr. Saicharan Aswartham for providing the Gd_2PdSi_3, $Cu_3Bi(SeO_3)_2O_2Cl$, and $Cr_2Ge_2Te_6$ samples, respectively. I thank Dr. Matthias Frontzek for discussions on Gd_2PdSi_3 and Dr. Saicharan Aswartham for his feedback on the $Cr_2Ge_2Te_6$ chapter.

Many people helped to proofread and improve what has been written in these pages. I want to thank Jan Arneth and Lukas Gries for the effort they put into reading through the whole thesis to find spelling errors, repetitions and hard to read sentences. A thanks goes to Marco Hoffmann for proofreading the experimental methods part, as well as to Ahmed Elghandour and Kaustav Dey for a final proofreading of the Gd_2PdSi_3 manuscript. I especially thank Martin Jonak for meticulously correcting the $Cu_3Bi(SeO_3)_2O_2Cl$ and $Cr_2Ge_2Te_6$ chapters and giving ideas on how to improve the wording. My gratitude extends to all of you for putting your time and efforts into helping me succeed. You have been great colleagues over the past years. This also includes Dr. Changhyun Koo, Dr. Liran Wang, Dr. Johannes Werner, Dr. Sven Sauerland, Waldemar Hergett, Lena Spillecke, Lennart Singer and the rest of present or past members of F25. Each one of you made our work group what it is with its spirit of support and encouragement. It was my pleasure to work alongside you and to have one or the other chat in between my often quite focused work. Thank you especially to Dr. Liran Wang and Dr. Sven Sauerland for teaching me how to do thermal expansion measurements and helping me with my first measurements.

Our experiments would not be possible had we not a constant supply of helium as well as one or the other new part from the precision mechanics workshop. Thank

you to Rudi Eitel for keeping the liquefier running and Werner Lamade, Julia Bing, and Christian Herdt for the support with new hardware, ranging from precisely cut Cu samples for calibration measurements to the many pieces of our new zero-field dilatometry setup.

My gratitude also goes to those who work (or worked) mostly in the background here at the Kirchhoff Institute and our graduate school, the HGSFP, to provide the environment for our scientific work, both in administration and IT. As representatives for many others I want to thank Dr. Harald Jacobsen, Dr. Robert Weis, apl. Prof. Sandra Klevansky, Beatrice Schwöbel, Corina Müller, and Jessica Bender for their direct or indirect support.

I had the pleasure to supervise Marco Hoffmann, Rahel Ohlendorf, Lukas Fischer, Lukas Gries and Jan Arneth for their bachelor and master theses. It was my joy and honor to walk through this part of your life with you and see you grow. Thank you for your willingness to learn and to let me teach you what I could.

Martin Jonak and Marco Hoffmann, I very much appreciate your friendship and I will not forget the intense weeks we lived through together at the EMFL facilities in Nijmegen and Dresden-Rossendorf.

Finally, on a more personal and emotional level: There are many more people who are not directly connected to this work, but whose friendship, encouragement and correction have shaped who I am, how I think and how I live. You also have part in this work and its success. I might not name you here, because the list would be fairly long, but still: thank you for your friendship! So to name but a few:

Thank you Jürgen and Sabine Spachmann, my dear parents, for your unceasing support and love. Your generosity is overwhelming and I am deeply grateful for who you are.

Thank you Matthias Keller, my mentor, for the wisdom and understanding you have shared with me over the past four years – and also for celebrating my scientific successes with me. Your guidance has already had a lasting effect on my thinking and I am looking forward to what is to come.

A thanks to my flat mates Aaron Bürger and Florian Friedrich. Our flat was a place of rest and joy for me. Thank you for your friendship, the brief or longer conversations, games nights and more.

And then there is one person who made many processes during the last one and a half years of this work feel much lighter and easier than they would have been otherwise. Rebekka Neumann, my fiancée, even though we were often separated by the much too large distance between Heidelberg and Berlin, your love and support have been invaluable to me over the past months. Thank you. I love you.

And last but not least: My deepest gratitude goes to the God I love and honor. The one who is love and life. My hope and peace, my strength and shield, in many situations when I was troubled or insecure. And my joy whenever I count the many blessings in my life.

Soli deo gloria.